Numerical Modeling of Granular Bulk Cargo

Vom Promotionsausschuss der
Technischen Universität Hamburg
zur Erlangung des akademischen Grades

Doktor-Ingenieurin (Dr.-Ing.)

genehmigte Dissertation (Monografie)

von
Wibke Ricarda Düsterhöft-Wriggers

aus
Hannover

2025

Gutachter:

1. Gutachter: Prof. Dr.-Ing. Thomas Rung

2. Gutachter: Prof. Antonia Larese, PhD

Tag der mündlichen Prüfung:

14. Februar 2025

Vorsitzender des Prüfungsausschusses:

Prof. Dr.-Ing. Robert Seifried

Digital Object Identifier (DOI): https://doi.org/10.15480/882.14966
Open Researcher Contributor ID (ORCID): https://orcid.org/0000-0003-3783-4837

Creative Commons Lizenzvertrag
Dieses Werk ist unter einer Creative-Commons-Lizenz Namensnennung 4.0 (CC BY 4.0) zugänglich. Das bedeutet, dass es vervielfältigt, verbreitet und öffentlich zugänglich gemacht werden darf, auch kommerziell, sofern dabei stets der Urheber, die Quelle des Textes und o. g. Lizenz genannt werden. Die genaue Formulierung der Lizenz kann unter
https://creativecommons.org/licenses/by/4.0/legalcode.de
aufgerufen werden.

Abstract

Simulating the mechanism of granular cargo transportation on vessels is a complex multiphysical problem, including the vessel's motion excited by waves and the behavior of the granular material on board. Several failure mechanisms such as, e.g., shifting of the cargo, a wet base scenario where saturated material is present at the bottom of a cargo pile, dynamic separation of the water inside the cargo and the cargo itself, or liquefaction are deemed possible to be responsible for bulk carrier losses transporting unsaturated nickel and iron ores.

To study cargo behavior on vessels during voyages, the thesis implements a monolithic multiphysics approach, including constitutive models representing the mentioned cargo failure mechanisms and applying these models to parameter studies exploring different loading scenarios. A rigid perfectly-plastic constitutive equation and an incompressible Neo-Hookean constitutive equation are introduced in the Finite Volume method and verified and validated on multiple test cases. A monolithic approach is chosen where the Volume of Fluid method indicates the different water, air, and granular medium phases.

A porous material model is introduced to represent the interaction of air-water and granular material, and three formulations of momentum and pressure equations for porous materials are thoroughly compared in several test cases. A simplified set of equations is validated, proving its applicability for specific porous Reynolds numbers. The resulting simplified porous momentum model is coupled with the rigid-perfectly plastic material to simulate water flow with a free surface through moving porous granular material. This coupled method is verified using an embankment failure problem and subsequently applied to several two-dimensional cargo hold studies which encompass various saturation levels of the material and different initial and excitation conditions. The two-dimensional studies clearly indicate that to prevent cargo motion, the cargo should always be loaded as flat as possible. Sliding can be observed for rolling amplitudes larger than 10°. Additionally, it is demonstrated that placing wet cargo on top of drier cargo can lead to catastrophic cargo sloshing.

In the final chapter of the thesis, a complete three-dimensional case study is presented, studying the incident of the "Jian Fu Star," a vessel that was lost in 2010 carrying Indonesian nickel ore. By applying a three-phase Volume of Fluid approach together with the rigid-perfectly plastic material model, wave boundary conditions, and a three-degrees-of-freedom rigid body motion solver, the incident is reconstructed from the given information in the incident report and a severe cargo shift and list of the vessel can be observed.

Acknowledgements

The opportunity to work at the Institute for Fluid Dynamics and Ship Theory at the Hamburg University of Technology within an inspiring, talented team under the supervision of Prof. Dr.-Ing. Thomas Rung is something I deeply appreciate. His scientific integrity, inimitable expertise, and commitment to Computational Fluid Dynamics, which he shared passionately during in-depth discussions, were invaluable for this work. Further, his insights helped me to develop skills I will continue using during my career, for which I am very grateful. I want to express my deepest gratitude for the constant trust in me to work independently from the first day until the end of the thesis and for the chance to develop as a lecturer and work with students and within projects.

Furthermore, I thank Prof. Antonia Larese for being my second assessor and Prof. Dr.-Ing. Robert Seifried for chairing the examination board.

Special thanks go to all my former colleagues at the Institute for Fluid Dynamics and Ship Theory. I thoroughly enjoyed the collegiate and motivated working atmosphere and will never forget our shared pizza lunches, naval architecture traditions, and institute Christmas parties. Further, I thank my former colleagues Jörn Kröger and Thierry Maquil for introducing me to the intricacies of FreSCo$^+$ and Niklas Kühl for his continuous encouragement during the later stages of this work. I am honored that many of my former colleagues have become lifelong friends, especially my favorite office mate, Marzia.

Finally, and most importantly, I thank my family, especially Christian and Onno, for their patience and continuous support.

Contents

Nomenclature

Abbreviations

3DoF	Three Degrees of Freedom
BM	Metacentric Radius
CDS	Central Differencing Scheme
CEDEX	Centre for Hydrographic Studies
CICSAM	Compressive Interface Capturing Scheme for Arbitrary Meshes
Co	Courant number
CoG	Center of Gravity
CPU	Central Processing Unit
CV	Control Volume
DEM	Discrete Element Method
FDM	Finite Difference Method
FEM	Finite Element Method
Fn	Froude number
FSI	Fluid-Structure Interaction
FV	Finite Volume
FVM	Finite Volume Method
GBWG	Global Bauxite Working Group
GM	Metacentric Height

HPC	High-Performance Cluster
$HRIC$	High Resolution Interface Capturing Scheme
$HSVA$	Hamburg Ship Model Basin
$IFSTTAR$	The French Institute of Science and Technology for Transport, development and networks
IGC	International Grain Code
IMO	International Maritime Organization
$IMSBC$	International Maritime Solid Bulk Cargoes Code
KB	distance from keel to center of buoyancy
KC	Keuler-Carpenter number
KG	distance from keel to center of gravity
LoA	Length over All
Lpp	Length between perpendiculars
MC	Moisture Content
NB	adjacent neighbor control volume centers
$NLLS$	Non-Linear Least-Squares
$PFEM$	Particle Finite Element Method
$QUICK$	Quadratic Upstream Interpolation for Convective Kinematics
Re	Reynolds number
Re_P	Porous Reynolds number
RHS	Right-Hand Side
$SIMPLE$	Semi-Implicit Method for Pressure Linked Equations
$SOLAS$	International Convention for the Safety of Life at Sea
SPH	Smoothed-Particle Hydrodynamics

TML	Transportable Moisture Limit
$TUHH$	Hamburg University of Technology
UDS	Upwind Differencing Scheme
VoF	Volume of Fluid

Lower-case Latin

Δl	length increment
Δt	time step size
Δx_1	grid spacing in the x_1-direction
Δx_2	grid spacing in the x_2 -direction
Δx_3	grid spacing in the x_3 -direction
$\dot{\hat{m}}$	porous mass flux
$\dot{m}$	mass flux
$\hat{f}^G$	gravity force
$\hat{f}^P$	pressure force
$\hat{f}^R$	porous resistance force divided by density
$\hat{m}$	initial mass
$\hat{v}_i$	Darcy velocity vector
$\hat{x}_i$	Eulerian coordinate of reference configuration
a_i	acceleration vector
a_i^C	convective term
a_i^D	diffusion term
a_i^I	inertia term
a_w	diffusion constant in elliptic relaxation
a_{fit}	constant for data fit

b_i^l	body force vector in moving reference system
b_i	body force vector in fixed reference system
b_{fit}	constant for data fit
c	Air mixture fraction
c_A	Air mixture fraction in coupled model
c_F	constant for non-linear term of diameter dependant resistance law
c_S	Soil mixture fraction
c_{fit}	constant for data fit
d	distance between control volume center and neighbor control volume center
d_i	distance vector between control volume center and neighbor control volume center
e	void ratio
$e_i^{t_0}$	initial Lagrangian coordinate system
$e_i^{t_1}$	current Lagrangian coordinate system
e_{ij}	Euler-Almansi strain tensor
f^R	porous resistance force
$f^{'}$	point at which face value is obtained if CDS is applied on unstructured mesh
f_b	boundary face
f_i	source term vector
$f_{i,expl}$	explicit wall boundary shear force
$f_{i,impl}$	implicit wall boundary shear force
g	gravity constant
g_i	gravity vector
h	height of water dam

h_0	initial height of water dam
h_w	free surface height
h_{cargo}	cargo pile height
h_{max}	maximum cargo pile height
$h_{wetlayer}$	height of wet cargo layer
i	hydraulic gradient
k	intrinsic permeability
k_0	initial permeability
k_c	Drucker-Prager material constant
k_{11}, k_{22}, k_{33}	radii of gyration
l	width of water dam
l_0	initial width of water dam
m	(current) mass
m^d	mass of dry granular material
m^{total}	total (wet) mass of granular material
m_c	constant for regularized Bingham fluid
m_{ch}	cargo mass in hold
n	porosity
n_c	constant porosity
n_i	normal vector at face
p	pressure
p_{ref}	reference pressure
q_i	divergence of deviatoric stress tensor of neo-Hookean material
$r_{P,i}$	distance vector between center of gravity and point P

s	cargo pile steepness
s^W	degree of saturation
t	time
t_i	tangential vector at face
u_i	displacement vector
v_i^{dsk}	velocity of neo-Hookean disk
v_i^{fix}	relative velocity to fix neo-Hookean cylinder in the center of the domain
v_i^{S*}	soil skeleton velocity vector in coupled model
v_i	velocity vector
$v_{m,i}$	mesh velocity vector
w_c	water content of granular material
x_i	Eulerian coordinate of current configuration
x_w	distance to wave generating boundary

Upper-case Greek

Γ_ϕ	generic diffusion coefficient
Ω^{t_0}	reference configuration
Ω^{t_1}	current configuration
Φ	yield function
Ψ	plastic potential
Θ	generic field variable

Lower-case Greek

α	constant for linear term of diameter dependant resistance law
α_R	time-dependent roll angle

$\alpha_w(x_w)$	smooth function defining sponge layer for wave generating boundary conditions
α_ϕ	Drucker-Prager material constant
α_{int}	constant weighting factor for the Rhie-Chow interpolation
β	constant for non-linear term of diameter dependant resistance law
β_w	factor for wave generating boundary conditions
δ_{ij}	Kronecker delta
$\dot{\epsilon}_{ij}$	strain rate tensor
$\dot{\lambda}$	plastic multiplicator
$\dot{\omega}_i$	local angular acceleration
ϵ	strain
ϵ_{ijk}	Levi-Civita symbol
ϵ_{small}	small constant
η_S	second Lamé constant
γ	constant for time derivative term of diameter dependant resistance law
γ_c	coefficient that determines the non-orthogonal correction approach
κ	coefficient that determines higher-order convection scheme
λ	first Lamé constant
λ_{CDS}	interpolation constant for CDS
μ	dynamic viscosity
μ^{G*}	modified dynamic viscosity of granular material in reduced coupled equations
μ^{S*}	modified dynamic viscosity of soil in reduced coupled equations
ν	kinematic viscosity

ω_i	angular velocity vector
ϕ	angle of repose
ρ	density
ρ_0	initial density
ρ_d	dry density of granular material
ρ_{wet}	wet density of granular material
$\sigma_{ij}^{'}$	effective stress tensor
σ_{ij}	Cauchy stress tensor
$\tau_{ij}^{'}$	deviatoric stress tensor
τ_{ij}^{A}	deviatoric stress tensor in fluid phase
τ_{ij}^{S}	deviatoric stress tensor in solid phase
τ_{ij}	deviatoric stress tensor
τ_y	yield stress
θ	flux-blending constant
υ	Poisson ratio

Sub- Superscripts

$(\cdot)^0$	trial state for elasto-plastic model
$(\cdot)^A$	air
$(\cdot)^F$	fluid
$(\cdot)^G$	granular
$(\cdot)^m$	iteration index of iterative algorithm
$(\cdot)^n$	time level of time discretization
$(\cdot)^S$	soil skeleton/solid
$(\cdot)^W$	water

$(\cdot)^{'}$	correction term
$(\cdot)^{m*}$	continuity fulfilling value in iteration
$(\cdot)^{non-ortogh.}$	non-orthogonal part
$(\cdot)^{ortogh.}$	orthogonal part
$(\cdot)_1$	first component of vector
$(\cdot)_2$	second component of vector
$(\cdot)_3$	third component of vector
$(\cdot)_D$	center of control volume downstream of face
$(\cdot)_f$	face of control volume
$(\cdot)_L$	center of control volume on the left of the face
$(\cdot)_P$	center of control volume
$(\cdot)_R$	center of control volume on the right of the face
$(\cdot)_U$	center of control volume upstream of face
$(\cdot)_{cargo}$	properties of loaded cargo
$(\cdot)_{empty}$	properties of hull without loaded cargo
$(\cdot)_{P_B}$	variable at center of boundary control volume
$(\cdot)_S$	properties of vessel loaded with cargo
$(\cdot)_{UU}$	center of control volume far-upstream of face
$\dot{(\cdot)}$	flux

Upper-case Latin

ΔD	interface width
ΔV_P	discrete volume of control volume
$\dot{\hat{V}}$	volume flux
$\hat{A}$	total area

$\hat{F}_{ij}$	Lagrangian deformation gradient
$\hat{V}$	initial volume
$\hat{X}_i$	Lagrangian coordinate of reference configuration
$\tilde{A}$	Darcy law coefficient
$\tilde{B}$	extended Forchheimer equation coefficient
$\tilde{C}$	extended Forchheimer equation coefficient
A	area, surface of control volume
A^*	linear coefficient for hydraulic gradient resistance law
A_i	face normal vector
A_{col}	area of 2D water dam
A_{NB}	neighbor coefficient matrix
A_P	main-diagonal coefficient matrix
A_R	maximum rolling amplitude
B	width of vessel
B^*	non-linear coefficient for hydraulic gradient resistance law
B_{ij}	Cauchy-Green deformation tensor
C	cohesion
C_{max}	maximum cohesion
C_{sat}	saturated cohesion
D	draft of vessel
D_{50}	mean grain diameter
D_{perm}	diameter of permeameter
E	Young’s modulus
E_{c_A}	deviation error for air mixture concentration

E_i	Eulerian coordinate system
F	freeboard of vessel
F_{ij}^{e}	elastic Eulerian deformation gradient
F_{ij}^{P}	plastic Eulerian deformation gradient
F_{ij}	Eulerian deformation gradient
F_i	force vector acting on rigid body
F_{wall}	constant for wall boundary condition of neo-Hookean material
G_{ij}	inverse of the Eulerian deformation gradient tensor
H	determinant of Eulerian deformation gradient tensor
I_1	first invariant
I_{ij}	inertia tensor
I_{wl}	transverse moment of inertia of the water plane area of vessel
J	Jacobi determinant
J_2	second invariant
K	hydraulic conductivity
L	length of computational domain
M	constant for arctan interpolation
M_j	moment vector acting on rigid body
N	constant for arctan interpolation
N_{CV}	number of control volumes
Q	volume flux
S	source term including explicit terms
T	time scale
T_R	rolling period

V	(current total) volume
$V^{air,F}$	air volume in two-phase fluid
V_w	displacement of vessel
X_i	Lagrangian coordinate of current configuration

Chapter 1

Introduction and Motivation

Ore is a valuable cargo worth several thousand dollars per tonne. Nickel ore, in particular, is a widely transported bulk cargo that is used, for example, to produce stainless steel, batteries and electronics. Therefore, imports to China have increased significantly from \$420M to \$3.51B between 2006 and 2013 [93].

In the period from 2009 to 2023, eleven bulk carriers carrying nickel or iron ore sank, and eight of them were on their way to China. This led to a large number of casualties, which is why nickel ore is called the ”deadliest cargo in the world” (e.g., Poulsen [99] and Schuler [107]). To illustrate the dramatic consequences, Fig. 1.1 depicts the capsizing of the vessel ”Trans Summer” during a typhoon, where, luckily, all crew members were saved. Other bulk carriers had to abort their voyage or take stability-enhancing measures to avoid capsizing. For example, Lee [73] describes the incident of the ”Alam Manis”, which experienced a cargo failure that resulted in a list of 17.5° to starboard, and is displayed in Fig. 1.2. The vessel carried nickel ore and could be saved by redistributing the cargo in the holds.

Figure 1.1: Capsizing of bulk carrier ”Trans Summer” carrying nickel ore. Photo courtesy to HKG Flying Service, extracted from DNV GL [24] and Munro et. al [89].

Table 1.1 lists all vessels lost between 2009 and 2022 and indicates their main dimensions as well as the type of cargo. It is noticeable that from 2010 onwards, predominantly Indonesian

(a) During towing (b) At safe anchorage

Figure 1.2: Stability incident of bulk carrier ”Alam Manis” carrying nickel ore (from Lee [73]).

(a) Dry stockpiles (b) Wet stockpiles

Figure 1.3: Nickel ore stockpiles in different weather conditions [109].

nickel ore led to the accidents. From 2010 to 2013, as well as in 2018 and 2019, Indonesia was the leading nickel ore exporter to China [93]. The ore in Indonesia is usually stored in stockpiles without coverage and can become wet due to heavy rainfall, as depicted by Fig. 1.3(b). Note that storing conditions are handled differently in other major ore exporting countries such as Australia and Brazil.

To ensure safety at sea the International Convention for the Safety of Life at Sea (SOLAS) was adopted by the International Maritime Organization (IMO) in 1974 and included a chapter on the carriage of cargo. Extensions of the provisions for bulk cargoes are given in the International Grain Code (IGC) and International Maritime Solid Bulk Cargoes Code (IMSBC), the latter of which includes the rules for the transportation of nickel and iron ore. Until the adopted version of the IMSBC code in 2022 [52], the group A cargoes, including nickel and iron ore, were defined as ”cargoes which may liquefy” if shipped at a moisture content (MC) exceeding their ”Transportable Moisture Limit” (TML) [53]. Liquid cargoes – that are not intended – substantially reduce the dynamic stability of the ship.

Table 1.1: List of bulk carriers carrying nickel or iron ore lost due to cargo shifting (liquefaction) between 2009 until 2022. Extracted from ”Bulk Carrier Casualty Reports” of INTERGARGO [54, 55].

Vessel name	DWT [t]	LoA [m]	B [m]	year	cargo	loss of lives
Black Rose	37657	187.7	28.4	2009	Indian iron ore fines	1
Asian Forest	14434	128.0	20.0	2009	Indian iron ore fines	0
Jian Fu Star	45108	189.8	31.3	2010	Indonesian nickel ore	13
Nasco Diamond	56893	185.6	32.3	2010	Indonesian nickel ore	22
Hong Wei	50149	189.8	32.3	2010	Indonesian nickel ore	10
Vinalines Queen	56040	190.0	32.3	2011	Indonesian nickel ore	22
Harita Bauxite	48891	192.0	32.0	2013	Indonesian nickel ore	15
Trans Summer	56824	190.0	32.0	2013	Indonesian nickel ore	0
Bulk Jupiter	56009	190.0	32.3	2015	Malaysian Bauxite	18
Emerald Star	57367	190.0	32.0	2017	Indonesian nickel ore	10
Nur Allya	52378	190.0	32.0	2019	Indonesian nickel ore	27

Liquefaction is a process in which the state of saturated or partially saturated soil changes from a solid to a liquid and is mostly studied in the context of earthquakes, e.g., Bian et al. [7], Di et al. [22, 23], Elgamal et al. [31] and Unno et al. [122]. In a geotechnical sense, liquefaction occurs when the pore water pressure exceeds the effective stress and the grains lose contact. In these cases, the compression of the soil skeleton increases the pore water pressure, and at the same time, the permeability of the soil is low so that the pore water cannot escape. Therefore, to model geotechnical liquefaction, a compressible constitutive equation, kinematic hardening, and a finite strain elasto-plastic formulation are required, cf. Bardet [5], Mrǒz et al. [88] and Yang et al. [137].

Since no exact cargo data was recorded for the ships involved in the accidents, it must be clarified whether their cargo experienced liquefaction in a geotechnical sense or other cargo failure mechanisms depending on saturation. Results of related centrifuge tests that mimicked the pressure conditions in the holds failed to detect pore water pressure levels that yield liquefaction [56]. Moreover, it is noted that the cargo was not fully saturated, and therefore much of the containing air must be displaced in order for the pore water pressure to exceed the effective stress. These findings reduce the likelihood that geotechnical liquefaction is the responsible failure mechanism.

Figure 1.4: Bauxite cargo exhibiting water separation on the top of the cargo pile and in the corners of the hold. Extracted from the report of the ”Global Bauxite Working Group” (GBWG) [41].

In order to study the behavior of iron ore after the accidents in 2009, a ”Technical Working Group” of the IMO was established, and the cargo was observed by laser techniques during four voyages. Slight compactions of the ore during voyages and a higher final moisture content at the bottom of the cargo were detected. This phenomenon was called ”wet base” and led to higher cargo displacements due to local slip failures at the corners of the hold [56]. Expressed water collected in the corners of the hold and further eroded the cargo pile.

Another ”Global Bauxite Working Group” (GBWG) was set up following the ”Bulk Jupiter” accident to study the behavior of Bauxite during a voyage, which – until then – was not classified as group A cargo [53]. To this end, preliminary results of two-dimensional cargo hold studies described in this thesis have been presented at project meetings where representatives of the GBWG were present. In the report of the GBWG [41], based on their accumulated knowledge, a new phenomenon leading to vessel instability was introduced. As seen in Fig. 1.4, water gathered on top of the cargo after the voyages. Correia [13] identified a process for finer bauxites in hexapod tests in which water is forced upwards from the cargo, hereinafter called ”dynamic separation”. In the current amendment of the IMSBC code [52], the definition of group A cargo was therefore modified to: ”A cargo which possesses a hazard due to moisture that may result in liquefaction or dynamic separation if shipped at a *MC* in excess of its TML.” Possible cargo failure mechanisms for unsaturated ores or grains are concluded to be

- shifting of cargo,
- wet base,
- dynamic separation and
- liquefaction.

Cargo shifting can occur for all granular cargo materials, including dry cargo. The other three mechanisms are influenced by the water content of the cargo.

Several review papers and numerical models addressing cargo transport on bulk carriers have been published in recent years. Zou et al. (2013) used a level-set based Finite Volume (FV) free-surface method to study the sloshing of highly viscous fluids in rectangular tanks [141]. They concluded that, for beam wave conditions, viscous fluids have an adverse effect on vessel stability. Munro et al. [89] published a review paper on the general dangers of nickel and iron ore on board bulk carrier vessels in 2016, which analyzes the available accident reports and investigates the causes of bulk carrier losses. A few years later, a Discrete Element Method (DEM) based model was introduced by Ju et al. [60, 59] to simulate liquefaction on merchant vessels. Coupling a non-newtonian fluid with a simplified body surface method to capture the vessel response was suggested by Zhang et al. [139] to study the vessel motion for different wave frequencies and amplitudes. In Zhang et al. [139] it is found that large wave amplitudes combined with resonance wave frequencies and the weakened stability restoring features of liquefied cargo are the primary reasons for capsizing. More recently, Airey et al. (2021) applied the Finite Element Method (FEM) to the different cargo failure mechanisms for unsaturated soils [3], but the results were compromised by numerical stability issues. Wang et al. (2022) applied the DEM method to analyze the influence of material parameters on the cargo motion [130], and determined a critical angle of repose in the range of 22.0°, below which the stability of the vessel is substantially weakened. Wu et al. (2022) analyze the liquefaction risk by comparing the externally induced load obtained with the help of 3D simulations of the vessel motion based on the potential theory with the cargo liquefaction load threshold given by experiments [135].

Most of the literature did not exist when this work was started, and a strong development in numerical modeling of cargo on bulk carriers is observed during the last four years. The hereafter presented approach was developed independently from the above mentioned literature.

1.1 Starting Point and Aim of the Thesis

The study is based upon the in-house FV free surface fluid solver FreSCo^{+}. The software can simulate the 3D flow around ships and the motion of ships in seaway and is jointly developed by Hamburg University of Technology (TUHH) and Hamburg Ship Model Basin (HSVA).

The framework is specifically tailored for marine applications and free surface phenomena. Preceding works on free surface discretization techniques within a Volume of Fluid (VoF) method include Kühl [64], Kühl et al. [65] and Manzke [84]. Farfield wave boundary conditions required for the present 3D vessel simulations in waves were developed by Wöckner-Kluwe [133].

Utilized rigid-body motion models based on quaternions were introduced in Koliha [62] and further developed and applied in Luo et al. [80], Luo-Theilen et al. [81] and Theilen [114]. An extension to compressible, i.e. cavitating, liquids that is at the root for modeling compressible soil was published in Yakubov et al. [136]. A three-phase approach needed for the 3D vessel simulation is described in Völkner et al. [126].

In order to study cargo behavior on vessels during voyages, the thesis aims to implement a monolithic multi-physics approach. The latter includes constitutive models representing the above mentioned cargo failure mechanisms. The framework is applied to parameter studies exploring different loading scenarios.

Another objective is to prove that a complete 3D ship in waves with cargo can be simulated using the fully coupled monolithic FV approach and provide quantitative results. Due to the complexity of liquefaction modeling and the uncertainty as to whether cargo liquefaction was responsible for the ship accidents, general monolithic soil models are initially implemented. These should cover as many failure mechanisms as possible and can be expanded into more complex models if necessary. These include a rigid-perfectly plastic soil model, a porous media approach for rigid materials, an incompressible elastic model, and a direct coupling of the rigid-perfectly plastic model with the porous media approach.

Since large displacements are always present if cargo failure occurs, they will thus be considered in all implemented models. The monolithic approach follows a VoF method to represent the cargo boundaries in order to be able to obtain arbitrary shapes of the cargo and its included water and air.

1.2 Present Contributions

The current literature on numerical modeling of granular cargo on bulk carriers is being expanded to include models that can represent the cargo behavior for the failure mechanisms ”cargo shifting”, ”wet base”, and ”dynamic separation” with arbitrary cargo shapes. The approaches developed ground on the VoF-FV scheme and include the following contributions

1. A thorough study on two-phase flow through a rigid porous medium, including a reduced formulation of the momentum equations and its effect on the accuracy of results. This two-phase porous media approach can be used to study the movement of water content through bulk regions. Parts of the presented results are published in Düsterhöft-Wriggers et al. [28].

2. A validated rigid-perfectly plastic model that can be used to study cargo shifting for different material properties and display the finite strain development. Parts of the presented results are published in Düsterhöft-Wriggers et al. [29].

3. A strongly coupled porous media approach is introduced for rigid-perfectly plastic materials experiencing large deformations. With this model, the behavior of the cargo during failure mechanisms ”wet base” and ”dynamic separation” can be studied for arbitrary loading and excitation conditions.

4. A monolithic incompressible Neo-Hookean model that can accurately depict the stresses acting in the elastic domain in a finite strain formulation. Results of this model are also presented in Wriggers et al. [134].

Application results of the above models for different external excitations, cargo loading conditions, and material properties are presented. Publications on numerical simulations that apply a coupled, saturation-dependent model for cargo studies are unknown to the author and represent an extension of the existing literature on cargo modeling. In addition, a 3D feasibility study for accident investigations based on the ”Jian Fu Star” accident will be performed. Such a monolithically coupled simulation of ship motion and cargo behavior has not yet been described in the literature. The general formulated ground models can be applied to various other 2D and 3D applications such as landslides, coastal engineering problems, scouring, and deformable seabed under waves.

1.3 Outline of the Thesis

Chapters two to five of this thesis present the implemented models to simulate different cargo failure mechanisms on vessels. Each chapter contains a section describing the mathematical model, a section describing the discretized equations, and a section validating and verifying the model.

The FV-based approximation is put into the focus of the second chapter; all subsequent chapters refer to this. In this second chapter, alternative formulations described in the literature for calculating free-surface flows in a porous material are compared. Intensive validation studies are carried out to lay the foundations for the coupled model of granular cargo motion and free surface flow through the cargo. The chapter also includes a comparison between a simplified and a complete formulation for a range of porous materials, the intent of which is to explore the material limits to the use of the simplifications.

The third chapter introduces a rigid perfectly-plastic material realized via variable viscosity. Subsequently, the fourth chapter combines the models explained in chapters two and three to a porous medium multi-phase formulation of rigid perfectly-plastic granular material with saturation-dependent strength parameters.

Since disadvantages of the rigid perfectly-plastic approach are observed during the validation and verification studies of chapters three and four, a monolithic approach for incompressible elastic materials is introduced in chapter five. A particular focus is on validation based on several academic test cases.

Chapter six includes two-dimensional application cases of holds excited with external acceleration and a three-dimensional proof of concept of a bulk carrier in waves with loaded rigid perfectly-plastic cargo. To this end, an immiscible three-phase formulation, a rigid body motion solver, and wave-generating boundary conditions are employed and briefly described in chapter six.

Concluding remarks, a summary and an outlook are provided in the last chapter of this thesis. The outlook addresses missing potential model components required to simulate the cargo failure mechanism liquefaction.

Throughout this thesis, the notation uses standard lowercase Latin subscripts to mark cartesian tensor coordinates, and Einsteins' summation is used over repeated lowercase indices. In addition, symbolic notations of vectors and tensors employ underlining (e.g., $\underline{v}$ denoting the velocity vector).

Chapter 2

Free Surface Flow Through Rigid Porous Media

The aim of this work is to simulate the behavior of granular cargo materials on bulk carriers in waves and its impact on the stability of the vessel. Oral and visual captains' reports suggest that accidents could be related to expressed water on top of the granular material. The failure mechanism is called dynamic separation in the current IMSBC code [52]. In addition, scenarios are considered possible where water diffuses into porous material and influences the yield strength of the cargo, as well as wet base scenarios, on which the cargo slides. Therefore, a model describing water flow through the porous material is required. This chapter represents an introduction into the modelling topic and considers the cargo as a rigid porous material. A coupling of a free surface flow through a porous media model with the perfectly-plastic granular material model is described in the next chapter.

Similar topics were addressed by geotechnical and coastal engineering researchers, e.g., de Lemos [18], Del Jesus et al. [20], Van Gent [38], Higuera [46], Higuera et al. [47], Hsu et al. [50], Jensen et al. [58], Larese et al. [70], Liu et al. [78], Losada et al. [79] and Uzuoka et al. [123]. A consistent comparison of related formulations of the problem presented in these studies can be found in Düsterhöft-Wriggers et al. [28] and the models are generally valid for incompressible, immiscible two-phase flows through rigid porous media, used, for example, in biomedical engineering or additive manufacturing.

The chapter outlines different formulations of the momentum and continuity equations. These are implemented into a cell-centered FV scheme that employs a VoF approach to solve the two-phase flow, as suggested in the work of Del Jesus et al. [20]. The first formulation coincides with the governing equations given in Del Jesus et al. [20] in all terms except the diffusion term and is coherent with the approach of Jensen et al. [58] for a steady porosity. The second formulation refers to Higuera et al. [47], except for neglecting the added mass in the Forchheimer equation. Finally, a third set of governing equations is introduced. The latter is considerably simplified and is based on the finding that the resistance force model of the porous medium is found to be dominant in the momentum equations, as is also stated in Losada et al. [79] and confirmed in Sec. 2.4.

The numerical implementation is described in detail, and the results of several 1D, 2D, and 3D test cases are discussed in combination with different parameter influences and particular modeling aspects, e.g., the porous force model, the different formulations, or the mesh refinement. Finally, the dependence of the accuracy – and thus also the limits of the applicability – of a simplified formulation on the porous Reynolds number and the mean grain diameter of the porous material is highlighted. Parts of this section were published in Düsterhöft-Wriggers et al. [28].

2.1 Mathematical Model

The present two-phase flow through rigid porous material is derived from an immiscible, incompressible formulation of the Navier-Stokes equation in an Eulerian framework assuming sharp interfaces. The VoF method introduced by Hirt et al. [48] is employed to identify the interface between the gas and the liquid phase. This interface-capturing approach assumes a unique velocity field for all participating phases and involves a single continuity and momentum equation for the virtual mixture of the two phases. Additionally, a partial differential equation to identify the local fluid phase and simple equations of state for the local fluid properties are considered.

Inside a (rigid) porous material with porosity n, the fluid only occupies a share of the total volume. As the basis for the subsequent sections, the definition of porosity n

$$n = \frac{V^F}{V} = \frac{V^F}{V^F + V^S} \tag{2.1}$$

serves to distinguish the fluid volume V^F ratio from the total volume V, which consists of the fluid volume V^F and the volume of the porous material V^S, as depicted in Fig. 2.1.

The fluid dynamic momentum equations provide the velocity of the two fluid phases in the fluid occupied volume. The problem can be expressed by either the fluid velocity v_i^F or the Darcy velocity $\hat{v}_i = n\, v_i^F$, i.e., the mean of the fluid and the solid velocity (which is assumed at rest). The following sections discuss different formulations of the governing equations.

2.1.1 Continuity Equation

The present study is devoted to immiscible two-phase flows of air and water within rigid porous materials. Although the local Eulerian properties of the flow might change, the material La-

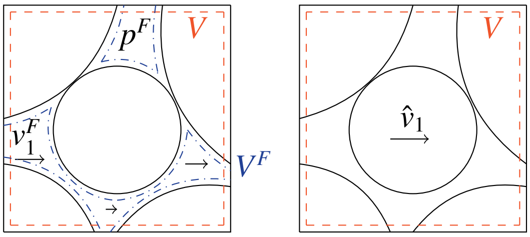

Figure 2.1: Schematic view of a flow through a porous medium. Left: The fluid velocity v_i^F is the velocity of the fluid inside the fluid volume V^F, and p^F is the fluid pressure. Right: The Darcy velocity $\hat{v}_i$ is the mean velocity over the complete volume V where the solid material is rigid and therefore $\hat{v}_i = n v_i^F$.

grangian properties of an immiscible fluid flow do not change, i.e., they obey the immiscible condition

$$\frac{Dc^A}{Dt} = \frac{Dc^W}{Dt} = 0 \ . \tag{2.2}$$

Here $c^A = 1 - c^W := c$ denotes air mixture fraction $c = V^A/V^F$ and the fluid density ρ is obtained from the air mixture fraction c and the constant bulk densities of air ρ^A and water ρ^W, viz.

$$\rho = c^A\rho^A + c^W\rho^W = c\rho^A + (1-c)\rho^W \ . \tag{2.3}$$

Due to the immiscible condition (2.2), i.e., $Dc/Dt = \partial c/\partial t + v_i^F \partial c/\partial x_i = 0$, the continuity equation for a two-phase incompressible fluid yields

$$\frac{D}{Dt}\int_{V^F}\rho dV = \int_{V^F}\left(\frac{\partial\rho}{\partial t} + \frac{\partial v_i^F\rho}{\partial x_i}\right)dV = \int_{V^F}\left[\rho^A - \rho^W\right]\left(\frac{\partial c}{\partial t} + \frac{\partial v_i^F c}{\partial x_i}\right)dV = 0 \ , \tag{2.4}$$

leading to the well-known zero-divergence differential form of the volume conservation

$$\int_{V^F}\frac{\partial v_i^F}{\partial x_i}dV = 0 \ . \tag{2.5}$$

Introducing the porosity n in the continuity equation (2.5) by integrating over the total volume V, gives

$$\int_V\left(n\frac{\partial\frac{\hat{v}_i}{n}}{\partial x_i}\right)dV = \oint_A \hat{v}_i dA_i - \int_V\left(\frac{\partial n}{\partial x_i}\frac{\hat{v}_i}{n}\right)dV = 0 \ , \tag{2.6}$$

where the fluid velocity is replaced by the Darcy velocity $\hat{v}_i = n v_i^F$. The benefit of the Eqn. (2.6) is that no precise geometric information is needed to divide the volume into a solid and fluid portion. For a spatially constant porosity, the second term vanishes, and for the problem at hand, the second term is only relevant at the boundaries of the porous material. Applying the Finite Volume method, the porosity gradient in the second term in Eqn. (2.6) is non-zero at the cell center only if the boundary is embedded in the control volumes. In an artificial test case where the resistance forces due to the porous medium are zero (cf. Sec. 2.3.3), it is shown that the second term in Eqn. (2.6) has a negligible influence on the results. In the following, the main focus is on assessing three different formulations of the momentum equations. The zero-divergence form (2.5) is employed in combination with a formulation using the fluid velocity v_i^F, while formulations using the Darcy velocity $\hat{v}_i$ employ (2.6) and neglect the second term in (2.6), i.e.

$$\int_V \frac{\partial \, \hat{v}_i}{\partial x_i} dV = 0 \; . \tag{2.7}$$

This simplification follows Hsu et al. [50], Jensen et al. [58], and Larese et al. [70].

Remarks on Literature

For a one-dimensional or two-dimensional flow, the porosity follows from the relation of fluid area A^F to total area $\hat{A}$

$$n = \frac{A^F}{\hat{A}} \; . \tag{2.8}$$

Therefore Eqn. (2.5) can be expressed as

$$\int_{V^F} \frac{\partial v_i^F}{\partial x_i} dV = \oint_{A^F} v_i^F dA_i = \oint_A \hat{v}_i dA_i \tag{2.9}$$

and the second term of Eqn. (2.6) vanishes. These arguments refute the statement of Jensen et al. [58] that the continuity equation stated in del Jesus et al. [20] ($\partial v_i^F / \partial x_i = 0$) is not applicable. Jensen et al. [58] show that for a 1D example, the fluid velocity gradient is not zero for constant volume flux and a decreasing porosity in the flow direction, while the Darcy velocity gradient vanishes. This statement is exact but neglects the correctness of Eqn. (2.5), where the fluid velocity divergence must be zero in the fluid volume.

2.1.2 Momentum Equations

To derive the momentum equations in porous media, first, the momentum equations of an incompressible fluid are derived from the force balance of a fluid inside a fluid volume dV^F. The change of momentum for incompressible fluids equals the pressure, viscous, and body forces

$$\frac{D}{Dt} \int_{V^F} \left(\rho v_i^F\right) dV = \int_{V^F} \left[\frac{\partial (\rho v_i^F)}{\partial t} + \frac{\partial \left(\rho v_i^F v_j^F\right)}{\partial x_j} \right] dV = \int_{V^F} \left[\rho g_i - \frac{\partial p^F}{\partial x_i} + \frac{\partial \tau_{ij}}{\partial x_j} \right] dV \; . \tag{2.10}$$

Here, only gravity body forces are taken into account. For an incompressible Newtonian fluid, the constitutive equation

$$\tau_{ij} = \mu \left(\frac{\partial v_i^F}{\partial x_j} + \frac{\partial v_j^F}{\partial x_i} \right) \tag{2.11}$$

relates the stress tensor τ_{ij} to the strain-rate tensor that, by construction, ensures angular momentum balance, hence

$$\int_{V^F}\left[\frac{\partial(\rho v_i^F)}{\partial t}+\frac{\partial\left(\rho v_i^F v_j^F\right)}{\partial x_j}\right]dV=\int_{V^F}\left[\rho g_i-\frac{\partial p^F}{\partial x_i}+\frac{\partial}{\partial x_j}\left(\mu\left(\frac{\partial v_i^F}{\partial x_j}+\frac{\partial v_j^F}{\partial x_i}\right)\right)\right]dV\,. \tag{2.12}$$

Introducing the porosity from (2.1) and an interaction force f_i^R acting from the rigid porous material on the fluid volume, one obtains the $(v_i^F,\, p^F)$-formulation of the momentum equations

$$\int_{V}n\left[\frac{\partial(\rho v_i^F)}{\partial t}+\frac{\partial\left(\rho v_i^F v_j^F\right)}{\partial x_j}\right]dV=\int_{V}n\left[\rho g_i-\frac{\partial p^F}{\partial x_i}+\frac{\partial}{\partial x_i}\left(\mu\left(\frac{\partial v_i^F}{\partial x_j}+\frac{\partial v_j^F}{\partial x_i}\right)\right)+\frac{f_i^R}{n}\right]dV\,. \tag{2.13}$$

Substituting the fluid velocity by the Darcy velocity $v_i^F = \hat{v}_i/n$ and integrating over the entire volume dV, one arrives at a $(\hat{v}_i,\, p^F)$-formulation of the momentum equations

$$\int_{V}n\left[\frac{\partial(\rho\frac{\hat{v}_i}{n})}{\partial t}+\frac{\partial\left(\rho\frac{\hat{v}_i}{n}\frac{\hat{v}_j}{n}\right)}{\partial x_j}\right]dV=\int_{V}n\left[\rho g_i-\frac{\partial p^F}{\partial x_i}+\frac{\partial}{\partial x_i}\left(\mu\left(\frac{\partial\frac{\hat{v}_i}{n}}{\partial x_j}+\frac{\partial\frac{\hat{v}_j}{n}}{\partial x_i}\right)\right)+\frac{f_i^R}{n}\right]dV\,. \tag{2.14}$$

This equation is divided by n assuming the porosity to be homogeneous and steady.

2.1.3 Porous Force Models

The porous force represents the contact force between the porous material and the fluid. This work is confined to well-established porous force models. The simplest model is the linear Darcy law

$$\hat{f}_i^R=\frac{f_i^R}{\rho}\sim-\tilde{A}\hat{v}_i\,, \tag{2.15}$$

which was introduced by Darcy in 1856 and relates the porous force to the Darcy velocity of the fluid and an empirical constant $\tilde{A}$. The linear Darcy law is sufficient to represent the resistance forces acting on the fluid for small porous Reynolds numbers, i.e.,

$$Re_P=\frac{\|\hat{v}\|_2\,D_{50}}{\nu}\,, \tag{2.16}$$

where D_{50} refers to the mean grain size of the porous material. As given in Gu et al. [43], the non-linear behavior of porous flow starts at $Re_P\in[1,10]$ and turbulent flows appear around $Re_P\in[60,150]$ as stated in Larese [69]. The range of applicability of the linear Darcy law is further discussed by Van Gent [39], Larese [69] and Polubarinova-Kochina [98]. Forchheimer [37] introduced a non-linear term to Darcy's law to capture contributions of turbulence and large-scale convective transport. An additional third term, which Polubarinova-Kochina [98] supplemented takes added mass phenomena into account and completes the extended Forchheimer equation that employs three empirical constants $\tilde{A}, \tilde{B}, \tilde{C}$

$$\hat{f}_i^R=-\left(\tilde{A}\hat{v}_i+\tilde{B}\,\hat{v}_i\,\|\hat{v}\|_2+\tilde{C}\frac{\partial\hat{v}_i}{\partial t}\right)\,. \tag{2.17}$$

As given in Düsterhöft-Wriggers [28], expression (2.17) still represents a state-of-the-art approach for flows through porous material. There exist numerous studies on the description of the resistance force factors $\tilde{A}$, $\tilde{B}$ and $\tilde{C}$ depending on the porosity n for different materials, the physical properties of the fluid, the mean grain diameter D_{50} and additional constants. Examples can be found in Bear et al. [6], Engelund [32], Ergun [33], Van Gent [38], Kozeny [63] or Losada et al. [79] among others.

Table 2.1: Different formulations of resistance law constants used in the literature.

literature	type of res. law	$\tilde{A}$	$\tilde{B}$	$\tilde{C}$
Uzuoka et. al [123]	general Darcy	$\frac{\mu n}{\rho k}$	-	-
De Lemos [19]	general nonlinear		$\frac{c_F n}{\sqrt{k}}$	-
Larese et. al [69] & De Lemos [18]	Ergun	$\alpha\frac{\mu(1-n)^2}{\rho n^2 D_{50}^2}$	$\beta\frac{(1-n)}{n^2 D_{50}}$	-
Van Gent [38] (1D) & Hsu et. al [50]	Van Gent			$\gamma\frac{(1-n)}{n}$
Del Jesus [20] & [38]	Engelund	$\alpha\frac{\mu(1-n)^3}{\rho n D_{50}^2}$		
Liu et. al [78]	Van Gent oscillating flow	$\alpha\frac{\mu(1-n)^2}{\rho n^2 D_{50}^2}$	$\beta\frac{\left(1+\frac{7.5}{KC}\right)(1-n)}{n^2 D_{50}}$	

Table 2.1 summarizes the models used in the previously mentioned literature. Uzuoka et al. [123] use Darcy's law in a general form. De Lemos et al. [18] and Larese et al. [69] employ the Ergun model. De Lemos et al. [19] refer to a general expression for $\tilde{A}$ and $\tilde{B}$ based upon the intrinsic permeability k which can be obtained from experiments or one of the models mentioned above. The Van Gent model is used by Van Gent et al. [38] and Liu et al. [78], where the former employs a more complex version that adjusts $\tilde{A}$ and $\tilde{B}$ with the help of the Keuler-Carpenter number $KC =\mid \hat{v}_i T \mid / D_{50}$ and a representative time scale T. The Van Gent model is also used in Hsu et al. [50]. Van Gent et al. [38] also applied the Engelund model for verification purposes. With the Engelund formula given in Tab. 2.1, a reproduction of Del Jesus [20] results is possible. A Forchheimer formula is applied in De Lemos [18] and Larese et al. [70], and a Forchheimer formula with an added mass term is used in Del Jesus [20], Van Gent [38], Higuera et al. [47], Hsu et al. [50], Jensen et al. [58] and Liu et al. [78]. The choice of porous resistance force model depends on the nature of the investigated flow field, which can be described, e.g., by the pore Reynolds number.

2.1.4 Two-Phase Representation by the Volume of Fluid Method

A Volume of Fluid (VoF) approach represents the free boundary between the two incompressible immiscible phases inside and outside the porous material in the present work. The VoF approach introduced by Hirt et al. [48] identifies the interface position from a scalar concentration function and is classified as an interface-capturing approach. Other interface-capturing approaches include the level-set method (e.g., Sussmann [112]), which offers the advantage of an inherently sharp interface for immiscible flows, and the diffuse-interface method (e.g., Anderson et al. [4]). Reviews on interface-capturing methods can be found in Tryggvason et al. [117] and Mirjalili et al. [87].

The VoF approach uses the (air) concentration field c, cf. Eqn. (2.2), to express the fluid properties density ρ and viscosity μ

$$\rho = c\rho^A + (1-c)\rho^W \qquad \text{and} \qquad \mu = c\mu^A + (1-c)\mu^W \,, \tag{2.18}$$

where ρ^A, ρ^W and μ^A, μ^W refer to the bulk properties of the two fluids. This work uses only constant bulk densities and mixture fraction values of $c = 0.5$ to identify the interface. As stated in Hirt et al. [48], the concentration c moves with the fluid flow, and the integral form of the immiscibility condition (cf. Sec. 2.1.1) follows from

$$\int_{V^F} \left(\frac{\partial c}{\partial t} + \frac{\partial \left(c v_i^F \right)}{\partial x_i} \right) dV = 0 \,. \tag{2.19}$$

In a Darcy-velocity $\hat{v}_i$ formulation equation (2.19) reads

$$\int_{V} n \left(\frac{\partial c}{\partial t} + \frac{\partial \left(c \frac{\hat{v}_i}{n} \right)}{\partial x_i} \right) dV = 0 \,. \tag{2.20}$$

Dividing the equation by the porosity yields

$$\int_{V} \left(\frac{\partial c}{\partial t} + \frac{\partial \left(c \frac{\hat{v}_i}{n} \right)}{\partial x_i} \right) dV = 0 \,. \tag{2.21}$$

2.2 Finite Volume Method

In the present work, a pressure-based FV formulation using a cell-centered, co-located variable arrangement on unstructured polyhedral grids is applied to approximate the free surface flows through porous material. The FV method approximates the integral form of the conservation equations by discretizing the computational domain into a set of control volumes (CVs) of size ΔV_P. Figure 2.2 displays an exemplary rectangular CV. The integral form of the conservation

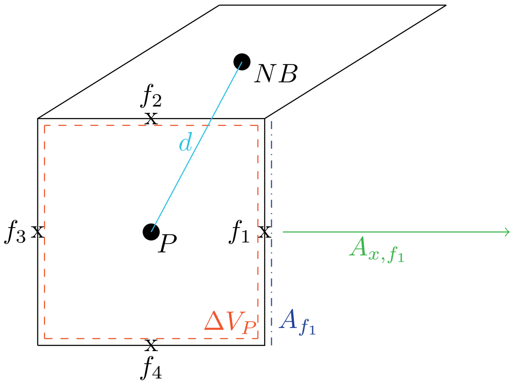

Figure 2.2: Schematic figure of a control volume (CV).

equations are solved for each finite CV, where the sum of all CVs complies with the entire domain and comprises the algebraic equation system, cf. Ferziger [36]. A sequential algorithm is used to solve the coupled system of linearized discrete algebraic equations (Large Eddy Simulation).

Local 1D Stencil

Fig. 2.2 illustrates a quadrilateral 2D control volume, where P denotes the location of the control volume and NB is the corresponding center of the control volume adjacent to face f_1. All dependent variables Θ are stored in the center of a control volume.

Next to the cell center, values of the variables Θ are also required at the face centers f_n, to approximate surface integrals that arise from integration by parts of the convection, diffusion (and pressure) terms, cf. below. To this end, face centered values are required, which follow from a 1D-reconstruction using (a) the corresponding face-neighboring cell center values Θ_P and Θ_{NB} as well as (b) their respective gradients $\underline{\nabla}\Theta_P$ and $\underline{\nabla}\Theta_{NB}$.

In the following sections, the subscript f marks the cell face locations or their corresponding variable values, A denotes the face area, and A_i the related outward pointing face vector (cf. Fig. 2.2). The scalar distance between the cell center P and adjacent neighbouring centers NB is labeled d.

Integral Approximation

The mid-point rule is applied to approximate both volume and face integrals

$$\int_V \Theta \, dV \approx \Theta_P \Delta V_P \tag{2.22}$$

and

$$\int_A \Theta \, dA \approx \Theta_f A_f \tag{2.23}$$

leading to second-order spatial accuracy of the integral approximation. Applying Gauss's theorem (integration by parts) to derivative terms yields

$$\int_V \frac{\partial \Theta}{\partial x_i} = \oint_{A(V)} \Theta dA_i = \sum_{f(V)} \int_A \Theta dA_i \, , \tag{2.24}$$

where (2.23) is subsequently employed to approximate the surface integrals.

Convective Fluxes

Using the above mentioned surface integral approximation, the convection terms are approximated by

$$\int_{V_P} \frac{\partial \left(\rho \Theta v_i\right)}{\partial x_i} \, dV = \oint_{A(V_P)} \left(\rho \Theta v_i\right) \, dA_i \approx \sum_{f(\Delta V_P)} \left[\rho A_i v_i\right]_f \Theta_f = \sum_{f(\Delta V_P)} \dot{m}_f \Theta_f \, , \tag{2.25}$$

Required face values for the mass flux $\dot{m}_f$ are obtained by a linear interpolation from the face adjacent cell centers P and NB. For locally equidistant, orthogonal meshes the approximation is second-order accurate in space. For irregular meshes, a non-orthogonality correction is introduced, which is further described in detail in Appendix A.1. Moreover, convective fluxes are reconstructed from blended first-order upwind and second-order central difference approximations, cf. Appendix A.1. The flux-blending contribution is cast into an implicit UDS part and an explicit deferred correction part.

Diffusive Fluxes

The diffusive fluxes of a generic variable follow from

$$-\int_V \frac{\partial}{\partial x_i} \left(\rho \Gamma_\phi \frac{\partial \Theta}{\partial x_i}\right) \, dV = -\int_A \left(\rho \Gamma_\phi \frac{\partial \Theta}{\partial x_i}\right) \, dA_i \approx -\sum_{f(\Delta V_P)} \left[\rho \Gamma_\phi \frac{\partial \Theta}{\partial x_i}\right]_f A_i \, , \tag{2.26}$$

where Γ_ϕ is a generic diffusion coefficient. For orthogonal grids, the gradient at the face becomes

$$\left[\frac{\partial \Theta}{\partial x_i}\right]_f A_i = \frac{\Theta_{NB} - \Theta_P}{d} A \, . \tag{2.27}$$

For non-orthogonal grids, where the direction of the face normal and the connection vector differ, a modification based upon the deferred correction approach is utilized and further explained in Appendix A.2.

Transient Approximation

A simple, first-order implicit Euler scheme is applied to approximate time derivatives

$$\int_V \frac{\partial \Theta}{\partial t} \, dV \approx \frac{\left(\Theta \Delta V_P\right)^n - \left(\Theta \Delta V_P\right)^{n-1}}{\Delta t} \, . \tag{2.28}$$

For each time step, the governing equations are iterated to convergence in a segregated manner as displayed in Fig. 2.3. The superscripts n and m denote the time step and the iteration index of the iterative procedure, respectively. As described in the next sections, a pressure correction scheme is applied to fulfill the continuity equation. The general algorithm follows Ferziger [36], and further details are given by Kühl et al. [67], Völkner et al. [125] and Yakubov et al. [136].

2.2.1 Discretized ($\hat{v}_i$, p^F)-Formulation

The continuity equation follows from Eqn. (2.7). The momentum equation follows from Eqn. (2.14) and is divided by a homogeneous porosity. A Forchheimer porous force is used with the added mass term being suppressed, i.e., $\tilde{C} = 0$. The mixture fraction transport is governed by Eqn. (2.21) and the equation system follows as

$$\oint_A \hat{v}_i dA_i = 0 \tag{2.29}$$

$$\begin{aligned} \int_V \frac{\partial}{\partial t}\left(\frac{\rho \hat{v}_i}{n}\right) dV + \oint_A \left(\rho \frac{\hat{v}_i}{n}\frac{\hat{v}_j}{n}\right) dA_j = \\ -\oint_A p^F dA_i + \int_V \rho g_i dV + \oint_A \mu \left(\frac{\partial \frac{\hat{v}_i}{n}}{\partial x_j} + \frac{\partial \frac{\hat{v}_j}{n}}{\partial x_i}\right) dA_j - \int_V \frac{\rho}{n} \hat{v}_i \left(\tilde{A} + \tilde{B}\, \|\hat{v}\|_2\right) dV \end{aligned} \tag{2.30}$$

$$\int_V \frac{\partial c}{\partial t} dV + \oint_A \frac{c \hat{v}_i}{n} dA_i = 0\ . \tag{2.31}$$

If the porosity is assumed to be constant in time, the momentum equations are entirely in line with Jensen et al. [58]. However, the resulting terms from applying Gauss's theorem, including the spatial derivative of the porosity, cf., Eqn. (2.6), are neglected, which is consistent with the employed continuity equation.

Discrete Momentum Equations

Equation (2.30) is discretized over a control volume $V = \Delta V_P$ with the center location P as depicted in Fig. 2.2. Using the mid-point integration rule together with a simple first-order implicit time discretization and an implicit upwind-difference scheme (cf. Appendix A.1) for

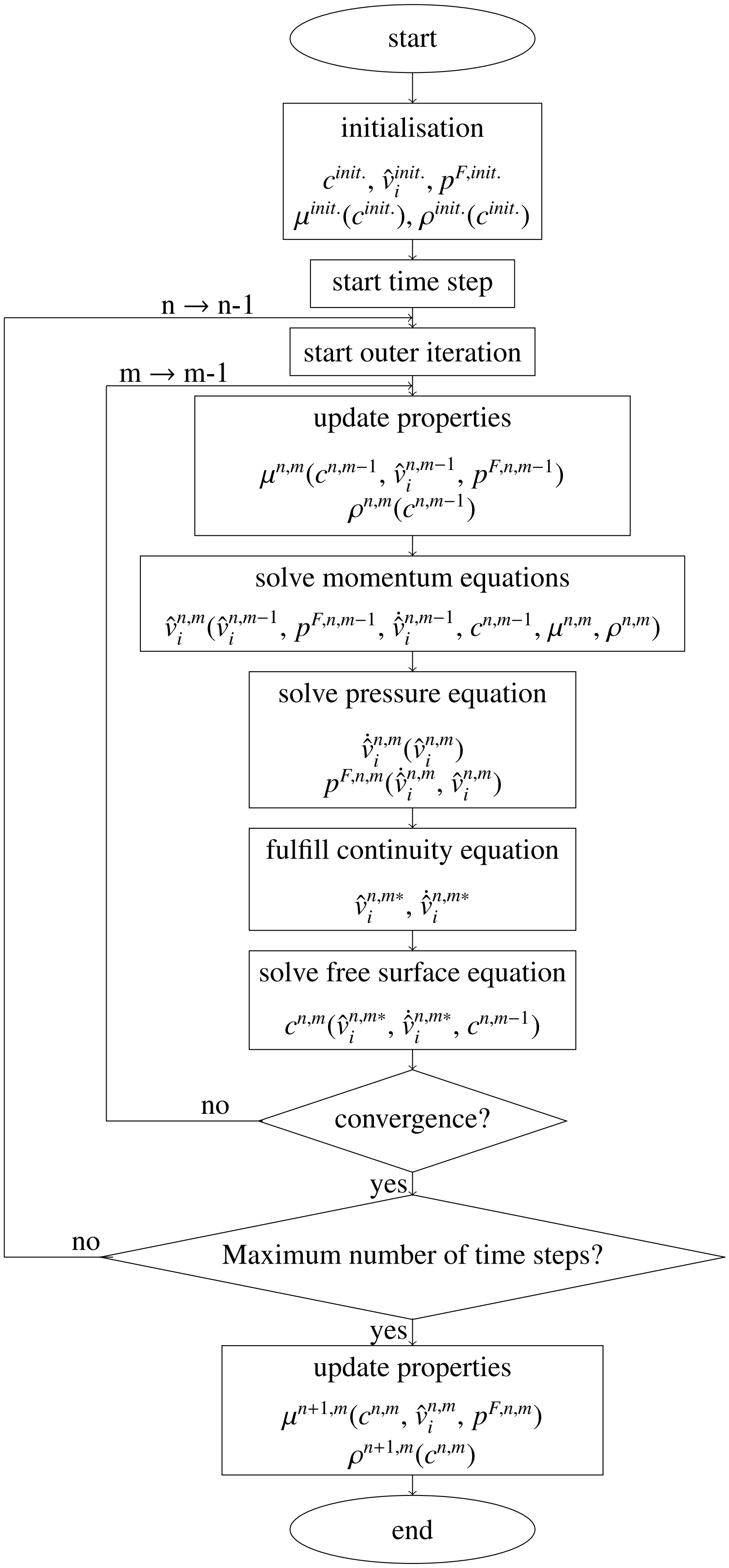

Figure 2.3: Procedure to simulate the free surface flow through rigid porous media.

the discrete equation reads

$$\begin{aligned} & \hat{v}_{i,P}^{n,m} \underbrace{\left[\Delta V_P \left(\frac{\rho}{n}\right)_P \left(\frac{1}{\Delta t} + \tilde{A} + \tilde{B} \, \|\hat{v}\|_2^{n,m-1} \right)_P + \sum_{f(\Delta V_P)} A_{NB}^{\hat{v}_i} \right]}_{A_P^{\hat{v}_i}} \\ & - \sum_{f(\Delta V_P)} \underbrace{\left[\left(\frac{1}{n} \, max \left[-\frac{\dot{\hat{m}}^{n,m-1}}{n}, 0 \right] \right)_f + \left(\frac{1}{n} \, \frac{\mu A}{d} \right)_f \right]}_{A_{NB}^{\hat{v}_i}} \hat{v}_{i,NB}^{n,m} = \\ & - \sum_{f(\Delta V_P)} \left(p_f^{F,n,m-1} A_i \right) + \rho_P \Delta V_P \left(g_i + \frac{\hat{v}_i^{n-1}}{n \Delta t} \right)_P + S_{\hat{v}_i} \; . \end{aligned} \tag{2.32}$$

Here $\dot{\hat{m}}_f = (\rho \hat{v}_i A_i)_f$ refers to the porous mass flux across a porous face. Porous resistance terms are implemented in an implicit manner to improve numerical stability. The source term $S_{\hat{v}_i}$ includes explicit terms which arise from different deferred correction contributions, e.g., higher-order convection and non-orthogonality corrections, which are detailed in Appendix A.1 and Appendix A.2.

Discrete Continuity Equation

As seen in the governing equations (2.29), (2.30) and (2.31), the pressure is only present in the momentum equations. After solving the momentum equations to obtain the Darcy velocity, no equation exists to explicitly compute the pressure. Since the computed velocities must also satisfy the continuity equation, a pressure link to the continuity equation is required. This should adjust the pressure so that the calculated velocities are compatible with the continuity equation. A Semi-Implicit Method for Pressure Linked Equations (SIMPLE) pressure correction scheme introduced by Caretto et al. [11] and Patankar et al. [97] is used to fulfill the continuity equation following closely the algorithms described in Ferziger [36] and Yakubov et al. [136]. It is important to note that the classical SIMPLE pressure correction scheme can be adopted without any change to solve porous two-phase flows in the ($\hat{v}_i$,p^F)-formulation due to the assumption that the Darcy velocity is divergence-free. The pressure correction scheme derived in this section will also be applied in combination with the equation systems given in chapters 3, 4, and 5 with the according velocity variables.

For the equation system (Eqns. (2.29), (2.30) and (2.31)), the scheme starts from the velocity and pressure values ($\hat{v}_i^{m-1}$, $p^{F,m-1}$) of the previous iteration state. An intermediate Darcy velocity $\hat{v}_i^m$ is obtained from the discrete momentum equations (2.32), which is usually not divergence-free. Therefore a velocity correction $\hat{v}_i^{'}$: $\hat{v}_i^{m*} = \hat{v}_i^m + \hat{v}_i^{'}$ is introduced to satisfy the discrete continuity equation for $\hat{v}_i^{m*}$ which is derived from Eqn. (2.29)

$$\sum_{f(\Delta V_P)} \left(\hat{v}_i^m + \hat{v}_i^{'}\right)_f A_i = 0 \; . \tag{2.33}$$

To link the velocity correction to a pressure correction p'

$$p^{F,m} = p^{F,m-1} + p^{F,'} \; , \tag{2.34}$$

a simplified momentum expression is derived from the discrete momentum equations. The intermediate Darcy velocity $\hat{v}_i^m$ follows from the solution of (2.32), viz.

$$A_P^{\hat{v}_i} \hat{v}_i^m = -\frac{\partial p^{F,m-1}}{\partial x_i} \Delta V_P - \sum_{NB} A_{NB}^{\hat{v}_i} \hat{v}_{i,NB}^m + f_{P,i} \Delta V_P \; , \tag{2.35}$$

where $A_P^{\hat{v}_i}$ refers to the main-diagonal coefficient, $A_{NB}^{\hat{v}_i}$ to the neighbour coefficients and $f_{P,i}$ to the source terms of the discrete momentum equations (2.32). The iterated velocity $\hat{v}_i^{m*}$ needs to fulfill the momentum and continuity equations. By subtraction of both discrete momentum equations, the source terms are eliminated, and a discrete equation for the corrected velocity $\hat{v}_i^{'}$ is obtained

$$A_P^{\hat{v}_i} \hat{v}_i^{'} = -\frac{\partial p^{F,'}}{\partial x_i} \Delta V_P - \sum_{NB} A_{NB}^{\hat{v}_i} \hat{v}_{i,NB}^{'} \, . \tag{2.36}$$

To obtain an explicit relation between the local pressure correction gradient and the local velocity correction vector, the neighbor coefficient term is neglected

$$\hat{v}_i^{'} = -\frac{\Delta V_P}{A_P^{\hat{v}_i}} \frac{\partial p^{F,'}}{\partial x_i} \; . \tag{2.37}$$

This relation is evaluated at the faces of all CVs to compute the related mass fluxes

$$\hat{v}_{f,i}^{'} n_i A_f = -\left(\frac{\Delta V}{A_P^{\hat{v}_i}}\right)_f \left(\frac{\partial p^{F,'}}{\partial x_i} n_i\right)_f A_f \tag{2.38}$$

where n_i is the normal vector at each face of a control volume. Approximating the volume around the face $(\Delta V)_f$ via

$$(\Delta V)_f = A_{f,i} d_{f,i} \; , \tag{2.39}$$

where $d_{f,i}$ is the distance vector between cell centers of the neighboring cells at face f and substitution the resulting expression into Eqn. (2.33) leads to

$$\sum_{f(\Delta V_P)} \hat{v}_{f,i}^m A_{f,i} - \sum_{f(\Delta V_P)} \left(\frac{A_i d_i}{A_P^{\hat{v}_i}}\right)_f \left(\frac{\partial p^{F,'}}{\partial x_i} n_i\right)_f A_f = 0 \; . \tag{2.40}$$

As described in Ferziger and Peric [35], the approximation of the pressure gradient in the direction of the face normal is split into an implicit orthogonal and an explicit non-orthogonal term

$$\left(\frac{\partial p^{F,'}}{\partial x_i} n_i\right)_f = \left(\frac{p_{NB}^{F,'} - p_P^{F,'}}{d}\right) + \left(\frac{\partial p^{F,'}}{\partial x_i} \left(\frac{A_i}{A} - \frac{d_i}{d}\right)\right)_f \; . \tag{2.41}$$

The non-orthogonal, second term on the RHS leads to a two-step pressure correction scheme. During the initial step, pressure corrections are zero. Therefore, the explicit gradient term does not exist and only the implicit orthogonal part of the approximation is used in Eqn. (2.40). This yields a coupled equation system for the pressure correction $p^{F,\prime}$

$$- p_P^{F,\prime} \underbrace{\sum_{\Delta V_P} \left(\frac{A_i d_i}{A_P^{\hat{v}_i} d} \right)_f}_{A_P^{p^{F,\prime}}} - \underbrace{\sum_{NB} \left(\frac{A_i d_i}{A_P^{\hat{v}_i} d} \right)_f}_{A_{NB}^{p^{F,\prime}}} p_{NB}^{F,\prime} = -\dot{\hat{V}}_{\Delta V_P}^m \ , \tag{2.42}$$

where $\dot{\hat{V}}_{\Delta V_P}^m = \sum_{f(\Delta V_P)} \hat{v}_{f,i}^m A_{f,i}$ refers to the volume flux in each control volume. Porous media influences are implicitly considered through the main diagonal coefficients $A_P^{\hat{v}_i}$. Subsequently, the obtained pressure correction $p^{F,\prime}$ is used to calculate the pressure $p^{F,m}$ from Eqn. (2.34) including relaxation and correcting the Darcy velocity and Darcy flux. The Darcy flux $\dot{\hat{v}}^{m*}$ at each face is corrected to fulfill the discrete continuity equation in each control volume by

$$\dot{\hat{v}}_f^{m*} = \dot{\hat{v}}_f^m + A_{NB}^{p^{F,\prime}} \left(p_{NB}^{F,\prime} - p_P^{F,\prime} \right) \ . \tag{2.43}$$

An associated correction of the velocities at the cell centers follows from Eqn. (2.37) and reads

$$\hat{v}_{i,P}^{m*} = \hat{v}_{i,P}^m + \left(- \frac{\Delta V_P}{A_P^{\hat{v}_{i,P}}} \right) \left(\frac{\partial p^{F,\prime}}{\partial x_i} \right)_P \ . \tag{2.44}$$

To avoid pressure oscillations often occurring for a collocated variable arrangement, a Rhie-Chow [101] interpolation of the fluxes in $(\hat{v}_i^m A_i)_f$ is applied as described in Appendix A.3. In subsequent stages of the SIMPLE algorithm, the complete approximation of the pressure gradient (2.41) is introduced into Eqn. (2.40), where non-orthogonality effects are included. Since the corrected Darcy velocity flux fulfills the continuity equation after the first stage, the entire pressure gradient approximation can be applied to obtain the second stage corrections with an updated pressure field. The pressure correction field $p^{F,\prime}$ is used to explicitly discretize the pressure gradient on the RHS of equation (2.41) and therefore, the coefficient matrix, i.e. $A_P^{p^{F,\prime}}$ and $A_{NB}^{p^{F,\prime}}$, is identical to the first stage of the algorithm. Having solved the pressure correction, the pressure and Darcy velocity are corrected.

Remark

To study the influence of the second term of Eqn. (2.6) in the artificial case with zero porous resistance forces in Sec. 2.3.3, the complete equation is discretized by adding two explicit terms in the equation, including the scalar product of the gradient of the porosity and the Darcy velocity divided by the porosity. Furthermore, the velocity correction is discretized by linking it to the pressure correction from the previous iteration with Eqn. (2.37)

$$\sum_{f(\Delta V_P)} \hat{v}^m_{f,i} A_{f,i} - \sum_{f(\Delta V_P)} \left(\frac{A_i d_i}{A_P^{\hat{v}_i}}\right)_f \left(\frac{\partial p^{F,'}}{\partial x_i} n_i\right)_f A_f = \frac{\partial n}{\partial x_i} \frac{\hat{v}^m_{i,P}}{n_P} \Delta V_P + \frac{\partial n}{\partial x_i} \frac{\partial p_P^{F,m-1}}{\partial x_i} \frac{\Delta V_P^2}{n_P A_P^{\hat{v}_i}} \,. \tag{2.45}$$

Discretized Air Mixture Fraction Equation for ($\hat{v}_i$, p^F) - Formulation

Applying a first-order implicit time integration scheme and an implicit upwind-difference scheme for the approximation of the convective term, the discrete mixture fraction transport reads

$$c_P^{n,m} \left[\frac{\Delta V_P}{\Delta t} + \sum_{f(\Delta V_P)} A^c_{NB}\right] - \sum_{f(\Delta V_P)} \underbrace{\left(max\left[-\frac{(\dot{\hat{m}}/\rho)}{n}^{n,m-1}, 0\right]\right)_f}_{A^c_{NB}} c_{NB}^{n,m} = \frac{\Delta V_P}{\Delta t} c_P^{n-1} + S_c \,, \tag{2.46}$$

where S_c hosts the deferred correction contributions of the compressive approximation. The mass flux $\dot{\hat{m}}$ is calculated from the updated Darcy flux $\dot{\hat{v}}^{m*}$ after solving the continuity equation. Two specific compressive approximations of the convective term are used in this work: the High Resolution Interface Capturing Scheme (HRIC), which was developed by Muzaferija et al. [91], and the Compressive Interface Capturing Scheme for Arbitrary Meshes (CICSAM), developed by Ubbink [118] and Ubbink et al. [119]. A description of the HRIC and CICSAM implementation in the FV procedure FreSCo$^+$ can be found in Kühl et al. [66]. The cell-centered density and viscosity values are updated at each iteration by the cell-centered values of c using the simple linear equation of state (2.18). Similarly, the face-centered material properties are reconstructed from the corresponding face values of c.

2.2.2 Discretized Equation System for (v_i^F, p^F) - Formulation

In a second implementation, the fluid velocity v_i^F and the fluid pressure p^F are dependent variables. Therefore the equation system is formulated for the fluid volume V^F and area A^F as explained in Secs. 2.1.1, 2.1.2, and 2.1.4. The momentum equations follow from Eqn. (2.13) divided by n, which is valid for a rigid porous material, and the set of equations for the (v_i^F, p^F) - formulation reads

$$\oint_{A^F} v_i^F dA_i = 0 \tag{2.47}$$

$$\begin{aligned} \int_{V^F} \frac{\partial}{\partial t}\left(\rho v_i^F\right) dV + \oint_{A^F} \left(\rho v_i^F v_j^F\right) dA_j = \\ -\oint_{A^F} p^F dA_i + \int_{V^F} \rho g_i dV + \oint_{A^F} \mu \left(\frac{\partial v_i^F}{\partial x_j} + \frac{\partial v_j^F}{\partial x_i}\right) dA_j - \int_{V^F} \rho v_i^F \left(\tilde{A} + n\tilde{B}\, \left\|v^F\right\|_2\right) dV \end{aligned} \tag{2.48}$$

$$\int_{V^F} \frac{\partial c}{\partial t} dV + \oint_{A^F} c v_i^F dA_i = 0 \,. \tag{2.49}$$

This formulation aligns with Higuera et al. [47] and only adds two resistance terms to the momentum equations. It uses a different diffusion term as in Jensen et al. [58] or Eqn. (2.30). The difficulty of this approach lies in the correct discretization of the continuity equation, as also stated in Higuera et al. [47].

Discretized Momentum Equations for (v_i^F, p^F) - Formulation

The governing equations should be integrated over the fluid volume ΔV^F and fluid areas dA_i^F. Using $dV^F = ndV$ and $dA_i^F = ndA_i$ together with a midpoint integration rule, the aforementioned discretization techniques yield

$$
\begin{aligned}
v_{i,P}^{F,n,m} & \left[\rho \Delta V_P \left(\frac{1}{\Delta t} + \tilde{A} + \tilde{B} n \left\| v^F \right\|_2^{n,m-1} \right)_P + \sum_{f(\Delta V_P)} A_{NB}^{v_i^F} \right] \\
& - \sum_{f(\Delta V_P)} \underbrace{\frac{n_f}{n_P} \left[\left(max \left[-\dot{m}_f^{n,m-1}, 0 \right] \right) + \left(\frac{\mu^F A}{d} \right) \right]}_{A_{NB}^{v_i^F}} v_{i,NB}^{F,n,m} = \\
& - \sum_{f(\Delta V_P)} \frac{n_f}{n_P} \left(p_f^{F,n,m-1} A_i \right) + \rho_P^F \Delta V_P \left(g_i + \frac{v_i^{F,n-1}}{\Delta t} \right)_P + S_{v_i^F} \, ,
\end{aligned}
\tag{2.50}
$$

where $\dot{m}_f = (\rho v_i^F A_i)_f$ refers to a mass flux. The term $S_{v_i^F}$ formally coincides with the term in the previous momentum equations (2.32). The Finite Volume Method (FVM) aims to obtain conservative fluxes, and therefore a unique porosity ratio n_f/n_P (porosity value at face/porosity value in cell center) is required in the flux terms. This suggests to interpolate the denominator n_P to the faces, which immediately yields $n_{P_f} = n_f$, and a simpler expression arises, viz.

$$
\begin{aligned}
v_{i,P}^{F,n,m} & \left[\rho \Delta V_P \left(\frac{1}{\Delta t} + \tilde{A} + \tilde{B} n \left\| v^F \right\|_2^{n,m-1} \right)_P + \sum_{f(\Delta V_P)} A_{NB} \right] \\
& - \sum_{f(\Delta V_P)} \underbrace{\left[\left(max \left[-\dot{m}_f^{n,m-1}, 0 \right] \right) + \left(\frac{\mu^F A}{d} \right) \right]}_{A_{NB}} v_{i,NB}^{F,n,m} = \\
& - \sum_{f(\Delta V_P)} \left(p_f^{F,n,m-1} A_i \right) + \rho_P^F \Delta V_P \left(g_i + \frac{v_i^{F,n-1}}{\Delta t} \right)_P + S_{v_i^F} \, .
\end{aligned}
\tag{2.51}
$$

It is important to note that $dA_i^F = ndA_i$ is an assumption only valid for 1D and 2D flows. Taking into account 3D effects using root-based approximations only induces minor influences at the corners of a 3D rigid porous dam.

Discretized Continuity Equation for (v_i^F, p^F) - Formulation

The same SIMPLE algorithm described in Sec. 2.2.1 is used to iteratively obtain the pressure. Equation (2.47) has to be integrated over the fluid volume, and therefore the face areas occurring in the discretized version are augmented by the face-centered porosities n_f and the semi-discrete pressure correction equation reads

$$\sum_{f(\Delta V_P)} \left(n v_i^{F,m} A_i\right)_f - \sum_{f(\Delta V_P)} \left[\left(\frac{n\,\Delta V}{A_P^{v_i^F}}\right)\left(\frac{\partial p^{F,\prime}}{\partial x_i}\right) A_i\right]_f = 0\ . \tag{2.52}$$

Note that Rhie-Chow type corrections are multiplied with n_f in line with Eqn. (2.52) to avoid pressure oscillations.

Discretized Air Mixture Fraction Equation for (v_i^F, p^F) - Formulation

In the air mixture fraction equation for the v_i^F, p^F-formulation, the discretization over the fluid area and volume leads to

$$c_P^{n,m}\left[\frac{\Delta V_P}{\Delta t} + \sum_{f(\Delta V_P)} A_{NB}^c\right] - \sum_{f(\Delta V_P)} \underbrace{\frac{n_f}{n_P}\left(max\left[-(\dot{m}/\rho), 0\right]\right)_f}_{A_{NB}^c} c_{NB}^{n,m} = \frac{\Delta V_P}{\Delta t} c_P^{n-1} + S_c \tag{2.53}$$

where $n_{P_f} = n_f$ is assumed in line with Eqn. (2.51). The fluid properties are updated using c^m and the equations of state (2.18).

2.2.3 Discretized Equation System for Simplified Momentum Equations with $(\hat{v}_i, p^F)$ - Formulation.

The simplified formulation is the set of governing equations from Sec. 2.2.1 with a reduction of the aforementioned momentum equations (2.30). This version of the momentum equations neglects the division of the left-hand terms of the discrete momentum equations by the porosity. Therefore, the transient, convective, and diffusive transport are effectively reduced. To summarize, the governing equations are given by

$$\oint_A \hat{v}_i dA_i = 0 \tag{2.54}$$

$$\begin{aligned} \int_V \frac{\partial}{\partial t}\left(\rho \hat{v}_i\right) dV + \oint_A \left(\rho \hat{v}_i \hat{v}_j\right) dA_j = \\ -\oint_A p^F dA_i + \int_V \rho g_i dV + \oint_A \mu\left(\frac{\partial \hat{v}_i}{\partial x_j} + \frac{\partial \hat{v}_j}{\partial x_i}\right) dA_j - \int_V \frac{\rho}{n} \hat{v}_i \left(\tilde{A} + \tilde{B}\ \|\hat{v}\|\right) dV \end{aligned} \tag{2.55}$$

$$\int_V \frac{\partial c}{\partial t} dV + \oint_A \frac{c \hat{v}_i}{n} dA_i = 0\ . \tag{2.56}$$

Only the momentum equations are modified, and subsequently combined with the discrete continuity equation and air mixture fraction equation outlined in Sec. 2.2.1. The discrete form of Eqn. (2.55) follows by applying the same discretization techniques as in previous sections resulting in

$$\begin{aligned}
&\hat{v}_{i,P}^{n,m} \left[\Delta V_P \, \rho_P \left(\frac{1}{\Delta t} + \frac{\tilde{A}}{n} + \frac{\tilde{B}}{n} \, \| \hat{v} \, \|_2^{n,m-1} \right)_P + \sum_{f(\Delta V_P)} A_{NB}^{\hat{v}_i} \right] \\
&- \sum_{f(\Delta V_P)} \underbrace{\left[\left(max \left[-\dot{\hat{m}}^{n,m-1}, 0 \right] \right)_f + \left(\frac{\mu A}{d} \right)_f \right]}_{A_{NB}^{\hat{v}_i}} \hat{v}_{i,NB}^{n,m} = \\
&- \sum_{f(\Delta V_P)} \left(p_f^{F,n,m-1} A_i \right) + \rho_P \Delta V_P \left(g_i + \frac{\hat{v}_i^{n-1}}{\Delta t} \right)_P + S_{\hat{v}_i} \; .
\end{aligned} \tag{2.57}$$

Mind that the deferred correction terms of the higher-order convective approximation, e.g. the flux blending scheme, are consistently simplified. Similar methods are mentioned in Higuera et al. [47], albeit a discussion on the exactness of the method is not given. The accuracy of the simplified equation system is explored in Sec. 2.4.

Remarks on Validity and Advantages of Simplified Strategy

A closer look at the discrete momentum equations leads to arguments that show why the simplification gives small deviations to a correct formulation in numerical results. To demonstrate, the diagonal coefficient $A_P^{\hat{v}_i}$ is split into a porous contribution and a remainder, viz.

$$A_P^{\hat{v}_i} = A_P^{*,\hat{v}_i} + \rho_P \Delta V_P \left(\tilde{A}_P + \tilde{B}_P \, \| \hat{v}_P \|_2 \right) \, . \tag{2.58}$$

Introducing this into the reduced momentum equations (2.35) used to derive the pressure-correction scheme leads to the semi-discrete momentum equations

$$\left(A_P^{*,\hat{v}_i} + \rho_P \Delta V_P \left(\tilde{A}_P + \tilde{B}_P \, \| \hat{v}_P \|_2 \right) \right) \hat{v}_{i,P} = - \frac{\partial p^F}{\partial x_i} \Delta V_P - \sum_{NB} A_{NB}^{\hat{v}_i} \hat{v}_{i,NB} + \rho_P g_i \Delta V_P \, . \tag{2.59}$$

For lower porous Reynolds numbers, creeping flow situations featuring small velocities, small velocity derivatives, and thus high porous force model constants can be expected. In the limit of small coefficients $A_P^{*,\hat{v}_i}$ and A_{NB}^*, one immediately recognizes that the semi-discrete momentum equations reduce to a subset of an equilibrium of porous, pressure and gravity forces. In this case, the semi-discrete momentum equations (2.59) converge to the "pure" Darcy flow equation. The higher the porous Reynolds number, the less acceptable the simplification of the momentum equations. This will be explored further in Sec. 2.4.

The advantage of using Eqn. (2.55) is the simplicity of the implementation into a state-of-the-art second-order accurate FVM fluid solver. No modification of the momentum equations is needed (the variable v^F is changed to $\hat{v}$) except for supplementing porous force contributions. The pressure correction scheme can be applied without changes. As explained above, a simple modification of the free surface equation, cf. Eqn. (2.31), has to be performed. Both modifications may easily be implemented in a user coding environment of commercial software packages. A further advantage of the simplified method is its higher robustness towards different treatments of the porosity value at faces since no face values of the porosity are needed in the discretization of the simplified method.

2.3 Verification and Validation

All three suggested FV models for free surface flow through rigid porous medium are assessed utilizing 2D and 3D validation cases. To this end, selected variants of unsteady dam-break flows and a steady embankment flow, are investigated using different porous materials. A single-phase 3D permeameter case introduced in Larese et al. [72] is used to study the different formulations and validate the implementation of the porous forces. Secondly, a 2D dam break case introduced by Lin [76] and also used for validation in Del Jesus et al. [20], Larese et al. [70] and Liu et al. [78] with two different rigid porous dam materials is considered to validate the two-phase formulation. Furthermore, a 2D and 3D flow through a homogenous porous dam introduced in Larese [69] and a 3D dam break case introduced by Del Jesus et al. [20] are used to verify the three-dimensional behavior as well as influences of higher porous Reynolds numbers. The cell-centered porosities n and constants of the porous resistance laws $\tilde{A}$, $\tilde{B}$, and $\tilde{C}$ are defined in line with data used by the previously mentioned computational and experimental work. Face values of the porosity follow from linear interpolation. Average and peak porous Reynolds numbers Re_P are calculated from the present simulations to estimate non-linear influences on the porous resistance. The unconstraint flows are characterized by low Reynolds numbers, which support a laminar representation. Moreover, turbulent effects inside the porous material are deemed to be captured by the porous resistance force model.

Results of the present simulations utilize a compressive HRIC approximation of convective concentration fluxes in test cases 2.3.2 and 2.3.5 as well as the CICSAM scheme in test case 2.3.4. A simple flux-blending scheme featuring 70% second-order central differencing is used to approximate the convective terms of the momentum equations, and a first-order implicit Euler scheme is employed to approximate time derivatives.

Throughout the section, remarks about the porous force model influence and the discretization influence on results are given. Furthermore, a comparison of the three alternative governing equation systems is presented for an artificial two-phase porous flow case without resistance forces.

2.3.1 Permeameter - Validation for Single-Phase Porous Flow

Experimental permeameter results from the Centre for Hydrographic Studies CEDEX presented in Larese et al. [72] are used to validate the present methods for single-phase flow through a porous material. A material with a porosity of $n = 0.4133$ and an average diameter of $D_{50} = 3.5 \cdot 10^{-2}$ m is filled in a cylindrical tube with an inner diameter of $D_{perm} = 0.388$ m and a length of $L = 2.0$ m, cf. Fig. 2.4. Emphasis is given to the pressure loss in steady flows of water ($\rho = 1000$ kg/m^3, $\mu = 0.001$ Pa s) for different flow rates, cf. Larese et al. [72]. Depending on the flow rates, the porous Reynolds numbers range from $Re_P = 30$ to $Re_P = 296$. Using the

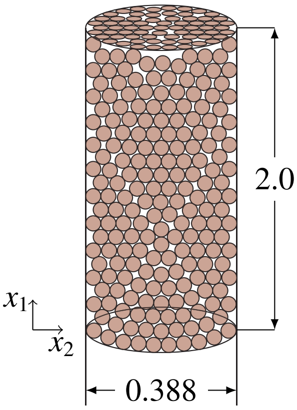

Figure 2.4: Permeameter case: Geometry of permeameter filled with porous material. Dimensions are given in meters.

expression

$$i = A^* \hat{v}_1 + B^* \hat{v}_1^2 \tag{2.60}$$

for the hydraulic gradient i ($i = \Delta p^F / \rho g L$), A^* and B^* are obtained to be $A^* = 0.2729$ s/m and $B^* = 29.766$ s^2/m^2 from experiments. The constants $\tilde{A}$ and $\tilde{B}$ are obtained from A^* and B^* by multiplication with the porosity n and the gravitational acceleration $g = 9.81$ m/s^2. Mind that the experiment is designed such that all other body forces, e.g. gravity, do not affect the analyzed gradient of pressure. The resulting pressure difference can be used directly to obtain the hydraulic gradient.

3D results are presented for three different unstructured meshes where a regular grid spacing is used for the longitudinal direction: a coarse mesh with $\Delta x_1 = L/41$ and $\Delta x_2 = \Delta x_3 \approx \sqrt{2\pi/56}\ D_{perm}/2$, a medium-sized mesh with $\Delta x_1 = L/82$ and $\Delta x_2 = \Delta x_3 \approx \sqrt{2\pi/224}\ D_{perm}/2$ and a fine mesh with $\Delta x_1 = L/164$ and $\Delta x_2 = \Delta x_3 \approx \sqrt{2\pi/1012}\ D_{perm}/2$.

A wall boundary condition is applied along the cylinder wall. The inlet faces at $x_1 = 0$ are assigned to Dirichlet conditions for the x_1-velocity according to a prescribed volume flux. A pressure outlet boundary is used at $x_1 = L$, where the pressure is set to a zero reference pressure. Pressure and velocity fields are initialized with the inlet velocity and the reference pressure.

Validation Results for Different Mesh Resolutions and Discrete Formulations

Simulations are conducted with the three different meshes for all three formulations of the governing equation system. Fig. 2.5 depicts the deviations of simulation results from the applied resistance law given for a range of volume fluxes Q. The deviation error, which is defined as error $= (i_{sim} - i_{resLaw})/i_{resLaw}$, remains below 1% for all resolutions and versions of governing equations. Since the influence of the convective and diffusive fluxes increases with an increasing volume flux Q, a slight enhancement of the error levels occurs with increasing Q due to the related non-linear effects. Improving the spatial resolution consistently leads to smaller deviations. The error magnitude varies for the different governing equations where the simplified $(\hat{v}_i, p^F)$ - formulation displays the most pronounced error. The best results are obtained with the (v^F, p^F) - formulation.

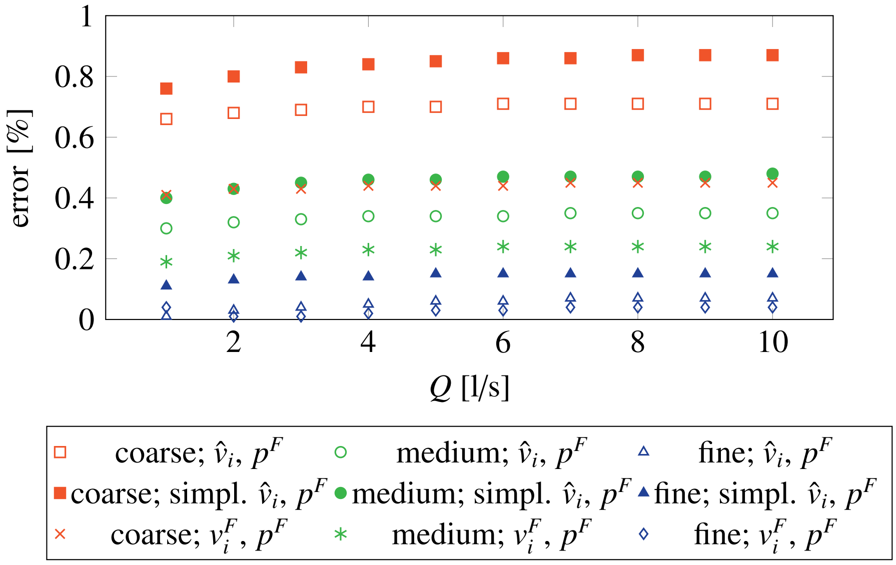

Figure 2.5: Evolution of the predictive error for the hydraulic gradient, cf. Eqn. (2.60), with increasing volume flux Q for the permeameter case. Results are obtained from the three investigated formulations for three different spatial resolutions: coarse mesh $\Delta x_1 = L/41$, $\Delta x_2 = \Delta x_3 \approx \sqrt{2\pi/56}\, D_{perm}/2$; medium-sized mesh $\Delta x_1 = L/82$, $\Delta x_2 = \Delta x_3 \approx \sqrt{2\pi/224}\, D_{perm}/2$; fine mesh $\Delta x_1 = L/164$, $\Delta x_2 = \Delta x_3 \approx \sqrt{2\pi/1012}\, D_{perm}/2$.

The deviation errors with respect to the experimental data are exemplarily displayed for Q = 6 l/s in Fig. 2.6. It can be seen that the values calculated by the resistance law in Eqn. (2.60)

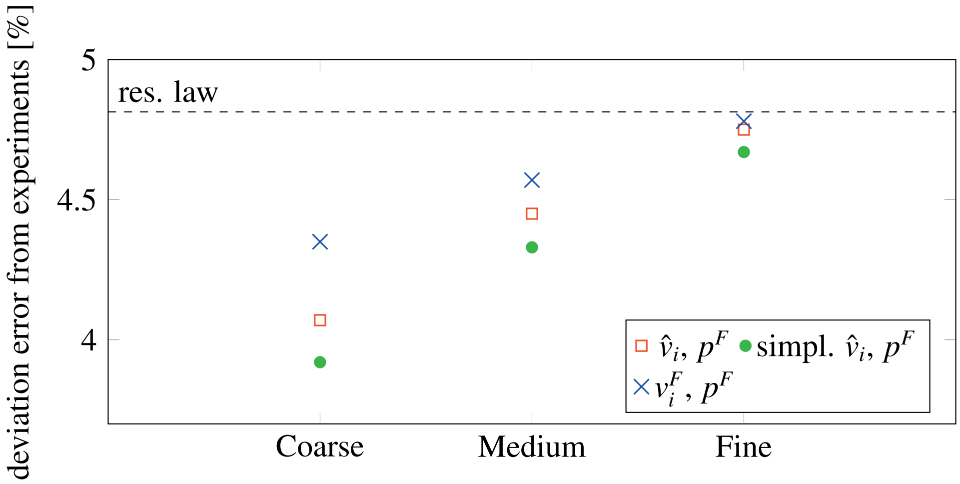

Figure 2.6: Deviation of the predictive and modeled (2.60) hydraulic gradient obtained for the permeameter case using a volume flux of $Q = 6\,l/s$ ($Re_P = 177$). Predictions are obtained with the three investigated formulations for three different spatial resolutions.

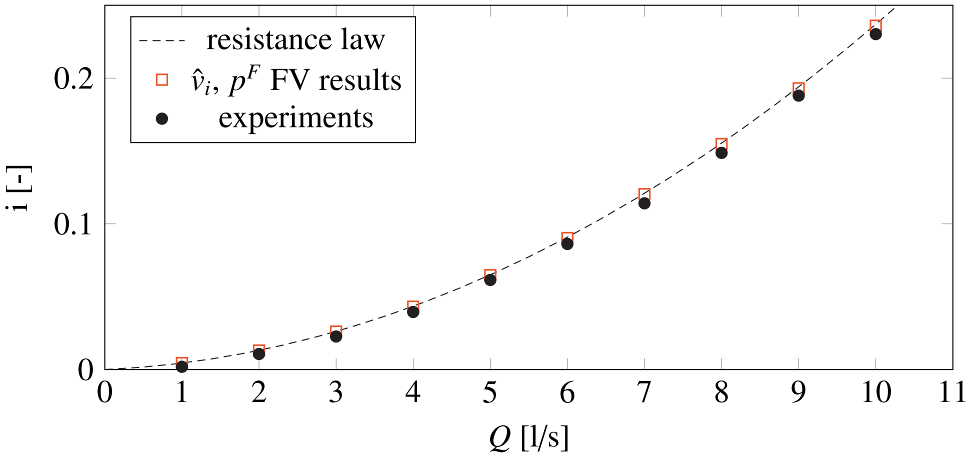

Figure 2.7: Evolution of the hydraulic gradient with increasing volume fluxes for the permeameter case ($Re_P = 30$ to $Re_P = 296$). Comparison of experimental and analytical data with results obtained for the finest mesh with $\Delta x_1 = L/164$ and $\Delta x_2 = \Delta x_3 \approx \sqrt{2\pi/1012}\, D_{perm}/2$ using the ($\hat{v}_i$, p^F) - formulation.

overestimate the hydraulic gradient of the experimental data by almost 5% (dashed line), and the simulation errors are generally close to the deviation of the resistance law. Coarser mesh resolutions lead to results closer to the experimental data, which is caused by the inlet velocity being defined as the volume flux divided by the theoretical area of the permeameter tube and the existing area of the computational domain being defined by the mesh resolution. Since the actual area of the inlet is smaller than the theoretical for coarser meshes, the corresponding volume flux is also smaller. Therefore the overestimation of the resistance law is balanced by a coarser mesh due to smaller velocity magnitudes. Furthermore, since the simplified method also leads to smaller velocity magnitudes, the resistance law's error is compensated better.

In Fig. 2.7, the results for the finest mesh of the ($\hat{v}_i$, p^F) - formulation are plotted against the experimental results and the theoretical resistance law values. Overall, the results of the FV method fit the resistance law as well as the experimental data.

2.3.2 Dam Break Flow Through Rigid Porous Material

The second validation case refers to a two-phase dam break flow through porous material proposed in Lin [76] and Liu et al. [78]. The experimental data from Liu et al. [78] is taken to validate the present model. The experiment features a water column with an initial height of h_0 = 14.0 cm and an initial width of l_0 = 28.0 cm, which passes through a matrix of glass beads with an average diameter of $D_{50} = 3 \cdot 10^{-3}$ m that forms a porous material with a porosity value of $n = 0.39$. The initial state configuration of the simulations is shown in Fig. 2.8. Three repre-

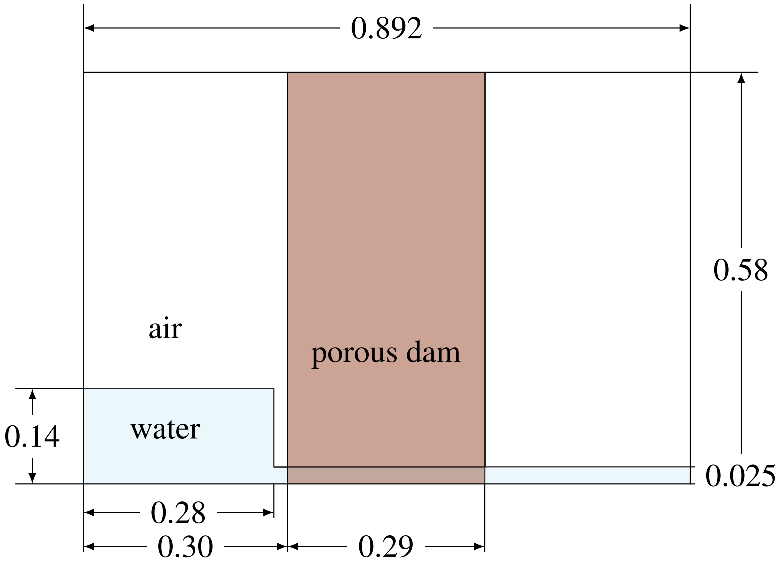

Figure 2.8: 2D porous dam break (h_0 = 14 cm): Initial geometry of porous dam break test case where all measurements are given in meters.

sentations of the porous forces $\hat{f}_i^R$ are applied in the literature for this validation case: Larese et al. [70] use the Engelund equation with $\alpha = 1000$ and $\beta = 0.25$, Del Jesus et al. [20] employ the Engelund equation with $\alpha = 700$ and $\beta = 0.5$ and Liu et al. [78] utilize the Van Gent equation with $\alpha = 1000$ and $\beta = 1.1$ and an added mass constant $\tilde{C} = 0.2074$. The difference between the results of these models is studied in this section. All other investigations are made using the same porous force model as Larese et al. [70].

Using the present results, a low average Reynolds number of $Re_P = 55$ follows from the space/time-mean Darcy velocity. The corresponding maximum velocity yields a Reynolds number of $Re_P = 125$. These values indicate that non-linear or turbulent effects become relevant for the resistance modeling.

Results for four different isotropic homogeneous grids are studied in the next section. The velocity field values are initialized at rest, and the pressure is set to a zero reference pressure. A zero pressure boundary is used along the top boundary, and all other boundaries employ slip wall conditions.

Mesh Study

To study the influence of spatial discretization, results from five different meshes are compared against experimental results from Liu et al. [78]. The mesh study has been conducted for all formulations. However, the results are only presented for the $(\hat{v}_i,\ p^F)$ - formulation, as the results of the other formulations differ only slightly. As a porous force model, the Engelund equation with $\alpha = 1000$ and $\beta = 0.25$ ($\tilde{A} = 64.667$ 1/s and $\tilde{B} = 334.210$ 1/m) is employed for the simulations on four isotropic homogeneous grids ($\Delta x_1 = h_0/10$, $\Delta x_1 = h_0/21$, $\Delta x_1 = h_0/42$ and $\Delta x_1 = h_0/84$) as well as one curvilinear grid with similar cell size as the second finest structured grid in the free surface region. Time steps are set in line with a Courant number well below 10^{-2} with Δt being $1 \cdot 10^{-4}$ s on the second finest mesh with $\Delta x_1 = h_0/42$.

Results displayed in Fig. 2.9 indicate a good mesh convergence against the finest mesh results for all time incidents. Satisfactory mesh convergence is obtained for the second finest grid with $\Delta x_1 = h_0/42$, which is therefore used for subsequent investigations.

For $t = 0.8$ s, numerical diffusion occurs in the air-mixture fraction variable close to the wall for the structured mesh with $\Delta x_1 = h_0/10$. It is interesting to note the difference in the free surface shape at the upstream boundary of the rigid porous material at $t = 0.4$ s for the coarsest mesh and the curvilinear mesh compared to predictions of the finer structured meshes. The differences result from linear interpolation of the porosity at the faces. Therefore, the discrete convective term of the air mixture fraction is influenced by the grid spacing. The curvilinear grid results mainly coincide with the results from the corresponding structured mesh.

Comparison of Different Formulations of the Discrete Governing Equations

Modeling influences are outlined by Fig. 2.10, which compares experimental data for the free surface evolution published in Liu et al. [78] with numerical results obtained from the $(\hat{v}_i, p^F)$ -, (v_i^F, p^F) - and simplified $(\hat{v}_i, p^F)$ - formulation (discussed in Sec. 2.2). The resistance law again refers to the Engelund approach used in the mesh study.

An excellent agreement of the results of all formulations with the experimental data can be noted for all time steps except at $t = 4.0$ s. Numerical results reported by Del Jesus [20] and Liu et al. [78] coincide with the present model results at this time, and Liu et al. [78] describe a possible cause as being the free surface sticking to the glass wall at some locations during the experiments at this specific time leading to an overestimation of the free surface level.

The simplified $(\hat{v}_i, p^F)$ - formulation coincides with the $(\hat{v}_i, p^F)$ - formulation for the time steps $t = 0.4$ s and $t = 0.8$ s. Subsequently, minimal visible differences occur in the position of the free surface upstream of the porous material induced by the different transport terms across the boundary of the rigid material. The results for the $(\hat{v}_i, p^F)$ - and (v_i^F, p^F) - formulation converge against the same steady state at $t = 4.0$ s. During earlier phases, slight differences upstream of the porous material are observed between the two formulations, which are also attributed to differences in modeling the transport across the rigid porous material boundary.

Porous Force Model Influences

Porous force model influences are displayed in Fig. 2.11 for simulations using the $(\hat{v}_i, p^F)$ - based VoF formulation to compute the dam break validation case. The different representations of the literature reported porous forces $\hat{f}_i^R$ follows Tab. 2.1.

As indicated by the two Van Gent results, the influence of the added mass coefficient is negligible, which explains why other authors hardly considered it. In contrast to the formulation and modeling differences assessed above, changes to the resistance law significantly affect the free surface's development. This highlights the dominance of the resistance law to balance pressure and gravity forces inside the momentum equations. The resistance law fitting best to the experimental data is the Engelund equation with $\alpha = 1000$ and $\beta = 0.25$, which is also used by Larese et al. [70].

Crushed Rocks Dam (h_0 = 25 cm)

Experimental data for a second 2D dam break through another porous material has been reported in Liu et al. [78]. This case is used to validate the present model for higher porous Reynolds numbers using the same computational domain, mesh and boundary conditions as in the previous case. The initial water column features a height of 25 cm and a width of 30 cm, and the porous material consists of crushed rocks with a porosity index of $n = 0.49$ and an average diameter $D_{50} = 1.59 \cdot 10^{-2}$ m. The case leads to $Re_P = 1267$ for the space/time-averaged Darcy velocity and $Re_P = 3473$ for the maximum Darcy velocity observed in space and time. Therefore, a turbulent Van Gent [38] resistance model based upon $\alpha = 1000$ and $\beta = 1.1$ ($\tilde{A} = 12.87$ 1/s, $\tilde{B} = 146.95$ 1/m) was employed. The added mass coefficient $\tilde{C}$ was neglected, cf. Table 2.1 in Sec. 2.1.3.

In Figs. 2.12 and 2.13, it can be seen that the visible results stemming from the three different implementation versions are only marginally different. A fair predictive agreement can be observed. Notably, the elevation dip observed downstream the porous layer from $t = 1.0 - 1.6$ s is represented well. Minor deviations between the two simulations and between simulated and measured data can be observed inside the porous material for $t \leq 0.8$ s. In conclusion, modeling influences are slightly more pronounced for the higher porous Reynolds number but still remain small.

Remark

For the glass beads and crushed rocks material, the dominance of the porous resistance force term in the momentum equations leads to coinciding results of the simplified momentum equations formulation with the non-simplified formulation.

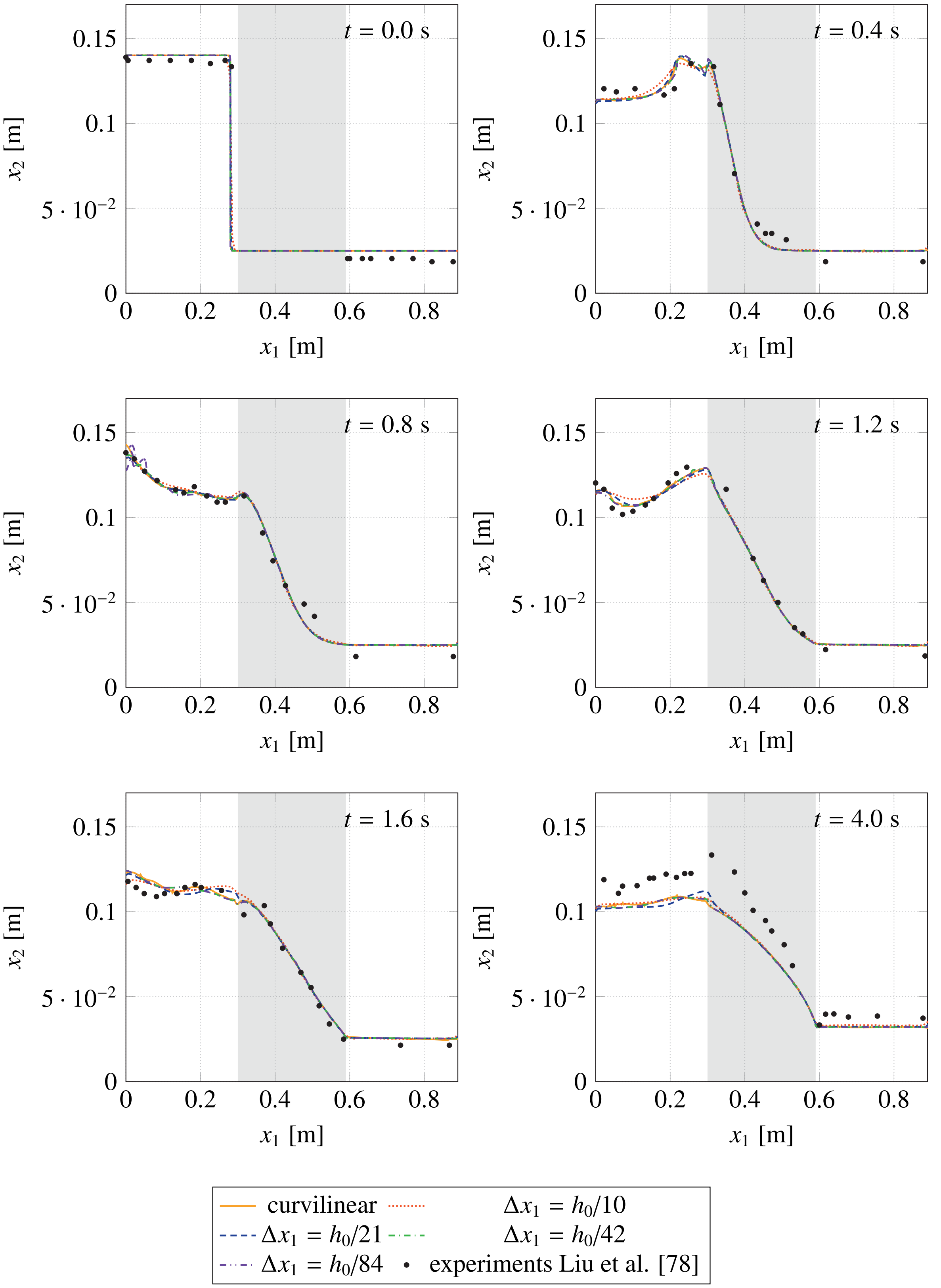

Figure 2.9: 2D porous dam break ($h_0 = 14$ cm, glass beads, mean $Re_P = 55$, max. $Re_P = 125$): Free surface elevation at six time incidents for varying meshes with ($\hat{v}_i$, p^F) - formulation.

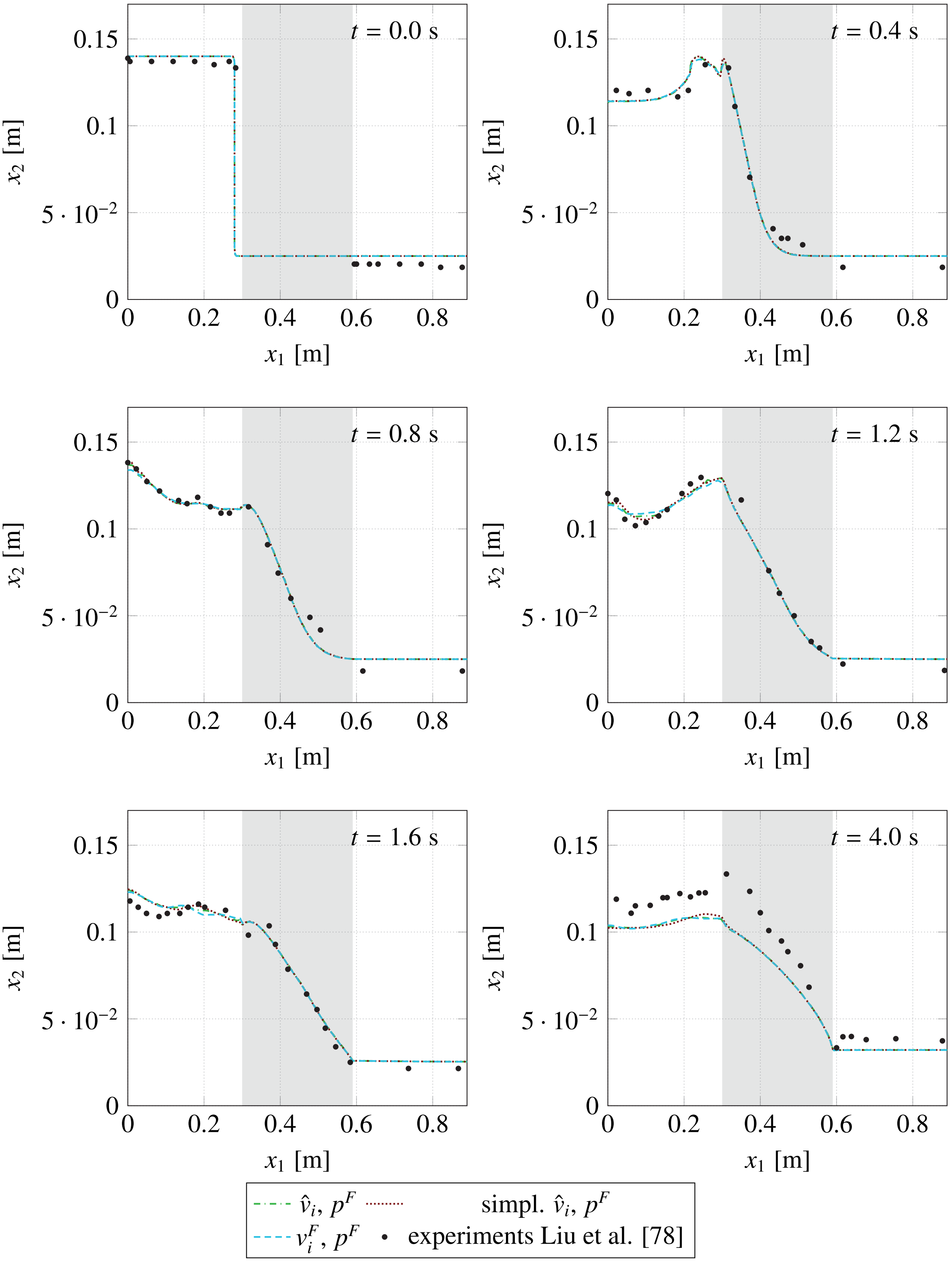

Figure 2.10: 2D porous dam break (h_0 = 14 cm, glass beads, mean Re_P = 55, max. Re_P = 125): Free surface elevation at six time incidents for different discrete formulations on the second finest mesh ($\Delta x_1 = h_0 /42$).

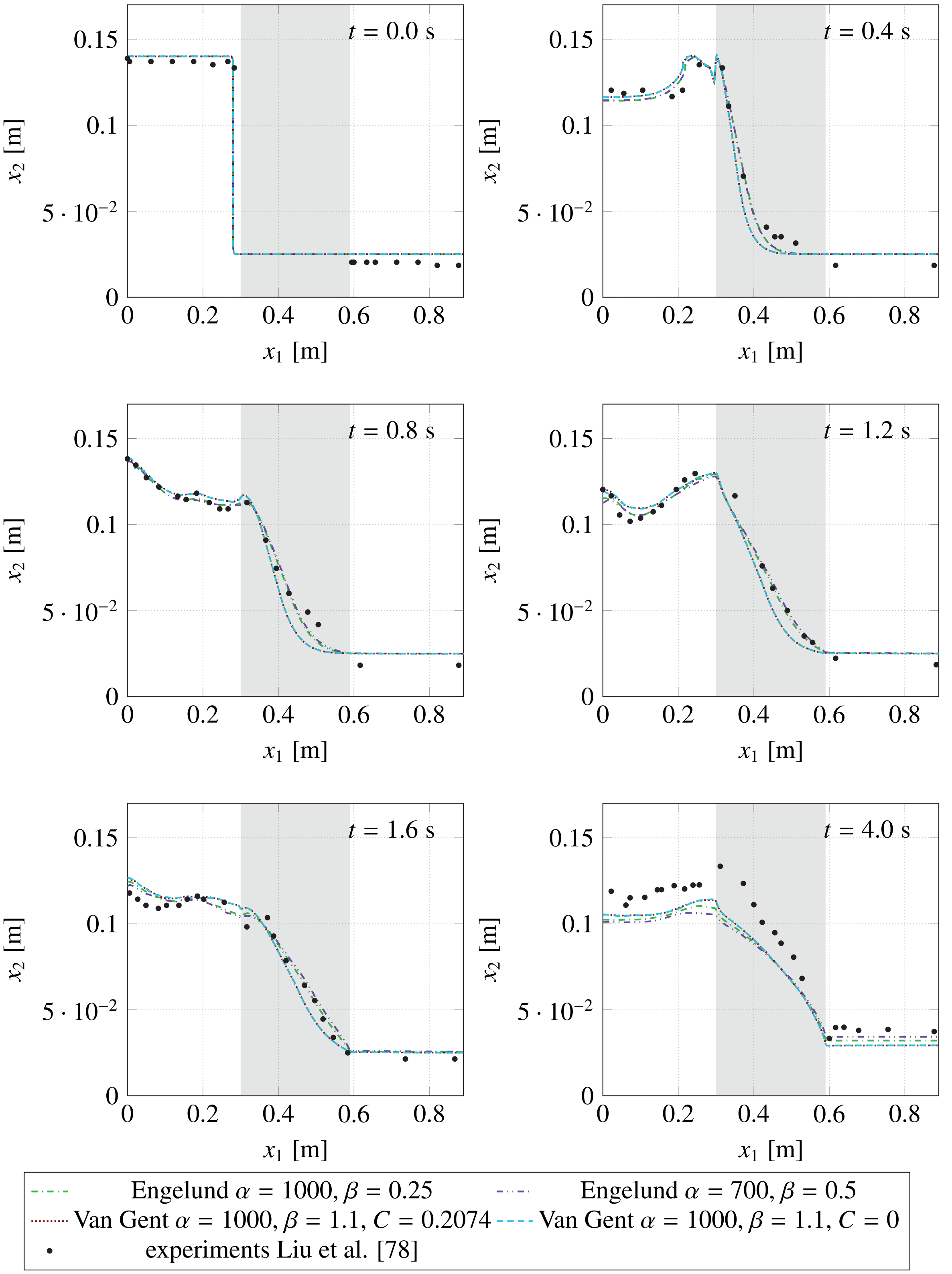

Figure 2.11: 2D porous dam break (h_0 = 14 cm, glass beads, mean $Re_P = 55$, max. $Re_P = 125$): Free surface elevation at six different time incidents for varying resistance laws, mesh size $\Delta x_1 = h_0/42$ and $(\hat{v}_i, p^F)$ - formulation.

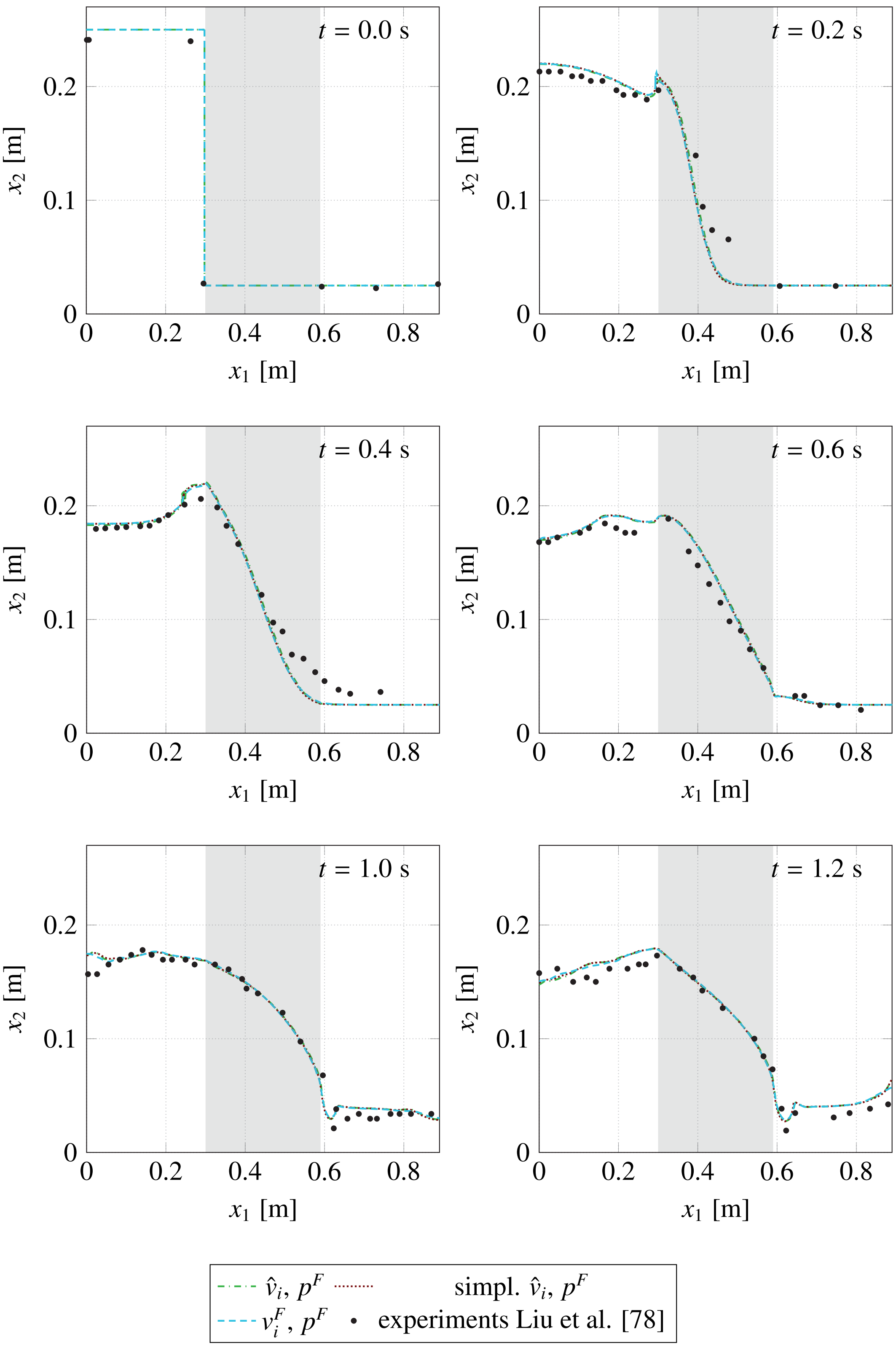

Figure 2.12: Free surface elevation at initial six time incidences obtained for the computation of the 2D porous dam break (h_0 = 25 cm, crushed rocks, mean Re_P = 1267, max. Re_P = 3473) with different formulations.

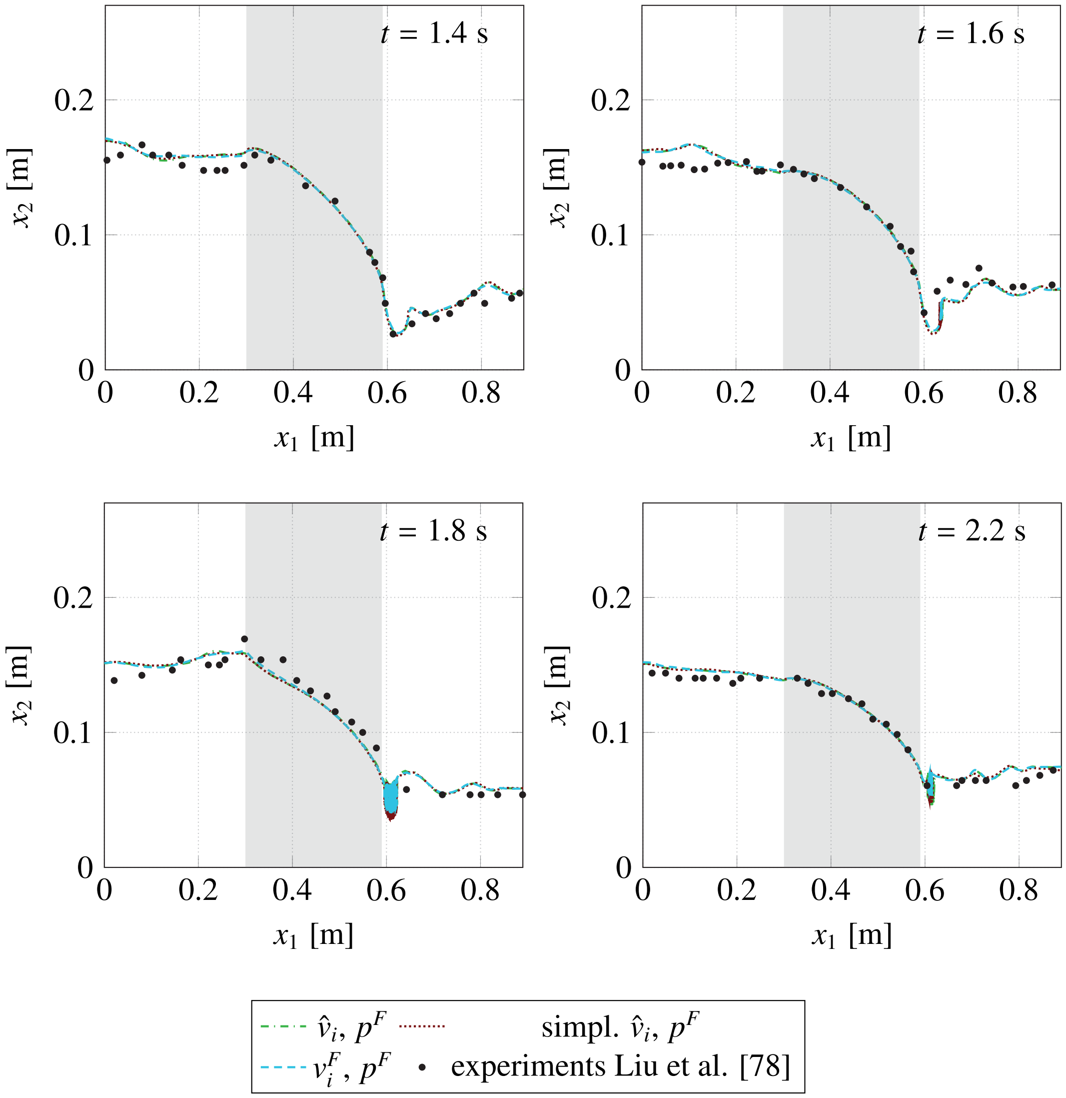

Figure 2.13: Free surface elevation at subsequent four time incidences obtained for the computation of the 2D porous dam break (h_0 = 25 cm, crushed rocks, mean Re_P = 1267, max. Re_P = 3473) with different formulations.

2.3.3 Flow Through Porous Medium with Zero Porous Forces

To scrutinize the attainable maximum differences for the three formulations described in Sec. 2.2, a generic test case without porous resistance forces serves as an illustrative example. To this end, the validation case described in Sec. 2.3.2 is revisited. Computations employ the same computational domain, mesh, and discretization, but the porous media model is modified by setting $\tilde{A} = 0, \tilde{B} = 0$ and $\tilde{C} = 0$.

Snapshots of the liquid body obtained from simulations without porous resistance are displayed in Figs. 2.14 and 2.15. In Fig. 2.14, the simulated liquid body is colored by the Darcy velocity for the $\hat{v}_i$,-based formulation and fluid velocity for the v_i^F-based formulation. The fluid velocity strongly accelerates in the porous medium without porous resistance due to the reduction of the wetted regime. It decelerates when leaving the porous media, as is expected by definition. This leads to large gradients at the boundaries of the rigid porous material, which even yields slight oscillatory velocities in the transition region (cf. Fig. 2.15) and might be related to the assumption $A^F = nA$ in the continuity equation of the v_i^F-based formulation. On the contrary, a more continuous spatial evolution is displayed in the Darcy velocity, and therefore the $\hat{v}_i$-based formulation yields a smoother velocity field in the transition region.

Adding the neglected term of the complete continuity equation (2.6), discretized as given in the remark in Sec. 2.2.1 leads to no visible differences in results for this extreme case which underlines that the assumption made in Sec. 2.1.1 is valid. In the absence of the usually dominating porous resistances, the formulation differences related to the transport terms lead to a visible difference in the free surface elevation. For the simplified momentum equations, a high deviation in free surface shapes can be noted, leading to the conclusion that the accuracy of the simplification depends on the relation between porous resistances and the non-linear terms of the momentum equations.

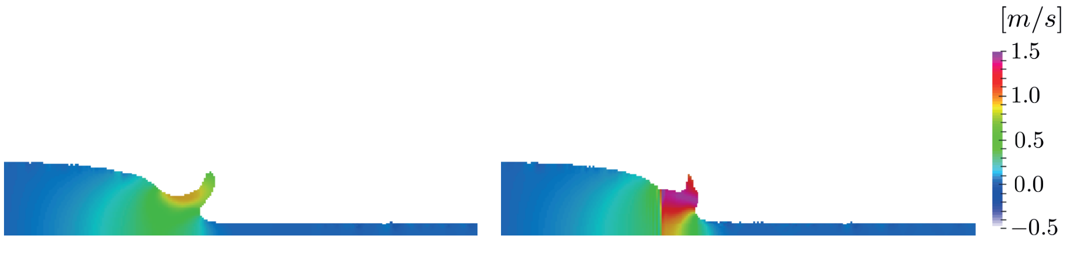

(a) $(\hat{v}_i, p^F)$ - formulation (b) (v_i^F, p^F) - formulation

Figure 2.14: Verification of the 2D porous dam break for zero porous forces: Snapshot of the liquid body predicted by the $\hat{v}_i$-based (left, Sec. 2.2.1) and the v_i^F-based (right, Sec. 2.2.2) VoF formulations coloured by the respective horizontal velocity.

(a) $(\hat{v}_i,\, p^F)$ - formulation

(b) $(v_i^F,\, p^F)$ - formulation

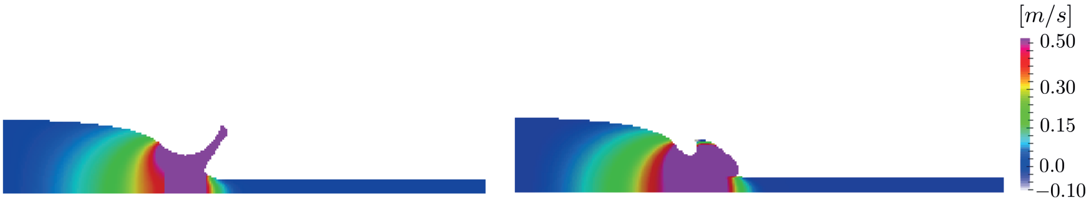

(c) $(\hat{v}_i,\, p^F)$ - formulation, complete continuity eq.

(d) $(\hat{v}_i,\, p^F)$ - formulation, simplified momentum eq.

Figure 2.15: Verification of the 2D porous dam break for zero porous forces: Snapshot of the liquid body predicted by the $\hat{v}_i$-based (top left & bottom left, Sec. 2.2.1), and the v_i^F-based (top right, Sec. 2.2.2) VoF formulations coloured by the horizontal fluid velocity component. Bottom left: $\hat{v}_i$-based with complete continuity equation. Bottom right: simplified $\hat{v}_i$-based.

2.3.4 Flow Through an Inclined Homogenous Porous Dam

To further validate the present method against experimental data, a validation case from Larese [71] is applied. Water flows through an inclined dam with a geometry illustrated in Fig. 2.16 (L = 4.0 m). The dam consists of homogeneous rockfill material with a porosity index of n = 0.4052. A constant volume flux of Q = 25.46 l/s enters the channel through an orifice of 5 cm (height) × 246 cm (width) from the left. The average particle diameter is $D_{50} = 3.504 \cdot 10^{-2}$ m and yields a (computed) Reynolds number of $Re_P = 1335$ using a space/time-averaged Darcy velocity and $Re_P = 4939$ using the maximum Darcy velocity.

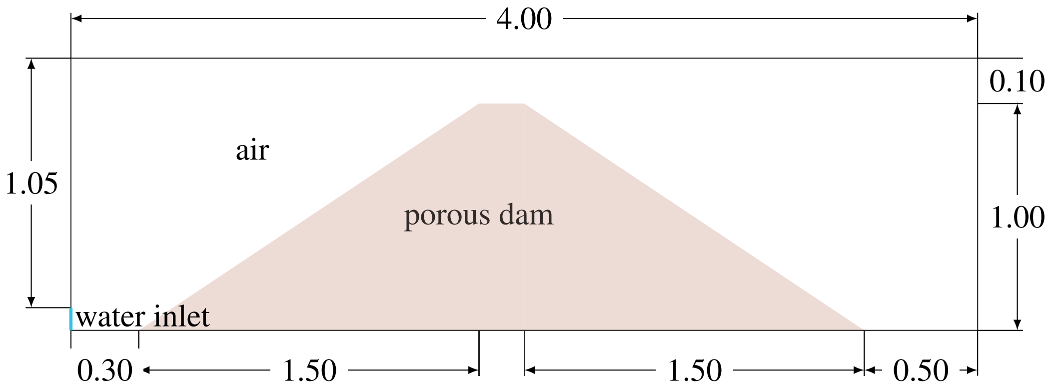

Figure 2.16: 2D inclined porous dam: Initial geometry of inclined homogenous porous dam validation case with measurements given in meters.

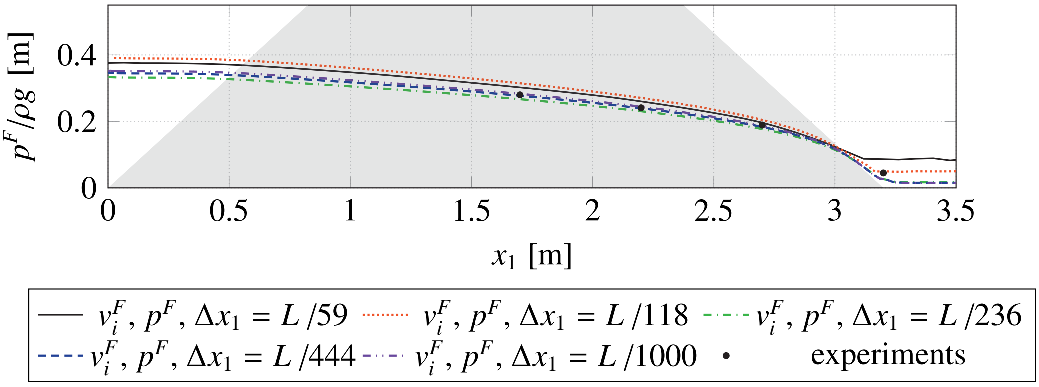

Figure 2.17: 2D inclined porous dam (mean $Re_P = 1335$, max. $Re_P = 4939$): Free surface location obtained for different spatial resolutions with the (v_i^F, p^F) - formulation.

As a porous force model, the Ergun approach is applied (cf. Tab. 2.1) with constants $\alpha = 150$ and $\beta = 1.75$. Employing a water density of 1000 kg/m^3 and dynamic viscosity of $\mu = 0.001$ Pa s yields the porous force constants $\tilde{A} = 0.26\ 1/s$ and $\tilde{B} = 180.93\ 1/m$.

A study with five different homogenous structured grids is carried out, and a grid spacing of $\Delta x_1 = L/1000$ is applied for subsequent studies with a time step of $\Delta t = 5.0 \cdot 10^{-4}$ s. Following the experiments, a Dirichlet condition using a homogeneous velocity $v_1^F = 0.207$ m/s is used to simulate the inflow, and zero-gradient conditions are used at the outlet. At the top boundaries, a zero pressure boundary condition is applied, and bottom boundaries employ a wall boundary condition. The size of the considered 2D domain is indicated by Fig. 2.16. Pressure data was experimentally recorded for the steady state flow at four different locations to detect the free surface which is used for comparison.

Mesh Studies

A mesh study is conducted for the $\hat{v}_i$- and v_i^F- based formulations, where the time step is adjusted for each mesh to return Courant numbers well under 0.01. A continuous initialization of the porosity and porous resistance law constants, using a linear interpolation between the face values is needed for finer meshes to converge for the $(\hat{v}_i, p^F)$ - formulation due to the division by the porosity in several terms of the momentum as well as the air-mixture fraction equation.

In Figs. 2.17 and 2.18, it can be observed that the position of the free surface is overestimated for both formulations on the coarser meshes. Predictive differences between the two formulations are more pronounced for coarser grids due to larger gradients in porosity. The coarse grid results indicate an improved agreement of the v_i^F- based formulation with experimental data, which might be related to the simplification of the continuity equation in the $\hat{v}_i$- based formulation.

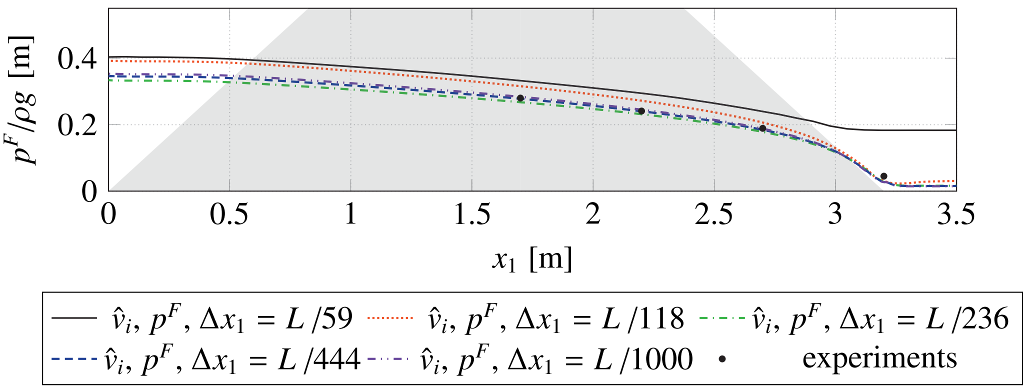

Figure 2.18: 2D inclined porous dam (mean Re_P = 1335, max. Re_P = 4939): Free surface location obtained for different spatial resolutions with the ($\hat{v}_i$, p^F) - formulation.

Using finer meshes, the results between the two formulations agree much better, and a mesh converged result is obtained at a relatively fine mesh of $\Delta x_1 = L/444$.

Run-time Evaluation

The computational effort of the $\hat{v}_i$- based and v_i^F- based formulations and four different mesh densities were assessed on a 12-node workstation. Results of the assessment are compared in Tab. 2.2. For simulations $\Delta x_1 = L/118$, $\Delta x_1 = L/236$ and $\Delta x_1 = L/444$ the run-times of the $\hat{v}_i$, p^F-formulation are smaller than the reference run with the v_i^F, p^F- formulation. The opposite is the case for the coarsest mesh, which is in line with the results of the mesh study, implying better performance for this formulation for coarse meshes and, therefore, faster convergence of the outer loop.

Table 2.2: 2D inclined porous dam (mean Re_P = 1335, max. Re_P = 4939): Run-times for mesh study simulations with different discrete formulations.

	Number Cells	Run-Time		
		($\hat{v}_i$, p^F)	(v^F, p^F)	
$\Delta x_1 = L/59$	928	0.270115E+05 s	0.227749E+05 s	-18.60%
$\Delta x_1 = L/118$	3712	0.227563E+05 s	0.304191E+05 s	25.19%
$\Delta x_1 = L/236$	14848	0.746491E+05 s	0.107350E+06 s	30.46%
$\Delta x_1 = L/444$	59392	0.194445E+06 s	0.218152E+06 s	10.87%

Comparison of Results for the Different Formulations of Governing Equations

Numerical results for the steady state of all three formulations are compared with experimental data in Fig. 2.19. The experimental data is available at three locations inside the downstream half of the dam. A supplementary measurement position is located just downstream of the dam. When attention is directed to the fine grid results obtained for the steady state depicted in Fig. 2.19, the free surface shapes returned by the investigated three formulations display hardly any difference and agree well with measured data. Therefore the formulation differences are deemed insignificant for this case.

Moreover, Fig. 2.20 compares data for the transient flow development which confirms steady state findings. Since no experimental data exists to compare the transient predictions, a verification against numerical results from an edge-based level-set solver introduced in Larese [69] is presented. Figure 2.20 reveals that the free surfaces obtained from the FV and the edge-based solvers travel with a similar forward speed through the porous material. However, a small vertical/up lift tendency is observed by the VoF simulations on the upstream end when compared to the edge-based results. The latter might be attributed to the different formulations of the convective term and an increased porosity index in the vertical direction. Also, a marginal difference in the vertical velocity of the free surfaces from the $\hat{v}_i$- based formulation and the v_i^F-based formulation can be observed in Fig. 2.20. This is thought to stem from the difference in the diffusion term of the two formulations, where the ($\hat{v}_i$, p^F) - formulation leads to a slightly higher diffusion term since the multiplication of the porosity and the fluid velocity is done inside the diffusion operator. It is remarked that for a higher pore Reynolds number, the formulation's differences increase.

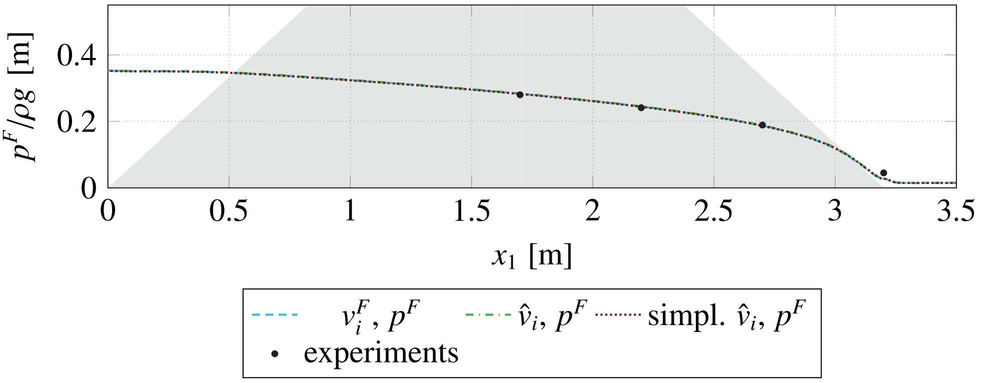

Figure 2.19: 2D inclined porous dam (mean Re_P = 1335, max. Re_P = 4939): Comparison of the measured and predicted steady state free surface locations for different discrete formulations using the fine mesh ($\Delta x_1 = L/1000$).

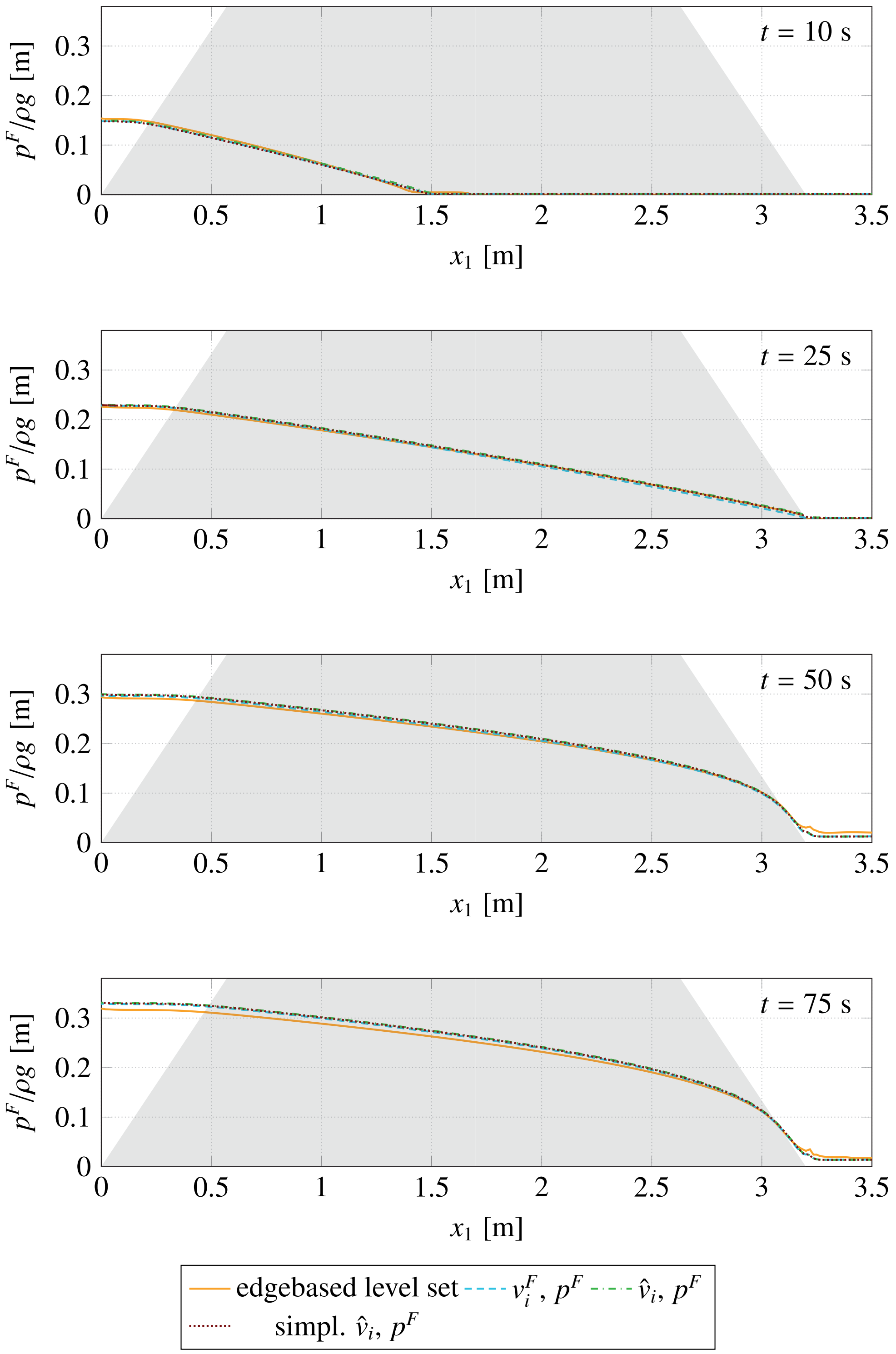

Figure 2.20: 2D inclined porous dam (mean Re_P = 1335, max. Re_P = 4939): Unsteady flow through an inclined porous dam. Comparison between free surface elevations from v_i^F- and $\hat{v}_i$-based VoF results with predictions of an edge-based level set solver for four time instants.

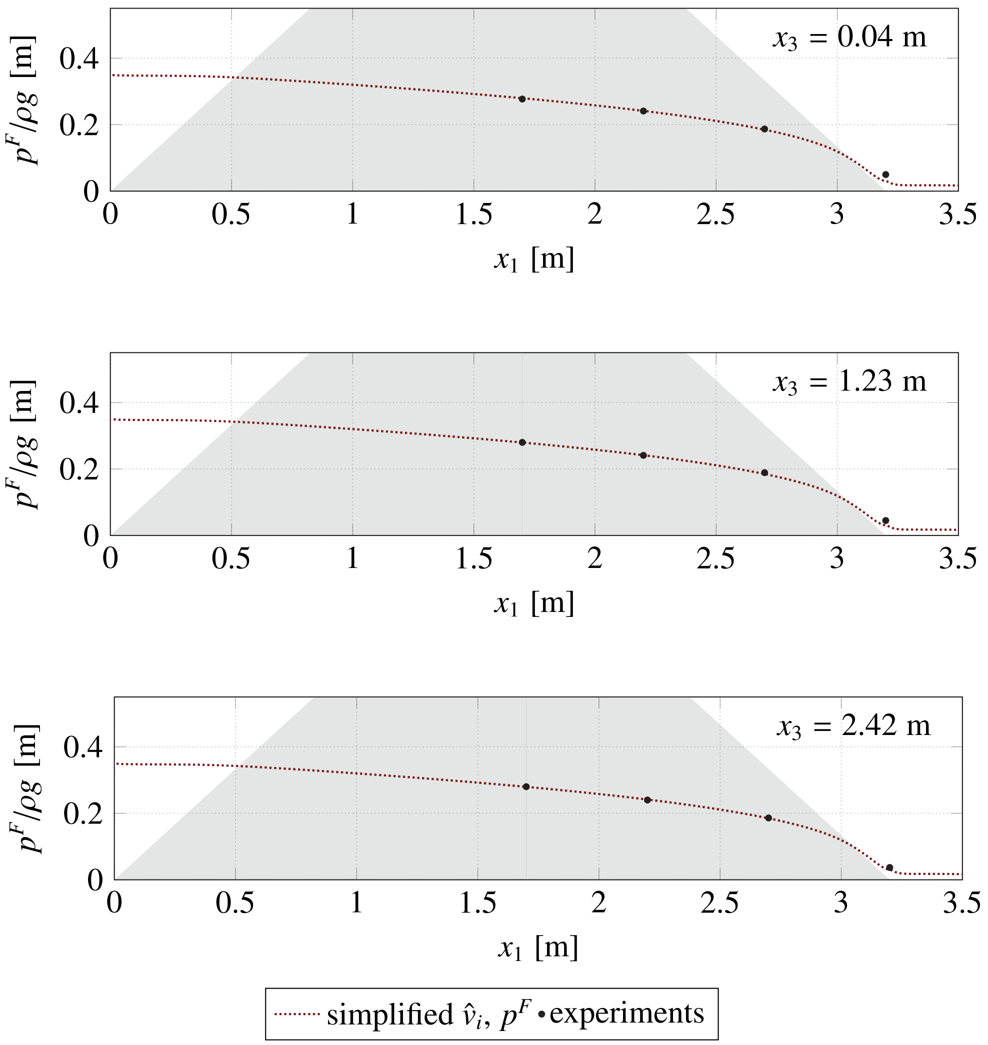

Figure 2.21: 3D inclined porous dam (mean $Re_P = 1335$, max. $Re_P = 4939$): Comparison of free surface elevation of simplified $\hat{v}_i$, p^F- formulation with experimental data for three different planes in x_3-direction.

Three-Dimensional Inclined Dam

Experimental results for the validation case stem from a 2.45 m wide channel where the rockfill dam fills the complete width of the channel. Therefore results from a 3D simplified momentum equations simulation are validated against the three-dimensional pressure measurements in Fig. 2.21. The computational domain is defined by the length and height given in Fig. 2.16 and a width of 2.45 m. A homogenous structured mesh with a grid spacing of $\Delta x_1 = \Delta x_2 = \Delta x_3 = L/286$ together with a time step of $\Delta t = 0.001$ s is applied for the simulation. Initial and boundary conditions are defined according to the 2D case, and wall boundary conditions are applied at the side walls consistent with the experimental setup. As a result, excellent agreement of the results with the experimental data can be observed in Fig. 2.21.

2.3.5 Three-Dimensional Porous Dam Break

To demonstrate the validity of the previous conclusions, an exemplary 3D verification case introduced by Del Jesus [20] is used. Results from the present method are compared with numerical results of Del Jesus [20] and Larese et al. [70]. The verification case is an extension of the crushed rocks case depicted in a previous section, using the same rigid porous dam material parameters in a 3D domain. As displayed in Fig. 2.22, the porous dam is positioned in a domain that is 0.6 m high, 0.6 m wide, and $L = 1.2$ m long. The dam features a height of 0.6 m, a width of 0.3 m and a length of 0.3 m. As in the 2D cases, a free surface height of 2.5 cm is initiated in the rest of the domain. The higher water column increases the porous Reynolds number regarding the 2D crushed rocks validation case. For the space/time-averaged Darcy velocity, this yields a pore Reynolds number $Re_P = 1761$. Using the maximum Darcy velocity observed in space and time, the pore Reynolds number reads $Re_P = 15099$. To obtain a similar resolution as Del Jesus [20], the horizontal grid spacing was assigned to $\Delta x_1 = \Delta x_2 = L/120$, the vertical spacing reads $\Delta x_3 = L/240$ and a time step of $\Delta t = 5 \cdot 10^{-5}$ s is employed. Except for the top, where the pressure is set to the reference pressure, all other boundaries are defined as slip walls.

In addition to the HRIC scheme, an explicit interface sharpening algorithm described in Manzke [84] was employed to diminish the interface smearing in later time steps. Results for the ($\hat{v}_i$, p^F) - and the (v^F, p^F) - formulation are compared against the numerical results from Del Jesus et al. [20] in Fig. 2.24 and snapshots of present 3D results are provided in Fig. 2.23 together with results published by Del Jesus et al. [20] and Larese et al. [70]. Characteristic features such as a sink behind the corner of the porous material at $t = 0.4$ s and the backwash reflected behind the dam at $t = 1.33$ s are present in all three results in Fig. 2.23. Nevertheless, the shape of the advancing water front at $t = 0.4$ s and the free surface shape at $t = 1.33$ s differ due to differences in discretization methods (FV-VoF /edge-based level set) and the applied model equations (with turbulence models: Del Jesus et al. [20] and without turbulence models: Larese et al. [70], present method Sec. 2.1). Due to similar discretization methods, the present results generally agree with the results from Del Jesus et al. [20].

Comparing the results of the ($\hat{v}_i$, p^F) - and the (v^F, p^F) - formulation of the governing equations with numerical results of Del Jesus et al. [20] in Fig. 2.24 at two lateral planes at $x_2 = 0.1$ m and $x_2 = 0.5$ m leads to the observation that both formulations deliver very close results. The difference in the formulation of the diffusion term in Eqn. (2.32) and Eqn. (2.48) seems to

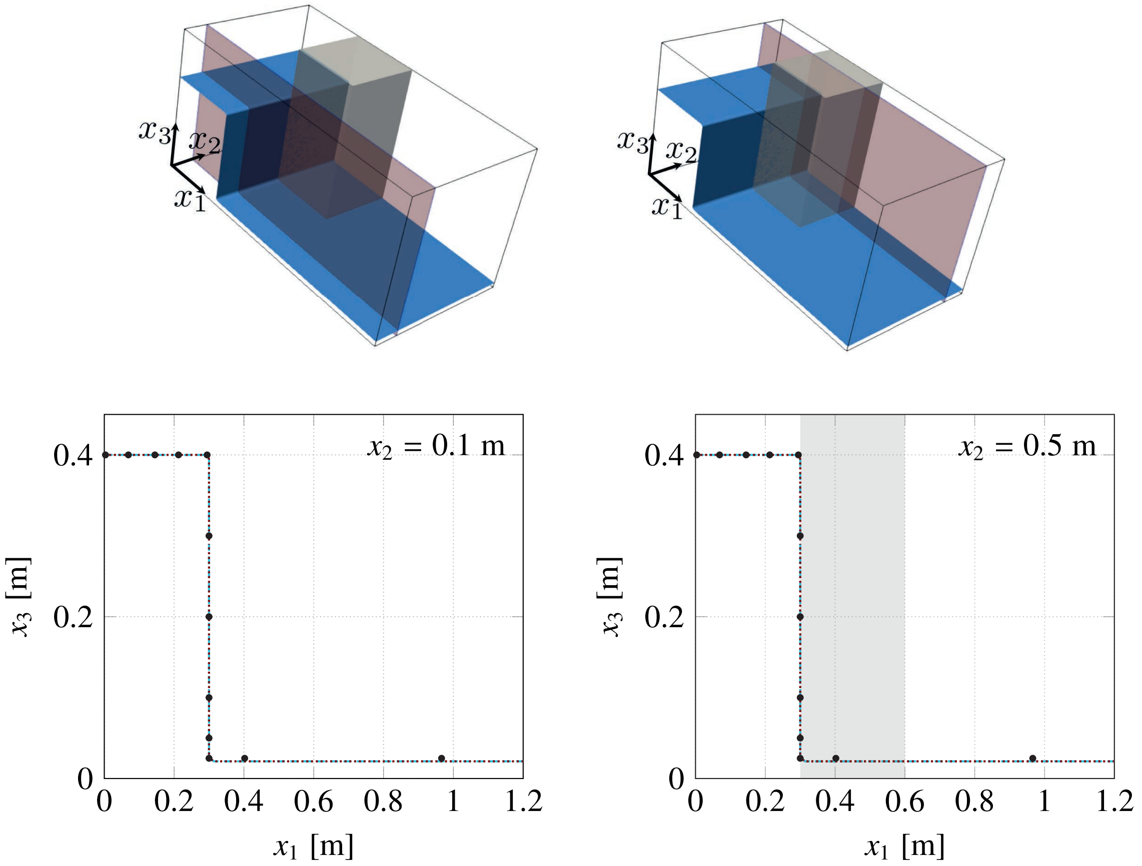

Figure 2.22: 3D porous dam break (mean $Re_P = 1761$, max. $Re_P = 15099$): Initial state of 3D example with a domain size 1.2 m × 0.6 m × 0.6 m. Porous dam expanding from $x_1 = 0.3$ cm to $x_1 = 0.6$ cm and $x_2 = 0.3$ cm to $x_2 = 0.6$ cm. Top: three-dimensional views of the initial state. Bottom: initial free surfaces in planes at $x_2 = 10$ cm and $x_2 = 50$ cm.

cause only minor deviations at the boundaries of the porous dam. Here a linear interpolation of the porosity at the faces is applied. In previous results with step-wise interpolation of the face values of the porosity, larger differences in formulations have been observed. Therefore the treatment of the porosity at the faces is of utmost importance to the results.

Inside the porous material, the free surfaces of both formulations agree well with the results from Del Jesus et al. [20]. In contrast, more significant deviations are experienced outside the porous material. Due to the dissimilar treatment of the continuity equation, different mass transport through the porous boundaries is caused, leading to an upstream shift in the free surface elevation of the present predictions at $t = 0.5$ s in the plane which does not cut through the porous dam. It indicates an increased damming experienced in the present predictions, which also explains why more water is found at $t = 0.5$ s in the results of [20] in the $x_2 = 0.5$ m plane of the dam. The same effect of different mass exchanges over the rigid porous boundary is thought to be responsible for the substantial differences of the observed free surface elevation at $t = 1.38$ s next to the dam. Mind that results for the simplified $\hat{v}_i$- based formulation are not shown due to their closeness with the complete $\hat{v}_i$- based formulation.

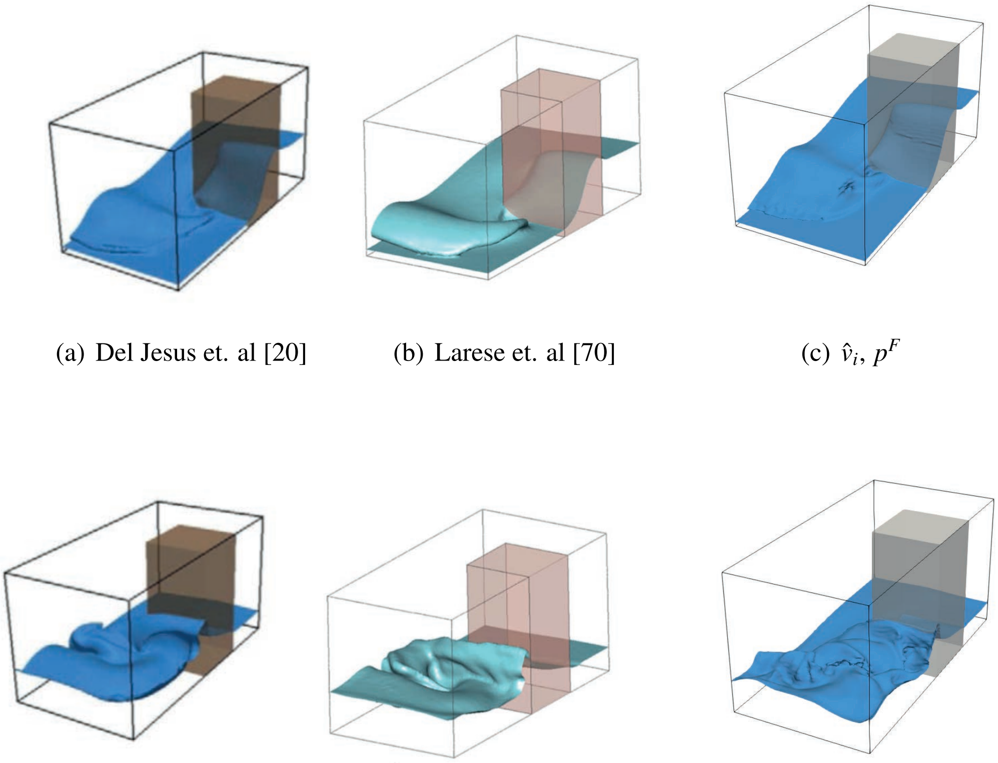

(a) Del Jesus et. al [20] (b) Larese et. al [70] (c) $\hat{v}_i$, p^F

(d) Del Jesus et. al [20] (e) Larese et. al [70] (f) $\hat{v}_i$, p^F

Figure 2.23: 3D porous dam break (mean $Re_P = 1761$, max. $Re_P = 15099$): Comparison of predicted free surfaces at $t = 0.40$ s (top) and $t = 1.33$ s (bottom) for the present and literature approaches.

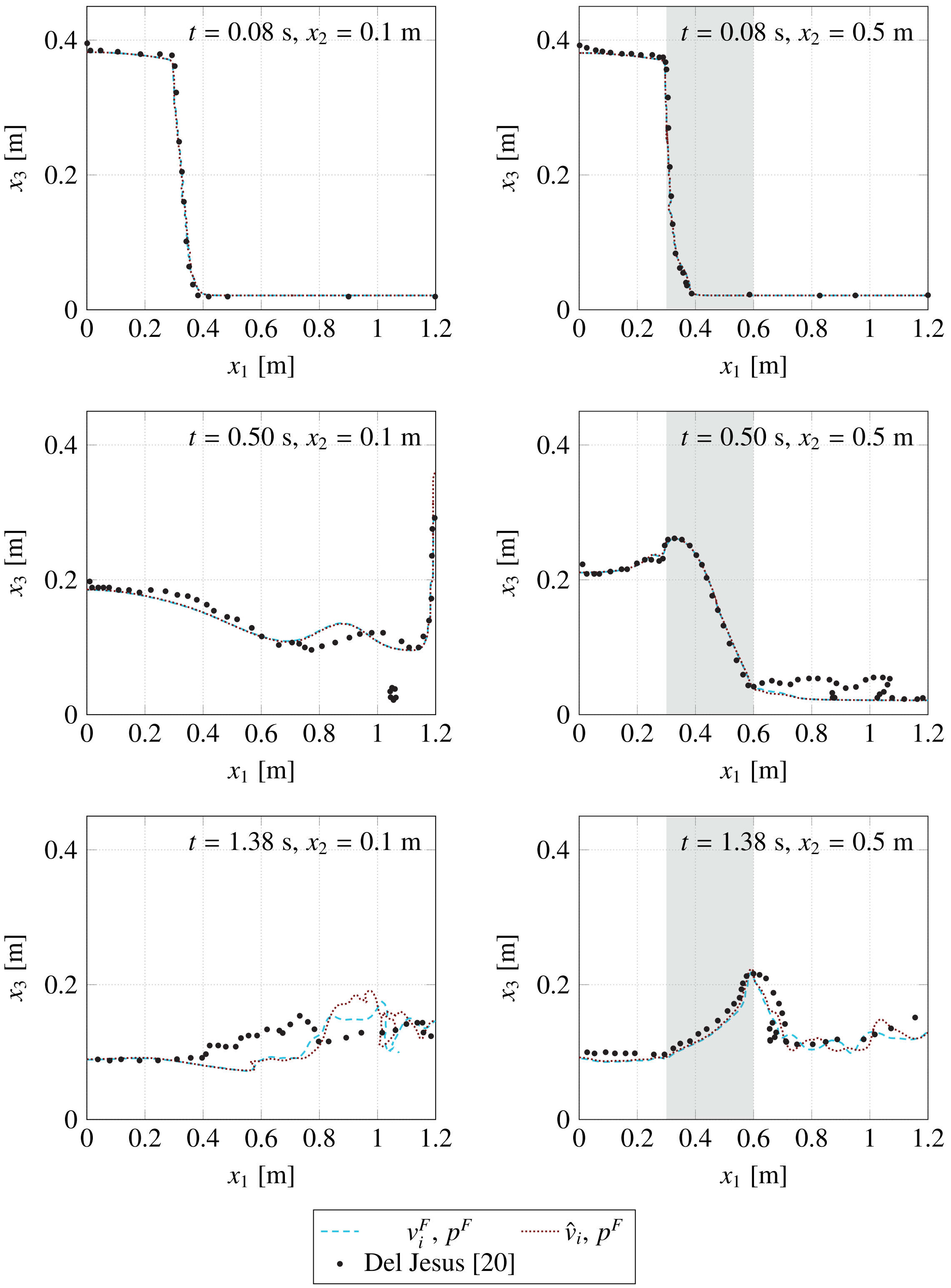

Figure 2.24: 3D porous dam break (mean Re_P = 1761, max. Re_P = 15099): Comparison of predicted free surface elevations (h = 40 cm, $\Delta x_3 = L/240$, HRIC + EIS) for different formulations with literature results.

2.4 Deviation Error Study

This section aims to obtain a correlation of the expected simplification error inherent to the reduced momentum equations (cf. Sec. 2.2.3) with the porosity n and the mean grain diameter D_{50}. This correlation should support/justify the application of the simplified approach during the subsequent coupled rigid-porous model applications. The study involves 36 different sets of material properties. The simulations in the study are conducted with the $(\hat{v}_i,\, p^F)$ - formulation, and the simplified $(\hat{v}_i,\, p^F)$ - formulation, and deviations are used to judge the error of the reduced formulation. The investigated configuration refers to the previously studied dam break flow through a rigid porous material, cf. Sec. 2.3.2 and Fig. 2.25.

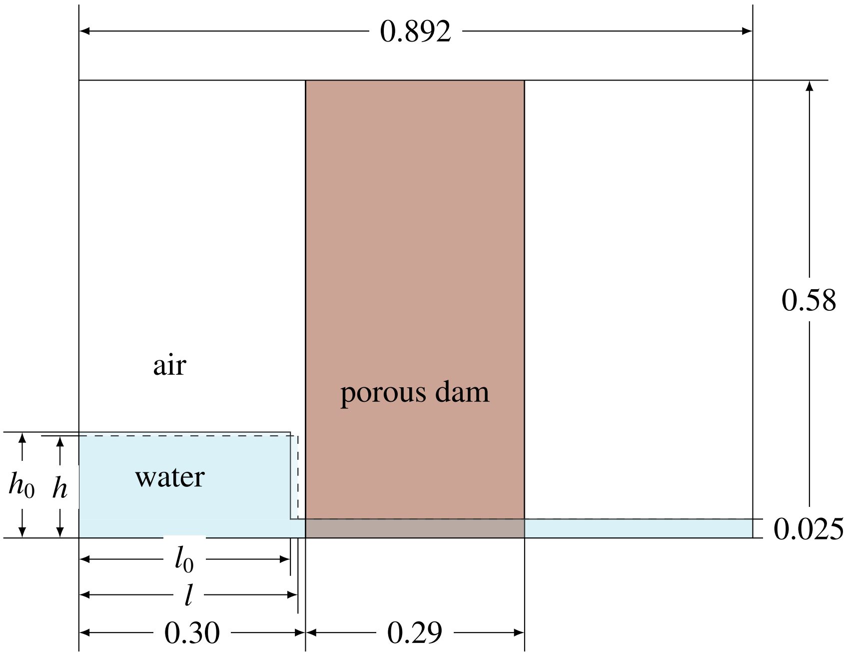

Figure 2.25: Error study for a 2D porous dam break: Initial geometry (all measurements in meters).

The porosity varies between $n = 0.1$ and $n = 0.9$, and the mean diameter of the grain is in the range from $D_{50} = 10^{-3}$ m to $D_{50} = 10^{0}$ m. The properties and the corresponding resistance factors for all 36 simulations are listed in Tab. B.1 of the Appendix B. To calculate the resistance force factors $\tilde{A}$ and $\tilde{B}$, the Engelund equation is used in combination with assumed factors $\alpha = 1000$ and $\beta = 1$ (cf. Tab. 2.1) where the turbulence parameter $\tilde{C}$ is set to zero. All simulations run for $t = 4.0$ s.

At the end of this section, the errors are plotted against the maximum Reynolds number. Universal estimates of the error are possible from this plot under the restriction that the Reynolds number can be determined, which is only possible when the mean velocity is known. Therefore, either experimental or simulation results have to be available. This error study aims to estimate the simplification error based solely on the material parameters to choose appropriate simulation techniques beforehand.

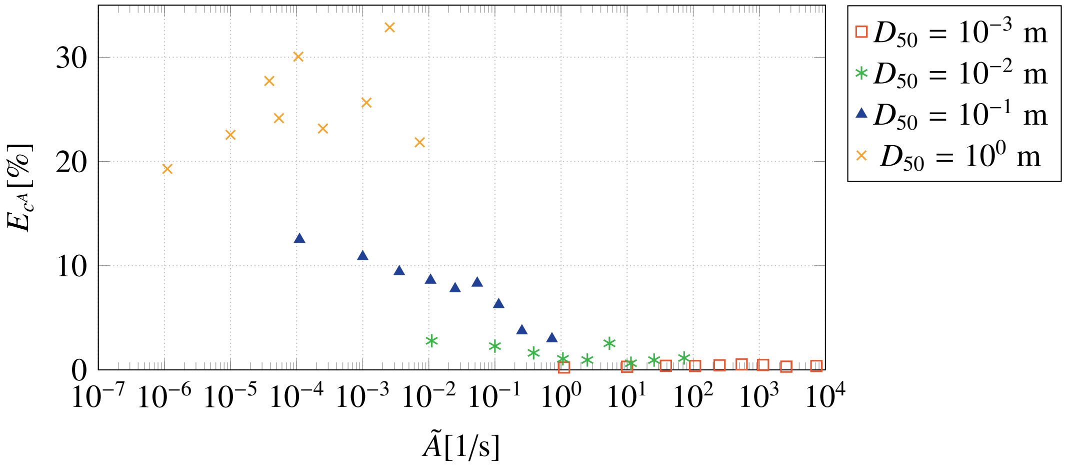

Figure 2.26: Error study for a 2D porous dam break: Evolution of the maximum error E_{c_A} over the resistance force factor $\tilde{A}$.

To obtain an error quantification for the simplified method, the difference between the air concentration fields of the simplified c_{simpl} and the correct method c_{corr} are averaged over the control volumes

$$E_{c_A} = \frac{\sum_{CV} \mid c_{corr} - c_{simpl} \mid \Delta V_P}{\sum_{CV} \Delta V_P} \ . \tag{2.61}$$

This is executed for a series of time steps ($t = 0.4$s, $t = 0.8$s, ..., $t = 4.0$s) and subsequently the maximum value of E_{c_A} from all time steps in the series is taken as result and depicted in Tab. B.2 in the Appendix B. In order to classify the deviation error E_{c_A}, a length-based conversion, explained in more detail in Appendix B.1, from the error measurement to an error in percent is accomplished. First, the maximum error in percent E_{c_A} is plotted over the resistance force factors $\tilde{A}$ and $\tilde{B}$ in Figs. 2.26 and 2.27, respectively. Separate curves are displayed for different mean grain diameters D_{50} since the magnitude of the error significantly depends on the mean diameters. For mean diameters of $D_{50} = 10^{-3}$ m (e.g., sand), the error always remains under 1%. For mean diameters of $D_{50} = 10^{-2}$ m (e.g., gravel) the error is under 4%, for diameters in the range of $D_{50} = 10^{-1}$ m (e.g., coarse gravel, crushed stones) the error is below 15% and for $D_{50} = 10^{0}$ m (e.g., boulders, crushed stones) the error is under 40%. These results can also be seen in Fig. 2.29. Restricting to Englund's law, it is seen that for $\tilde{A} < 0.2$ 1/s the error is smaller than 5% and for $\tilde{A} < 100.0$ 1/s the error is smaller than 1%. The dependence on the resistance factor $\tilde{B}$ is not considered generalizable because the resistance factor $\tilde{A}$ dominates the resistance force for the chosen constants α and β.

Due to the dependence of the error on the mean diameter D_{50} and the porosity n, a regression

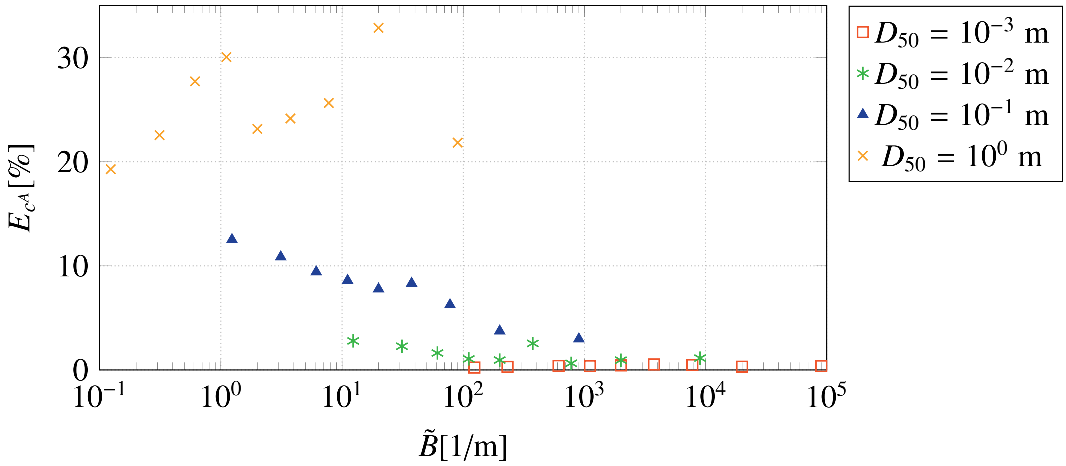

Figure 2.27: Error study for a 2D porous dam break: Evolution of the maximum error E_{c_A} over the resistance force factor $\tilde{B}$.

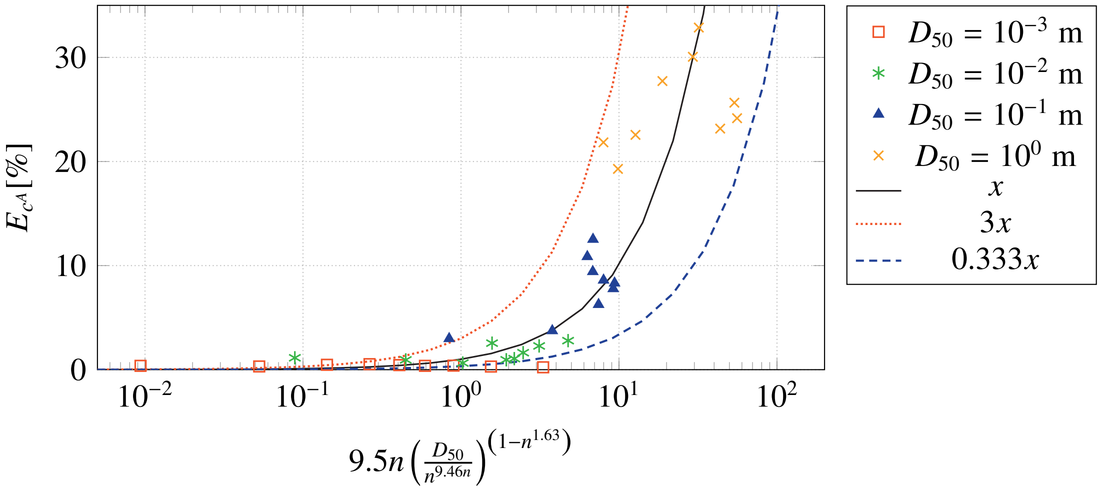

Figure 2.28: Error study for a 2D porous dam break: Comparison of predicted error using the correlation (B.2) (lines) and experienced errors (symbols).

formula to estimate the error magnitude based on these two parameters has been developed. The derivation of this approximation is described in Appendix B.2. The true error is plotted over the estimated error in Fig. 2.28. It can be seen that many data points lie close to the estimated error (cf. curve $y = x$). Most of the data points are located inside a corridor between three times the correlation Eqn. (B.2) and a third of Eqn. (B.2), i.e.,

$$3.17n\left(\frac{D_{50}}{n^{9.46n}}\right)^{(1-n^{1.63})} < E_{c_A}^{est.} < 28.50n\left(\frac{D_{50}}{n^{9.46n}}\right)^{(1-n^{1.63})} \quad . \tag{2.62}$$

Since the approach is conservative, as explained in Appendix B.1, it is well suited to estimate the expected error magnitude of the simplified formulation with the aid of the porosity n and the mean grain diameter D_{50}.

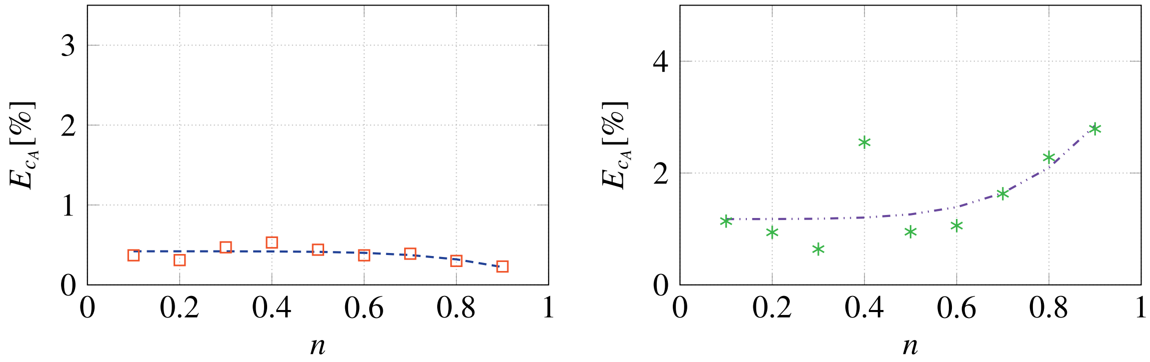

(a) $D_{50} = 10^{-3}$ m (b) $D_{50} = 10^{-2}$ m

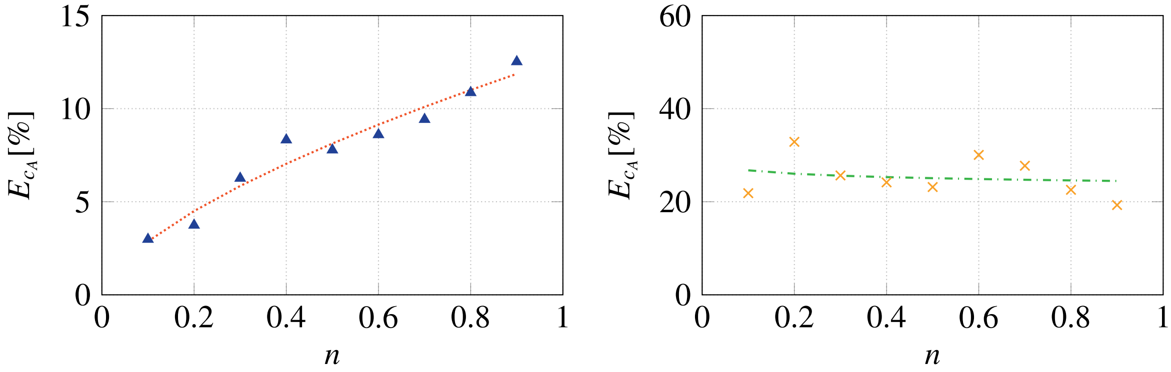

(c) $D_{50} = 10^{-1}$ m (d) $D_{50} = 10^{0}$ m

Figure 2.29: Error study for a 2D porous dam break: Error in percentage over porosity for different mean diameters ($D = 10^{-3}$ m: □, $D_{50} = 10^{-2}$ m: ✳, $D_{50} = 10^{-1}$ m: ▲, $D_{50} = 10^{0}$ m: ×). Individual regressions for each mean diameter are displayed by the corresponding lines $-0.36n^{5.72} + 0.42$: ----, $2.86n^{5.08} + 1.18$: -··-, $12.72n^{0.64} - 0.02$: ·······, $42.08n^{-0.02} - 17.72$: -·-·.

In order to have a more accurate estimation tool, individual fits of the error over the porosity for each diameter are displayed in Fig. 2.29. Displayed curves are obtained with the nonlinear least-squares (NLLS) Marquardt-Levenberg algorithm. A further estimation formula is obtained by plotting the error over the porous Reynolds number $Re_P = \|\hat{v}\|_2 \, D_{50}/\nu$ in Fig. 2.30. Using the same NLLS Marquardt-Levenberg algorithm as above for acquiring a fit and excluding all data points with the large mean grain diameter $D_{50} = 10^0$ m leads to

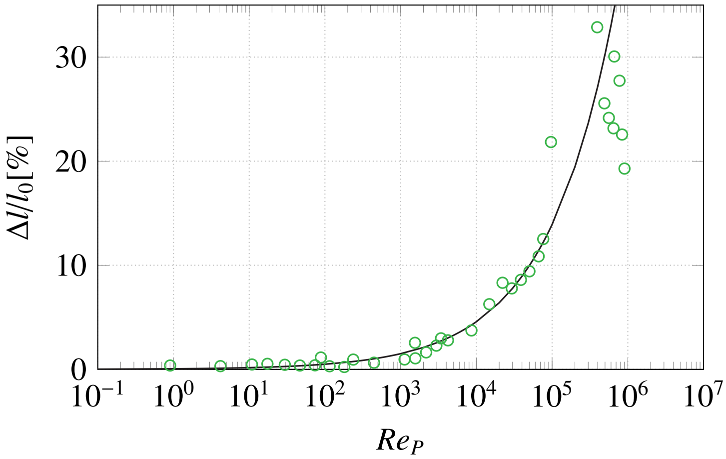

Figure 2.30: Error study for a 2D porous dam break: Maximum length based error in percent plotted over maximum Reynolds number.

$$E_{CA}^{est.,Re_P} = (0.00233211 \; Re_P)^{0.482901} \; . \tag{2.63}$$

Overall, the presented error study provides an excellent overview of the scaling for the expected error with the mean diameter, porosity, and porous Reynolds number. Depending on the desired accuracy, the mean diameter of the grains for which a simplified formulation is justifiable can be obtained. Taking an error limit of 5% as an example, all materials with diameters under $D_{50} = 10^{-2}$ m can be simulated with simplified momentum equations. Looking at Fig. 2.30, the limit of an acceptable porous Reynolds number can be set to 10^4. These include many granular materials since all sand and gravel are in this range, cf. Van Gent [39]. Materials with a mean grain diameter of $D_{50} = 10^{-2}$ m (categorized as coarse gravel and crushed stones in [39]) do exceed the error limit of 5% for the usual porosity range. For mean grain diameters in the magnitude of $D_{50} = 10^0$m, a simplified simulation method is not applicable.

This work aims to simulate the liquefiable cargo on bulk carriers in waves. The properties of nickel and iron ore will be reviewed in chapter 6, where the largest grain size diameter is found to be $2 \cdot 10^{-3}$ m. In [41], a limit value for the classification of Bauxite is given as $D_{30} = 10^{-2}$m. According to IMO rules, for finer Bauxite cargo ($D_{30} < 10^{-3}$m), liquefaction can occur, and for larger grain sizes, the cargo is safe to be transported. In order to simulate liquefiable cargo, the grain sizes of the materials are in a range in which the error of the simplification of the momentum equations is negligibly small.

Chapter 3

Rigid-Perfectly Plastic Granular Material

A perfectly-plastic approach based on a non-Newtonian flow is presented and validated to simulate cargo shifting. The advantage of the method lies in the ability to simulate large displacements and arbitrary cargo geometries. The elastic behavior is not considered. To this end, a variable viscosity is introduced into the momentum equations of an incompressible two-phase flow, where a soil mixture VoF equation is used to distinguish the granular material from the air flow. To obtain a strain measure, an Eulerian displacement equation is introduced in the equation system, and an Euler-Almansi strain is used as a strain measure. Difficulties occurring at the boundaries of the two-phase model are discussed, and a non-linear interpolation function for the phases is suggested. Finally, several validation and verification cases for different material properties are considered to obtain a validated approach. Parts of the chapter are published in Düsterhöft-Wriggers et al. [29].

3.1 Mathematical Model

In traditional soil mechanics, perfect plasticity describes the yielding of granular materials. Coulomb used the concept of perfect plasticity in 1773 to calculate the strength of geotechnical structures, cf. Yu et al. [138]. In a rigid-perfectly plastic material, the yield stress is constant and has a stress-strain relationship as depicted in Fig. 3.1. A general finite strain plasticity model consists of the following ingredients

- elastic-plastic decomposition of deformation gradient,
- yield criterion (yield surface),
- flow rule/ plastic potential,

- hardening rule,
- stress-strain relations,
- loading/unloading criterion.

Further details of the theory of finite strain elasto-plasticity is given in Neto et al. [92] and Simo et al. [108]. In order to reduce the complexity of the overall model, a rigid-plastic approach is implemented, verified and validated. For this approach, the above mentioned building blocks reduce to the following set of relations

- yield criterion (yield surface),
- flow rule/ plastic potential,
- stress-strain relations.

Following the approach of Larese [69], Leppert [75], Ulrich [120] and Ulrich et al. [121], a variable viscosity will be used to emulate the rigid-perfectly plastic behavior. All simulations in this chapter are two-phase simulations of granular material and air. The transition between the rigid-perfectly plastic material and the air phase is identified by the mixture fraction value $c_S = 0.5$ obtained from the VoF method. The velocity field that covers the soil and the air phase is denoted v_i in the present chapter and will be labeled v_i^S in the coupled model in chapter 4.

Figure 3.1: Stress-strain relationship of rigid-perfectly plastic material.

3.1.1 Stress-Strain Relations

To model stress-strain relations with a variable viscosity, the deviatoric part of the fluid stress tensor is used. The related general momentum equations in differential Eulerian form

$$\frac{\partial \rho v_i}{\partial t} + \frac{\partial \rho v_i v_j}{\partial x_j} = \rho g_i + \frac{\partial \sigma_{ij}}{\partial x_j} \tag{3.1}$$

can be derived from Eqn. (2.10). The Cauchy stress tensor σ_{ij} can be divided into a hydrostatic ($-p\delta_{ij}$) and deviatoric (τ_{ij}) part

$$\sigma_{ij} = -p\delta_{ij} + \tau_{ij} \, , \tag{3.2}$$

For incompressible (Newtonian) media, the deviatoric stress tensor τ_{ij} can be expressed as

$$\tau_{ij} = \mu \left(\frac{\partial v_i}{\partial x_j} + \frac{\partial v_j}{\partial x_i} \right) = \mu 2\dot{\epsilon}_{ij} \tag{3.3}$$

with $\dot{\epsilon}_{ij}$ being the strain rate tensor. Applying a VoF approach where the viscosity of the two-phase flow consists of the granular phase viscosity μ^S and the fluid viscosity μ^A ($\mu = c_S \mu^S + (1 - c_S)\, \mu^A$) leads to the deviatoric stress tensor for the granular phase as

$$\tau^S_{ij} = \mu^S \left(\frac{\partial v_i}{\partial x_j} + \frac{\partial v_j}{\partial x_i} \right) = \mu^S 2\dot{\epsilon}_{ij} \, . \tag{3.4}$$

Since a rigid-perfectly plastic material behavior is assumed, $\dot{\epsilon}_{ij}$ corresponds to the plastic strain rate tensor in the granular phase.

3.1.2 Yield Criterion

The yield function is important since it distinguishes between non-plastic (elastic/rigid) and plastic behavior domains. In conjunction with the current rigid-plastic model, the yield function differentiates between the rigid and the plastic domain. The yield function is generally given by

$$\Phi(\tau_{ij}, \tau_y) = \mid \tau_{ij} \mid - \tau_y \, , \tag{3.5}$$

where τ_{ij} is the deviatoric part of the Cauchy stress tensor which is equal to the deviatoric Kirchhoff tensor for incompressible media. The variable τ_y refers to the Kirchhoff yield stress, and the modulus signs denote the yield criterion. The yield stress τ_y can also include internal variables for hardening models. All points where the yield function falls below zero form the elastic or rigid domain. When the yield function is zero, the soil behaves plastically. Therefore, the stress cannot be higher than the yield stress. The surface in stress space, obtained for all stresses if the yield function vanishes, is called the yield surface.

Several yield criteria are applied in soil mechanics, including, among others, the Mohr-Coulomb [15], Drucker-Prager [25], Rankine [100], Tresca [116] and Von Mises [127] criterion. The Mohr-Coulomb criterion follows from

$$\Phi = |\tau| - p \; tan\phi - C \, . \tag{3.6}$$

It is frequently applied for modeling granular materials, where $|\tau|$ is a one-dimensional deviatoric stress. It states that if the deviatoric stresses from external loads exceed the shear strength, given by the cohesion C and the pressure times the internal friction coefficient $tan\ \phi$, sliding starts to occur. The angle of repose ϕ is a material property determining the internal strength against frictional sliding. The difficulty in using this criterion is to obtain a general 3D-stress state expression of $|\tau|$. To avoid calculating principal stresses, an invariant-based formulation is desirable. Without further simplifications, this leads to complex formulations as can be seen, e.g., in Abbo et al. [1] and Schajer [106].

To avoid the difficulties, the Drucker-Prager yield stress, usually formulated via the invariants, is used to derive the variable viscosity in this work. The approach is an idealization of the Mohr-Coulomb criterion, and the shape of its yield surface is a cone instead of a pyramid. Therefore the derivative of the plastic potential is unique at each point on the yield surface. Drucker-Prager introduced the Drucker-Prager yield function in Drucker-Prager [25] to be

$$\Phi = \sqrt{J_2} + \alpha_\phi I_1 - k_c \ . \tag{3.7}$$

Here J_2 is the second invariant of the deviatoric stress

$$J_2 = \frac{1}{2}\tau_{ij}\tau_{ij} \tag{3.8}$$

and I_1 is the first invariant of the stress tensor, which equals the trace of the stress tensor

$$I_1 = \sigma_{11} + \sigma_{22} + \sigma_{33} = -3p \ . \tag{3.9}$$

The material constants α_ϕ and k_c are defined by

$$\alpha_\phi = \frac{tan\phi}{\sqrt{9 + 12tan^2\phi}} \tag{3.10}$$

and

$$k_c = \frac{3C}{\sqrt{9 + 12tan^2\phi}} \ . \tag{3.11}$$

Using the deviatoric stress tensor of a viscous fluid from Eqn. (3.4) for the calculation of the second invariant in the granular phase, the second invariant can be expressed by

$$J_2 = 2\left(\mu^S\right)^2 \dot{\epsilon}_{ij}\dot{\epsilon}_{ij} \ . \tag{3.12}$$

In the plastic domain, the yield function is zero, giving a condition at which the material starts to flow. For perfectly plastic materials, the yield function is always zero, and therefore, by rearrangement of the yield function (3.7), the variable viscosity

$$\mu^S = \frac{3\alpha_\phi p + k_c}{\sqrt{2\dot{\epsilon}_{ij}\dot{\epsilon}_{ij}}} \tag{3.13}$$

is obtained.

Yield Criteria in Reference Literature

A theoretical comparison of the applied yield criteria is necessary to compare present results to the works of Larese [69] and Ulrich [120]. In Larese [69], the Mohr-Coulomb criterion (3.6) is used by assuming that the 1D yield stress is also valid for the 3D stress state leading to a yield criterion of

$$\Phi = \sqrt{J_2} - p\ tan\ \phi - C\ . \tag{3.14}$$

In Ulrich [120], the Mohr-Coulomb criterion (3.6) is used by assuming that the Lode angle is zero meaning that the stress state is a pure shear stress state or that the direction of the principal stresses coincides with the directions of the present 3D stress state and the yield criterion becomes

$$\Phi = \sqrt{J_2} - p\ sin\ \phi - C\ cos\ \phi\ . \tag{3.15}$$

Fig. 3.2 compares the yield criteria for terms not involving the second invariant of the deviatoric stress for the Drucker-Prager approach and the yield stresses of Larese [69] and Ulrich [120] mentioned above. The variables ϕ and C are in the bounds of $0° < \phi < 52°$ and $0 < C < 2$ Pa, respectively, and the pressure is assumed to be $p = 1$ Pa. The values for all yield criteria coincide inside the boundaries described above when the material is cohesionless ($C = 0$ Pa).

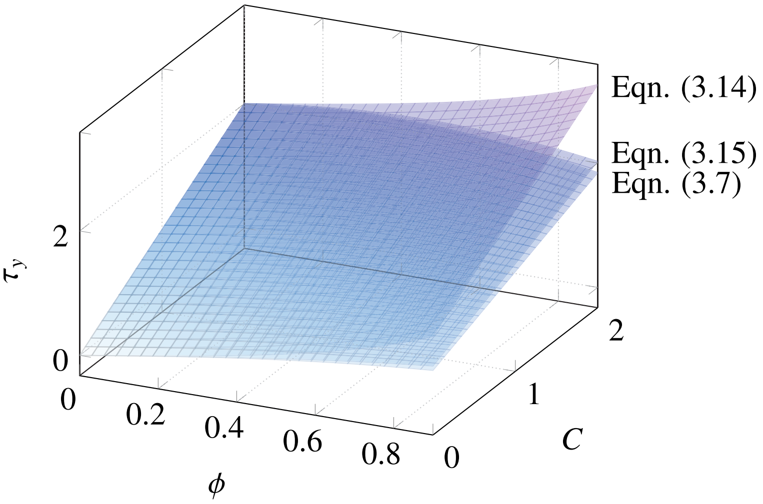

Figure 3.2: Theoretical comparison of terms in yield criteria (3.7), (3.15) and (3.14) with ϕ being in radiants.

3.1.3 Flow Rule

A classical flow rule is not applied since the deformation of the granular material is not calculated from the plastic strain rate tensor directly. However, the material flows according to momentum equations (3.1) driven by the variable viscosity (3.13). The model is non-associative because the plastic potential is not equal to the yield function, and therefore the resulting plastic strain is not always normal to the yield surface. Assuming the plastic potential of a non-associative, incompressible Drucker-Prager material (cf. Bui et al. [9] and Sumelka [111])

$$\Psi(\sigma_{ij}) = \sqrt{J_2}\ , \tag{3.16}$$

the derivative of the plastic potential by the stress tensor reads

$$\frac{\partial \Psi(\sigma_{ij})}{\partial \sigma_{ij}} = \frac{1}{2\sqrt{J_2}} \tau_{ij}\ . \tag{3.17}$$

Evaluating the flow rule expression for small deformations

$$\dot{\epsilon}_{ij} = \dot{\lambda} \frac{\partial \Psi}{\partial \sigma_{ij}} \tag{3.18}$$

with the aid of the definition of J_2 (3.8) and the fluid stress tensor τ_{ij} (3.4), the multiplier $\dot{\lambda}$ is obtained from

$$\dot{\lambda} = \sqrt{2\dot{\epsilon}_{ij}\dot{\epsilon}_{ij}}\ . \tag{3.19}$$

3.1.4 Regularisation of the Variable Viscosity

The relation (3.13) for the variable viscosity μ^S inheres singularities for vanishing strain rates, and must be regularised to obtain stable simulations. Rewriting the equation in a general form

$$\mu^S = \frac{\tau_y}{\sqrt{2\dot{\epsilon}_{ij}\dot{\epsilon}_{ij}}} = \frac{\tau_y}{\dot{\lambda}} \tag{3.20}$$

where the multiplier $\dot{\lambda}$ is a measure of the strain rate which is used for visualizing purposes. Looking at Eqn. (3.13), it can be seen that infinite viscosities are obtained for $\dot{\lambda}$ approaching zero. Furthermore, in Eqn. (3.13), the viscosity reaches zero for infinite $\dot{\lambda}$. Therefore for numerical stability, the variable viscosity must approach a minimum value μ^S_{min} and a maximum value μ^S_{max}. To still obtain perfectly-plastic behavior, the minimum viscosity has to be as small as possible. To this end, a value of $\mu^S_{min} = 10^{-3}$ Pa s gives good results. The higher the maximum viscosity μ^S_{max} gets, the steeper the stress-strain rate curve for small strain rates and, therefore, the closer to rigid-perfectly plastic behavior. It can also be noted that a parametrisation of μ^S_{max} can be used to mimic elasto-plastic behaviour. Two regularisation approaches are theoretically compared in Figs. 3.3 and 3.4. All green lines represent the approach given in Ulrich [120] and Ulrich et al. [121]

$$\mu^S = \max\left(\min\left(\frac{\tau_y}{\dot{\lambda}}, \mu^S_{max}\right), \mu^S_{min}\right)\ , \tag{3.21}$$

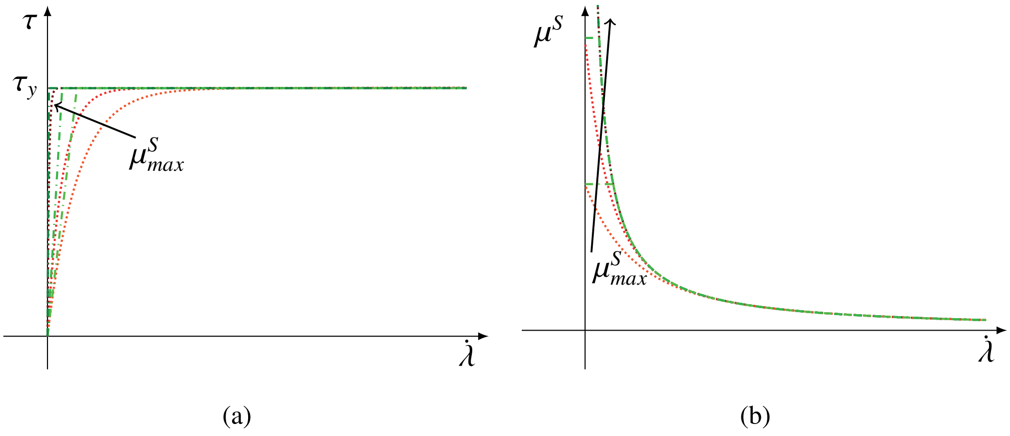

Figure 3.3: Strain rate dependency of the regularized deviatoric stress (a) and the regularized viscosity (b) for two different μ^S_{max} and two regularisation approaches indicated by the green (3.21) and the red (3.22) lines ($\mu^S_{min} = 7.5 \cdot 10^{-5}$ Pa s).

where the variable viscosity is clipped beyond μ^S_{min} and μ^S_{max}. Another way to look at the solution of a rigid-perfectly plastic material is to use a regularised Bingham model as described in Larese [69] and Papanastasiou [96]. The variable viscosity μ^S is then given as

$$\mu^S = \mu^S_{min} + \frac{\tau_y}{\dot{\lambda}}\left(1 - e^{(-m_c\dot{\lambda})}\right) \tag{3.22}$$

with a constant minimum viscosity μ^S_{min} and a constant m_c which determines the maximum viscosity. When the plastic multiplier $\dot{\lambda}$ reaches zero, the maximum viscosity is obtained with a value of $\mu^S_{max} = m_c\tau_y$. The constant m_c has to go to infinity to obtain perfectly plastic behavior. In Fig. 3.3 the stress strain-rate relation and the variable viscosities obtained by the two alternatives (3.21) and (3.22) are compared for a fairly small minimum viscosity μ_{min}, where the green lines denote Eqn. (3.21) and the red lines denote Eqn. (3.22). The higher the maximum viscosity, the steeper the stress-strain rate relation. Analogous graphs are shown in Fig. 3.4 for different μ^S_{min} levels at constant μ^S_{max}. The figure reveals, that the stress-strain rate curves do not fit the ideally rigid plastic behavior for larger values of μ^S_{min}. The advantage of the regularized Bingham approach (3.22) is the smoothness of the stress-strain rate curve and the related variable viscosity. Therefore this approach is chosen for all simulations in this work.

3.1.5 Euler-Almansi Strain Based on Eulerian Formulation of Deformation Gradient Tensor

To identify the deviatoric strain inside the rigid perfectly-plastic material, an Eulerian displacement equation is added to the equation system, and the Eulerian deformation gradient F_{ij} is

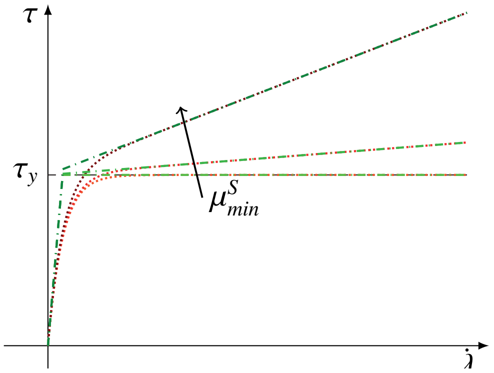

Figure 3.4: Strain rate dependency of the regularized deviatoric stress at constant μ^S_{max} for three different μ^S_{min} and two regularisation approaches indicated by the green (3.21) and the red (3.22) lines.

used to obtain the Euler-Almansi strain tensor e_{ij}

$$e_{ij} = \frac{1}{2}\left(\delta_{ij} - G_{ik}G_{jk}\right) , \tag{3.23}$$

were G_{ik} is the inverse of the Eulerian deformation gradient F_{ij} and is defined as given in the next section.

Lagrangian/Eulerian Formulation of Deformation Gradient Tensor

A point of the undeformed body Ω^{t_0} (reference configuration) can be described by either its Lagrangian (material) coordinate $\hat{X}_i$ or its Eulerian (spatial) coordinate $\hat{x}_i$. The same material point at time $t = t_1$ possesses a different material coordinate $X_i^{t_1}$ because the body Ω^{t_1} (current configuration) is deformed. If the displacement u_i is introduced as the difference of the position vectors of the current and the reference configuration, the following relationship is true (cf. Figs.

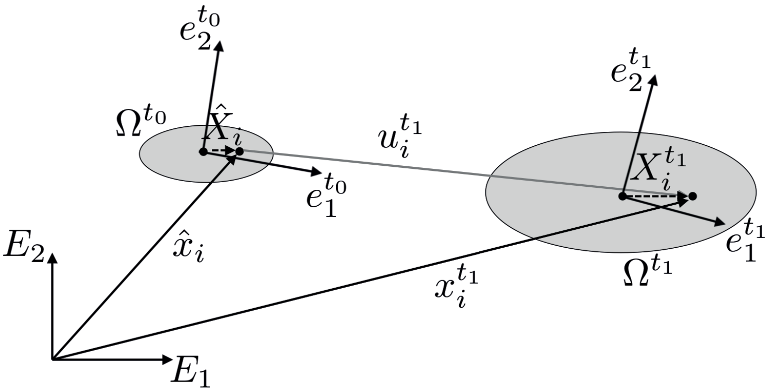

Figure 3.5: Material ($\hat{X}_i$) and spatial ($\hat{x}_i$) coordinates for the reference (Ω^{t_0}) and the current configuration (Ω^{t_1}) employed to derive the relation between the Lagrangian ($\hat{F}_{ij}$) and the Eulerian (F_{ij}) deformation gradient tensor.

3.5 and 3.6)

$$x_i = \hat{x}_i + u_i \ . \tag{3.24}$$

If the Eulerian coordinate system (reference coordinate system E_i) is equal to the initial Lagrangian coordinate system ($e_i^{t_0}$) then $\hat{X}_i$ is equal to $\hat{x}_i$ and the differentiation $\partial x_i / \partial \hat{X}_i$ can be expressed by $\partial x_i / \partial \hat{x}_i$. With the help of Eqn. (3.24), the differentiation gets

$$\frac{\partial x_i}{\partial \hat{x}_j} = \delta_{ij} + \frac{\partial u_i}{\partial \hat{x}_j} = \hat{F}_{ij} \tag{3.25}$$

with $\hat{F}_{ij}$ being the Lagrangian deformation gradient tensor. The deformation of a material line element $d\hat{x}_i$ from the reference configuration to the current configuration material line element dx_i can be calculated by a transformation with the Lagrangian deformation gradient tensor

$$dx_i = \frac{\partial x_i}{\partial \hat{x}_i} d\hat{x}_i = \hat{F}_{ij} d\hat{x}_i \ . \tag{3.26}$$

Rearranging Eqn. (3.24) to

$$\hat{x}_i = x_i - u_i \ , \tag{3.27}$$

the partial derivation of the material coordinates by the spatial coordinates gets

$$\frac{\partial \hat{x}_i}{\partial x_j} = \delta_{ij} - \frac{\partial u_i}{\partial x_j} = F_{ij} \ , \tag{3.28}$$

where F_{ij} is the Eulerian deformation gradient tensor. Equivalently to relationship (3.26), the transformation of the current material line element dx_i to the reference material line element $d\hat{x}_i$ can be calculated with the help of the Eulerian deformation gradient F_{ij}

$$d\hat{x}_i = \frac{\partial \hat{x}_i}{\partial x_i} dx_i = F_{ij} dx_i \ . \tag{3.29}$$

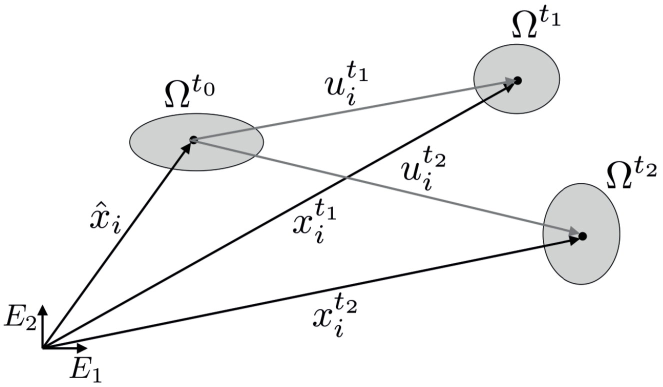

Figure 3.6: Relationship between the reference configuration (Ω^{t_0}) and two different current configurations (Ω^{t_1}, Ω^{t_2}).

If Eqns. (3.26) and (3.29) are compared, it can be seen that the inverse of the Lagrangian gradient deformation tensor is equal to the Eulerian deformation gradient tensor

$$\hat{F}_{ij}^{-1} = F_{ji} \ . \tag{3.30}$$

The inverse of the Eulerian deformation gradient F_{ij} can be expressed as G_{ij} in index notation

$$G_{ij} = \frac{1}{H} \epsilon_{ipq} \epsilon_{jkl} F_{pk} F_{ql} \tag{3.31}$$

where H is the determinant of the Eulerian deformation gradient F_{ij}

$$H = \epsilon_{ijk} F_{1i} F_{2j} F_{3k} \tag{3.32}$$

and ϵ_{ijk} refers to the Levi-Civita symbol.

Displacement Equation and Norm of Euler-Almansi Strain

The Eulerian displacement u_i is obtained by solving the convective transport equation

$$\frac{\partial u_i}{\partial t} + \frac{\partial v_j^S u_i}{\partial x_j} = v_i^S \tag{3.33}$$

where v_i^S is the velocity of the granular material obtained by multiplication with the soil mixture fraction c_S ($c_S = V^G/V$)

$$v_i^S = c_S v_i \ . \tag{3.34}$$

To compare against an accumulated deviatoric plastic strain, for example utilized in Bui et al. [9], the norm of the Euler-Almansi strain is calculated via

$$||e_{ij}|| = \sqrt{\sum_{i=1}^{3} \sum_{j=1}^{3} e_{ij} e_{ij}} \ . \tag{3.35}$$

It shall be noted that the Euler-Almansi strain does not influence the behavior of the material and can be considered a passive quantity.

3.2 Finite Volume Method

The material model for a rigid, perfectly-plastic granular material is solved for incompressible two-phase flows where one is the granular material, and the other is a fluid. Therefore the momentum equations (2.12) and continuity equation (2.5) of an incompressible two-phase flow are solved as explained in chapter 2. In this chapter, the velocity of the field is denoted v_i, and a soil mixture fraction $c_S = V^G/V$ is introduced for a complete volume V and granular volume

V^G. The soil mixture equation can be derived parallel to Eqn. (2.19), where the properties are calculated by

$$\rho = c_S \rho^S + (1 - c_S)\rho^A \qquad \text{with} \qquad \mu = c_S \mu^S + (1 - c_S)\mu^A \,. \tag{3.36}$$

The algorithmic procedure of the FV fluid solver is not changed, cf. Fig. 3.7. Once the material properties are updated, the equation for the variable viscosity (3.36), including the effective viscosity μ^S from Eqn. (3.22), is used to calculate the viscosity depending on the pressure, angle of repose, and soil mixture fraction. Mind that the solution of the displacement equation is not depicted in Fig. 3.7 since it is a passive quantity. Nevertheless, if the Euler-Almansi strain is required, the Eulerian displacement equation is solved after solving the soil mixture fraction equation.

3.2.1 Discrete Equation System

The equation system governing the incompressible two-phase flow with one phase being used to describe the rigid-perfectly plastic material is composed of the continuity (3.37), momentum (3.38), soil concentration (3.39) and displacement equation (3.40), viz.

$$\oint_A v_i dA_i = 0 \,, \tag{3.37}$$

$$\int_V \frac{\partial}{\partial t}(\rho v_i)\, dV + \oint_A \left(\rho v_i v_j\right) dA_j = - \oint_A p dA_i + \int_V \rho g_i dV + \oint_A \mu \left(\frac{\partial v_i}{\partial x_j} + \frac{\partial v_j}{\partial x_i}\right) dA_j \,, \tag{3.38}$$

$$\int_V \frac{\partial c_S}{\partial t} dV + \oint_A c_S v_i dA_i = 0 \,, \tag{3.39}$$

$$\int_V \frac{\partial u_i}{\partial t} dV + \oint_A c_S v_j u_i \, dA_j = \int_V c_S v_i dV \,, \tag{3.40}$$

where the same approximation techniques as described in Sec. 2.2 are applied.

Discretized Momentum Equations

The momentum equation (3.38) is discretized over a control volume ΔV_P. Using the same discretization methods as in Sec. 2.2. i.e., a mid-point integration rule together with a first-order implicit time discretization, a central differencing scheme to approximate the diffusion fluxes and an upwind-biased scheme to approximate the implicit part of the convective flux, the

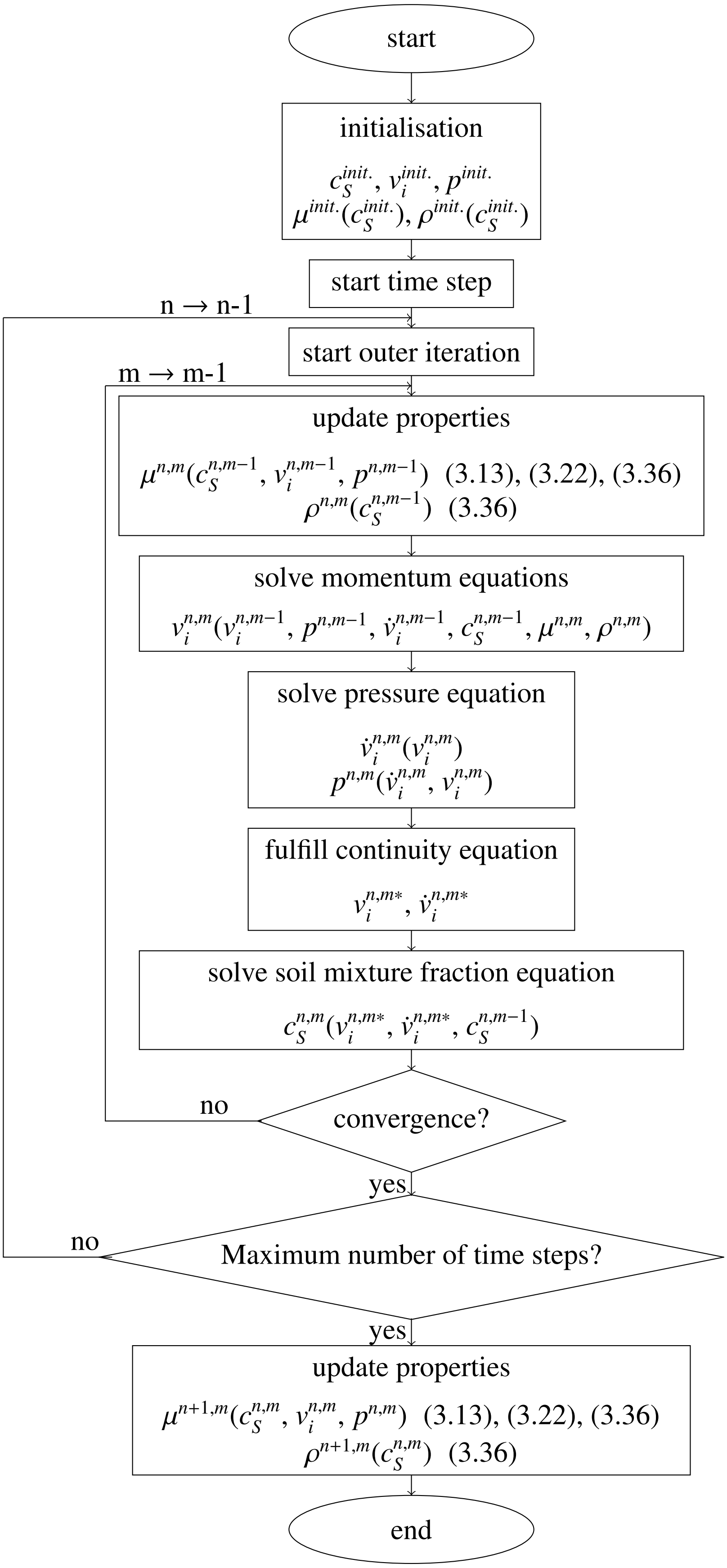

Figure 3.7: Algorithm of the two-phase rigid perfectly-plastic soil model.

discrete form of the momentum equation reads

$$\begin{aligned} v_{i,P}^{n,m}\left[\Delta V_P \frac{\rho_P}{\Delta t} + \sum_{f(\Delta V_P)} A_{NB}^{v_i}\right] - \sum_{f(\Delta V_P)} \underbrace{\left[\left(max\left[-\dot{m}^{n,m-1}, 0\right]\right)_f + \left(\frac{\mu A}{d}\right)_f\right]}_{A_{NB}^{v_i}} v_{i,NB}^{n,m} = \\ - \sum_{f(\Delta V_P)} \left(p_f^{n,m-1} A_i\right) + \rho_P \Delta V_P \left(g_i + \frac{v_i^{n-1}}{\Delta t}\right)_P + S_{v_i} \ . \end{aligned} \tag{3.41}$$

were $\dot{m}_f = (\rho v_i A_i)_f$ refers to the outward facing mass flux and S_{v_i} to a generalized source term including all deferred-corrections.

Discretized Continuity Equation

Only the first stage of the pressure correction $p^{'}$ equation is outlined here since the full pressure correction scheme can be derived as explained in 2.2.1 from Eqns. (3.37) and (3.38)

$$\sum_{f(\Delta V_P)} v_{f,i}^{m} A_{f,i} - \sum_{f(\Delta V_P)} \left(\frac{A_i d_i}{A_P^{v_i}}\right)_f \left(\frac{\partial p^{'}}{\partial x_i}\right)_f A_f = 0 \ . \tag{3.42}$$

A Rhie-Chow [101] interpolation of the velocities is used to compute the fluxes in (3.42) to avoid pressure oscillations for the employed collocated variable arrangement. The computed pressure correction $p^{'}$ is used to update the pressure from p^{m-1} to p^m where v_i^m is the uncorrected velocity obtained from the momentum equations, cf. Fig. 3.7. Moreover, the velocities and the related fluxes are also corrected in line with the descriptions in Sec. 2.2.1

$$\dot{v}_f^{m*} = \dot{v}_f^{m} + A_{NB}^{p^{'}}\left(p_{NB}^{'} - p_P^{'}\right) \ , \tag{3.43}$$

$$v_{i,P}^{m*} = v_{i,P}^{m} + \left(-\frac{\Delta V_P}{A_P^{v_{i,P}}}\right)\left(\frac{\partial p^{'}}{\partial x_i}\right)_P \ . \tag{3.44}$$

Discretized Soil Mixture Fraction Equation

As in Sec. 2.2, a first-order implicit time integration scheme and an upwind-differencing scheme for the implicit part of the convective approximation are applied to the soil mixture fraction equation

$$c_{S,P}^{n,m}\left[\frac{\Delta V_P}{\Delta t} + \sum_{f(\Delta V_P)} A_{NB}^{c_S}\right] - \sum_{f(\Delta V_P)} \underbrace{\left(max\left[-(\dot{m}/\rho)^{n,m-1}, 0\right]\right)_f}_{A_{NB}^{c_S}} c_{S,NB}^{n,m} = \frac{\Delta V_P}{\Delta t} c_{S,P}^{n-1} + S_{c_S} \ , \tag{3.45}$$

where S_{c_S} hosts the deferred correction terms of the actual compressive approximation of the convective fluxes, which mostly refers to the Quadratic Upstream Interpolation for Convective Kinematics (QUICK) scheme, introduced by Leonard [74] in this chapter.

Discretized Displacement Equation

The Eulerian displacement equation (3.40) is approximated. Applying a first-order implicit time integration scheme and an upwind-difference scheme for the implicit part of the approximation of the convective term yields

$$\begin{aligned} u_{i,P}^{n,m}\left[\frac{\Delta V_P}{\Delta t} + \sum_{f(\Delta V_P)} A_{NB}^u\right] - \sum_{f(\Delta V_P)} \underbrace{\left(max\left[-\dot{v}^{S,n,m-1}, 0\right]\right)_f}_{A_{NB}^u} u_{i,NB}^{n,m} = \\ \frac{\Delta V_P}{\Delta t} u_{i,P}^{n-1} + c_{S,P} v_{i,P}^{n,m-1} \Delta V_P + S_u \, , \end{aligned} \tag{3.46}$$

where $\dot{v}_f^S = (c_S v_i A_i)_f$ refers to a volume flux and S_u again includes explicit terms which arise from different deferred correction contributions, e.g., higher-order convection, non-orthogonality, and interpolation corrections.

3.2.2 Non-Linear Interpolation of Material Properties

Significant creeping effects will be present for the granular material, if a linear interpolation is used to reconstruct the properties from the concentration field, as in Eqn. (3.36). In conjunction with the VoF method, at least one cell inside the transition region features an intermediate concentration value, i.e., $0 < c_S < 1$. To comply with the rigid behavior, the viscosity has to approach an infinitely large viscosity value, cf. Fig. 3.3. However, a linear interpolation between a small viscosity (air) and a large enough viscosity (rigid soil) leads to a viscosity that fails to represent a rigid behavior but blurs the interface. The related "interpolation" error induces a constant flow where the rigid-ideally plastic material faces the air phase and adverse influences are clearly indicated by the green line in Fig. 3.8. Therefore, a nonlinear interpolation technique is sought to simulate rigid-ideal plastic behavior with the VoF method.

To control both, the steepness of the transition and the concentration value of the interface/transition position, an interpolation method based on the arctan function is proposed

$$\begin{aligned} \mu = \mu^A + \left(\frac{arctan\left(N\left(c_S - M - 0.5\right)\right)}{\pi} + 0.5\right)\left(\mu^S - \mu^A\right) \\ -\left(1 - \left(c_S - M\right)\right)\epsilon_0\left(\mu^S - \mu^A\right) + \left(c_S - M\right)\epsilon_1\left(\mu^S - \mu^A\right) \, , \end{aligned} \tag{3.47}$$

with

$$\epsilon_0 = \frac{arctan\left(-0.5N\right)}{\pi} + 0.5 \tag{3.48}$$

and

$$\epsilon_1 = 0.5 - \frac{arctan\left(0.5N\right)}{\pi} \, . \tag{3.49}$$

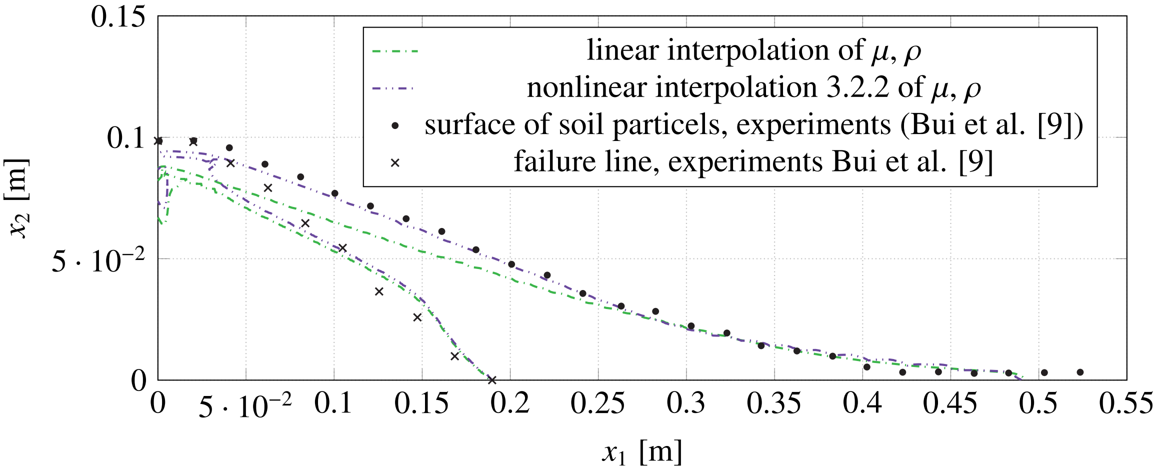

Figure 3.8: Simulation of a 2D soil collapse with a rigid plastic soil model (cf. Sec. 3.3.1). Comparison of measured (Bui et al. [9]; symbols) soil surfaces and failure lines with simulation results obtained in combination with a linear (green) and a nonlinear (purple) interpolation of the material properties.

Here the parameters N and M control the steepness of the interpolation function, and the location of the interface/transition, i.e. the concentration value with the steepest gradient. The parameters ϵ_0 and ϵ_1 serve to keep the interpolation bounded between μ^A and μ^S for $M = 0$. Fig. 3.9 displays the behavior of the interpolation function for different N values, where $\Delta\mu = \mu^S - \mu^A$ and μ^S being constant for illustrative purposes. The interpolation function sharpens the properties when using higher N values, but retains a smooth characteristic due to the chosen arctangent function. Negative values of the shift parameter M shift the transition further to the solid phase, and positive values of M further to the fluid phase. It is seen in Fig. 3.10 that activating the shift parameter M leads to unbounded material properties, an effect that is more pronounced for larger values of N. Therefore, correction terms have to be added for $M \neq 0$, which are obtained from modifications of the interpolation function (3.47)

$$\delta_0 = \left(\frac{arctan\,(N\,(-M-0.5))}{\pi} + 0.5\right) - (1+M)\,\epsilon_0 - M\epsilon_1 \tag{3.50}$$

$$\delta_1 = \left|\left(\frac{arctan\,(N\,(1-M-0.5))}{\pi}\right) - M\epsilon_0 - M\epsilon_1 - \left(\frac{arctan\,(N\,(1-0.5))}{\pi}\right)\right| . \tag{3.51}$$

The final version of the interpolation function is case-dependent due to the formulation of δ_1

$$\begin{aligned} \mu = \mu^A + &\left(\frac{arctan\,(N\,(c_S - M - 0.5))}{\pi} + 0.5\right)(\mu^S - \mu^A) \\ &- (1-(c_S - M))\,\epsilon_0\left(\mu^S - \mu^A\right) + (c_S - M)\,\epsilon_1\left(\mu^S - \mu^A\right) \\ &- (1-c_S)\,\delta_0\left(\mu^S - \mu^A\right) + T_{corr.}\,. \end{aligned} \tag{3.52}$$

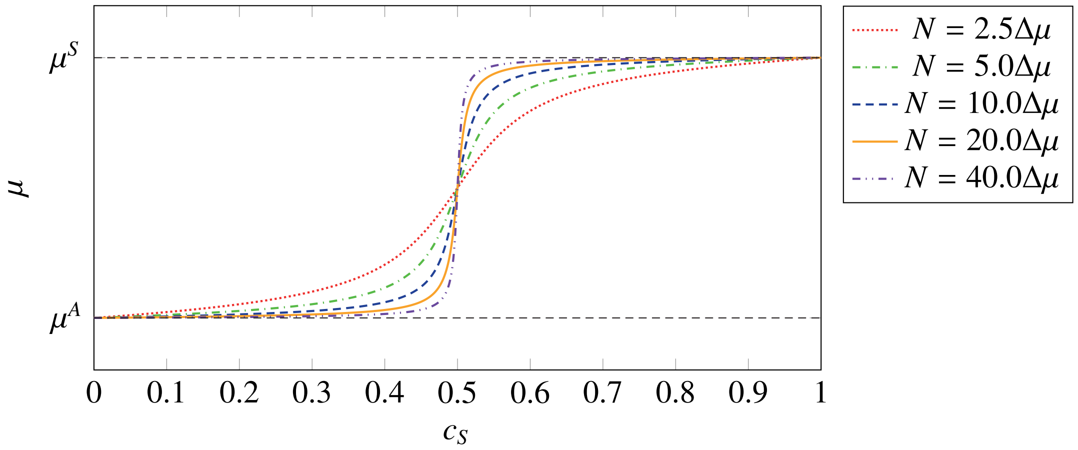

Figure 3.9: Illustration of the interpolation function (3.47) used in the equation of state for different steepness parameter values N. The displayed example refers to the apparent viscosity with a location parameter of $M = 0$.

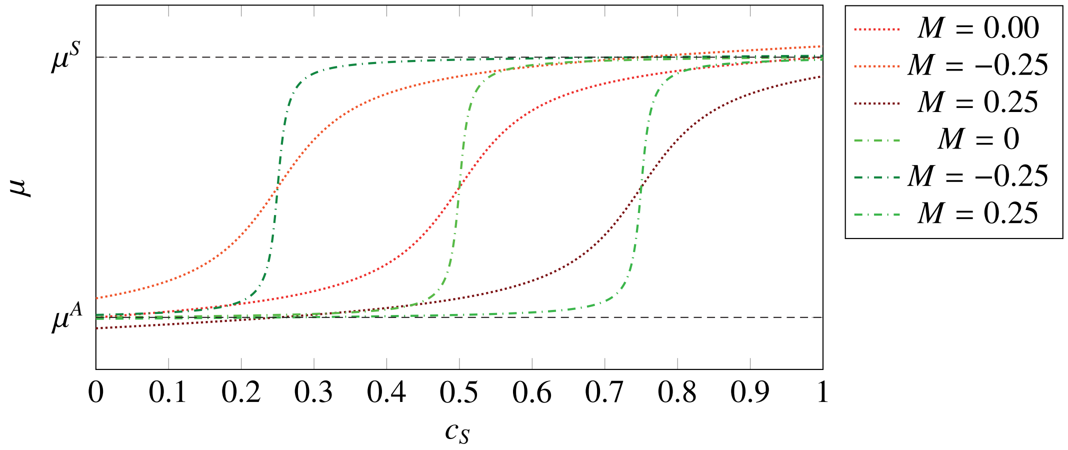

Figure 3.10: Influence of the variation of the shift parameter M on the unbounded interpolation function (3.47) for two different steepness parameters, i.e., $N = 20.0\Delta\mu$ (green) and $N = 2.5\Delta\mu$ (red).

with

$$T_{corr.} = \begin{cases} c_S \delta_1 \left(\mu^S - \mu^A\right), & \text{if } M > 0 \\ -c_S \delta_1 \left(\mu^S - \mu^A\right), & \text{if } M < 0\,. \end{cases} \tag{3.53}$$

The bounded property interpolations (3.52) are illustrated in Fig. 3.11. Note that if the phases are switched, all operations can be adjusted. It is also important to note that the density and viscosity are always interpolated consistently by using the same interpolation function.

To consider the dependency of N on resolution Δx_1, a graphical derivation is given in Fig. 3.12. For the concentration value c_S, a linear dependency between the mesh size Δx_1 and the interface width ΔD is assumed. In Fig. 3.12, three interface widths $\Delta D = 0.5 = 1.0 = 2.0$ with the boundary between rigid solid and fluid material being at $x_1 = 1$. The constant N is matched to obtain the most similar interpolation function behavior for different meshes and prevent the

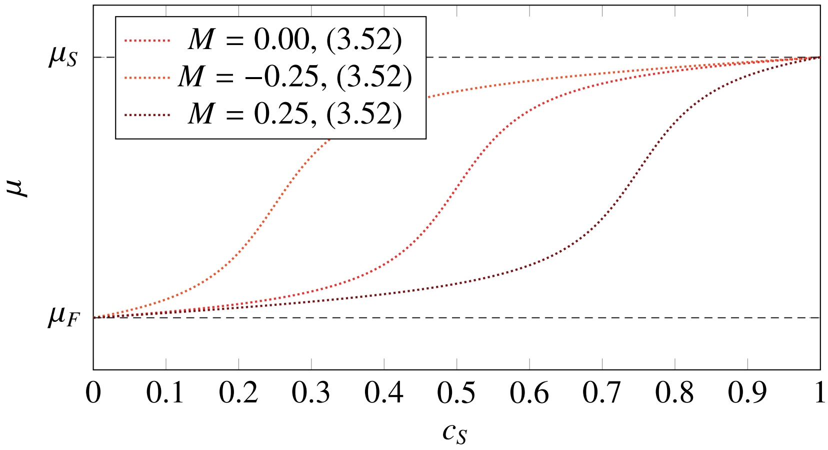

Figure 3.11: Bounded interpolation function (3.52) for $N = 2.5\Delta\mu$.

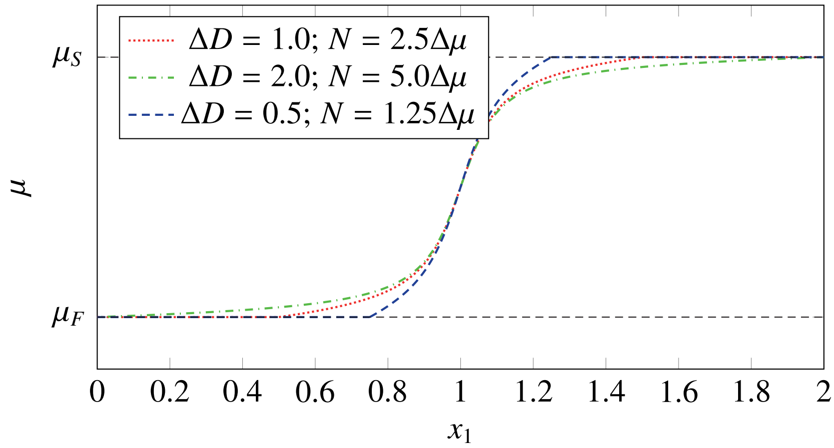

Figure 3.12: Influence of the steepness parameter N on the bounded interpolation function (3.47) for different sizes of numerical interface ΔD ($M = 0$).

interpolation from becoming too steep for finer mesh sizes and too smooth for coarser meshes. The dependency of N on Δx_1 is found to be

$$N = N_{ref} \frac{\Delta x_1}{\Delta x_{ref}} \,. \tag{3.54}$$

3.3 Verification and Validation

Several test cases are simulated to verify and validate the behavior of the rigid-plastic material model.

The first study uses experimental data for a non-cohesive artificial material to validate the final static configuration of the granular material model. The case is also used to analyse the parameter influences. The granular model is subsequently more rigorously compared against two different literature reported results: an elasto-plastic Smoothed Particle Hydrodynamics (SPH) model by Bui et al. [9] and a perfectly-plastic Particle Finite Element Method (PFEM) model by Larese et al. [70]. The aim of the analysis is to shed light on the transient behavior of the implemented granular model and to confirm its accuracy in representing the material behavior under different angles of repose. The case reported in Larese [70] again represents an artificial material and does not include larger-scale dimensions of real-life problems. In opposition to this, the test case reported in Bui et al. [9] deals with dimensions up to 4 m and realistic granular material properties, indicating if the proposed model is applicable to real-world applications. To verify the cohesive behavior of the granular model, results obtained for a cohesive material verification case are compared with results reported by Bui et al. [9] at the end of this section.

An implicit first-order time discretization is applied in all test cases of this section. The convective approximation of momentum equations employs a flux-blending scheme between a first-order upwind-biased (UDS) approach and central difference (CDS), where 70% of the fluxes are approximated with the CDS scheme, cf. Appendix A.1. The discretization of the convective term in the concentration equation utilizes the Quadratic Upstream Interpolation for Convective Kinematics (QUICK) scheme, introduced by Leonard [74].

3.3.1 Two-Dimensional Soil Collapse

Bui et al. [9] performed a series of experiments on the collapse of a two-dimensional soil to validate numerical simulations. The two-dimensional environment is emulated by employing aluminum bars with diameters of 1 mm and 1.5 mm, each possessing a length of 50 mm, to simulate the soil material. As outlined in Fig. 3.13, the initial configuration is a rectangular enclosure measuring $l = 0.2$ m in width and $h = 0.1$ m in height, with both sides enclosed by retaining walls to secure the aluminum bars in position. The collapse is initiated by the swift removal of a gate at the right end. The material density of the simulated soil is recorded at 2650kg/m^3. Parameters for the constitutive equation are obtained through shear box tests, revealing that the aluminum bars exhibit a complete absence of cohesion. Furthermore, the friction angle ϕ is empirically determined to be 19.8°. The Poisson's ratio was estimated to a value of approximately 0.3 and allows the quantification of the elastic bulk modulus K, which is found to be approximately 0.7 MPa. The employed rigid-perfectly plastic granular material model requires the closure of only two parameters, i.e., the cohesion C and the internal friction angle ϕ, which are assigned to $C = 0$ kPa and $\phi = 19.8°$, respectively.

The computational domain spans 0.6 m in length L and $H = 0.2$ m in height. The left and bottom boundaries of the domain are configured as a wall. The top and right far field boundaries are assigned to atmospheric pressure boundaries. No mobile gate is included in the computation

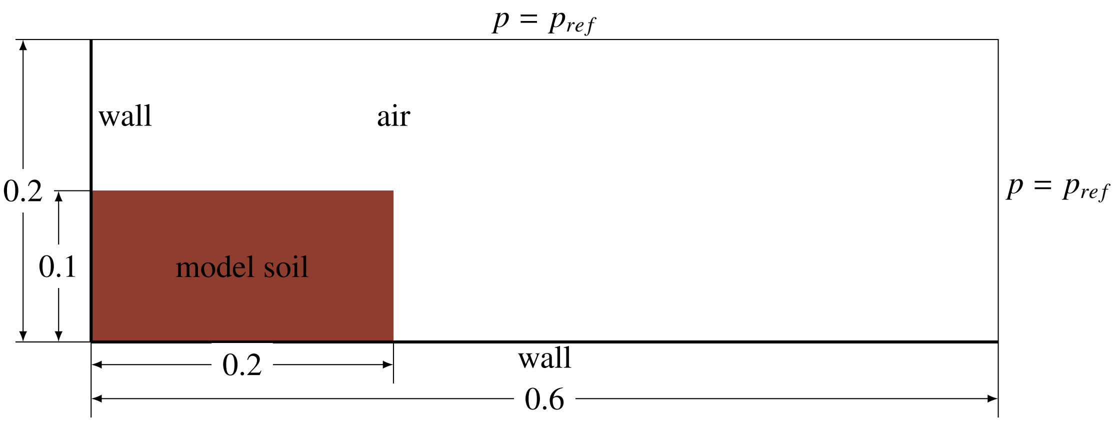

Figure 3.13: Initial configuration of the 2D soil collapse case (dimensions given in meter).

and the simulation initiates with the collapse of the initially rectangular soil. A structured, uniform mesh is used for all simulations. Following the results of an initial resolution study outlined below, a grid spacing of $\Delta x_1 = \Delta x_2 = L/300$ together with a time step of $\Delta t = 10^{-4}$ s is applied for all subsequent studies. The pressure field inside the soil is initialized to correspond to the hydrostatic pressure. The reference pressure p_{ref} is set as Dirichlet value to the atmospheric pressure at sea level $p_{ref} = 10^5$ Pa at the top and right domain boundary.

Mesh Resolution Study

The results of a mesh resolution study for the two-dimensional soil collapse of Bui et al. [9] are reported in this section where the time steps are adjusted to obtain the same Courant number for all meshes, i.e., $\Delta t = 20\ \Delta x_1/\sqrt{gh}$. When linearly interpolating the variable viscosity by Eqn. (3.36), the creeping behavior of the rigid-plastic material can be observed for all mesh sizes as is displayed in Fig. 3.14. At the left wall, the finest mesh leads to the results closest to experiments, as expected. At the bottom wall, the medium mesh size yields the best results. This is thought to stem from higher velocities in the air phase close to the soil surface for finer meshes, which leads to different free surface behavior and a different material behavior for concentration values $0 < c_S < 1$.

When the nonlinear interpolation function (3.52) is employed in combination with $M = -0.45$ and $N = 25$, the creeping phenomena can be reduced for all mesh sizes as can be seen in Fig. 3.15. The mesh study is conducted with constant values for N and M in the arctangent interpolation function, neglecting the mesh dependency of N and resulting in different soil surface behaviors of the two finer meshes. For the failure line, results converge for finer meshes. Out of computational efficiency reasons, a resolution of $\Delta x_1 = L/300$ is chosen for the upcoming validation and verification cases.

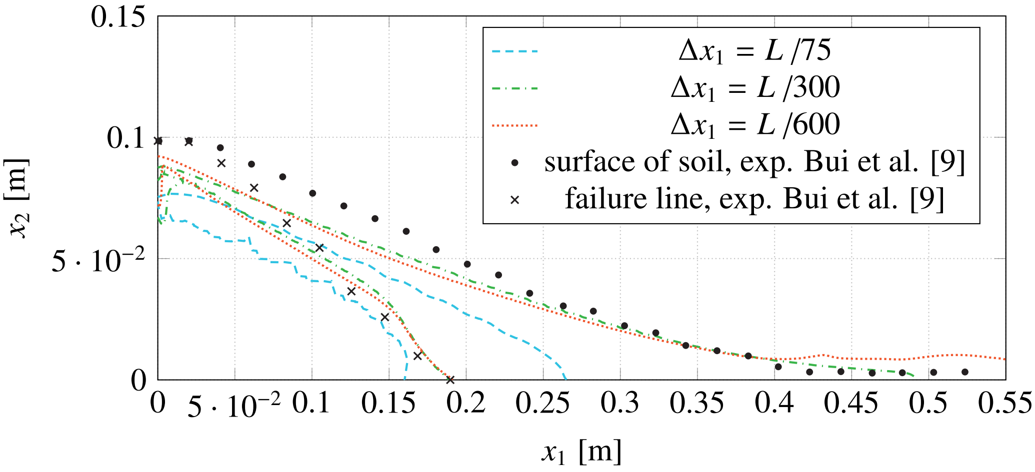

Figure 3.14: Comparison of final soil surfaces and failure lines for the 2D soil collapse case. Resolution influence using the linear interpolation for the material properties.

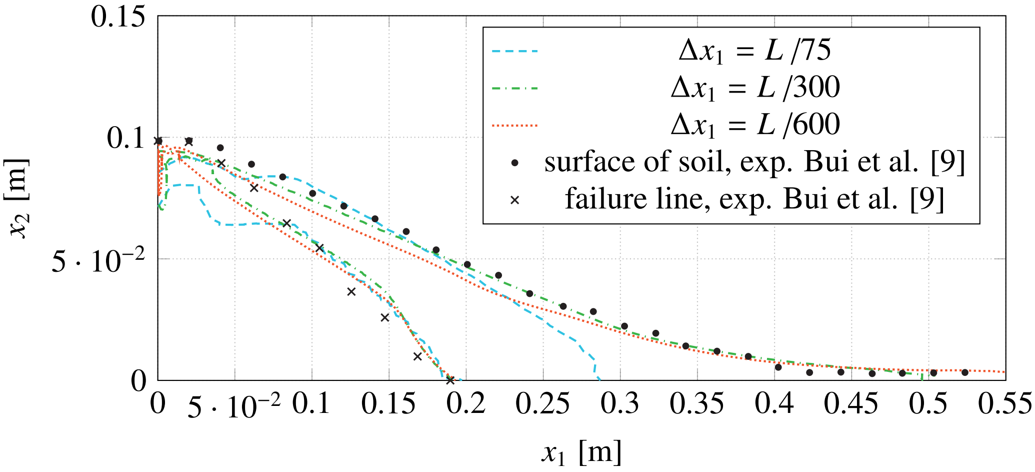

Figure 3.15: Comparison of final soil surfaces and failure lines for the 2D soil collapse case. Resolution influence using the nonlinear interpolation (3.52) based on $M = -0.45, N = 25$ for the material properties.

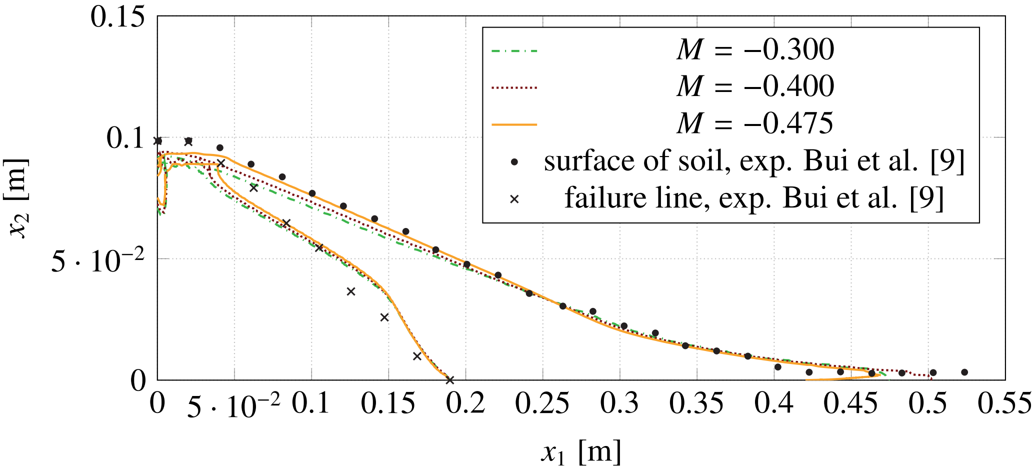

Figure 3.16: Comparison of final soil surfaces and failure lines for the 2D soil collapse case. Influence of different M parameters employed in the nonlinear EoS (3.52) (N=25).

Influence of Interpolation Function Parameters M and N

The variation of M (3.52) allows to shift the phase transition location in the interpolation function. For $N = 25$ and $\Delta x_1 = \Delta x_2 = L/300$, Fig. 3.16 indicates the benefits of a negative factor M. The latter shifts the boundary of the rigid-plastic material further towards smaller soil mixture fraction values c_S and reduces creeping effects. The effect is also slightly reflected in the failure line, which separates the rigid material behavior from the plastic behavior. In this study, the failure line is associated with the norm of a deviatoric Euler-Almansi strain to comply with a value of 0.5. At the left wall, the creeping of the material leads to an indentation of the failure line, which should not be present for a rigid material. However, the overall agreement of the failure line with the experimental data is reasonable, but not as well as in the SPH simulations of Bui et al. [9], who use an elastio-plastic constitutive equation. The lower M, the better the predicted free surface agrees with the experiment for $x_1 < 0.25$ m. Nevertheless, for $x_1 > 0.4$ m, the rigid-plastic material adheres too much to the wall for the smallest M. The transition parameter is set to $M = -0.45$ for the remainder.

Subsequently, the influence of the steepness parameter N in (3.52) is studied for a frozen $M = -0.45$. As seen in Fig. 3.17, the lower N, the better the soil surface for $x_1 > 0.4$ m coincides with the experimental data. The opposite is true for $x_1 < 0.25$ m where the soil surface fits the data better for larger values of N, except directly at the wall. For $N = 100$, strong creeping occurs at the left wall. Therefore $N = 25$ will be taken as the reference point in the remainder.

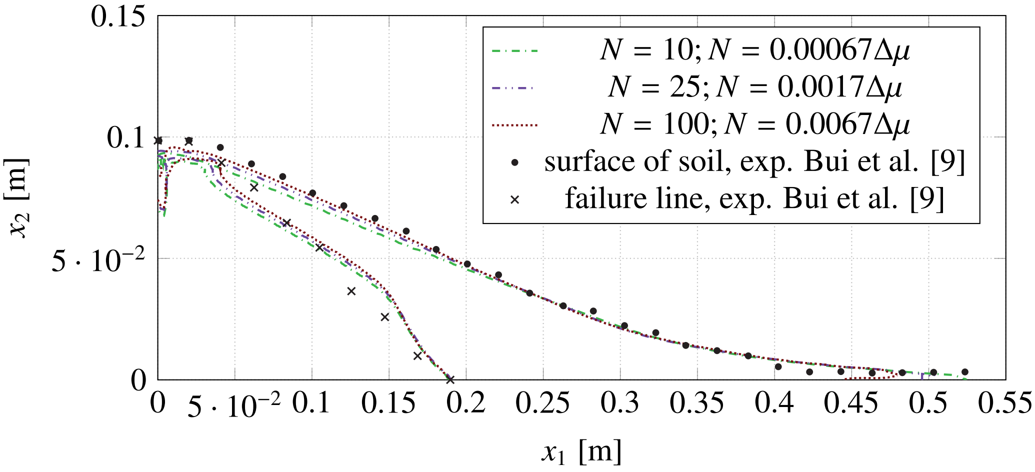

Figure 3.17: Comparison of final soil surfaces and failure lines for the 2D soil collapse case. Influence of different N parameters employed in the nonlinear EoS (3.52) (M=-0.45).

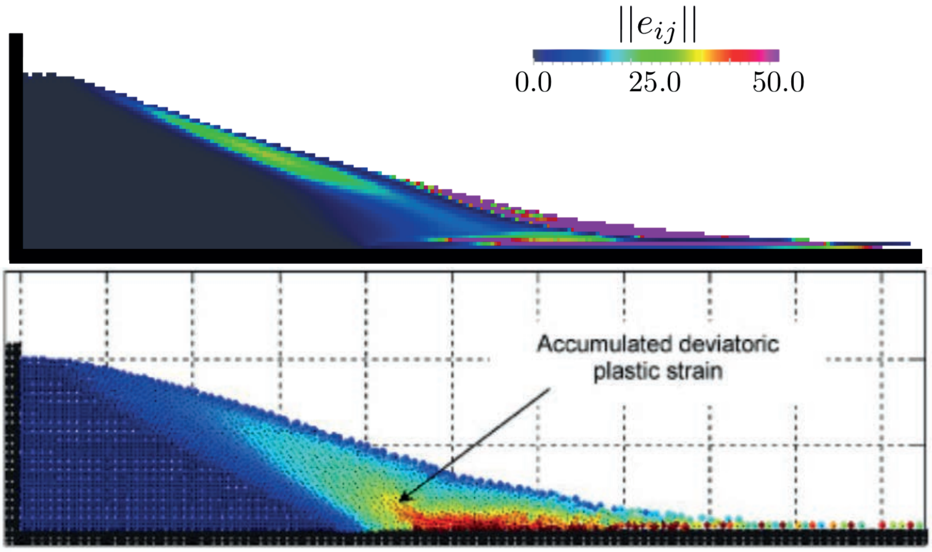

Figure 3.18: Qualitative comparison of the norm of the deviatoric Euler-Almansi strain tensor at the final position predicted by the current approach ($\Delta x_1 = L/300$, $N = 25$, $M = -0.45$; top) with SPH results from Bui et al. [9] (bottom) for the 2D soil collapse case.

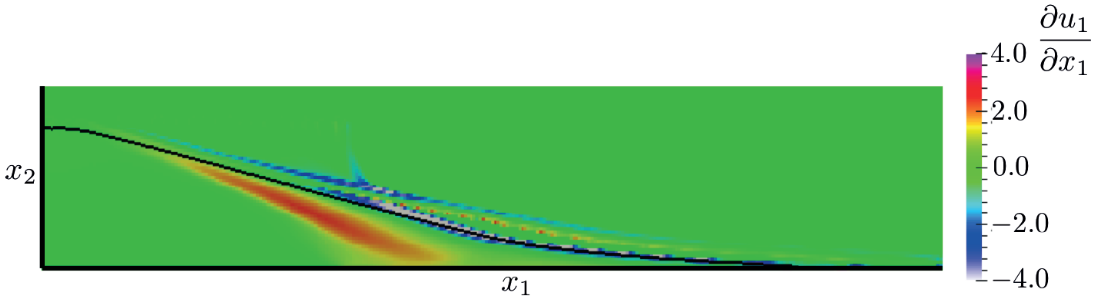

Figure 3.19: First trace component of the displacement gradient for 2D soil collapse case at a final time, where the black line represents the soil surface.

Deviatoric Strain

Comparing the norm of the Euler-Almansi strain tensor e_{ij} (3.35) predicted by the current rigid-plastic model for $N = 25$ and $M = -0.45$ with the accumulated deviatoric strain field of the reference elasto-plastic model from Bui et al. [9] in Fig. 3.18, clearly reveals the influence of the different material models. Mind that no legend for the accumulated deviatoric strain is given in Bui et al. [9]. Nevertheless, an augmented level of accumulated strain is predicted at the lower wall with both material models. The high accumulated strain at the soil surface for the current rigid perfectly-plastic model stems from the definition of soil velocity v_i^S in the Eulerian displacement equation (3.33). Since the velocity field v_i is multiplied by the soil mixture fraction, a high displacement gradient at the soil/air boundary occurs. Therefore the Eulerian deformation gradient tensor F_{ij} obtained by the displacement gradients contains values that are too large in the boundary region ($0 < c_S < 1$) as depicted in Fig. 3.19. This transfers to the values in the norm of the deviatoric Euler-Almansi strain. In order to mitigate this effect, an elliptic relaxation procedure could be introduced for the soil velocity, cf. Eqn. (5.3), but is omitted herein because the Eulerian deformation gradient tensor is a passive property and does not affect the material behavior.

The present model is considered to be validated. Nevertheless, an elasto-plastic approach could enhance the model results as suggested in Appendix F.2.

3.3.2 Verification of Angle of Repose Influences and Unsteady Behaviour

To verify the transient behavior of the rigid-plastic model, verification cases suggested by Bui et al. [9] and Larese [69] are studied which also address the influence of the angle of repose.

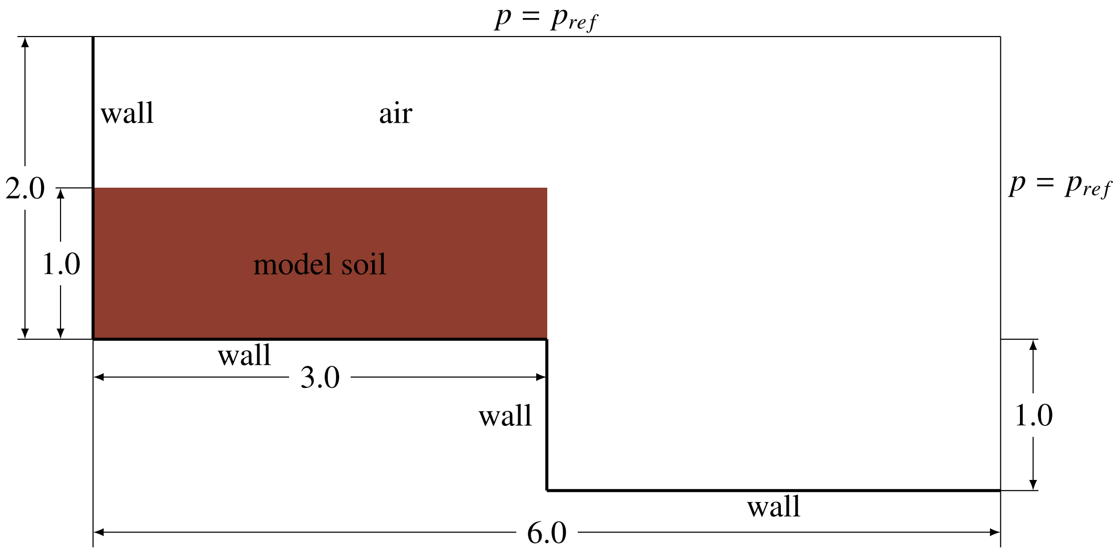

Figure 3.20: 2D soil dam breaking over a backward facing step. Initial set up by Larese [69] with measurements given in meters.

Non-Cohesive Soil Dam Breaking Down a Step

To assess the the transient behavior, a soil dam of 3 m width and 1 m height is positioned on a 3 m wide step and subsequently released as described in Larese [69]. The initial geometry, as well as the boundary conditions, are depicted in Fig. 3.20, where the length of the computational domain L is equal to 6.0 m and the total height reads $H = 3$ m. Artificial material properties are chosen with a soil density of 1000 kg/m^3 and a minimum soil viscosity of 10^{-6} Pa s and the reference pressure is taken to be $p_{ref} = 0.0$ Pa. The angle of repose is assigned to $\phi = 30°$.

Results are compared against results obtained with the PFEM approach, cf. Larese [69]. For further insight into the PFEM method, the reader is referred to Oñate et al. [95]. Since the material model and the yield criterion (3.14) agree with the model used in [69], the compared computational models only differ in the discretization methods as well as in the considered amount of phases, i.e., single-phase approach [69] vs. the current two-phase treatment.

In Fig. 3.21, results obtained in combination with a linear property interpolation, using a homogenous structured mesh with grid spacing of $\Delta x_1 = \Delta x_2 = L/300$ and a time step of $\Delta t = 10^{-3}$ s, are compared against the PFEM results with an average mesh dimension of $\Delta x_1 = L/120$. It can be seen that the FV results adhere stronger to the wall throughout the entire period, but generally, a good agreement between both methods is observed. Results returned by the FV method for the same mesh and time step in combination with the nonlinear interpolation (3.52) of material properties using $M = 0$ and $N = 25$ are depicted by Fig. 3.22. FV results are quite similar to the results of a finer PFEM mesh with $\Delta x_1 = L/600$, which

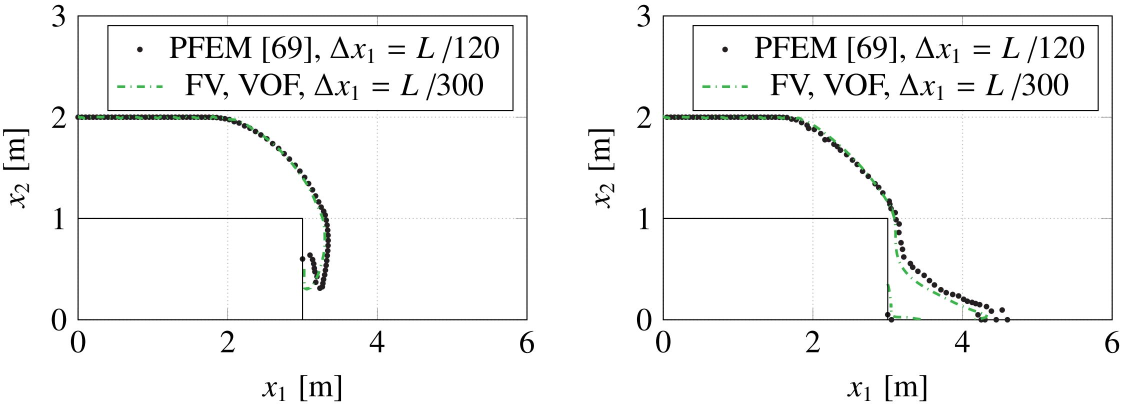

(a) t = 0.5 s (b) t = 1.0 s

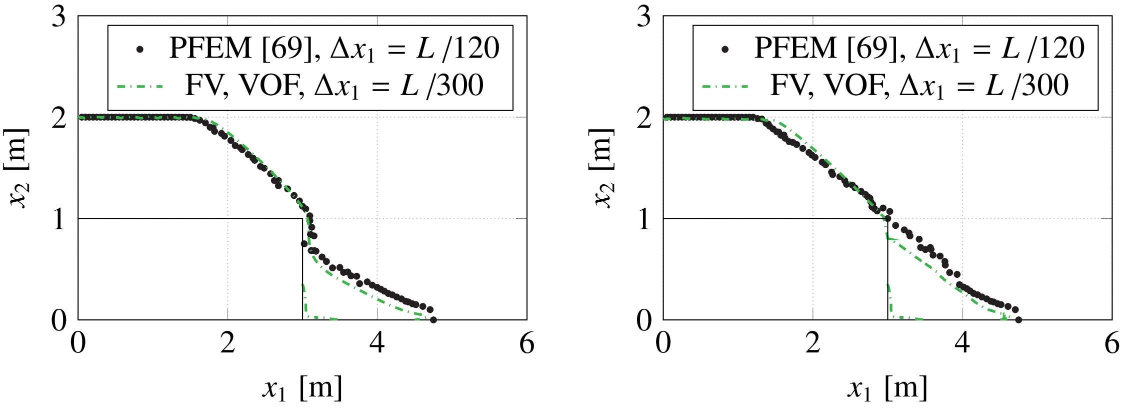

(c) t = 1.5 s (d) t = 10.0 s

Figure 3.21: 2D soil dam breaking over a backward facing step. Comparison of soil surfaces predicted by the current FV method using a linear interpolation of the material properties and the PFEM method from Larese [69] for four time instants.

highlights the effectiveness of the non-linear interpolation method.

Non-Cohesive Soil Dam Break for Different Angle of Reposes

A second case to verify the transient behavior of the model as well as its response to different angles of repose has been suggested in Bui et al. [9]. Three angles of repose (ϕ = 25°, 45°, and 65°) are simulated and compared to the elasto-plastic SPH results of Bui et al. [9]. The initial geometry is similar to the two-dimensional rectangular soil dam outlined in Fig. 3.13, but features a width of 4 m, a height of 2 m which is positioned in a computational domain of length L = 12 m and height 4 m. Moreover, a more realistic soil density of 1850 kg/m^3 is applied in this verification case.

A homogenous structured mesh with $\Delta x_1 = \Delta x_2 = L/300$ together with a time step of Δt =

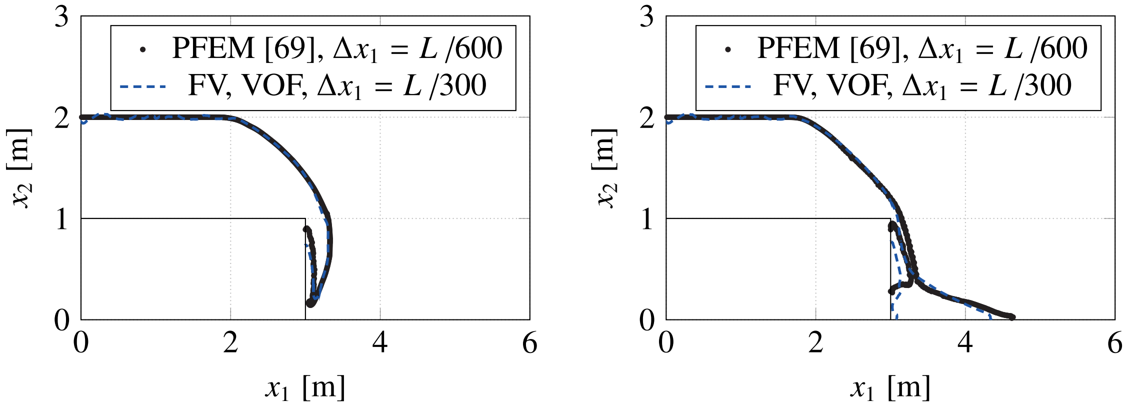

(a) $t = 0.5$ s

(b) $t = 1.0$ s

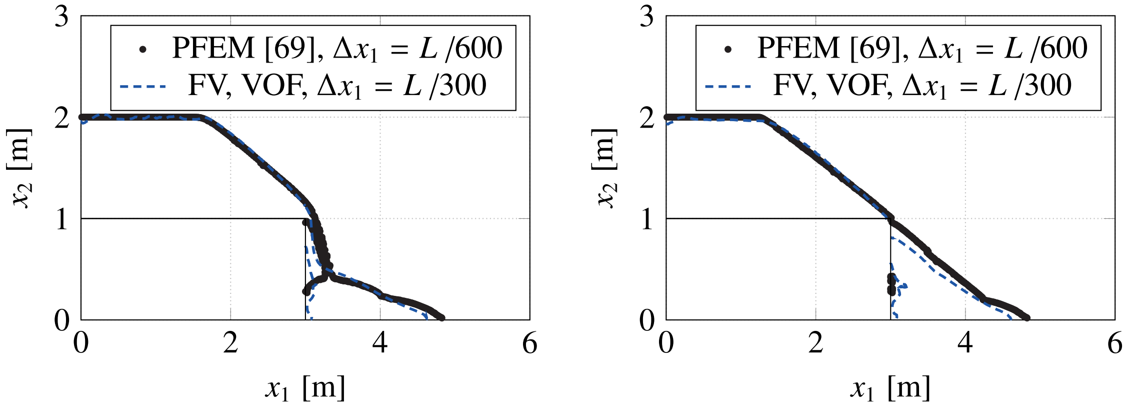

(c) $t = 1.5$ s

(d) $t = 10.0$ s

Figure 3.22: 2D soil dam breaking over a backward facing step. Comparison of soil surfaces predicted by the current FV method using a non-linear interpolation of the material properties (3.52) ($M = 0$, $N = 25$) and the PFEM method from Larese [69] for four time instants.

10^{-4} s is used for all three simulations, thereby neglecting a potential dependence of the time step on the flow velocities determined by the material properties. The initial and boundary conditions are defined as in Sec. 3.3.1. To prevent divergence in the first time step, the density is initially set to 20 kg/m^3 and subsequently increased to 1850 kg/m^3 at the tenth time step. This is needed since the resulting static pressure inside the soil column increases due to a higher density and greater spatial dimensions concerning the artificial validation cases. Due to the two-phase formulation, the pressure gradient at the boundary of the soil column, especially at the bottom of the soil column, increases, resulting in divergence in the momentum equations. Again, the regularized Bingham fluid approach and the Drucker-Prager material model Eqn. (3.13) are applied. However, the choice of the factor m_c for calculating the upper viscosity threshold was found to be critical. Too large values of m_c and μ^S_{max} hamper the convergence. Since increasing the angle of repose also increases the soil viscosity, the factor m_c has to be adjusted accordingly.

Figs. 3.23, 3.24 and 3.25, display the results for all three investigated soils in comparison with SPH results of Bui et al. [9] at $t = 0.8$ s, $t = 1.1$ s and $t = 1.4$ s and a fourth time instant.

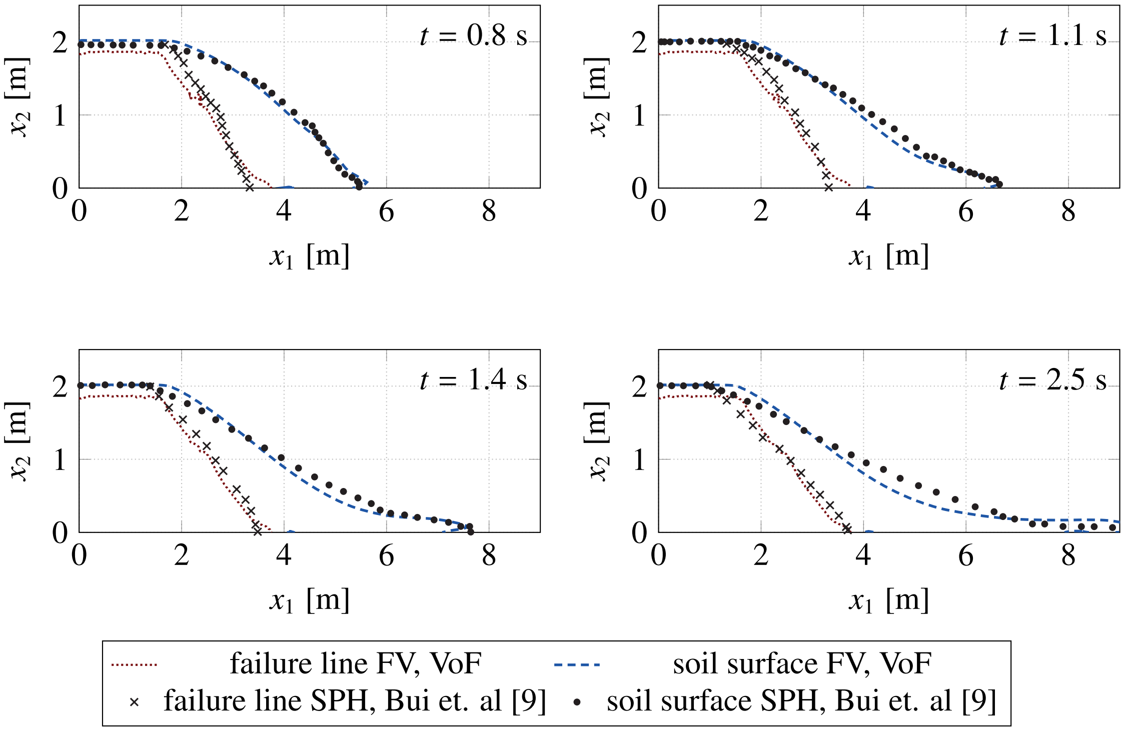

Figure 3.23: 2D soil collapse (4 m x 2 m, angle of repose $\phi = 25°$, zero cohesion): Comparison of soil surfaces and failure lines between present model (FV, VoF) vs. SPH results from Bui et al. [9] at four different time steps.

For an angle of repose of $\phi = 25°$ the settings from Sec. 3.3.1 have been adopted, i.e., $M = -0.45$, $N = 25$ and $m_c = 10^5$. Since the case represents realistic spatial dam dimensions, the hydrostatic pressure is significantly higher than in Sec. 3.3.1, which also induces higher yield stresses. Therefore, although the angle of repose is very close to the one studied in the previous section, results are expected to differ.

The results displayed in Fig. 3.23 show good agreement of the failure lines predicted by the current FV model and the SPH model [9] for all time instants. The influence of the VoF method, especially the effects of the solid velocity definition (cf. Sec. 3.3.1), is traceable by the lower failure line for $x_1 < 1.5$ m. Applying a linear interpolation for the viscosity leads to an even lower failure line, and an elasto-plastic model which does express the stress tensor directly in the momentum equations might improve the representation of the failure line in this regard. The diagonal part of the failure line in Fig. 3.23 is in good agreement with the SPH results, taking into account that the plotted SPH results were manually extracted from the deformation pattern

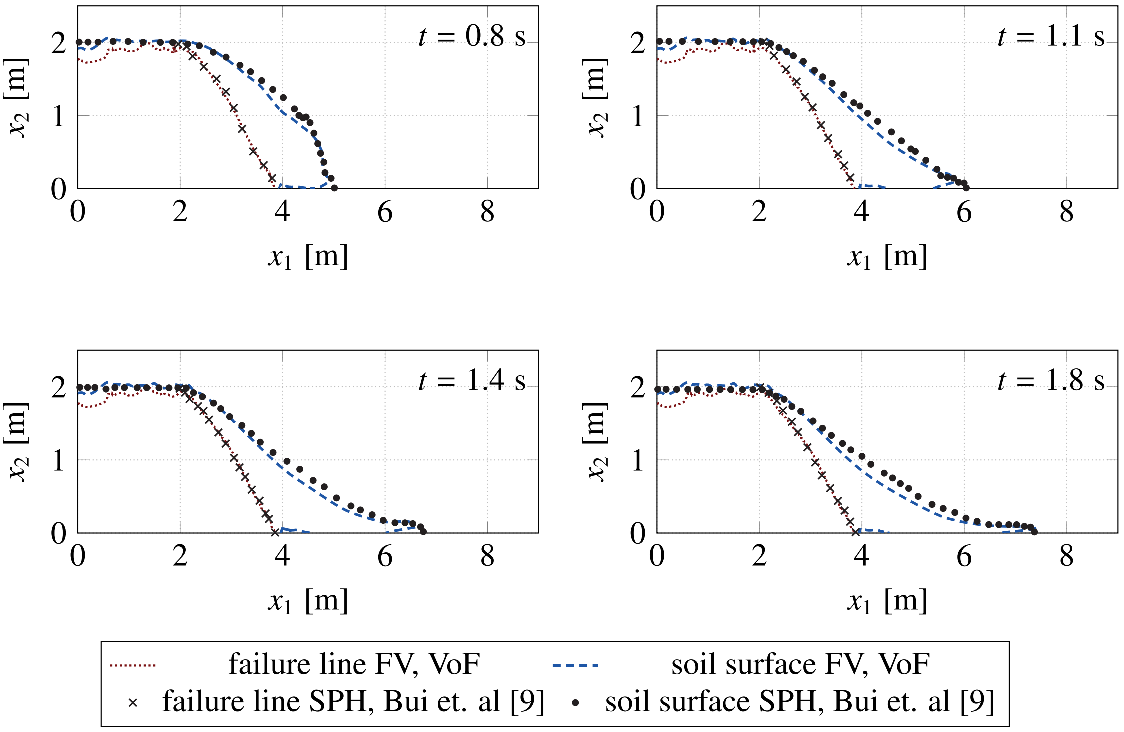

Figure 3.24: Comparison of soil surfaces and failure lines returned by the present FV-VoF method and an SPH method (Bui et al. [9]) for the 2D soil collapse (4 m × 2 m, $\phi = 45°$, C=0) at four different time instants.

figures in [9]. The soil surface is initially represented well, but tends to be more convex than the SPH solution at later times. At $t = 2.5$ s, the surface is higher for $x_1 > 8.0$ m due to the mesh resolution being unable to represent the size of single bottom particles.

For an angle of repose of 45° it is found that different settings for the interpolation function and m_c have to be applied. This is due to the resulting larger yield stress when the angle of repose increases. To this end, the factor m_c is reduced to $m_c = 10^4$. A linear interpolation of the viscosity and density is applied to keep a smooth transition between soil and air properties. A remarkable aspect of the results displayed in Fig. 3.24 is the good agreement of the failure line in its diagonal part. The reference solution and the present model match for this part of the failure line, but a higher dump at the left wall in the failure line shows the weakness of the displacement equation approach again. The dump in the failure line coincides with a smaller dump in the soil surface at the left wall. A positive note is that the dump does not increase over time but occurs at the beginning of the simulation. A second positive outcome is the model's ability to represent a steep soil surface at $t = 0.8$ s. Again, a more convex shape of the soil

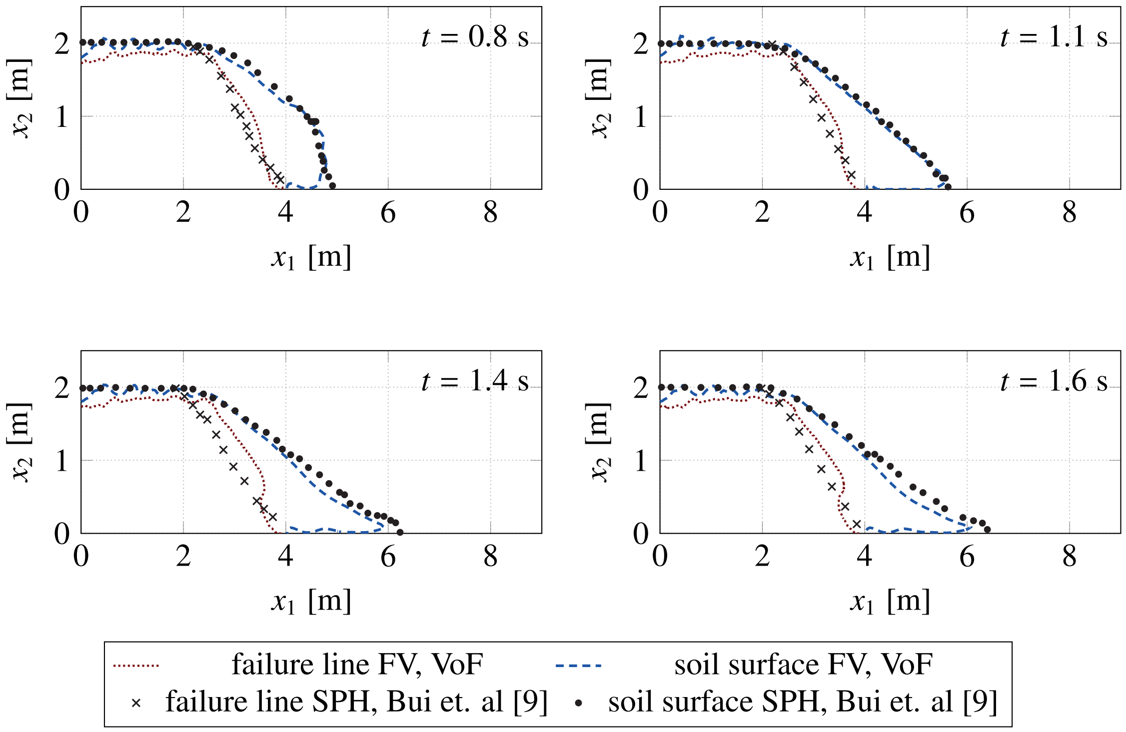

Figure 3.25: Comparison of soil surfaces and failure lines returned by the present FV-VoF method and an SPH method (Bui et al. [9]) for the 2D soil collapse (4 m × 2 m, $\phi = 65°$, C=0) at four different time instants.

surface is predicted during the later period. This is attributed to the difference in the applied constitutive equations. The air inclusion at the bottom wall at $x_1 = 4.0$ m is a further issue. It results from a very high viscosity at the lower right corner of the original dam geometry which stems from a high-pressure value. The high pressure value can be explained by the boundary wall force opposing the movement of the granular material in the x_1-direction at the lower right corner of the dam. Due to the large viscosity in this confined region, the velocity of the granular material gets reduced, and it has to flow over the high-viscosity cell. Furthermore, the soil concentration c_S is not transported close to this point due to the small velocities, and therefore the air inclusion remains present up to $t = 2.5$ s. In the soil collapse test case in Sec. 3.3.1, the final results are taken from time step $t = 20.0$ s when possible air inclusions are already dissolved. An elasto-plastic model is expected to resolve the issue of air inclusion.

For the simulations with an angle of repose of $\phi = 65°$ the factor m_c for the regularised Bingham approach is taken to be $m_c = 10^2$ while also maintaining a linear interpolation method of the material properties. Issues observed for $\phi = 45°$ are intensified for an angle of repose of

$\phi = 65°$ as can be seen in Fig. 3.25. Due to higher yield stress, the values which have to be represented by the viscosity are also larger. Furthermore, the soil surface has a crooked shape in the rigid part of the dam ($x_1 < 2$ m). This stems from the higher stress gradient at the soil surface for granular material with higher yield stress. The failure line does not match the SPH data as well as for the material with $\phi = 45°$, but the agreement is still generally satisfying.

The higher the plastic yield stress, the more difficult simulations of granular material become with a rigid perfectly-plastic VoF method.

3.3.3 Verification of the Cohesive Soil Model

To test the performance of the soil model for cohesive materials, the unsteady case assessed in Sec. 3.3.2 is revisited. The 2D dam break involves granular material with an angle of repose of $\phi = 25°$ and a cohesion of $C = 5$ kPa for which results are reported in Bui et al. [9]. The additional cohesion increases the yield stress similar to the above studies enhanced angle of repose of $\phi = 65°$. The factor m_c that scales the upper viscosity for the regularised Bingham approach is, therefore, again set to $m_c = 10^2$. The study employs the non-linear interpolation based upon $M = 0$ and $N = 5$.

In Fig. 3.26, the blue line represents the surface of the granular material simulated with the present method which is compared against the results of the SPH model by Bui et al. [9]. As previously seen in conjunction with higher angles of repose, the higher yield stress induced by the cohesion yields indentations of the free surface at the downstream end of the rigid part of the dam. Similar to the results for higher angles of repose, a fairly small air enclosure is observed between the granular material and the bottom wall at a later phase. Furthermore, it can be seen that there is a good agreement between the two results.

The red dotted lines represent the failure lines of the present model. They are defined by an Euler-Almansi strain norm level of 0.3. As mentioned in the previous section 3.3.1, artificial displacement gradients near the soil surface lead to higher Euler-Almansi strains. This effect is, of course, not present in the single-phase SPH model. A positive aspect is the observation of constant distances between the soil surface and the failure over time. Therefore, the rigid part of the granular material is represented well also in later periods. For the smaller rigid part on the downstream (right) side, the relevant strain norm contour lines are only partly plotted to obtain an improved visual comparison with the SPH results. The lines not plotted correspond to the effects explained in Sec. 3.3.1. With the exception of the modeling-related differences, the selected failure lines of the SPH and the FV-VoF method displayed in Fig. 3.26 agree very well.

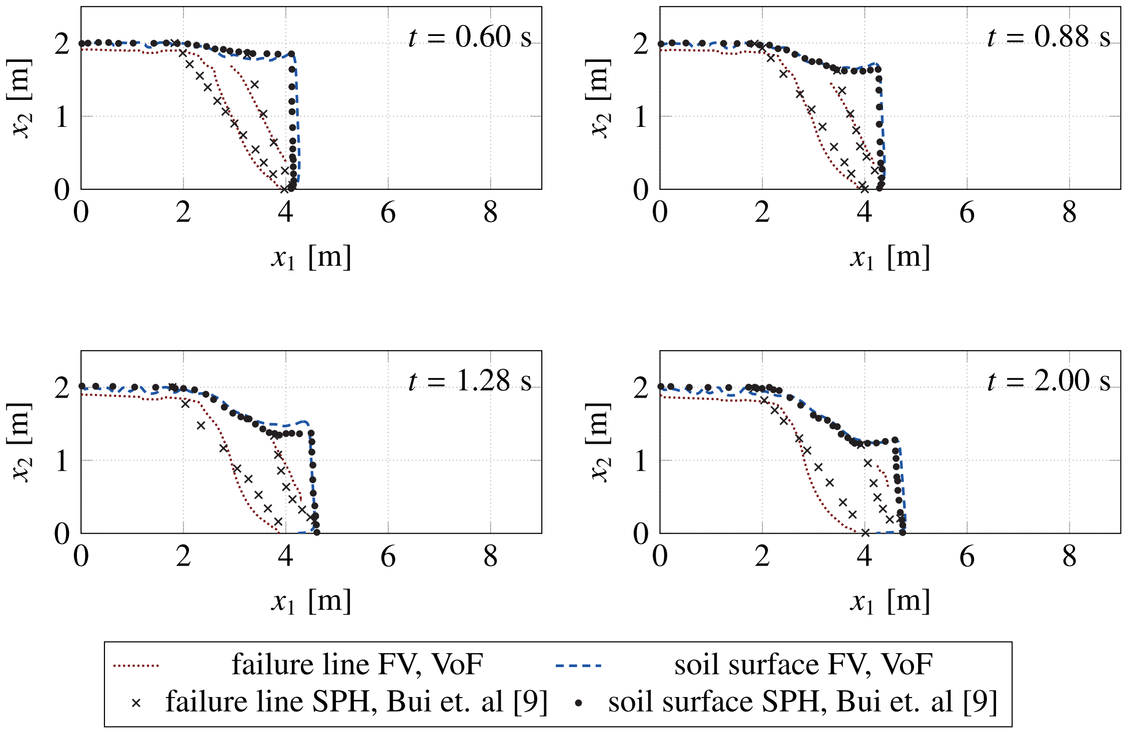

Figure 3.26: Comparison of soil surfaces and failure lines returned by the present FV-VoF method and an SPH method (Bui et al. [9]) for the 2D cohesive soil collapse (4 m × 2 m, $\phi = 25°$, C=5 kPa) at four different time instants.

Fig. 3.27 compares the accumulated deviatoric strain magnitudes predicted the present method and the reference SPH model qualitatively. Mind that no legend was provided for the SPH result in Bui et al. [9]. The general deformation pattern agrees well, except for regions close to the soil-air interphase surface. Using the present two-phase VoF model inherently introduces strain close to this interface. It could be enhanced by applying a different constitutive model (e.g., with surface tension, elasto-plastic model) or an elliptic relaxation of the solid velocity. Inside the granular phase $c_S > 0.99$, the Euler-Almansi strain norm of the current approach matches the accumulated deviatoric strain results of the SPH model [9]. For the first three ($t = 0.6$ s, $t = 0.88$ s and $t = 1.28$ s) time instants, the failure cone is wider for the elasto-plastic SPH model than the present perfectly-plastic FV-VoF model at the top of the dam. The SPH model predicts a smaller accumulated strain in the dam's elastic right corner part than the Euler-Almansi strain norm in the rigid part of the present model. Future work should explore an elasto-plastic VoF approach, cf. Appendix F.2.

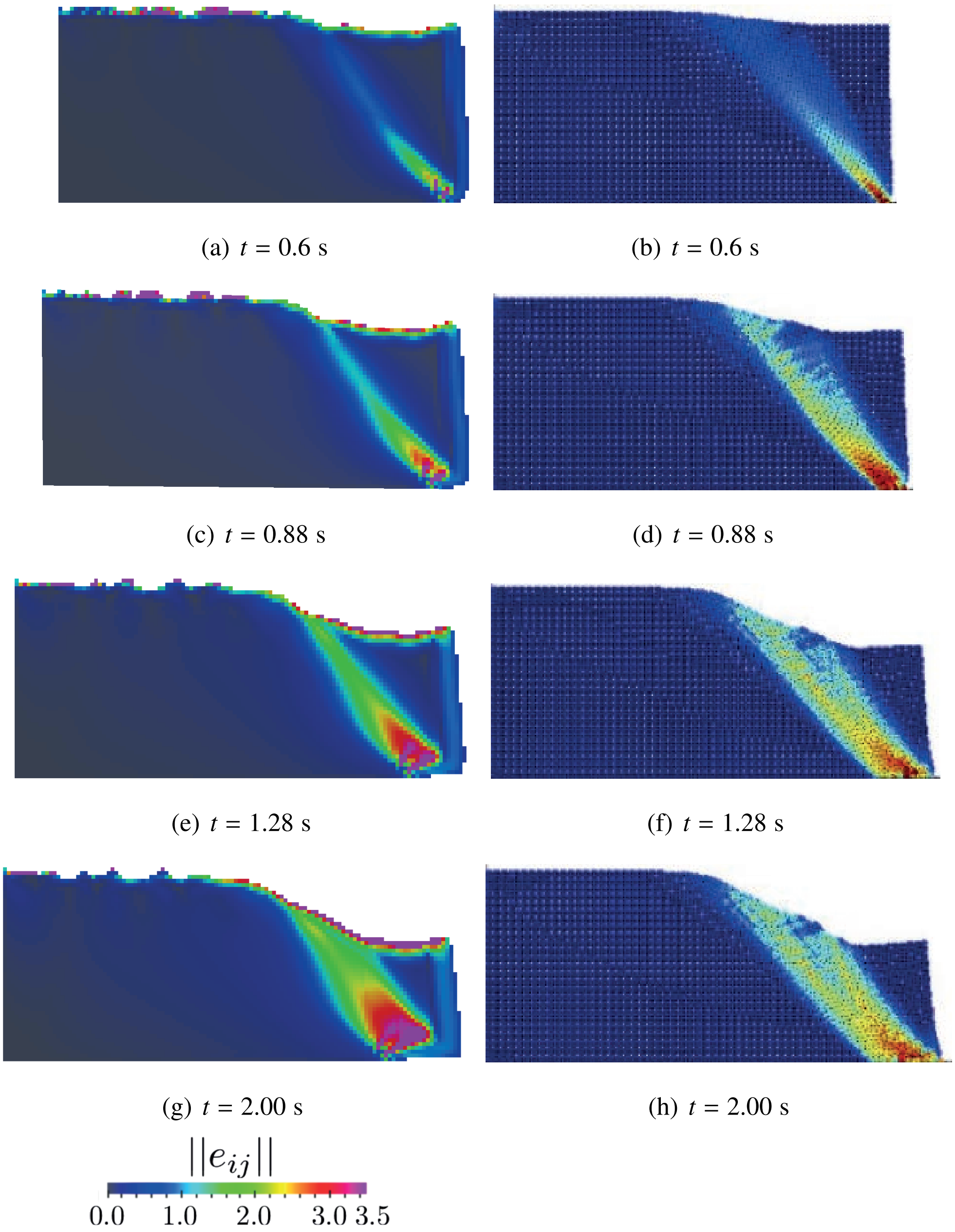

(a) t = 0.6 s (b) t = 0.6 s

(c) t = 0.88 s (d) t = 0.88 s

(e) t = 1.28 s (f) t = 1.28 s

(g) t = 2.00 s (h) t = 2.00 s

Figure 3.27: : Qualitative comparison of the deviatoric Euler-Almansi strain norm returned by present method (threshold at c_S = 0.5; left) and SPH results of Bui et. al [9] (right) for the 2D cohesive soil collapse (4 m × 2 m, ϕ = 25°, cohesion C = 5 kPa).

Chapter 4

Coupled Flow Through Porous Plastic Material

As mentioned in the introduction, the saturation level of the granular cargo and the water distribution in the cargo plays a major role in the transportation of nickel-, iron ore, and bauxite. Therefore a model that can represent two potential failure failure mechanisms, i.e., ”wet base” and ”dynamic separation”, is introduced in this chapter. Four phase combinations are needed to model a two-phase fluid flowing through a perfectly-plastic porous material. Fig. 4.1 illustrates an exemplary (initial) state of the granular material inside a vessel hold. The figure also provides enlarged control volumes of all four possible phase combinations.

This work aims at coupling two sets of two-phase flows, which consist of the previously described models “rigid perfectly-plastic granular material” (chapter 3) and “free surface flow through rigid-porous media” (chapter 2), respectively. The VoF method is applied to represent the free surface in both sets of two-phase flows, and the coupling occurs via a phase-dependent porosity, a phase-dependent resistance force, and phase-dependent material properties.

4.1 Mathematical Model

To look closely at one exemplary CV, including air, water and soil material, Fig. 4.2 displays the fluid and soil skeleton phase. The cell volume V consists of two contributions from the fluid phases V^F and granular phase V^G (cf. Fig. 4.2)

$$V = V^F + V^G \,, \tag{4.1}$$

where both phases (V^F and V^G) consist of a mixture of two immiscible phases. The fluid phase comprises air and water, and the granular phase includes air and soil. The relation between fluid

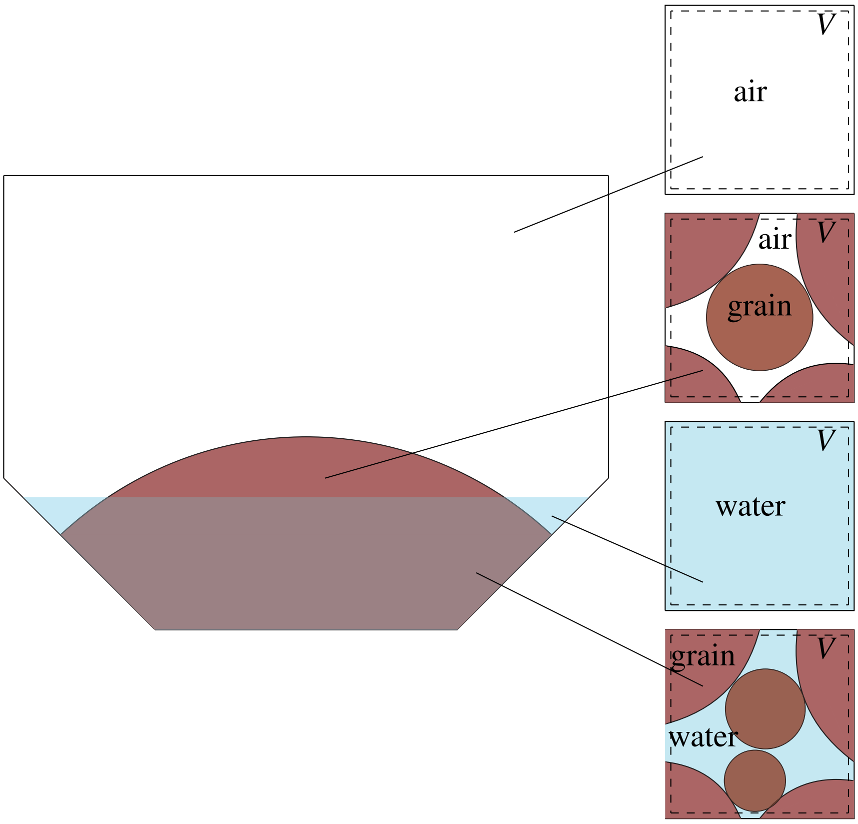

Figure 4.1: Example geometry of granular material in a vessel hold with a water-air free surface which can intersect the granular material. The enlarged FVs of the four different resulting phases are displayed on the right side.

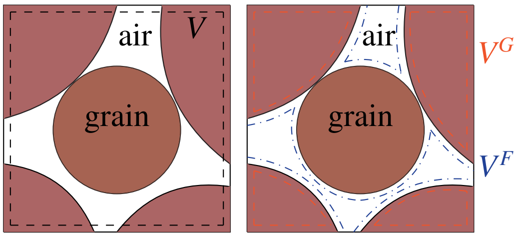

Figure 4.2: Left: dashed lines represent the cell volume dV. Right: blue dashed lines represent the fluid volume dV^F, and red dashed lines the granular volume dV^G.

volume and overall volume defines the porosity n

$$n = \frac{V^F}{V} \tag{4.2}$$

and therefore the relationship between porosity n and granular volume V^G is given by

$$1 - n = \frac{V^G}{V} \ . \tag{4.3}$$

In the current monolithic FV approach, the continuity, momentum, and mixture equations are solved for both the granular and fluid phases and are strongly coupled. The granular equations are formulated by applying the immiscible condition to the water and air phases. Therefore the granular material is fully saturated or unsaturated depending on the free surface equation of the fluid phase. An extension to partially saturated granular material could be made by applying a miscible fluid VoF equation.

4.1.1 Continuity Equations

Both the fluid phases and the granular phases are solved as incompressible materials. For the granular phase, this simplifies the model, which can be extended to compressible materials as explored in Appendix F.1. For the fluid phases, the continuity equation follows from the mass conservation of the fluid inside the fluid volume as given in Eqn. (2.4) in chapter 2, and it leads to the usual zero-divergence differential form (2.5) with constant fluid density ρ^F. i.e.

$$\int_{V^F} \frac{\partial v_i^F}{\partial x_i} dV = 0 \ .$$

The same derivation can be made for the conservation of the granular mass inside the granular volume V^G, which results in

$$\frac{D}{Dt}\int_{V^G} \rho^G dV = \int_{V^G} \left(\frac{\partial \rho^G}{\partial t} + \frac{\partial v_i^S \rho^G}{\partial x_i} \right) dV = 0 \ , \quad \rightarrow \quad \int_{V^G} \frac{\partial v_i^S}{\partial x_i} dV = 0 \ . \tag{4.4}$$

If the integration is applied over the total volume V, cf. Eqns. (4.2) and (4.3), these relations become

$$\int_V n \frac{\partial v_i^F}{\partial x_i} dV = 0 \tag{4.5}$$

and

$$\int_V (1 - n) \frac{\partial v_i^S}{\partial x_i} dV = 0 \ . \tag{4.6}$$

Splitting the Darcy velocity $\hat{v}_i = n v_i^F + (1 - n) v_i^S$ into two parts $\hat{v}_i^F$ and $\hat{v}_i^S$ which are defined as

$$\hat{v}_i^F = n v_i^F \tag{4.7}$$

$$\hat{v}_i^S = (1-n)v_i^S \tag{4.8}$$

and introducing them into Eqns. (4.5) and (4.6) leads to

$$\int_V \left(n \frac{\partial \left(\frac{\hat{v}_i^F}{n} \right)}{\partial x_i} \right) dV = \oint_A \hat{v}_i^F dA_i - \int_V \left(\frac{\partial n}{\partial x_i} \frac{\hat{v}_i^F}{n} \right) dV = 0 \tag{4.9}$$

and

$$\int_V \left((1-n) \frac{\partial \left(\frac{\hat{v}_i^S}{1-n} \right)}{\partial x_i} \right) dV = \oint_A \hat{v}_i^S dA_i - \int_V \left(\frac{\partial (1-n)}{\partial x_i} \frac{\hat{v}_i^S}{(1-n)} \right) dV = 0\ . \tag{4.10}$$

Since the spatial derivative of the porosity is only relevant at the boundary of the granular material, the second term of these equations is neglected in the current approach. The full continuity equations would need to be solved for a compressible granular material. In the present method, equations

$$\int_V \frac{\partial\, \hat{v}_i^F}{\partial x_i} dV = 0 \tag{4.11}$$

and

$$\int_V \frac{\partial\, \hat{v}_i^S}{\partial x_i} dV = 0 \tag{4.12}$$

are solved in line with the formulations in chapter 2.

4.1.2 Momentum Equations

Starting from the derivation of the momentum equations in Sec. 2.1.2 for two-phase flow through a porous material, the momentum equations for coupled fluid phases and porous granular phases are derived. Formulating the momentum equations for an incompressible fluid over the complete control volume $dV = dV^F/n$ and introducing the porous resistance force f^R, which represents the force acting between the grains and the fluid, leads to Eqn. (2.13) in the integral form which is recalled here to facilitate the understanding of the following sections

$$\begin{aligned} &\int_V n \left[\frac{\partial(\rho^F v_i^F)}{\partial t} + \frac{\partial \left(\rho^F v_i^F v_j^F \right)}{\partial x_j} \right] dV = \\ &\int_V n \left[\rho^F g_i - \frac{\partial p^F}{\partial x_i} + \frac{\partial}{\partial x_i} \left(\mu^F \left(\frac{\partial v_i^F}{\partial x_j} + \frac{\partial v_j^F}{\partial x_i} \right) \right) + \frac{f^R}{n} \right] dV\ . \end{aligned} \tag{4.13}$$

The momentum equations of the incompressible granular phase can be derived in a similar way from the force equilibrium in the granular volume dV^G

$$\frac{D}{Dt} \int_{V^G} \left(\rho^G v_i^S \right) dV = \int_{V^G} \left[\frac{\partial(\rho^G v_i^S)}{\partial t} + \frac{\partial \left(\rho^G v_i^S v_j^S \right)}{\partial x_j} \right] dV = \int_{V^G} \left[\rho^G g_i + \frac{\partial \sigma_{ij}^S}{\partial x_j} \right] dV \tag{4.14}$$

where σ^S_{ij} is the stress acting in the granular phase. By now applying dV^G=$(1-n)\ dV$ and introducing the porous resistance force f^R, which is acting with the opposite sign on the granular phase than on the fluid phases, the equation in the integral form gets

$$\int_V (1-n)\left[\frac{\partial(\rho^G v^S_i)}{\partial t} + \frac{\partial\left(\rho^G v^S_i v^S_j\right)}{\partial x_j}\right] dV = \int_V (1-n)\rho^G g_i dV + \int_V \frac{\partial \sigma^S_{ij}}{\partial x_j} dV - \int_V f^R_i dV\ . \tag{4.15}$$

The constitutive equations defining the granular stress tensor σ^S_{ij} are given in Sec. 4.1.4, and the porous resistance force f^R_i for the coupled model is based on the relative velocity between fluid and solid material and is formulated in a Forchheimer model with constants $\tilde{A}$ and $\tilde{B}$

$$f^R_i = -\rho^F (v^F_i - v^S_i)\left(n\tilde{A} + n^2\tilde{B}\ \left\|v^F - v^S\right\|_2\right) \tag{4.16}$$

similar to the porous resistance forces in Sec. 2.1.3. The coupled formulation can also apply the same constants as in Sec. 2.1.3.

The above equations formulate the momentum equations based on the granular velocity v^S_i and fluid velocity v^F_i. Since the approach solving the set of equations for the Darcy velocity $\hat{v}_i$ and not the fluid velocity v^F_i was found to be more robust and efficient in chapter 2 and in Düsterhöft-Wriggers et al. [28], here the momentum equations are also formulated with the two parts of the Darcy velocity $\hat{v}^S_i$ and $\hat{v}^F_i$ (defined in Eqns. (4.7) and (4.8)). Dividing the fluid phase momentum equations by the porosity and introducing $\hat{v}^F_i$, the momentum equations for the fluid phase reads

$$\int_V \left[\frac{\partial\left(\rho^F \frac{\hat{v}^F_i}{n}\right)}{\partial t} + \frac{\partial\left(\rho^F \frac{\hat{v}^F_i}{n}\frac{\hat{v}^F_j}{n}\right)}{\partial x_j}\right] dV = \int_V \left[\rho^F g_i - \frac{\partial p^F}{\partial x_i} + \frac{\partial}{\partial x_i}\left(\mu^F\left(\frac{\partial \frac{\hat{v}^F_i}{n}}{\partial x_j} + \frac{\partial \frac{\hat{v}^F_j}{n}}{\partial x_i}\right)\right) + \frac{f^R_i}{n}\right] dV\ . \tag{4.17}$$

This formulation of the momentum equations for the fluid phase neglects the spatial and temporal variability of the porosity.

For the momentum equations of the granular phase, the variable $\hat{v}^S_i$ is directly introduced in Eqn. (4.15), leading to

$$\int_V \left[\frac{\partial(\rho^G \hat{v}^S_i)}{\partial t} + \frac{\partial\left(\frac{\rho^G \hat{v}^S_i \hat{v}^S_j}{(1-n)}\right)}{\partial x_j}\right] dV = \int_V (1-n)\rho^G g_i dV + \int_V \frac{\partial \sigma^S_{ij}}{\partial x_j} dV - \int_V f^R_i dV\ . \tag{4.18}$$

The expressions of the resistance force f^R_i in regards to the variables $\hat{v}^S_i$ and $\hat{v}^F_i$ follow directly from Eqn. (4.16) and the definitions of the variables in Eqns. (4.7) and (4.8)

$$f^R_i = -\rho^F\left(\hat{v}^F_i - \frac{n\hat{v}^S_i}{(1-n)}\right)\left(\tilde{A} + \tilde{B}\left\|\hat{v}^F - \frac{n\hat{v}^S}{1-n}\right\|_2\right)\ . \tag{4.19}$$

4.1.3 Mixture Equations (VoF)

The employed VoF equations for a formulation based on the fluid velocity v_i^F and the soil velocity v_i^S, governing the mixture fractions c_A and c_S, follow from the continuity equations (2.5) and (4.4) and the immiscibility conditions $Dc_A/Dt = 0$, $Dc_S/Dt = 0$

$$\int_{V^F} \left(\frac{\partial c_A}{\partial t} + \frac{\partial \left(c_A v_i^F \right)}{\partial x_i} \right) dV = 0 \tag{4.20}$$

$$\int_{V^G} \left(\frac{\partial c_S}{\partial t} + \frac{\partial \left(c_S v_i^S \right)}{\partial x_i} \right) dV = 0 \; . \tag{4.21}$$

Mixture fraction values $c_A = 0.5$, and $c_S = 0.5$ are used to identify the interface. The position of the soil skeleton is mapped to the fluid phase equations by calculating the porosity in each iteration at each time step from a constant porosity n_c

$$n = c_S n_c \; . \tag{4.22}$$

If parts of the Darcy velocity defined in (4.7) and (4.8) are used as variables and the integral is solved over the total volume V, the transport of the mixture fractions reads

$$\int_{V} \left(\frac{\partial c_A}{\partial t} + \frac{\partial \left(\frac{c_A \hat{v}_i^F}{n} \right)}{\partial x_i} \right) dV = 0 \tag{4.23}$$

$$\int_{V} \left(\frac{\partial c_S}{\partial t} + \frac{\partial \left(\frac{c_S \hat{v}_i^S}{(1-n)} \right)}{\partial x_i} \right) dV = 0 \; , \tag{4.24}$$

introducing a division by zero outside the granular material in the transport equation for the soil mixture fraction transport. How the term is treated will be explained in detail in the approximation section.

The material properties are calculated by interpolating the properties of each two-phase flow via either a linear function (following equations) or an arctangent function (cf. Sec. 3.2.2). With $(\cdot)^F$ denoting the fluid material properties of the air-water free surface flow and $(\cdot)^G$ denoting the soil-air material properties, the density, and viscosity get

$$\rho^F = c_A \rho^A + (1 - c_A) \rho^W \tag{4.25}$$

$$\rho^G = c_S \rho^S + (1 - c_S) \rho^A \tag{4.26}$$

$$\mu^F = c_A \mu^A + (1 - c_A) \mu^W \tag{4.27}$$

$$\mu^G = c_S \mu^S + (1 - c_S) \mu^A \; . \tag{4.28}$$

Here $(\cdot)^A$ represents air, $(\cdot)^W$ water, and $(\cdot)^S$ is the soil skeleton for the bulk material properties.

4.1.4 Constitutive Law for Solid Phase

For pore water pressures not exceeding a value where it can support the complete load, the strength of the soil skeleton depends on the effective stress rather than the pore water pressure. This principle of effective stress is widely known as being introduced by Terzaghi [113]. As mentioned in de Boer et al. [17] also, other scientists were applying the concept of effective stress in their work independently from Terzaghi.

Using the Terzaghi [113] principle of effective stress σ'_{ij}, the stress tensor σ^S_{ij} for the granular material can be expressed as

$$\sigma^S_{ij} = \sigma'_{ij} - p^F \delta_{ij} \tag{4.29}$$

which is shown by Ehlers [30] to be valid for incompressible soil skeletons independent from the properties of the fluid inside the pores. Also, the thermodynamically consistent effective stress approach for unsaturated soils by Borja [8] is in line with the Terzaghi principle when the Biot coefficient is considered equal to one for soils. It shall be remarked here that the fluid pressure p^F in the present method consists of the air and water pressure

$$p^F = c_A p^A + (1 - c_A) p^W \tag{4.30}$$

and the granular pressure p^G consists of the air and solid skeleton pressure

$$p^G = c_S p^S + (1 - c_S) p^A \tag{4.31}$$

depending on the air mixture fraction c_A and soil mixture fraction c_S.

Applying the principle of equivalent effective stress to the averaged Cauchy stress tensor of the soil skeleton σ^S_{ij} and thereby following Bui et al. [10] and Uzuoka et al. [123] leads to

$$\sigma^S_{ij} = \sigma'_{ij} - (1 - n) p^F \delta_{ij} \, . \tag{4.32}$$

Both Bui et al. [10] and Uzuoka et al. [123] use compressible soil skeleton materials, which differs from the incompressible assumption in this work. Therefore an underestimation of stabilizing fluid pressure forces in the momentum equations of the soil skeleton may arise following the definition of effective stress for incompressible soil skeletons in Ehlers [30].

For the effective stress σ'_{ij}, either the elastic model from chapter 5 or the rigid-plastic material model from chapter 3 is applied. In both approaches, the stress is divided into a volumetric and deviatoric part, where the volumetric part of the stress equals the pressure in the underlying FV - incompressible fluid solver

$$\sigma'_{ij} = -p^G \delta_{ij} + \tau'_{ij} \, . \tag{4.33}$$

Therefore τ'_{ij} is determined either from the deviatoric part of the incompressible Neo-Hooke equation (5.1) or from the rigid-plastic approach using the incompressible Newtonian fluid viscous stress (3.4) with variable viscosity (3.13). Inserting Eqns. (4.32) and (4.33) in the granular momentum equations (4.15) results in the full granular momentum equations

$$\begin{gathered}\int_V (1-n)\rho^G \frac{\partial(v_i^S)}{\partial t} dV + \int_V (1-n)\rho^G v_j^S \frac{\partial\left(v_i^S\right)}{\partial x_j} dV = \\ \int_V (1-n)\rho^G g_i dV - \int_V \frac{\partial p^G}{\partial x_i} dV + \int_V \frac{\partial \tau'_{ij}}{\partial x_j} dV - \int_V \frac{\partial (1-n) p^F}{\partial x_i} dV - \int_V \hat{f}_i^R dV\end{gathered} \tag{4.34}$$

or in the $\hat{v}_i^S$ - based formulation

$$\begin{gathered}\int_V \left[\frac{\partial(\rho^G \hat{v}_i^S)}{\partial t} + \frac{\partial\left(\frac{\rho^G \hat{v}_i^S \hat{v}_j^S}{(1-n)}\right)}{\partial x_j} \right] dV = \\ \int_V (1-n)\rho^G g_i dV - \int_V \frac{\partial p^G}{\partial x_i} dV + \int_V \frac{\partial \tau'_{ij}}{\partial x_j} dV - \int_V \frac{\partial (1-n) p^F}{\partial x_i} dV - \int_V f_i^R dV\ .\end{gathered} \tag{4.35}$$

Introducing the Bingham fluid approach for the rigid perfectly-plastic granular material with the variable viscosity μ^S from Eqn. (3.13) and Eqn. (3.22) for the tensor τ'_{ij} leads to

$$\begin{gathered}\int_V \left[\frac{\partial(\rho^G \hat{v}_i^S)}{\partial t} + \frac{\partial\left(\frac{\rho^G \hat{v}_i^S \hat{v}_j^S}{(1-n)}\right)}{\partial x_j} \right] dV - \int_V \frac{\partial}{\partial x_i} \left(\mu^G \left(\frac{\partial \frac{\hat{v}_i^S}{(1-n)}}{\partial x_j} + \frac{\partial \frac{\hat{v}_j^S}{(1-n)}}{\partial x_i} \right) \right) dV = \\ \int_V (1-n)\rho^G g_i dV - \int_V \frac{\partial p^G}{\partial x_i} dV - \int_V \frac{\partial (1-n) p^F}{\partial x_i} dV - \int_V f_i^R dV\ .\end{gathered} \tag{4.36}$$

4.1.5 Eulerian Displacement Equation and Euler-Almansi Strain

An Eulerian displacement equation is solved to calculate the strain in the granular material. The Eulerian displacement u_i is transported with the velocity of the soil skeleton v_i^{S*} which is defined by

$$v_i^{S*} = c_S v_i^S \tag{4.37}$$

leading to the displacement equation in differential form as

$$\frac{\partial u_i}{\partial t} + \frac{\partial v_j^{S*} u_i}{\partial x_j} = v_i^{S*}\ . \tag{4.38}$$

The norm of the Eulerian-Almansi strain (3.23) is applied to compare the results from the present method to other simulation results in the verification case. The Euler-Almansi strain is calculated by the inverse of the Eulerian deformation gradient G_{ij} which is explained in more detail in chapter 3 Sec. 3.1.5.

4.1.6 Reduced Momentum Equations

As described in Sec. 2.4 and in Düsterhöft-Wriggers et al. [28], a simplification of the momentum equations for free surface flows through a rigid porous medium is acceptable for porous Reynolds numbers $Re_P \leq 5000$ which roughly translates to grain diameters below 1 cm. For the application of granular cargo on vessels, the mean grain diameters of the granular material are under 2 mm (cf. Sec. 6.2). Therefore the simplified approach introduced in Sec. 2.2.3 for the fluid phases is applicable and is used in the present method for the coupled model. In line with Eqn. (2.55), the simplified momentum equations of the fluid phase gets

$$\begin{gathered}\int_V \left[\frac{\partial \left(\rho^F \hat{v}_i^F \right)}{\partial t} + \frac{\partial \left(\rho^F \hat{v}_i^F \hat{v}_j^F \right)}{\partial x_j} \right] dV = \\ \int_V \left[\rho^F g_i - \frac{\partial p^F}{\partial x_i} + \frac{\partial}{\partial x_i} \left(\mu^F \left(\frac{\partial \hat{v}_i^F}{\partial x_j} + \frac{\partial \hat{v}_j^F}{\partial x_i} \right) \right) + \frac{f_i^R}{n} \right] dV \,. \end{gathered} \tag{4.39}$$

The momentum equations of the granular phase (4.36) differ from the momentum equations of the fluid phase (4.17) by the proportionality to the porosity coefficient. Therefore the simplification of the left side of Eqn. (4.36) to

$$\begin{gathered}\int_V \left[\frac{\partial \left(\rho^G \hat{v}_i^S \right)}{\partial t} + \frac{\partial \left(\rho^G \hat{v}_i^S \hat{v}_j^S \right)}{\partial x_j} \right] dV - \int_V \frac{\partial}{\partial x_i} \left(\mu^{G*} \left(\frac{\partial \hat{v}_i^S}{\partial x_j} + \frac{\partial \hat{v}_j^S}{\partial x_i} \right) \right) dV = \\ \int_V (1-n) \rho^G g_i dV - \int_V \frac{\partial p^G}{\partial x_i} dV - \int_V \frac{\partial (1-n) p^F}{\partial x_i} dV - \int_V f_i^R dV \end{gathered} \tag{4.40}$$

is less prominent than in the fluid momentum equations. The simplification in the viscous term is counteracted for spatially constant porosities by calculating the plastic viscosity directly from the Darcy velocity $\hat{v}_i^S$

$$\mu^{S*} = \frac{\tau_y}{\sqrt{\frac{1}{2} \left(\frac{\partial \hat{v}_i^S}{\partial x_j} + \frac{\partial \hat{v}_j^S}{\partial x_i} \right) \left(\frac{\partial \hat{v}_i^S}{\partial x_j} + \frac{\partial \hat{v}_j^S}{\partial x_i} \right)}} \,, \tag{4.41}$$

$$\mu^{G*} = c_S \mu^{S*} + (1 - c_S) \mu^A \tag{4.42}$$

which is equal to the viscosity μ^G divided by the porosity coefficient ($\mu^{G*} = \mu^G/(1-n)$) inside the granular material. Therefore, only the convective term is reduced in the momentum equations of the granular phase 4.40. This simplification is applied in the present coupled model to prevent numerical instabilities due to the division by $1-n$ equal to zero outside the granular dam.

4.2 Finite Volume Method

Applying the same spatial discretization techniques as in the last two chapters or, more precisely, combining the FV model approximations of Secs. 2.2 and 3.2, leads to an algorithm which is displayed in Fig. 4.3. Here the equation system given in 4.2.1 is solved sequentially, where the core routines of the FV solver (pressure correction algorithm, momentum equations, and update of properties) are solved for both two-phase flows by setting pointers to the variables of each of the flows before solving them. After the loop of solving the two momentum and continuity equations, the air mixture fraction equation and soil mixture fraction equation are solved. The porosity is updated in each iteration depending on the soil mixture fraction, and then the displacement equation is solved to obtain the strain values.

The Euler-Almansi strain tensor and its norm are calculated from the Eulerian displacement by Eqn. (3.23) for every time step in a user coding interface. In Fig. 4.3, the superscripts n and m denote the iterative procedure's time step and iteration index, respectively. The FV discretized governing equations for the coupled free surface flow through rigid-perfectly plastic granular porous material are detailed in the following sections.

4.2.1 Discretized Reduced Equation System for ($\hat{v}_i^F$, p^F, $\hat{v}_i^S$, p^G) - Formulation

The employed Eqns. (4.11), (4.12), (4.39), (4.40), (4.19), (4.23), (4.24) and (4.38) have already been outlined in the last sections. Again, the theorem of Gauss is applied to change the volume integrals of the convective terms into a flux-based formulation. The full equation system solved in the coupled model is given by

$$\oint_A \hat{v}_i^F dA_i = 0 \tag{4.43}$$

$$\oint_A \hat{v}_i^S dA_i = 0 \tag{4.44}$$

$$\begin{aligned}\int_V \frac{\partial}{\partial t}\left(\rho^F \hat{v}_i^F\right) dV + \oint_A \left(\rho^F \hat{v}_i^F \hat{v}_j^F\right) dA_j - \oint_A \mu^F \left(\frac{\partial \hat{v}_i^F}{\partial x_j} + \frac{\partial \hat{v}_j^F}{\partial x_i}\right) dA_j = \\ - \oint_A p^F dA_i + \int_V \rho^F g_i dV \qquad (4.45) \\ - \int_V \rho^F \frac{\hat{v}_i^F}{n} \left(\tilde{A} + \tilde{B} \left\| \hat{v}^F - \frac{n\hat{v}^S}{1-n} \right\|_2\right) dV + \int_V \rho^F \frac{\hat{v}_i^S}{1-n} \left(\tilde{A} + \tilde{B} \left\| \hat{v}^F - \frac{n\hat{v}^S}{1-n} \right\|_2\right) dV\end{aligned}$$

$$\begin{aligned}\int_V \frac{\partial}{\partial t}\left(\rho^G \hat{v}_i^S\right) dV + \oint_A \left(\rho^G \hat{v}_i^S \hat{v}_j^S\right) dA_j - \oint_A \mu^{G*} \left(\frac{\partial \hat{v}_i^S}{\partial x_j} + \frac{\partial \hat{v}_j^S}{\partial x_i}\right) dA_j = \\ - \oint_A (1-n) p^F dA_i - \oint_A p^G dA_i + \int_V (1-n) \rho^S g_i dV \qquad (4.46) \\ - \int_V \rho^F \frac{n\hat{v}_i^S}{(1-n)} \left(\tilde{A} + \tilde{B} \left\| \hat{v}^F - \frac{n\hat{v}^S}{1-n} \right\|_2\right) dV + \int_V \rho^F \hat{v}_i^F \left(\tilde{A} + \tilde{B} \left\| \hat{v}^F - \frac{n\hat{v}^S}{1-n} \right\|_2\right) dV\end{aligned}$$

$$\int_V \frac{\partial c_A}{\partial t} dV + \oint_A \frac{c_A \hat{v}_i^F}{n} dA_i = 0 \tag{4.47}$$

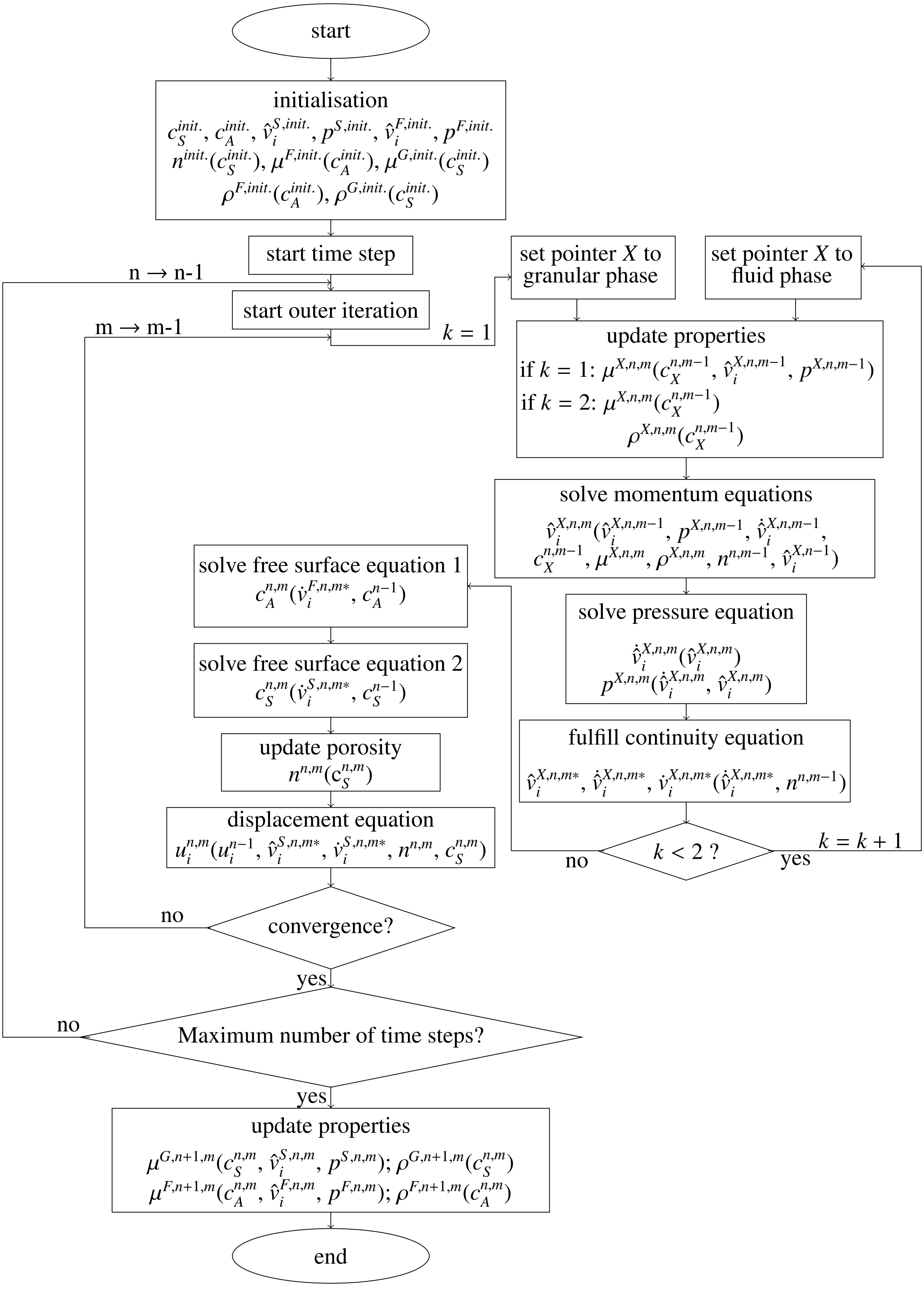

Figure 4.3: Algorithm of the coupled model of water flow through a deformable porous rigid perfectly-plastic material.

$$\int_V \frac{\partial c_S}{\partial t} dV + \oint_A \frac{c_S \hat{v}_i^S}{1-n} dA_i = 0 \tag{4.48}$$

$$\int_V \frac{\partial u_i}{\partial t} dV + \oint_A c_S \frac{\hat{v}_j^S}{(1-n)} u_i dA_j = \int_V c_S \frac{\hat{v}_i^S}{(1-n)} dV \ . \tag{4.49}$$

Several terms with $(1-n)$ in the denominator exist in this equation system. Since these terms become singular outside the porous soil skeleton, the detailed treatment of each will be discussed in the following discrete equations.

Discretized Momentum Equations

It is important that the terms including a division by $(1-n)$ in the momentum equations of the coupled model are not divided by this term in the complete computational domain. Instead only where porous material is present, e.g., $c_S = 1$, the terms are included leading from Eqn. (4.45) to

$$\begin{aligned}
\hat{v}_{i,P}^{F,n,m} & \left[\Delta V_P \rho_P^F \left(\frac{1}{\Delta t} + \frac{\tilde{A}}{n} + \frac{\tilde{B}}{n} \left\| \hat{v}^F - \frac{c_S \, n \hat{v}^S}{1-n} \right\|_2^{n,m-1} \right)_P + \sum_{f(\Delta V_P)} A_{NB}^{\hat{v}_i^F} \right] \\
& - \sum_{f(\Delta V_P)} \underbrace{\left[\left(max\left[-\dot{\hat{m}}^{F,n,m-1}, 0 \right] \right)_f + \left(\frac{\mu^F A}{d} \right)_f \right]}_{A_{NB}^{\hat{v}_i^F}} \hat{v}_{i,NB}^{F,n,m} = \\
& \qquad - \sum_{f(\Delta V_P)} \left(p_f^{F,n,m-1} A_i \right) \\
+ \rho_P^F \Delta V_P & \left[g_i + \frac{\hat{v}_i^{F,n-1}}{\Delta t} + \frac{c_S^{n,m-1} \, \hat{v}_i^{S,n,m-1}}{1-n} \left(\tilde{A} + \tilde{B} \left\| \hat{v}^{F,n,m-1} - \frac{n \hat{v}^{S,n,m-1}}{1-n} \right\|_2 \right) \right]_P + S_{\hat{v}_i^F}
\end{aligned} \tag{4.50}$$

where $\dot{\hat{m}}_f^F = (\rho^F \hat{v}_i^F A_i)_f$ refers to the porous mass flux of the fluid phases (air and water) across a face. Parts of the porous resistance terms are implemented implicitly. Where explicit terms cannot be prevented, a direct coupling to the soil skeleton velocity is implemented using the soil skeleton's velocity from the previous iteration in each iteration. The source term $S_{\hat{v}_i^F}$ includes explicit terms arising from different deferred correction contributions, e.g., higher-order convection, non-orthogonality, and interpolation corrections further deployed in Appendix A. The same discretization principles are now applied to the momentum equations of the granular/air phases (4.46), leading to

$$\begin{aligned}\hat{v}^{S,n,m}_{i,P}&\left[\Delta V_P\left(\frac{\rho^G}{\Delta t}+\frac{c_S^{n,m-1}\,\rho^F\,n\tilde{A}}{(1-n)}+\frac{c_S^{n,m-1}\,\rho^F\,n\tilde{B}}{(1-n)}\left\|\hat{v}^F-\frac{n\hat{v}^S}{1-n}\right\|_2^{n,m-1}\right)_P+\sum_{f(\Delta V_P)}A^{\hat{v}_i^S}_{NB}\right]\\&-\sum_{f(\Delta V_P)}\underbrace{\left[\left(max\left[-\dot{\hat{m}}^{S,n,m-1},0\right]\right)_f+\left(\frac{\mu^{G*}A}{d}\right)_f\right]}_{A^{\hat{v}_i^S}_{NB}}\hat{v}^{S,n,m}_{i,NB}=\\-\sum_{f(\Delta V_P)}&\left(p_f^{G,n,m-1}A_i\right)-(1-n)_P\sum_{f(\Delta V_P)}\left(p_f^{F,n,m-1}A_i\right)+\rho^G_P\Delta V_P\left[(1-n)g_i+\frac{\hat{v}_i^{S,n-1}}{\Delta t}\right]_P\\&+\rho^F_P\Delta V_P\left[\hat{v}_i^{F,n,m-1}\left(\tilde{A}+\tilde{B}\left\|\hat{v}^{F,n,m-1}-\frac{c_S^{n,m-1}\,n\hat{v}^{S,n,m-1}}{1-n}\right\|_2\right)\right]_P+S_{\hat{v}_i^S}\ .\end{aligned}\tag{4.51}$$

Here $\dot{\hat{m}}^S_f=(\rho^G\hat{v}^S_iA_i)_f$ is the porous mass flux of the granular and second air phase across a face.

Discretized Continuity Equations

The full pressure correction scheme for the coupled model will not be presented here since it coincides with the equations described in Sec. 2.2.1. Therefore only the first stage equation for the pressure corrections $p^{F,'}$ and $p^{G,'}$ following from Eqns. (4.43) and (4.44) are given as

$$\sum_{f(\Delta V_P)}\hat{v}^{F,m}_{f,i}A_{f,i}-\sum_{f(\Delta V_P)}\left(\frac{A_id_i}{A_P^{\hat{v}_i^F}}\right)_f\left(\frac{\partial p^{F,'}}{\partial x_i}n_i\right)_fA_f=0\tag{4.52}$$

$$\sum_{f(\Delta V_P)}\hat{v}^{S,m}_{f,i}A_{f,i}-\sum_{f(\Delta V_P)}\left(\frac{A_id_i}{A_P^{\hat{v}_i^S}}\right)_f\left(\frac{\partial p^{G,'}}{\partial x_i}n_i\right)_fA_f=0\ .\tag{4.53}$$

Velocity-, flux-, and pressure correction are calculated as in Sec. 2.2.1 for both two-phase flows.

Discretized Mixture Equations

The air mixture equation (4.47) is exactly discretized as in Eqn. (2.46) but is stated here for completeness

$$c^{n,m}_{A,P}\left[\frac{\Delta V_P}{\Delta t}+\sum_{f(\Delta V_P)}A^c_{A,NB}\right]-\sum_{f(\Delta V_P)}\underbrace{\left(max\left[-\frac{(\dot{\hat{m}}^F/\rho^F)^{n,m-1}}{n},0\right]\right)_f}_{A^c_{A,NB}}c^{n,m}_{A,NB}=\frac{\Delta V_P}{\Delta t}c^{n-1}_{A,P}+S_{c_A}\ .\tag{4.54}$$

For the soil mixture equation (4.48) the concentration c_S is transported with the soil velocity flux $\dot{v}^{S*}$

$$c^{n,m}_{S,P}\left[\frac{\Delta V_P}{\Delta t}+\sum_{f(\Delta V_P)}A^c_{S,NB}\right]-\sum_{f(\Delta V_P)}\underbrace{\left(max\left[-\dot{v}^{S*,n,m-1},0\right]\right)_f}_{A^c_{S,NB}}c^{n,m}_{S,NB}=\frac{\Delta V_P}{\Delta t}c^{n-1}_{S,P}+S_{c_S}\ ,\tag{4.55}$$

where the direct translation of Eqn. (4.48) leads to

$$\dot{v}^{S*} = \frac{(\dot{m}^S/\rho^S)}{1 - n + \epsilon_{small}} \tag{4.56}$$

with ϵ_{small} being a small positive constant preventing singularities. This approach is used in the verification and application cases in this work. An improvement by using a continuous formulation over the soil/air boundary could be made with

$$\dot{v}^{S*} = \frac{(\dot{m}^S/\rho^S)}{c_S(1 - n) + (1 - c_S)} \, . \tag{4.57}$$

For both mixture equations, the compressive HRIC scheme is applied for the convective term, explicitly included in the source terms S_{c_A} and S_{c_S}.

Discretized Displacement Equation

For the calculation of the Euler-Almansi strain, the Eulerian displacements are needed. The displacement is calculated via the soil skeleton velocity v^{S**}, which is obtained by multiplying the soil mixture fraction with the soil velocity field. Applying the same discretization techniques as above, Eqn. (4.49) gets

$$\begin{aligned} u_{i,P}^{n,m}\left[\frac{\Delta V_P}{\Delta t} + \sum_{f(\Delta V_P)} A_{NB}^u\right] - \sum_{f(\Delta V_P)} \underbrace{\left(max\left[-\dot{v}^{S**,n,m-1}, 0\right]\right)_f}_{A_{NB}^u} u_{i,NB}^{n,m} = \\ \frac{\Delta V_P}{\Delta t} u_{i,P}^{n-1} + v_{i,P}^{S**,n,m-1} \Delta V_P + S_u \, , \end{aligned} \tag{4.58}$$

where S_u again includes explicit terms which arise from different deferred correction contributions, e.g., higher-order convection, non-orthogonality, and interpolation corrections. In the verification and application cases, a simple flux blending scheme featuring 50% is applied. Using a multiplication with the soil mixture fraction and $\dot{v}^{S*}$ from (4.56) leads to divergence of the cases. Therefore a simplification of using the granular part of the Darcy velocity is applied in this work, underestimating displacements and Eulerian strains. The simplification could be circumvented by applying Eqn. (4.57) to the displacement equation.

4.3 Verification and Validation

To validate the presented coupling algorithm, a seepage flow-induced failure of a granular dam introduced by Bui et al. [10] is considered. This section compares the coupling of rigid, perfectly-plastic porous material exhibiting large movements with an air/water two-phase flow determining the flow inside the porous voids against a two-phase elasto-plastic SPH method, cf. Bui et al. [10].

An implicit Euler time integration is applied for the presented FV, VoF results in this section. The convective terms in the momentum equations are solved with a flux-blending scheme with interpolation factor 0.7 and the convective terms in the mixture equations are discretized with the compressive HRIC scheme.

4.3.1 Seepage Flow-Induced Failure of Granular Dam

In Bui et al. [10], numerical and experimental results for the seepage flow-induced failure of a granular dam are published. Water flows through an embankment consisting of Masa soil (granite typically found in Japan) and leads to the failure of the embankment. The embankment is 0.4 m high and 0.4 m wide at the top with slopes of 45°. The initial geometry of the embankment is displayed in Fig. 4.4. Initial material properties for the Masa soil are given by Bui et al. [10] as: initial water content 5%, Young's modulus $E = 3$ MPa, Poisson ratio $\upsilon = 0.3$, angle of repose $\phi = 31.2°$, initial cohesion $C_{max} = 0.55$ kPa, particle density $\rho_S = 2.6$ g/cm^3, initial porosity $n = 0.4$ and initial permeability k_0 of $1.1 \cdot 10^{-4}$ m/s. Material properties for air are set to $\mu^A = 1.0 \cdot 10^{-5}$ Pa s and $\rho^A = 1.2$ kg/m^3 and the properties of water are taken to be $\mu^W = 1.0 \cdot 10^{-3}$ Pa s and $\rho^W = 1000.0$ kg/m^3.

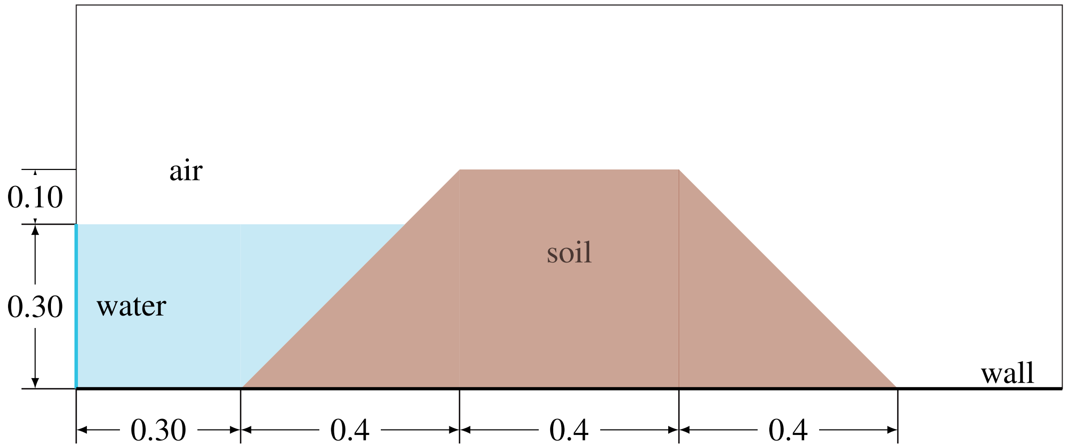

Figure 4.4: 2D seepage flow-induced soil collapse: Initial geometry of 2D seepage flow-induced soil collapse test case with dimensions given in meter.

Bui et al. [10] model the saturation depending cohesion C of the Masa soil with a linear relationship between the saturated cohesion C_{sat} and the maximum cohesion C_{max} depending on the saturation level

$$C = C_{sat} + (C_{max} - C_{sat})(1 - c_A) . \tag{4.59}$$

In the present model, the saturation level is replaced by the reciprocal air mixture fraction $1-c_A$. For the Masa soil, the saturate cohesion C_{sat} is assumed to be 0.01 kPa, and the maximum cohesion C_{max} is set to 0.55 kPa with an initial water content of 5%.

For the resistance force, Bui et al. [10] apply the Darcy model ($\tilde{B} = 0$, $\tilde{C} = 0$) due to the low permeability of the Masa soil together with a porosity gradient dependent term, which is included in the momentum equations in the present approach. Therefore the constant $\tilde{A}$ of the resistance force f_i^R gets

$$\tilde{A} = \frac{|g_i|\, n^2}{k_0} , \tag{4.60}$$

where g_i is the gravitational acceleration set to 9.81 m/s^2. The stress inside the dam is initialized by gravity loading. Photographic results of the experiments from Bui et al. [10] are displayed in Fig. 4.5. The numerical results from Bui et al. [10] employ a different discretization method, a different constitutive model for the granular material, and a different approach to the multiphase problem. In Bui et al. [10], the SPH method is applied for both the water flow and the granular continuum mechanics. The air phase is not taken into account explicitly.

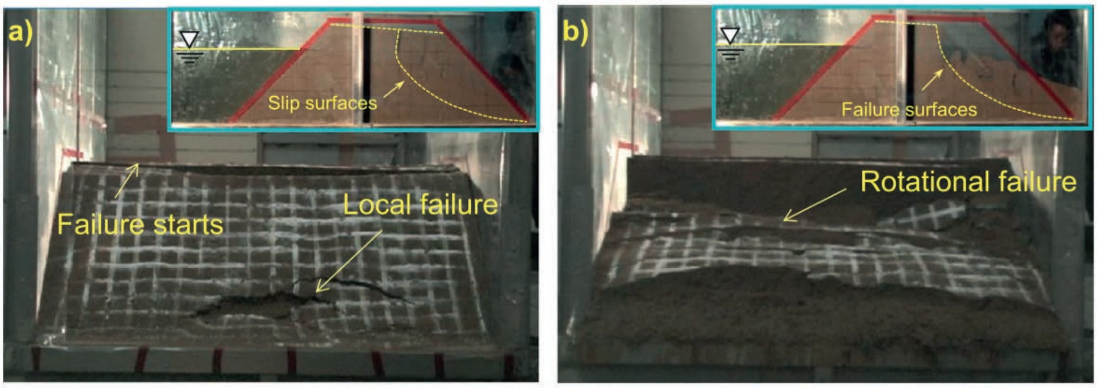

Figure 4.5: 2D seepage flow-induced soil collapse: Photographic determination of slip surfaces and failure surfaces from 3D experimental results by Bui et al. [10].

A compressible elasto-plastic constitutive equation with the Drucker-Prager yield criterion is applied for the granular material in Bui et al. [10] which is explained in detail in Bui et al. [9]. Due to the current approach employing an incompressible perfectly-plastic constitutive equation, albeit with the same yield criterion (Eqn. (3.13)), differences in the behavior of the granular dam are expected.

The 2D computational domain used for the seepage flow-induced failure of a granular dam is a rectangular domain with length $L = 2.0$ m and height 0.7 m and an unstructured mesh with predominantly rectangular grid cells is utilized. The mesh exhibits a grid spacing of $\Delta x_1 = \Delta x_2 = L/500$ where the free surface of the water and the free surface of granular material are present and below these surfaces. Towards the domain's top boundary, the mesh size stepwise gets wider up to a size of $\Delta x_1 = \Delta x_2 = L/80$. The time step is chosen depending on the initial permeability of the granular dam.

The initial conditions for the test case depend on the dam's permeability and are given in the results section. At the left boundary of the domain, a Dirichlet boundary condition for the velocities and the mixture fractions is applied with the velocity in the air phase being set to zero at each time and the velocity in the water phase being set to a value consistent with the permeability of the dam. At the top of the domain, the pressure reference value is set to zero as a Dirichlet value, and the bottom boundary is a wall boundary condition as described in Appendix A.5. At the right boundary of the domain, a second-order zero-gradient boundary condition is applied for all variables.

Alterations of Settings for Simulations with Current Method

Some adjustments to the initial settings are employed to obtain coinciding results with the present method and save computational power. Since the two-phase flow through porous material has been validated extensively in Sec. 2.3, the initial water surface of the seepage flow through the porous granular dam is set to be a linear extension of the intersection of the water phase with the granular dam and the bottom right corner of the granular dam to save computing time.

Applying a minimum saturated cohesion of $C_{sat} = 0.01$ kPa leads to the sliding of the dam at the water inlet side in the present method. This is due to the rigid-perfectly plastic model formulation via the variable viscosity, where the maximum viscosity depends on the maximum yield strength. The maximum viscosity needed to obtain a rigid behavior of the dam is significantly smaller where water flows through the dam (the air mixture fraction being zero) than in the dry granular material when using Eqn. (4.59). The forces from the water movement and pressure on the dam are too small to counteract the creeping for $C_{sat} = 0.01$ kPa. The present method could be enhanced by introducing an elasto-plastic constitutive model (cf. Appendix F.2). In the following cases, the saturation cohesion C_{sat} is set to be 0.1 kPa to prevent creeping on the water inlet side of the granular dam.

Also, applying the given initial permeability of $1.1 \cdot 10^{-4}$ m/s leads to the creeping of the granular material on the inlet side. Using this permeability, the water velocities inside the porous material become very small and, therefore, do not act as stabilizing forces on the dam. To avoid this drawback of the rigid perfectly-plastic material model and speed up the computation time (the larger the permeability, the higher the appropriate simulation time step), two simulation results

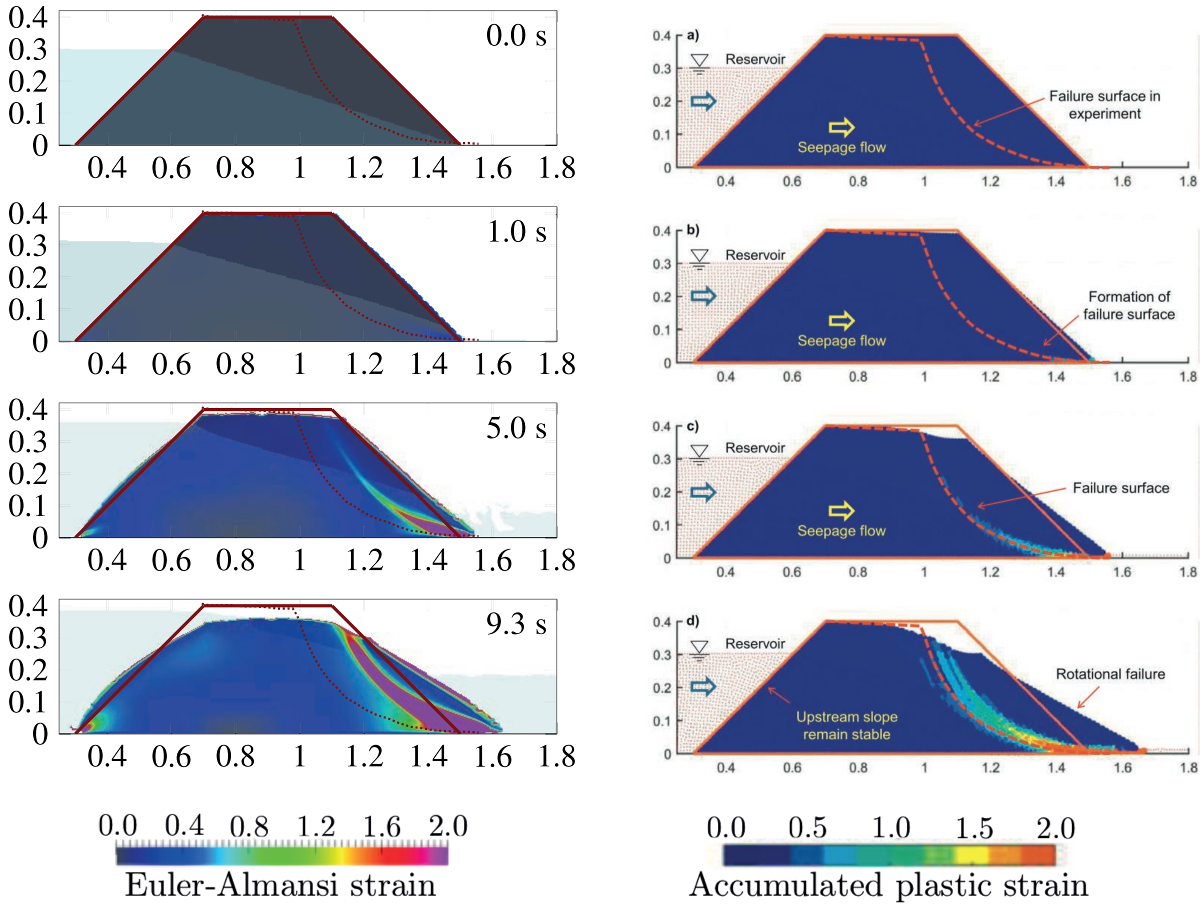

Figure 4.6: 2D seepage flow-induced soil collapse: Visual comparison of Euler-Almansi strain norm and free surface elevations at four time steps obtained by the present VoF method (permeability $1.1 \cdot 10^{-1}$ m/s thresholded at $c_S = 0.5$ and $c_A = 0.5$; left) with SPH results of Bui et al. [10] (right).

are presented with a permeability of $1.1 \cdot 10^{-2}$ m/s and $1.1 \cdot 10^{-1}$ m/s.

Results for Present Coupled Method with Permeability of $1.1 \cdot 10^{-1}$ m/s

A time step of $1 \cdot 10^{-4}$ is used for the current settings with a permeability of $1.1 \cdot 10^{-1}$ m/s and the Dirichlet boundary condition for the velocities is set to $\hat{v}_1^F = v_1^F = 0.0825$ m/s in the water phase for the 0.3 m high water column at the inflow boundary in the water phase. The fluid Darcy velocity component $\hat{v}_1^F$ is initialized with 0.055 m/s in the water phase outside the porous material and with 0.1375 m/s in the water phase inside the porous material. The Darcy velocity component $\hat{v}_1^S$ and the second components of both Darcy velocity parts and the fluid Darcy velocity part in the air phase are initialized with zero velocity.

A factor m_c of 500 is applied for the variable viscosity formulation, and the arctangent interpolation is applied with constants $N = 1$ and $M = 0$. In Fig. 4.6, the results of the present method are visually compared against the numerical results of Bui et al. [10]. Notice that the predicted failure line in the result of Bui et al. [10] does not coincide with the shape of the experimental failure line. Nevertheless, the displayed material is confined to a comparison of numerical results. Also, it shall be remarked that in Bui et al. [10], no time stamps are given for the presented results. The results of the present method are displayed at 0.0 s, 1.0 s, 5.0 s, and 9.3 s.

Due to the high permeability, the water/air-interface inside the granular dam rises higher than in the SPH predictions. The applied boundary condition on the right boundary of the FV simulations yields insufficient drainage and a progressive filling of the domain with water. Nevertheless, the movement of the right side of the dam coincides with the reference results. At the third time snapshot, the Eulerian-Almansi strain norm forms a sliding plane with similar values as in the SPH simulation, but displaced further to the right. This results from the higher water/air surface leading to more material with a lower cohesion on the right side of the dam.

The effect of high strains at the edge of the granular material resulting from the definition of v^{S**} in the displacement equation has already been explained in chapter 3. Further, it can be observed that the height of the incompressible rigid perfectly-plastic granular dam shrinks over time. High strain values are observed in the bottom left corner of the dam, which are not present in the reference compressible elasto-plastic model results. An elasto-plastic model is thought to significantly enhance the behavior of the left side of the dam by introducing elastic stresses to the momentum equations. It shall be remarked that in all validation cases considered in chapter 3, the granular material was experimentally and in all associated numerical results supported by a wall on one side, which is not the case in the present verification case. Therefore, the missing elastic stresses play a higher role in the present study.

Results for Present Coupled Method with Permeability of $1.1 \cdot 10^{-2}$ m/s

To confirm that the height of the free surface inside the granular material induces a shifted sliding plane, the case is also simulated with a permeability of $1.1 \cdot 10^{-2}$ m/s on the same mesh. Since the water flow is significantly slower, a time step of $5 \cdot 10^{-5}$ is applied. A linear interpolation of all material properties is used together with a factor m_c of 500 for the ideally-plastic viscosity approach. The velocity at the inlet is set to 0.009 m/s, and the initial velocity is set to 0.009 m/s outside the porous material and 0.0225 m/s inside. All other settings remain as in the simulation with higher permeability, and the results are displayed in Fig. 4.7, plotted at times 0.0 s, 0.3 s, 0.8 s and 5.8 s. Due to the lower permeability value, the dam's failure occurs at earlier times, and therefore, results are plotted at other time steps than for higher permeability. The reference results by Bui et al. [10] do not include time information. An improved agreement

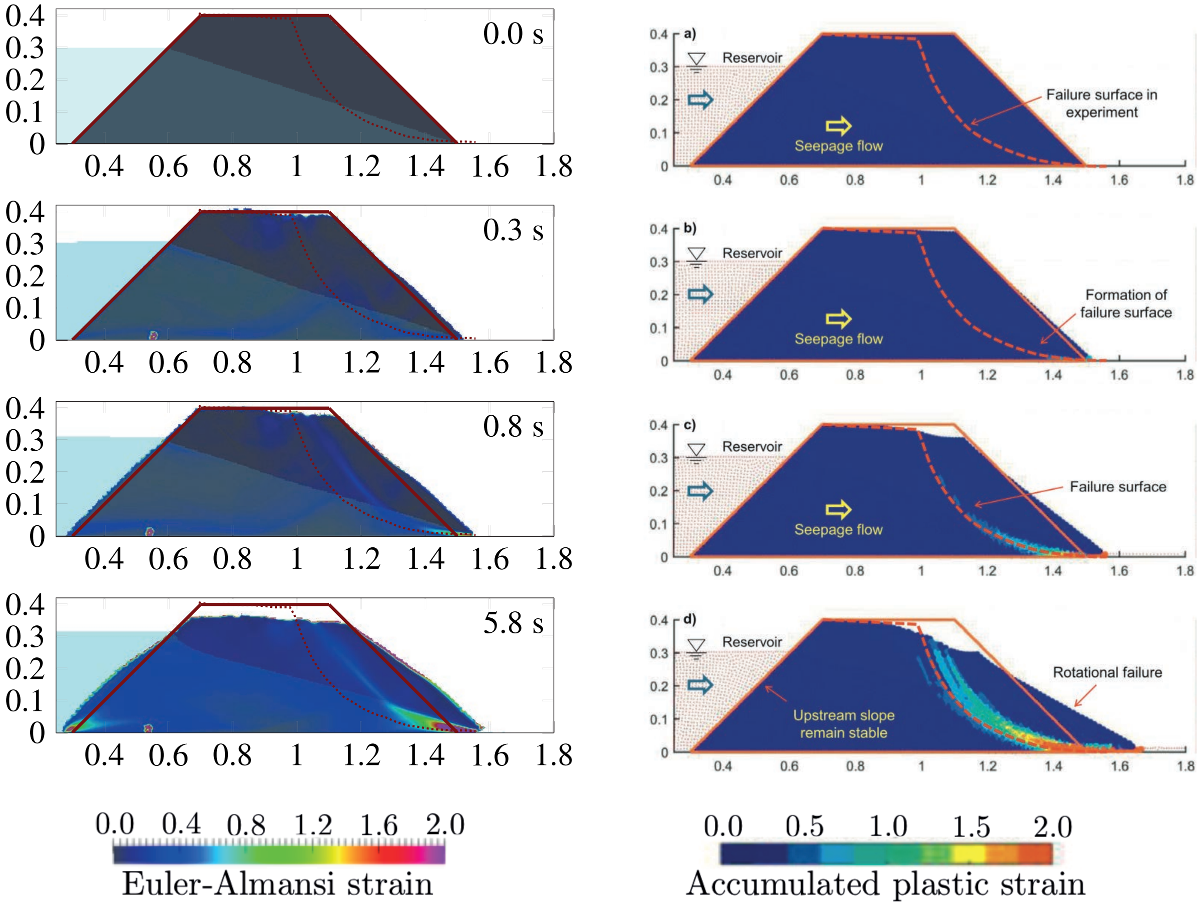

Figure 4.7: 2D seepage flow-induced soil collapse: Visual comparison of Euler-Almansi strain norm and free surface elevations at four time steps obtained by the present VoF method (permeability $1.1 \cdot 10^{-2}$ m/s thresholded at $c_S = 0.5$ and $c_A = 0.5$; left) with SPH results from Bui et al. [10] (right).

with the reference results can be observed for the lower permeability. Due to the lower permeability, the water surface only penetrates the right granular boundary in the last snapshot. At the beginning of the simulations, a high soil velocity value inside the dam leads to an increased strain spot. The dam shape in the third snapshot highly agrees with the reference results. It shall be remarked that the behavior of the reference results differs from the experimental results displayed in Fig. 4.5. The crack that can be observed at the top of the dam in the experimental results is not present in either the numerical reference results or the presented FV-VoF results, cf. Fig 4.7. The sliding plane in the third snapshot is still positioned further right in comparison with the reference data. At the fourth time step of the numerical reference results, multiple sliding planes combining to an area of higher accumulated strain also exist to the right of the labeled sliding plane. Therefore the present results are deemed sufficiently verified to be used in the application cases while remarking that the accuracy of the present method can be improved. As already mentioned, an elasto-plastic constitutive equation is thought to improve the model, and a monolithic incompressible elastic model will be introduced in the next chapter.

Chapter 5

Monolithic Incompressible Elastic Model

An elasto-plastic model to depict the behavior of the granular cargo is sought to enhance the quality of the results. Especially if liquefaction, as defined in geotechnical literature, shall be modeled, more complex phenomena and the related constitutive equations, including, e.g., kinematic hardening, do have to be considered. Therefore a monolithic elastic model is implemented in the FV fluid solver as a first step towards more complex material models.

The novelty of this work is implementing a fully Eulerian Fluid-Structure Interaction (FSI) approach in a FVM and its combination with a pressure correction scheme. Furthermore, the incompressible Neo-Hookean model is used to calculate the forces and stresses acting in the granular cargo. Several validation and verification cases are presented.

5.1 Mathematical Model

Several authors have explored monolithic FSI in Eulerian coordinates using a VoF or level-set tracking technique. Dunne [27] and Richter et al. [104] introduced this technique using FEM with the level-set method. Sugiyama et al. [110] modified the approach by combining the Finite Difference method (FDM) and the VoF method.

In the dissertation of Feghali [34], the approach of Sugiyama is translated to FEM, and the level-set method is used. Further work on Eulerian FSI can be found in Cottet et al. [14], He et al. [44], Hoogstraten et al. [49], Ii et al. [51], Laadhari et al. [68], Liu et al. [77], Okazawa et al. [94], Richter et al. [102], Richter et al. [103], and Mosher et al. [105] among others.

In this work, the original method of Dunne [27] and Richter et al. [104] is combined with the VoF approach that is used in the majority of multiphase flow solvers. The governing equations are discretized with the FV method, where the algorithm of the fluid solver is only slightly modified. A pressure correction scheme is used to fulfill the continuity equation. In this section, the mathematical formulation of the problem is derived in the differential form.

5.1.1 Governing Equations for Eulerian Fluid-Structure Interaction

The general Eulerian momentum equations (3.1) for incompressible materials as derived in chapter 2 and given in chapter 3 are used for the FSI formulation. An incompressible neo-Hookean constitutive equation is chosen due to its ability to support the decomposition of stresses into a hydrostatic and deviatoric part. The stress tensor σ_{ij}^S for an incompressible neo-Hookean material reads

$$\sigma_{ij}^S = -p\delta_{ij} + \eta_S(G_{ik}G_{jk} - \delta_{ij})\,, \tag{5.1}$$

where G_{ij} is the inverse of the deformation gradient F_{ij} expressed in index notation in Eqn. (3.31) in chapter 3, Sec. 3.1.5. The derivation of the Eulerian formulation of the deformation gradient tensor F_{ij} follows also from Sec. 3.1.5 in chapter 3. The multiplication of the inverse of the Eulerian deformation gradient tensor and the transpose of the inverse of the Eulerian deformation gradient tensor $G_{ik}G_{jk}$ provides the Cauchy-Green deformation tensor B_{ij}.
The behavior of the Neo-Hookean material is governed by the second Lamé constant η_S

$$\eta_S = \frac{E}{2(1+\upsilon)} \tag{5.2}$$

which consists of the Young's Modulus E and the Poisson's ratio υ. As explained in Sec. 3.1.5, the Eulerian deformation gradient F_{ij} depends on the displacement in Eulerian coordinates u_i, cf. Eqn. (3.28) and the Eulerian displacement can be calculated by the convective transport equation (3.33). Since the displacement is only needed for the calculation of the stress tensor σ_{ij} inside the Neo-Hookean material, the displacement equation can be transported by the velocity of the Neo-Hookean material v_i^S. Dunne et al. [27] suggest a harmonic continuation of the velocity of the Neo-Hookean material to the computational domain by introducing an elliptic relaxation equation on the solid velocity, that is, e.g., also found in Manceau et al. [82]. The velocity of the Neo-Hookean material v_i^S is therefore calculated by

$$c_S v_i^S - a_w \frac{\partial^2 v_i^S}{\partial x_j^2} = c_S v_i\,, \tag{5.3}$$

where a_w is a positive number of dimension [m^2] and c_S is the solid mixture fraction. From the validation cases, a good choice is found to be $a_w = const. = 0.001$ for meshes with $\Delta x \approx 0.01$ m. The momentum equations are solved for the incompressible fluid and the Neo-Hookean material by using the appropriate deviatoric stress tensor depending on the solid concentration c_S

$$\tau_{ij} = c_S\tau_{ij}^S + (1-c_S)\,\tau_{ij}^A\,, \tag{5.4}$$

where $(\cdot)^S$ denotes the deviatoric part of the neo-Hookean stress and $(\cdot)^A$ the deviatoric fluid stress tensor given in (3.4) applying a viscosity μ^A. The hydrostatic part is solved with the same pressure correction scheme (continuity equation) as applied in chapters 2 and 3, and the alterations made are explained in the upcoming approximation section. The mixture fraction equation (3.39) given in Sec. 3.2 is solved for the two-phase problem, and the properties are interpolated by Eqns. (3.36).

5.1.2 Relation of Continuity Equation and Deformation Gradient Tensor

The Jacobi determinant J is the determinant of the Lagrangian deformation gradient tensor, and the determinant of the Eulerian deformation gradient tensor is expressed as J^{-1}

$$J = det(\hat{F}_{ij}) \tag{5.5}$$

$$J^{-1} = det(F_{ij}) \; . \tag{5.6}$$

In order to fulfill the continuity equation, the initial mass $d\hat{m} = \rho_0 d\hat{V}$ has to be equal to the current mass $dm = \rho dV$

$$\rho dV = \rho_0 d\hat{V} \tag{5.7}$$

and the transformation from current to reference volume elements follows from the Jacobi determinant

$$\frac{dV}{d\hat{V}} = \frac{\rho_0}{\rho} = J \; . \tag{5.8}$$

For incompressible materials, the Jacobi determinant and the determinant of the Eulerian deformation gradient tensor must be equal to one to preserve a constant density. If the continuity equation is fulfilled, this condition should be fulfilled when using the Neo-Hookean material. A difficulty of the current implementation is that by introducing the elliptic relaxation, the velocity v_i^S is not divergence-free. Therefore, the determinant of the deformation gradient can deviate from unity, as will be discussed later.

5.1.3 Adapted Constitutive Equation for Artificial Diminishing of the Trace of the Deviatoric Stress

The trace of the Eulerian Cauchy Green tensor should be zero, as well as the trace of the deviatoric stress tensor. To ensure a traceless property one third of the trace is subtracted from the Cauchy Green tensor inside the constitutive equation, viz.

$$\sigma_{ij} = -p\delta_{ij} + \eta_S \left(G_{ik}G_{jk} - \frac{1}{3}\,\mathrm{tr}\left(G_{mk}G_{nk}\right)\delta_{ij} - \delta_{ij} \right) \; . \tag{5.9}$$

5.2 Finite Volume Method

The algorithm used for the FSI simulations with an elastic material is displayed in Fig. 5.1. It is observed that the adequate ordering of the equation sequence is essential to obtain correct results. Especially the displacement equation has to be solved before the pressure equation when the elliptic relaxation of the solid velocity is conducted at the end of the algorithm. Subsequently, the solution of the pressure equation fulfills the continuity condition, and the fluxes are updated. To transport the displacement with fluxes of the same iteration $m-1$ as the momentum equations, the displacement equation has to be solved prior to the pressure equation. Since the viscosity is set to zero or a negligibly small value for the Neo-Hookean material, the wall shear does not affect the momentum equations and is not suitable for a boundary condition. Therefore, a new (Dirichlet) condition has to be formulated for the Neo-Hookean material, cf. Sec. 5.2.2.

Adherence to the incompressibility condition is found to be crucial for stable convergence and accurate results. Moreover, a too-small determinant of the Eulerian deformation tensor yields unstable simulations since the determinant occurs in the denominator when the inverse of the deformation tensor is calculated.

In the following sections, the discretization of the governing equations is described in more detail, and different discretization approaches are discussed, mainly concerning the incompressibility condition.

5.2.1 Discretized Equation System

The continuity, momentum, and soil mixture equations, as well as the elliptic relaxation procedure and the displacement equation, are first converted into a flux-based integral form, viz.

$$\oint_A v_i dA_i = 0 \tag{5.10}$$

$$\begin{aligned}\int_V \frac{\partial}{\partial t}(\rho v_i)\, dV + \oint_A \left(\rho v_i v_j\right) dA_j - \oint_A \tau_{ij} dA_j = \\ -\oint_A p dA_i + \int_V \rho g_i dV\end{aligned} \tag{5.11}$$

$$\int_V \frac{\partial c_S}{\partial t} dV + \oint_A c_S v_i dA_i = 0 \tag{5.12}$$

$$\int_V c_S v_i^S dV - \oint_A a_w \left(\frac{\partial v_i^S}{\partial x_j}\right) dA_j = \int_V c_S v_i dV \tag{5.13}$$

$$\int_V \frac{\partial u_i}{\partial t} dV + \oint_A v_j^S u_i dA_j = \int_V v_i^S dV\ . \tag{5.14}$$

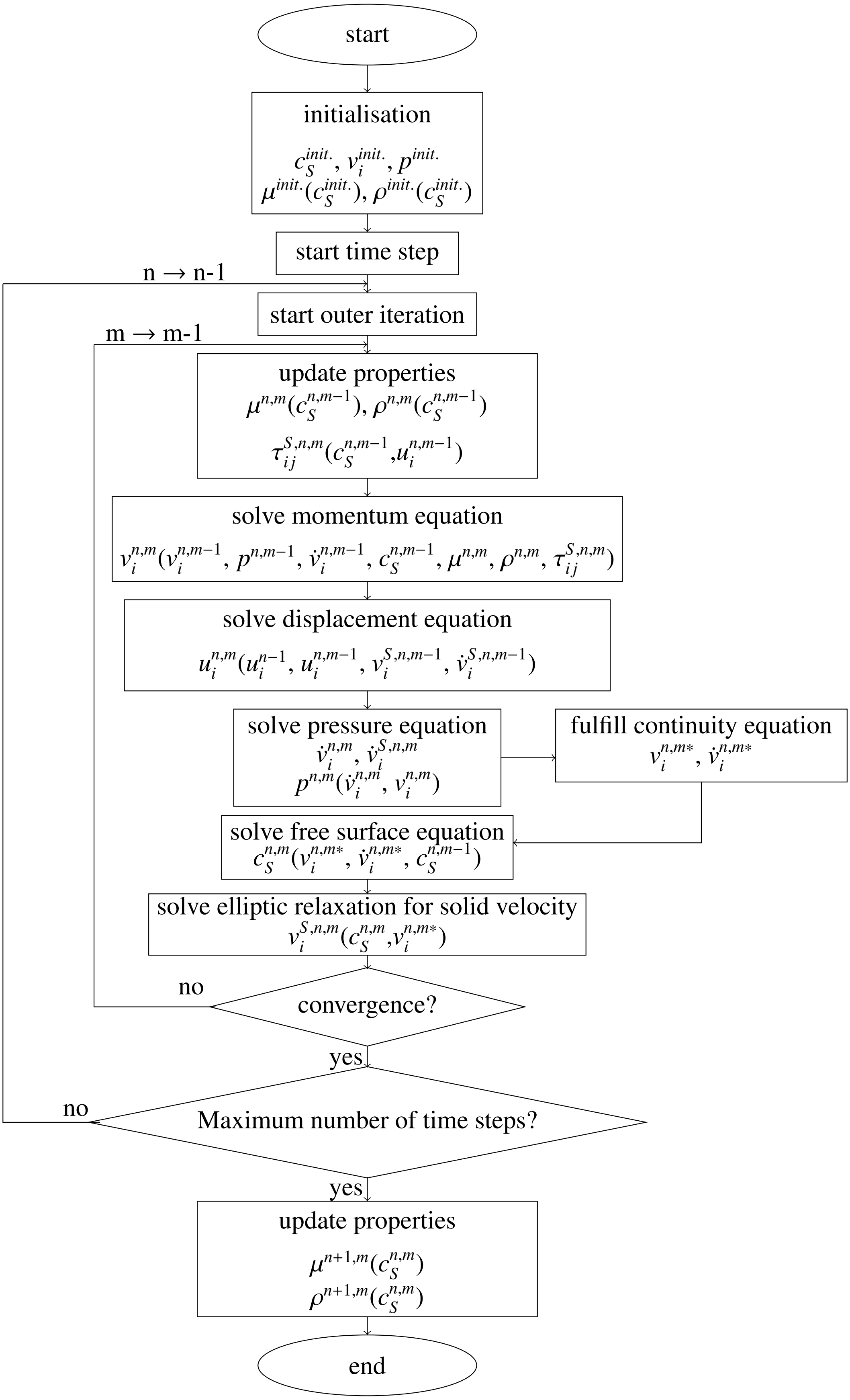

Figure 5.1: Algorithmic procedure of monolithic Eulerian Fluid-Structure interaction for elastic materials in FV, VoF.

In the following sections, the exact discretizations of each equation are explained, and auxiliary techniques are introduced.

Discretized Momentum Equations

The divergence of the deviatoric stress tensor τ^S_{ij} of the neo-Hookean material is explicitly added on the RHS of the momentum equations and is discretized with the help of the divergence theorem

$$q_i = c^{n,m-1}_{S,P} \sum_{f(\Delta V_P)} \eta_S \left(G^{n,m-1}_{il} F^{n,m-1}_{jl} - \delta_{ij} \right)_f \cdot A_i \,. \tag{5.15}$$

In order to stabilize the equation system, the implicit viscous fluid stress term is applied for both phases as in the standard momentum equations for incompressible two-phase flows. To subtract the viscous stress in the solid phase, a multiplication with the soil mixture fraction of the viscous stress is explicitly added on the momentum equations' RHS. The momentum equations for the two-phase FSI follow by applying the same discretization techniques as explained in chapter 2.2 to

$$\begin{aligned} v^{n,m}_{i,P} \left[\rho_P \frac{\Delta V_P}{\Delta t} + \sum_{f(\Delta V_P)} A^{v_i}_{NB} \right] - \sum_{f(\Delta V_P)} \underbrace{\left[\left(max\left[-\dot{m}^{n,m-1}, 0 \right] \right)_f + \left(\frac{\mu A}{d} \right)_f \right]}_{A^{v_i}_{NB}} v^{n,m}_{i,NB} = \\ - \sum_{f(\Delta V_P)} \left(p^{n,m-1}_f A_i \right) + \rho_P \Delta V_P \left(g_i + \frac{v^{n-1}_i}{\Delta t} \right)_P + c^{n,m-1}_{S,P} \sum_{f(\Delta V_P)} \eta_S \left(G^{n,m-1}_{il} F^{n,m-1}_{jl} - \delta_{ij} \right)_f \cdot A_i \\ + c^{n,m-1}_{S,P} \left[\sum_{f(\Delta V_P)} R_{NB} \right] v^{n,m-1}_{i,P} - c^{n,m-1}_{S,P} \sum_{f(\Delta V_P)} \underbrace{\left(\frac{\mu A}{d} \right)_f}_{R_{NB}} v^{n,m-1}_{i,NB} + S_{v_i} \,. \end{aligned} \tag{5.16}$$

where $\dot{m}_f = (\rho v_i A_i)_f$ is the mass flux. Applying Eqn. (5.16) with μ^S being zero or very small, the incompressibility condition $det(F_{ij}) = 1$ is fulfilled well, and results close to the literature values are obtained.

Remark

Initially, the momentum equations were implemented by only adding the elastic forces on the right side of the momentum equations and setting the viscosity of the elastic Neo-Hookean material to zero. It was found that this leads to softer material behavior and a non-fulfillment of the incompressibility condition. Since the elastic forces are linearly dependent on the solid concentration, the material behaves less stiff for concentration values $0.5 < c_S < 1$.

When the elastic material is treated as a visco-elastic material ($\mu^S = \mu^A$), the implicit viscous fluid tension stabilizes the simulations, but on the other hand it leads to determinants of F_{ij}

which are not equal to one and compared to Sugiyama et al. [110] and Zhao et al. [140], the visco-elastic material behaves too soft.

Discretized Continuity Equation

The continuity equation (5.10) is solved with the same pressure correction scheme as explained in the previous chapters concerning the FVM. Hence, Eqn. (3.2) as in the rigid perfectly-plastic two-phase approach is applied.

Addition of Trace of Deviatoric Stress to Pressure Equation

To enhance model results, a modification of the continuity equation, as suggested in Sugiyama et al. [110], is applied for some of the test cases, and its performance is compared against simulations without the modification. Sugiyama et al. [110] introduce the existing trace of the deviatoric elastic stress tensor in the pressure equation. The trace of the deviatoric elastic stress tensor should be zero, so this is a technique to counteract an imperfect stress tensor by adding the actual trace to the pressure equation. The deviatoric stress tensor is thereby corrected to be

$$\tau_{ij} \to \tau_{ij} - \frac{1}{3}\,\mathrm{tr}(\tau_{ij})\delta_{ij} \tag{5.17}$$

and the pressure is modified by

$$p \to p + \frac{1}{3}\,\mathrm{tr}(\tau_{ij}) \tag{5.18}$$

in the solid phase. The latter is realized by adding the existing trace of the deviatoric stress tensor on the RHS of the pressure equation (2.42), i.e.

$$RHS\, = -\dot{v}^{*} + c_{S,P}\, A_P^p\, \frac{1}{3}\,\mathrm{tr}(\tau_{ij})\ . \tag{5.19}$$

The elastic force, which is added on the right side of the momentum equations, changes from Eqn. (5.15) to

$$q_i = c_{S,P}^{n,m-1} \sum_{f(\Delta V_P)} \left(\eta_S \left(G_{il,f}^{n,m-1} F_{jl,f}^{n,m-1} - \delta_{ij} \right) - \frac{1}{3}\,\mathrm{tr}\left(\eta_S \left(G_{il,f}^{n,m-1} F_{jl,f}^{n,m-1} - \delta_{ij} \right)\right) \delta_{ij} \right) \cdot A_{j,f}\ . \tag{5.20}$$

Discretized Artificial Solid Velocity Equation

The elliptic relaxation equation for the artificial solid velocity equation (5.3) is discretized as

$$v_{i,P}^{S,n,m} \left[c_{S,P}^{n,m-1} \Delta V_P + \sum_{f(\Delta V_P)} A_{NB}^{v^S} \right] - \sum_{f(\Delta V_P)} \underbrace{\left(\frac{a_w A}{d} \right)_f}_{A_{NB}^{v^S}} v_{i,NB}^{S,n,m} = c_{S,P}^{n,m-1} \Delta V_P v_{i,P}^{n,m-1}\ . \tag{5.21}$$

The difficulty with this approach is the weak diagonal of the matrix inside the fluid domain due to the diffusive term being the only term determining the artificial solid velocity in the fluid material. Therefore, the factor a_w has to be chosen in accordance with stability requirements.

Divergence Diminishing Treatment for Artificial Solid Velocity

Since the elliptic relaxation equation is solved at the end of each iteration and is not connected to the pressure equation directly, cf. algorithm 5.1, the divergence of the velocity v_i^S is not guaranteed to vanish. In order to ensure a unit determinant of the Eulerian displacement gradient tensor, manipulation of the RHS of the artificial solid velocity equation is proposed herein. A divergence-free artificial solid velocity is generated by subtracting the gradient of the artificial solid velocity's divergence from the equation's RHS.

Using constant a_w, the diffusion term in the artificial solid velocity equation can be expressed in symbolic notation by

$$a_w \frac{\partial^2 v_i^S}{\partial x_j^2} = a_w \operatorname{div} \operatorname{grad} v_i^S \tag{5.22}$$

and can be expressed by the following vector identity

$$\operatorname{div} \operatorname{grad} v_i^S = \operatorname{grad} \operatorname{div} v_i^S - \operatorname{rot} \operatorname{rot} v_i^S \, . \tag{5.23}$$

If the divergence of the artificial solid velocity is zero, the first term on the RHS is also zero. The resulting difference of this term from zero is subtracted from the RHS of the artificial solid velocity equation (5.3) to diminish the divergence of the artificial solid velocity, i.e.

$$c_S v_i^S - a_w \operatorname{div} \operatorname{grad} v_i^S = c_S v_i - c_S a_w \left(\operatorname{div} \operatorname{grad} v_i^S + \operatorname{rot} \operatorname{rot} v_i^S \right) \tag{5.24}$$

in symbolic notation. In the FV discretization, Eqn. (5.24) reads

$$\begin{gathered} v_{i,P}^{S,n,m} \left[c_{S,P}^{n,m-1} \Delta V_P + \sum_{f(\Delta V_P)} A_{NB}^{v^S} \right] - \sum_{f(\Delta V_P)} \underbrace{\left(\frac{a_w A}{d} \right)_f}_{A_{NB}^{v^S}} v_{i,NB}^{S,n,m} = \\ c_{S,P}^{n,m-1} \Delta V_P v_{i,P}^{n,m-1} - a_w c_{S,P}^{n,m-1} \Delta V_P \left(\operatorname{div} \operatorname{grad} v_{i,P}^S + \operatorname{rot} \operatorname{rot} v_{i,P}^S \right) \end{gathered} \tag{5.25}$$

where the gradients in the terms

$$\operatorname{div} \operatorname{grad} v_{i,P}^S = \begin{Bmatrix} \dfrac{\partial^2 v_{1,P}^S}{\partial x_1^2} + \dfrac{\partial^2 v_{1,P}^S}{\partial x_2^2} + \dfrac{\partial^2 v_{1,P}^S}{\partial x_3^2} \\ \dfrac{\partial^2 v_{2,P}^S}{\partial x_1^2} + \dfrac{\partial^2 v_{2,P}^S}{\partial x_2^2} + \dfrac{\partial^2 v_{2,P}^S}{\partial x_3^2} \\ \dfrac{\partial^2 v_{3,P}^S}{\partial x_1^2} + \dfrac{\partial^2 v_{3,P}^S}{\partial x_2^2} + \dfrac{\partial^2 v_{3,P}^S}{\partial x_3^2} \end{Bmatrix} \tag{5.26}$$

and

$$\operatorname{rot} \operatorname{rot} v_{i,P}^S = \begin{Bmatrix} \dfrac{\partial^2 v_{2,P}^S}{\partial x_1 \partial x_2} - \dfrac{\partial^2 v_{1,P}^S}{\partial x_2^2} - \dfrac{\partial^2 v_{1,P}^S}{\partial x_3^2} + \dfrac{\partial^2 v_{3,P}^S}{\partial x_1 \partial x_3} \\ \dfrac{\partial^2 v_{3,P}^S}{\partial x_2 \partial x_3} - \dfrac{\partial^2 v_{2,P}^S}{\partial x_3^2} - \dfrac{\partial^2 v_{2,P}^S}{\partial x_1^2} + \dfrac{\partial^2 v_{1,P}^S}{\partial x_1 \partial x_2} \\ \dfrac{\partial^2 v_{1,P}^S}{\partial x_1 \partial x_3} - \dfrac{\partial^2 v_{3,P}^S}{\partial x_1^2} - \dfrac{\partial^2 v_{3,P}^S}{\partial x_2^2} + \dfrac{\partial^2 v_{2,P}^S}{\partial x_2 \partial x_3} \end{Bmatrix} \tag{5.27}$$

are calculated with the least square method (cf. Appendix A, Eqn. (A.9)) using the most recently computed values.

Discretized Eulerian Displacement Equation

The Eulerian displacement is transported with the artificial velocity v_i^S obtained by the elliptic relaxation equation. The implicit Euler time scheme is used to discretize the time derivative in the equation for the displacement (5.14). The convective part in the displacement equation is discretized with a simple UDS method and the discretized equation becomes

$$u_{i,P}^{n,m}\left[\frac{\Delta V_P}{\Delta t}+\sum_{f(\Delta V_P)} A_{NB}^u\right]-\sum_{f(\Delta V_P)} \underbrace{\left(max\left[-\dot{v}^{S,n,m-1},0\right]\right)_f}_{A_{NB}^u} u_{i,NB}^{n,m}=\frac{\Delta V_P}{\Delta t}u_{i,P}^{n-1}+v_{i,P}^{S,n,m-1}\Delta V_P+S_u\,, \quad (5.28)$$

where the flux of the artificial solid velocity is $\dot{v}_f^S = (v_i^S A_i)_f$.

5.2.2 Dirichlet Wall Boundary Condition for Neo-Hookean Material

The wall boundary condition applied for fluids is described in Appendix A.5. Since the shear stress for the fluid depends on the viscosity, no wall force is acting on the elastic material if the viscosity is set to zero or a minimal value. Therefore an additional force has to be introduced to obtain a wall boundary condition for the elastic material. Since the deviatoric stress depends not directly on velocity values but on displacement values, a similar approach as in Appendix A.5 was unsuccessful. Applying an explicit force term derived from the deviatoric stresses of the last iteration in the first fluid cell above the wall yields bad convergence behavior. Best results are obtained by subtracting a damping term from the coefficient matrix $A_{NB}^{v_i}$ at the boundary face f_b

$$A_{f_b}^{v_i} -> A_{f_b}^{v_i} - c_{S,P} F_{wall}\,, \quad (5.29)$$

where a user defined factor F_{wall} is applied. This leads to an addition of the damping term to the $A_P^{v_i}$ of the cell closest to the boundary and on the RHS of the momentum equations in that cell $RHS_P^{v_i}$,

$$A_P^{v_i} -> A_P^{v_i} - A_{f_b}^{v_i} = A_P^{v_i} + c_{S,P} F_{wall}\,, \quad (5.30)$$

$$RHS_P^{v_i} -> RHS_P^{v_i} - A_{f_b}^{v_i} |v_{f_b}| = RHS_P^{v_i} + c_{S,P} F_{wall} |v_{f_b}|\,, \quad (5.31)$$

where the velocity magnitude in the boundary cell $|v_{f_b}|$ is set to zero for a wall condition. However, care has to be taken to extend this approach to moving grids.

For the displacement and the artificial solid velocity equations, Dirichlet conditions are set at the wall.

5.3 Verification and Validation

Three validation cases are studied to demonstrate the performance of the present FV discretized monolithic incompressible Neo-Hookean FSI model. First, the reversibility of the elastic material is proven. Then a deformable incompressible disk is studied in a two-dimensional lid-driven cavity where the pure lid-driven cavity is validated against reference values from Ghia et al. [40]. The third case comes closest to the aim for modeling cargo in holds since it is a lid-driven cavity case with an elastic bottom.

In all cases of this section, the implicit first-order Eulerian time integration scheme is applied together with the compressive CICSAM scheme for the convective term of the soil mixture equation. For the convective terms of the displacement equations, a QUICK scheme is used. Similarly, the flux-blending scheme with a CDS-biased blending factor of 0.85 is employed for the convective approximations of the momentum equations.

5.3.1 Reversibility of Neo-Hookean Material Deformation

To test the reversibility behavior of the monolithic Neo-Hookean elastic material model, a two-dimensional shear flow is acting on an elastic disk as described by Sugiyama et al. [110]. A disk with a radius of 0.75 m is positioned in the middle of a domain with a length of $L = 8.0$ m and a height of 2.0 m as depicted in Fig. 5.2. The gravitational force is acting in x_2- direction with a magnitude of 9.81 m/s^2. The domain's top and bottom boundaries are driven by walls with opposing velocities with $|v_1| = 1.0$ m/s for a period of 4.0 s. After 4.0 s, the walls are put at rest ($|v_1| = 0.0$ m/s), the fluid settles and the elastic material should return to its initial shape. At the two vertical boundaries, zero-gradient conditions are applied for both, the pressure and the velocities.

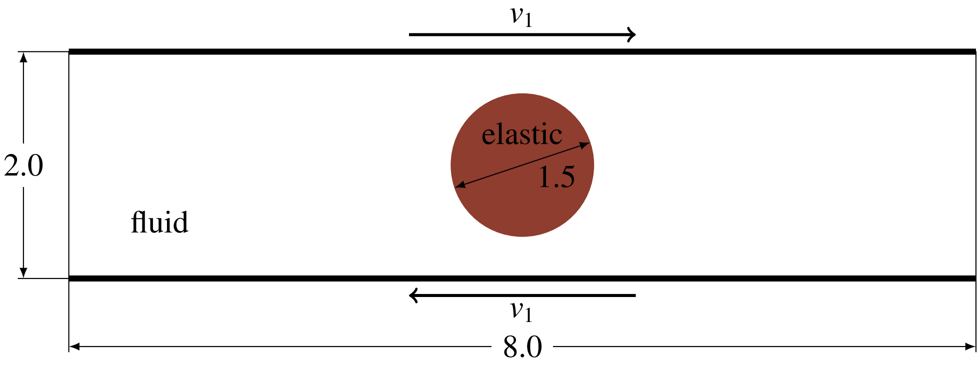

Figure 5.2: 2D reversibility study: Initial position of the elastic disk exposed to shear flow introduced by Sugiyama et al. [110].

The material densities are $\rho^A = \rho^S = 1$ kg/m^3, and the fluid viscosity refers to $\mu^A = 1$ kg/m^3. The Lamé constant η_S in the neo-Hookean constitutive equation is given as 4 N/m^2. A rectangular, equidistant grid with $\Delta x_1 = \Delta x_2 = L/128$ is used. The time step is set to $\Delta t = 10^{-3}$ s and the simulation runs for a period of 400 s to obtain a stable reversed final shape. The constant a_w employed by the elliptic relaxation of the solid velocity is set to 10^{-2}.

In Willing [131], it was found that without fixing the centre of the elastic disk to the centre of the domain, the disk is vertically displaced and loses its original round shape in the reversed configuration. Therefore a fixation method as documented by Willing [131] is introduced solely for this case.

Fixation of Cylinder in Shear Flow

Since the free floating disk is displaced by the shear flow, the average velocity of the disk v_i^{dsk} is subtracted from the solid velocity v_i^S (obtained by elliptic relaxation) to compute a relative velocity

$$v_i^{fix} = v_i^S - v_i^{dsk} \tag{5.32}$$

that replaces v_i^S in the displacement equation (5.14) and mixture fraction equation (5.12). The averaged velocity of the disk is obtained by

$$v_i^{dsk} = \frac{\sum_{CV} v_{i,P}}{N_{CV}} \, . \tag{5.33}$$

Results

The displacement in the x_1-direction inside the elastic material is depicted in Fig. 5.3 for $t = 0$ s, $t = 4$ s and $t = 400$ s as well as the elastic force component in the x_1-direction of the deviatoric stress tensor. In Fig. 5.3, the maximum displacement in the x_1-direction of the elastic disk is found to be 0.64 m at $t = 4.0$ s. For $t = 400$ s, it can be seen that no displacement is left, and a near-circular shape is obtained for the elastic disk. At $t = 4.0$ s, the acting elastic forces can be recognized. A small vertical shift of the disk downwards can be observed at $t = 400$ s in Fig. 5.4, which stems from a slightly unsymmetrical velocity field v_i^S due to the elliptic relaxation. Nevertheless, the reversibility of the elastic deformation is confirmed by comparing its initial and final shape in Fig. 5.4.

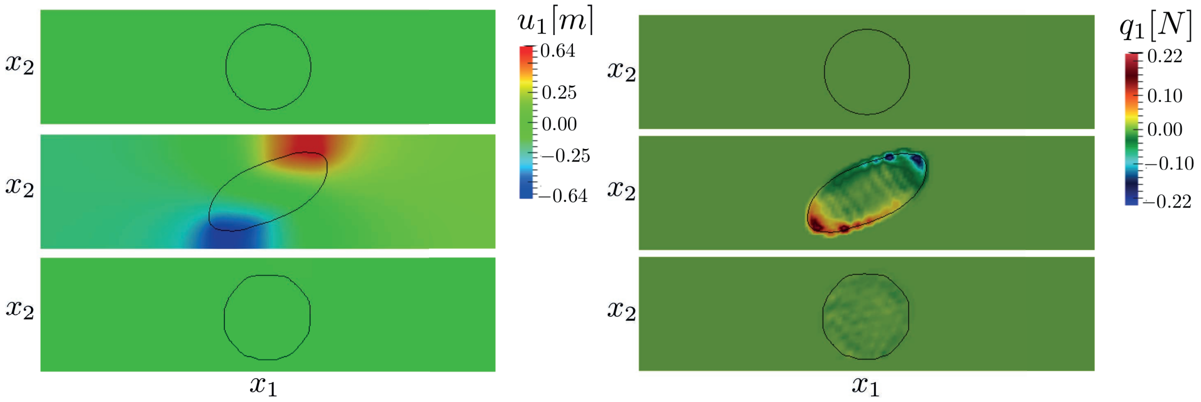

Figure 5.3: 2D reversibility study: Field values of the elastic disk in shear flow at three different time steps (top: $t = 0.0$ s, middle: $t = 4.0$ s, bottom $t = 400.0$ s) where the black line represents the boundary of the elastic disk ($c_S = 0.5$). Left graphs display the amount of displacement in the x_1-direction. Right graphs display the first component of elastic force (q_1) resulting from the deviatoric part of the neo-Hookean constitutive equation (5.15) .

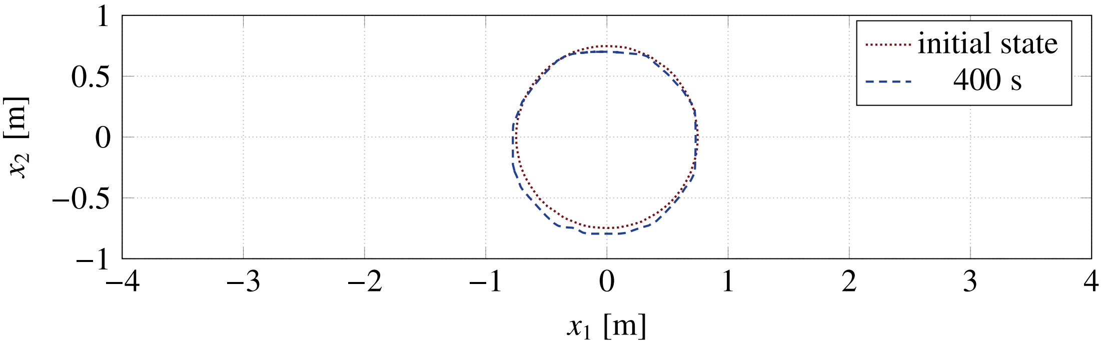

Figure 5.4: Comparison of the initial (dotted) and final (dashed) shape of the 2D elastic circular disk exposed to a temporal shear flow, indicating the reversibility of the deformation.

5.3.2 Deformable Elastic Disk in a Two-dimensional Lid-driven Cavity

A two-dimensional test case where an elastic disk is floating in a lid-driven cavity is described in Sugiyama et al. [110] and Zhao et al. [140]. All physical variables and dimensions are given without a unit by the literature and are assigned to SI-units for this study. The initial position of the elastic disk in the lid-driven cavity, as well as the dimensions of the domain, are illustrated in Fig. 5.5. The center of the disk is located at $x_1 = 0.6$ m; $x_2 = 0.5$ m, the radius of the disk reads 0.2 m, and the domain length is $L = 1.0$ m). The Neo-Hookean constitutive equation is applied to the elastic material as described in Sec. 5.1.1. The density of the fluid and the elastic material are $\rho^A = \rho^S = 1$ kg/m^3, such that the disk is not subjected to buoyancy. The fluid viscosity is $\mu^A = 0.01$ Pa s, and the Lamé constant of the elastic material is $\eta_S = 0.1$ N/m^2. The lid-driven cavity consists of three solid walls and a top lid that moves with the speed of $v_1 = 1$ m/s. No gravitational force is considered. For the results presented in the next sections, a structured homogeneous mesh composed of rectangular elements with $\Delta x_1 = \Delta x_2 = L/120$ is used. The applied time step is $\Delta t = 5 \cdot 10^{-4}$ s and yields a Courant number of $\Delta t\, v_1/\Delta x_1 = 0.06$.

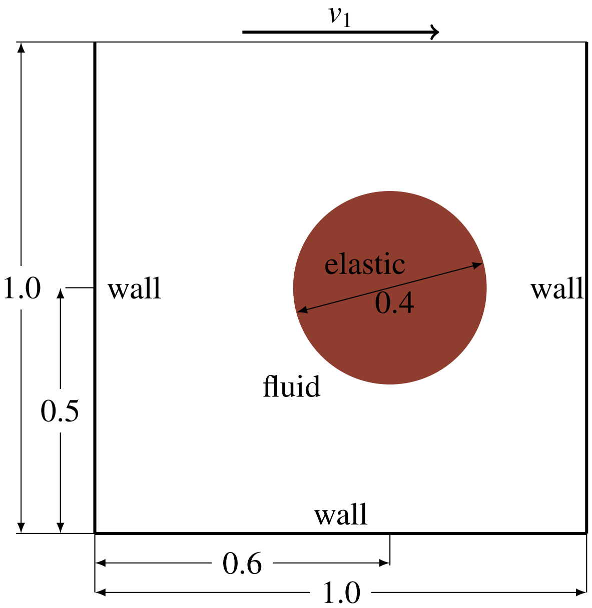

Figure 5.5: 2D elastic disk in cavity: Initial position of the elastic disk and dimensions of the lid-driven cavity in meters given by Zhao et al. [140] and Sugiyama et al. [110].

Validation of the Lid-driven Cavity Case without an Elastic Disk

In order to validate the fluid field without FSI, a lid-driven cavity is compared to the frequently employed reference values of Ghia et al. [40]. The described algorithm in this section is applied without solving the elliptic relaxation equation or displacement equation and by setting the

Lamé constant to zero. The numerical settings coincide with the described settings from the last paragraph. The lid-driven cavity has a Reynolds number of 100. In Fig. 5.6 (a), the values of the velocity component v_1 obtained with the presented FV approach are plotted over the vertical x_2-coordinate along the horizontal center of the cavity ($x_1 = 0.5$ m). The current CFD approach yields an excellent predictive agreement with reference values reported by Ghia et al. [40]. In Fig. 5.6 (b), the predicted vertical velocity v_2 is compared to the reference values along a horizontal center line through $x_2 = 0.5$ m. The related maximum is slightly overestimated. Nonetheless, the current predictions are again very close to the reference values. Therefore most discrepancies between current simulations and reference data for the elastic disk in the cavity case are attributed to the FSI model.

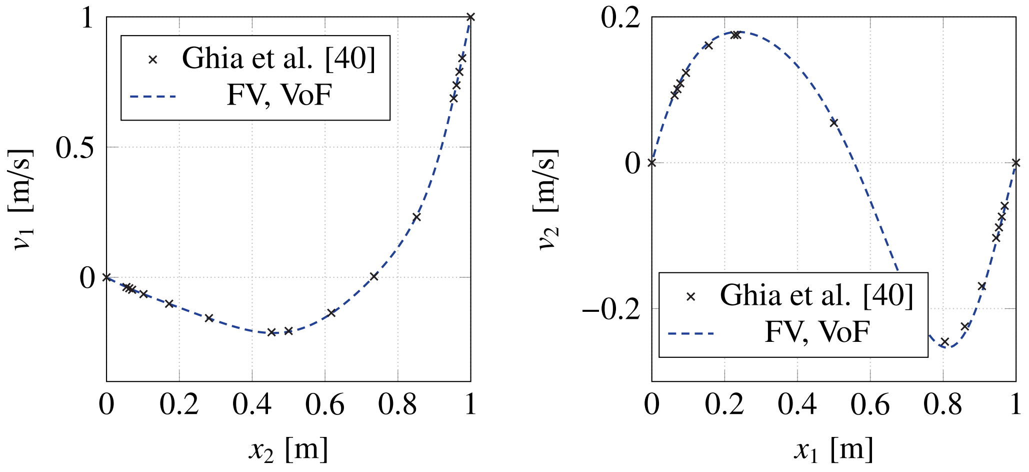

(a) v_1 over x_2 at $x_1 = 0.5$ m

(b) v_2 over x_1 at $x_2 = 0.5$ m

Figure 5.6: 2D lid-driven cavity flow: Profile of velocity components v_1 and v_2 over x_2-coordinate at $x_1 = 0.5$ m and x_1-coordinate at $x_2 = 0.5$ m simulated with $\Delta t = 5 \cdot 10^{-4}$ s and $\Delta x_1 = \Delta x_2 = L/120$ compared to results from Ghia et al. [40].

Notes on Studies of the Influence of Numerical Techniques on Results of the Lid-driven Cavity Case

Some remarks on other findings resulting from applying different numerical techniques and settings to this test case, which are not displayed in detail in this work, are given in this section. The Eulerian displacement calculated from Eqn. (5.28) is the basis to calculate the elastic stresses in this approach. When the displacement equation is solved with the fluid velocity v_i instead of the artificial solid velocity v_i^S, the displacement gradient is very sharp at the solid boundary, leading to overestimated elastic stresses acting close to the solid boundary. These stresses lead to a too soft material behavior. Formulating the solid velocity as $v_i^S = c_S v_i$ and using it in Eqn. (5.28) leads to an overestimation of the elastic stresses at the solid boundary since the solid velocity is not continuous over the boundary. These findings are consistent with the notes from chapter 3 on high strains at the soil/air boundary.

A factor that highly influences the artificial solid velocity values v_i^S outside the solid material is the elliptic relaxation factor a_w. Therefore the value of a_w greatly impacts the Eulerian displacement and solid stress tensors. It was found that a constant a_w, depending on the mesh size, gives the best results. If a_w is too large, the gradient of the Eulerian displacement will be too small, leading to small values of elastic forces acting on the solid and, therefore, too soft behavior. For a_w approaching zero, the $A_P^{v^S}$ of the elliptic relaxation Eqn. (5.25) also approaches zero inside the fluid domain leading to numerical instability. Therefore a value a_w as small as possible without inducing numerical problems has to be found. For $\Delta x_1 = \Delta x_2 = L/120$ ($\Delta t = 5 \cdot 10^{-4}$) this value is found to be $a_w = 10^{-3} \sim (4\,\Delta x_1)^2$. For the reversibility test case a $a_w \sim (2\,\Delta x_1)^2$ was applied.

Several other numerical techniques were tested (e.g., non-linear subtraction of fluid stress, non-linear interpolation of viscosity, application of Tait's equation as pressure source) but were unsuccessful in improving the results.

Discussion of Differences Between Two Model Configurations and the Influence on Several Field Values

Two successful configurations of the present Eulerian FSI model are applied to the elastic disk in a lid-driven cavity test case, and differences in model field values are discussed in this section. The first reference model configuration (hereafter called the present FV, VoF method) uses Eqns. (5.16), (5.21), (5.28) and (3.42) with the solid viscosity being zero. Results closest to the literature results were obtained with the same model plus a combination of three techniques which are described in Secs. 5.1.3 and 5.2.1. Therefore the second model configuration (hereafter called the present FV, VoF method with extra/additional techniques) consists of Eqns. (5.16) with constitutive formulations (5.9) and (5.20), (5.25), (5.28), (3.42) with RHS (5.19) and the viscosity inside the elastic disk is set to be $\mu^S = 2 \cdot 10^{-3}$ Pa s. Nevertheless, in Eqn. (5.16), the viscous fluid stress is subtracted from the momentum equations inside the elastic material. Hence, the main difference is in the viscosity values at the boundary of the solid material (for $0 < c_S < 1$). The small viscosity in the solid part stabilizes the simulations. For both simulations, an elliptic relaxation constant $a_w = 10^{-3}$ is used.

Two conditions arise from the incompressible continuity equation and can be used to verify the results, i.e.

- the divergence of the velocity has to be zero
- the determinant of the Eulerian deformation gradient F_{ij} has to be equal to one .

Both conditions are displayed in Fig. 5.7 for the present FV model of the incompressible neo-Hookean material without applying a solid viscosity ($\mu^S = 0$) and the same model applying three above mentioned additional techniques to obtain an incompressible neo-Hookean material. On the left column of Figs. a) and b), the results for the present model without additional treatment are presented. It can be seen, that during later time steps, the divergence of the artificial velocity deviates from zero, and the determinant of the Eulerian deformation gradient is not one. Improvements are observed for the present model if additional techniques are

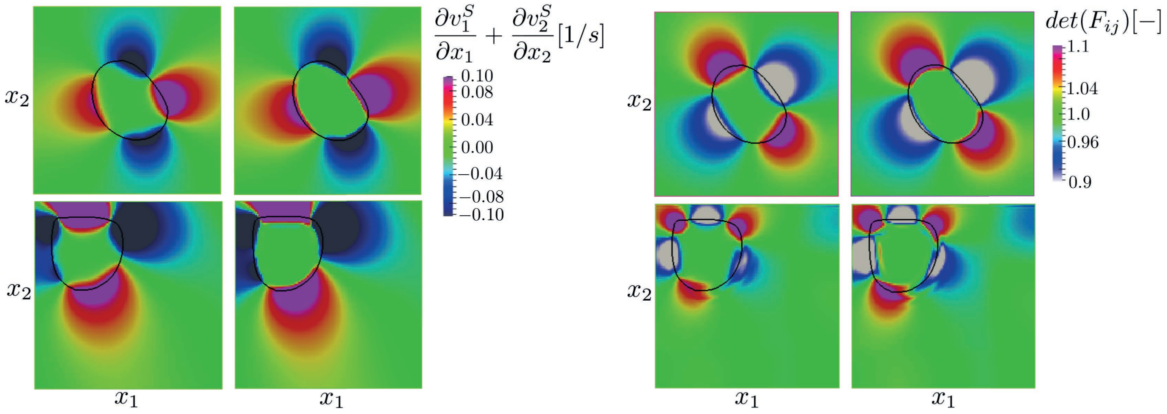

(a) Divergence of solid velocity v_i^S.

(b) Determinant of the Eulerian deformation gradient F_{ij}.

Figure 5.7: 2D elastic disk in cavity: Comparison of field values for FV, VoF model with $\mu^S = 0.0$ (left in (a) and (b)) and FV, VoF model with $\mu^S = 0.002$ + techniques (5.19), (5.20), (5.9), (5.25) (right in (a) and (b)) at two time steps $t = 1.2$ s (top) and $t = 3.5$ s (bottom).

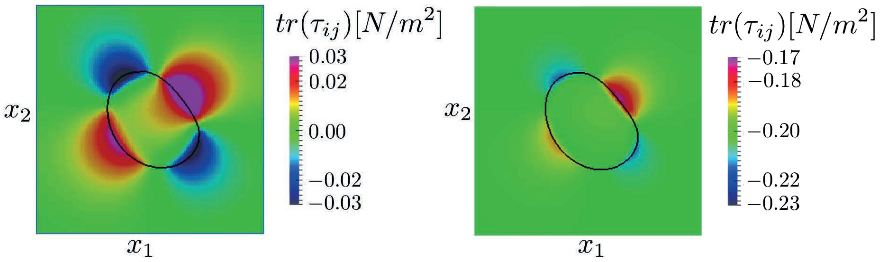

Figure 5.8: 2D elastic disk in cavity: Field values of the trace of the deviatoric stress tensor at $t = 1.2$ s. Left: present FV, VoF method; Right: present FV, VoF method with additional techniques.

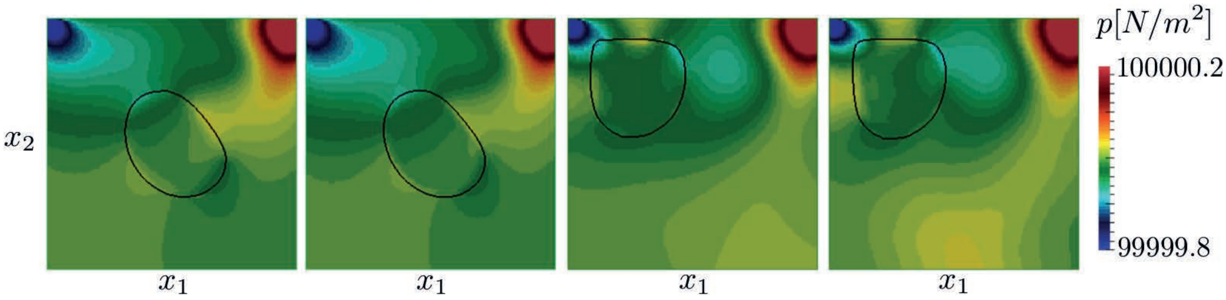

Figure 5.9: 2D elastic disk in cavity: Pressure field values at $t = 1.2$ s (left) and $t = 3.5$ s (right). Left: present FV, VoF method; Right: present FV, VoF method with additional techniques.

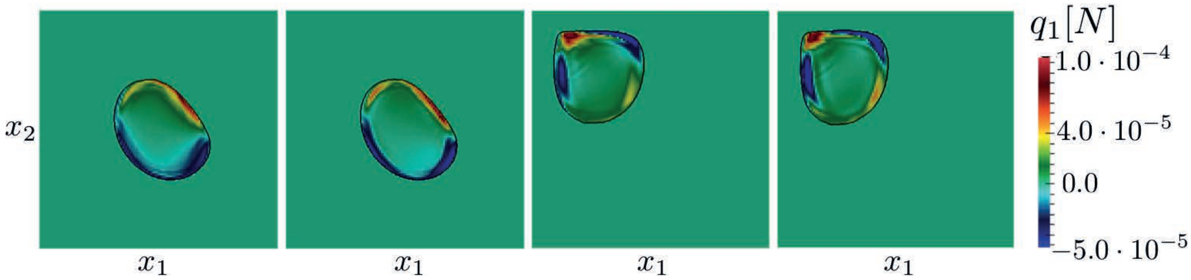

Figure 5.10: 2D elastic disk in cavity: Field values of elastic force in x_1-direction acting on the elastic disk at $t = 1.2$ s (left) and $t = 3.5$ s (right). Left: present FV, VoF method; Right: present FV, VoF method with additional techniques.

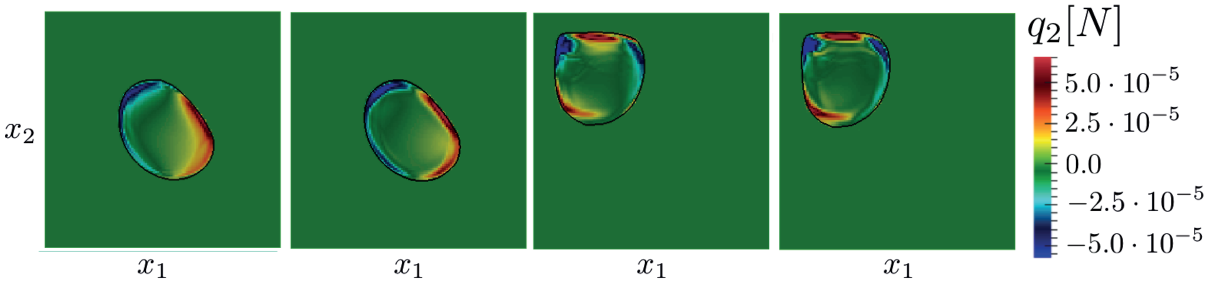

Figure 5.11: 2D elastic disk in cavity: Field values of elastic force in x_2-direction acting on the elastic disk at $t = 1.2$ s (left) and $t = 3.5$ s (right). Left: present FV, VoF method; Right: present FV, VoF method with additional techniques.

utilized to enforce both conditions inside the solid disk. However, the constraints are not entirely satisfied at the boundary of the elastic material. The largest influence on the divergence of the artificial solid velocity comes from manipulating the artificial solid velocity equation by introducing the divergence of the gradient of the artificial solid velocity and the rotation of the artificial solid velocity. Suppose this approach is added to the RHS of the artificial solid velocity equation for the solid and the fluid part. In that case, the elastic disk behaves too soft, and the divergence is not small in the whole domain but only inside the solid.

Both the application of an Eulerian Cauchy Green tensor with zero trace (cf. Sec. 5.1.3) and adding the erroneous volumetric part of the stress tensor to the pressure equation (5.2.1) aim to obtain a strictly deviatoric stress tensor. The results of applying both techniques can be studied in Fig. 5.8 on the right side. In opposite to the results without additional techniques, the trace of the deviatoric stress tensor is uniform inside the elastic disk. Nonetheless, it does not fluctuate around zero but around -0.2. Therefore, these approaches obtain the best results for this test case but do not use the entirely correct constitutive equations.

Due to the Sugyiama technique from Sec. 5.2.1, adding a volumetric part on the RHS of the pressure equation, the pressure field values also differ (cf. Fig. 5.9). It shows higher pressures acting on the boundary of the elastic material for the FV, VoF model with additional techniques and at $t = 1.2$ s a more uniform pressure inside the elastic material.

In Figs. 5.10 and 5.11, the elastic forces included in the momentum equations (5.15) are displayed for the x_1- and x_2- directions. It can be seen that for the present FV, VoF method with additional techniques, the force concentrates closer to the elastic material boundary than for the present FV, VoF method.

Comparison of Results From Present Monolithic Neo-Hookean Fluid-Structure Interaction Model with Zhao et al. [140] and Sugiyama et al. [110]

This section compares the best results from the above-presented methods against the work of Sugiyama et al. [110] and Zhao et al. [140]. Sugiyama et al. [110] introduce a fully Eulerian FDM using the VoF formulation for simulating FSI on fixed cartesian grids. Zhao et al. [140] use a mixed Lagrangian and Eulerian formulation where the elastic stress is calculated using a Finite-Element method on a Lagrangian mesh that overlaps a fixed Eulerian mesh. The transferred elastic stresses are then introduced to a joint momentum and continuity equation on the Eulerian mesh. Sugiyama et al. [110] show that their results fully coincide with the results of Zhao et al. [140], and therefore the displayed reference results are only taken from one source. A concentration value of $c_S = 0.5$ is used to define the boundary of the elastic disk, which is displayed in Figs. 5.12 and 5.13 for several time steps. Results of the presented model with and without extra techniques to fulfill the continuity equation inside the elastic material are compared to the results given by Sugiyama et al. [110]. The dashed blue line represents the basic

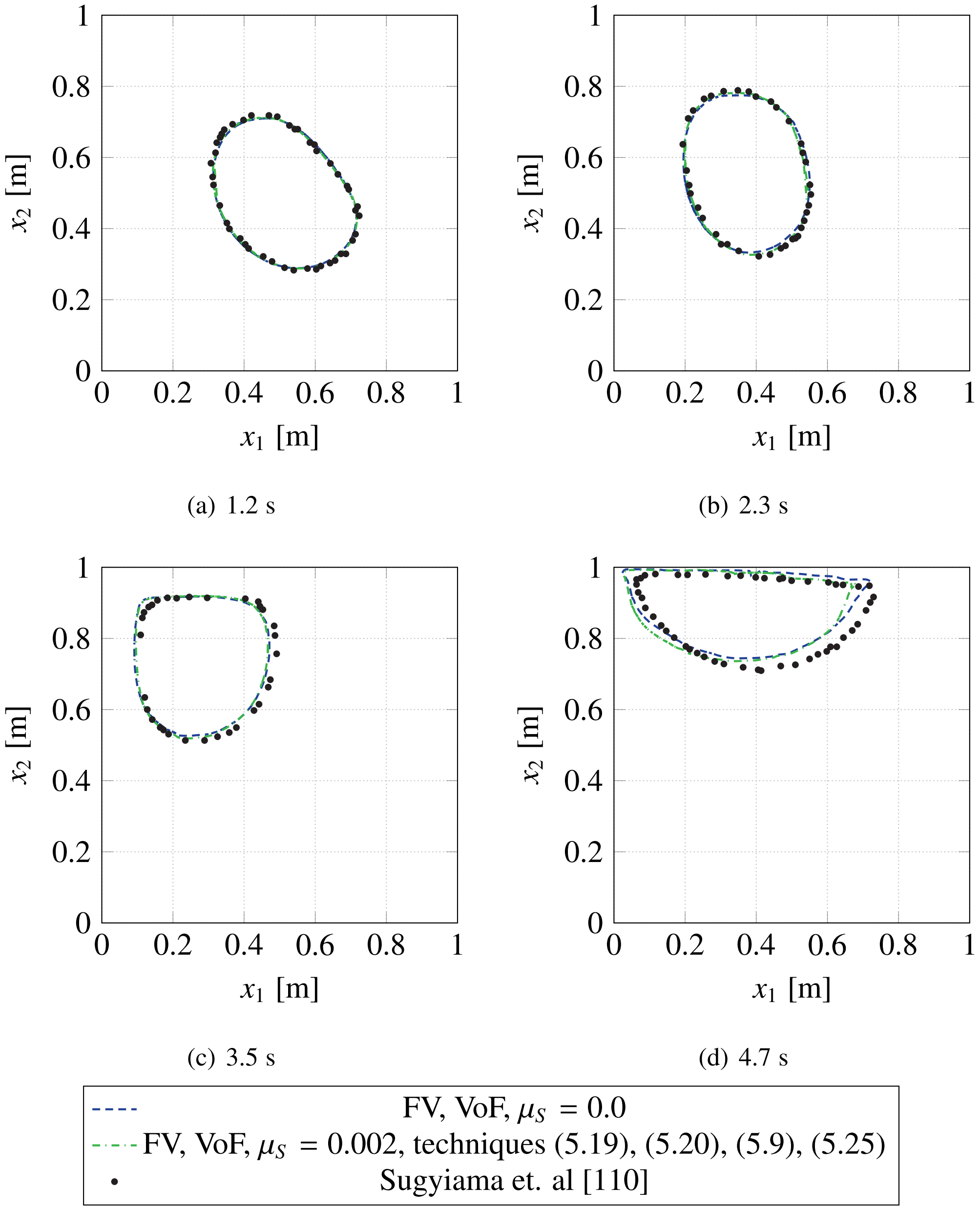

(a) 1.2 s

(b) 2.3 s

(c) 3.5 s

(d) 4.7 s

Figure 5.12: Evolution of the disk for an elastic incompressible Neo-Hookean medium immersed in a 2D lid-driven cavity during the first four time steps.

present FV, VoF model of the incompressible Neo-Hookean material without applying a solid viscosity ($\mu^S = 0.0$). An excellent agreement with the reference results exists for the first two time steps $t = 1.2$ s and $t = 2.3$ s. At times $t = 3.5$ s and $t = 4.7$ s, the quality of the FVM results without extra techniques is still acceptable, but for $t = 5.9$ s, the deformation of the disk is larger than in the reference results. Afterward, the disk is transported faster through the fluid

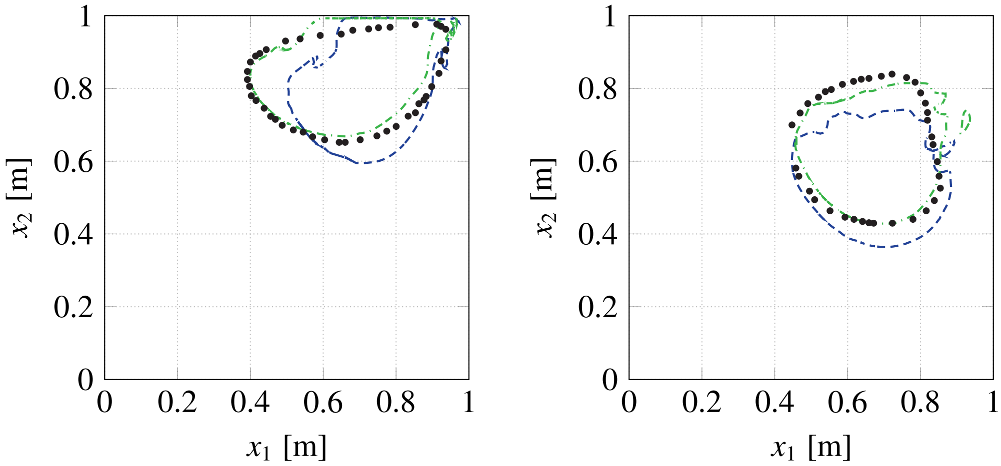

(a) 5.9 s (b) 7.0 s

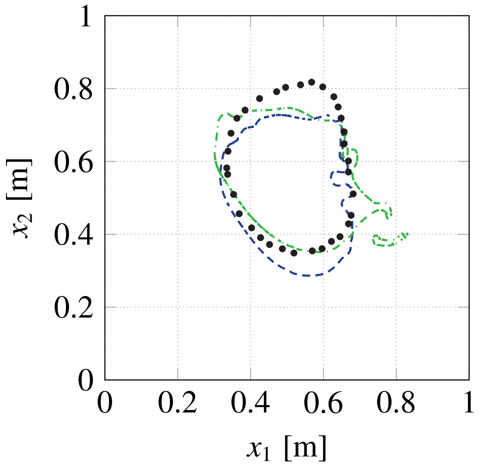

(c) 8.2 s

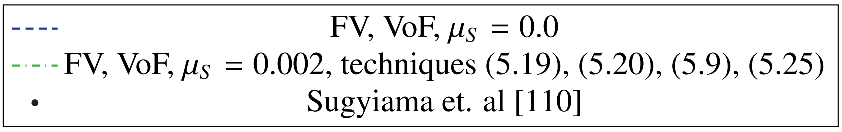

Figure 5.13: Evolution of the disk for an elastic incompressible Neo-Hookean medium immersed in a 2D lid-driven cavity during the last three time steps.

domain than the reference results.

The results of the present model using the additional numerical techniques presented in the previous Sec. 5.3.2 are displayed with the green line. The first three time steps coincide for the model configurations. At t = 4.7 s, a stiffer behavior of the elastic material can be observed for the model with additional techniques. This matches the slightly higher deviatoric stresses at the edges of the elastic material displayed in Figs. 5.10 and 5.11. At t = 5.9 s, the results of the model with additional numerical techniques are significantly closer to the literature results than without the techniques. As can be seen in Fig. 5.9, a different pressure field results for the two configurations due to the additional term on the RHS of the pressure equation in the Sugiyama approach (5.19). At t = 3.5 s, it can be seen that a higher pressure acts on the elastic disk at the upper boundary. This leads to the larger distance to the lid at the left side of the elastic material at t = 5.9 s for the results without extra techniques to fulfill the continuity equation.

Due to the left side and middle of the elastic material being positioned lower for results from the model without extra techniques at t = 5.9 s, the elastic disk is located roughly 0.1 m lower in the computational domain at t = 7.0 s than the disk from the model with extra techniques. The shape of the disk at that time is very similar for both configurations, both displaying difficulties in preserving one continuous shape on the right side of the material. For the results from the model with extra techniques, the upper boundary of the elastic disk is smoother, which is closer to the shape of the literature references.

At t = 8.2 s, the shift between positions of the disks is present only at the lower part between the results from the two model configurations. However, the shift is present for the whole material between results without additional numerical treatments and the literature values. Therefore the shape of the model results without additional numerical techniques is closer to the literature results at this time.

Overall the results from the model with additional numerical treatments coincide better with the literature values for this test case. This may follow from the fact that the reference values are data from other numerical models partly exhibiting the same additional numerical treatments.

Verification of Deformable Elastic Disk with Higher Stiffness in a 2D Lid-driven Cavity

The same test case which was described in the last paragraph with a higher stiffness η_S = 10.0 N/m^2 of the elastic material was investigated by Zhao et al. [140]. The FV, VoF method is evaluated against these results in Fig. 5.14. The elastic disk does keep its round shape during the simulation in the reference results from Zhao et al. [140] as well as in the present FV, VoF method. A slight deformation of the elastic disk occurs when it is close to the lid in both

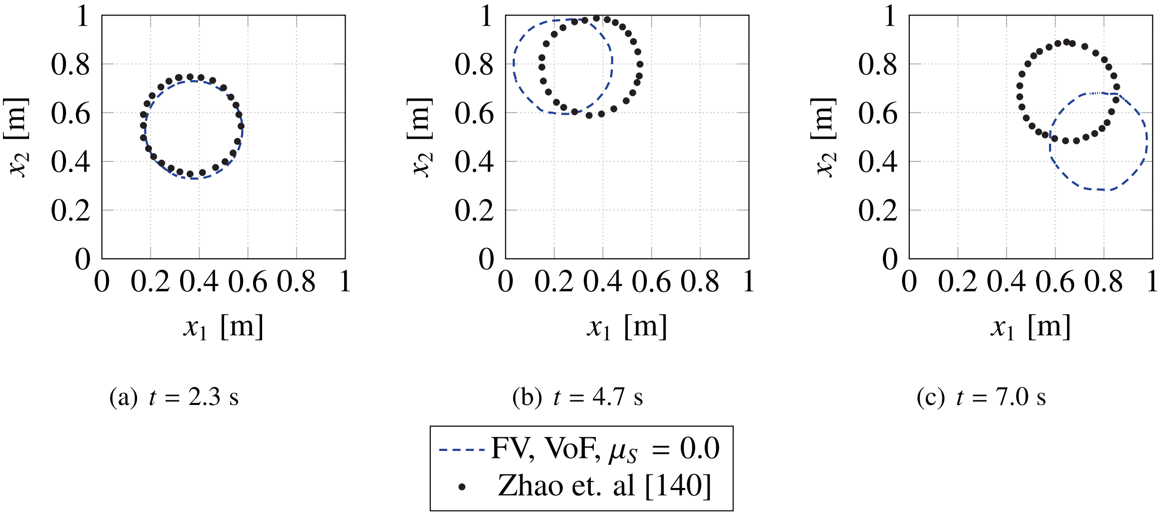

(a) $t = 2.3$ s (b) $t = 4.7$ s (c) $t = 7.0$ s

Figure 5.14: Evolution of the disk for an exemplary stiff (stiffness $\eta_S = 10.0$) elastic incompressible Neo-Hookean medium immersed in a 2D lid-driven cavity at selected three time steps.

methods. Nevertheless, the speed with which the disk moves in the domain is larger for the present method than for the reference simulations. This stems from differences in the pressure stagnation values in the top corners of the lid-driven cavity or the transmission of fluid forces on the disk at the elastic materials boundary. Since the application cases in this thesis will not include elastic material moving in a fluid of the same density but rather solid-skeleton/air interfaces, this disagreement needs to be studied in future research.

5.3.3 Deformation of an Elastic Wall in a Lid-Driven Cavity

Targeting for the application cases in this work, the behavior of a solid skeleton inside a vessel hold will be simulated. Therefore, this section discusses an additional test case closer to the application problem. In Dunne [26] and Zhao et al. [140], a two-dimensional lid-driven cavity including a fluid phase at the top and a neo-Hookean material phase at the bottom is introduced as a test case. Two similar cases are described in Dunne [27], and Richter et al. [104] with a different top lid speed definition and geometry. Results for both test cases are presented in Fig. 5.16. First, the case defined by Dunne [27] with an initial geometry as displayed in Fig. 5.15 and a domain length of $L = 2.0$ m is discussed.

The Lamé constant of the neo-Hookean material is $\eta_S = 2.0$ N/m^2, and the fluid viscosity is set to $\mu^A = 0.2$ Pa s. The fluid and neo-Hookean material have a density of $\rho^S = \rho^A = 1.0$ kg/m^3, and gravity is not considered. A different lid speed is applied to the top boundary than in the

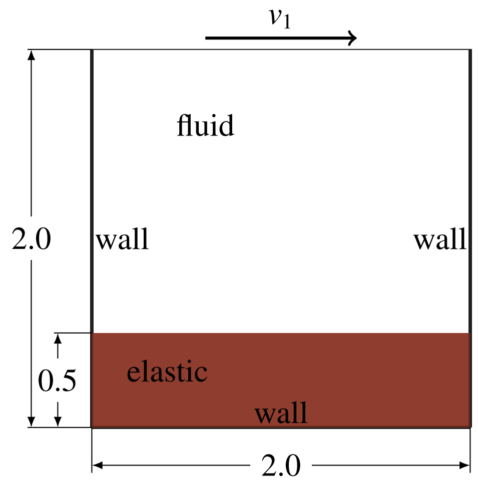

Figure 5.15: 2D elastic wall in cavity: Initial position of the elastic bottom in the lid-driven cavity given by Dunne [27] with dimensions given in meter.

test cases in the last section. Here, the lid is moving periodically, viz.

$$v_1 = 0.5 \begin{cases} 4x_1 \; m/s, & for \;\; x_1 \leq 0.3 \; m \\ 1 \; m/s, & for \;\; 0.3 \; m < x_1 < 1.7 \; m \\ 4(2 - x_1) \; m/s, & for \;\; x_1 \geq 1.7 \; m \; . \end{cases} \tag{5.34}$$

A regular mesh with $\Delta x_1 = \Delta x_2 = L/40$ is used to simulate the test case with the present FV, VoF method, and the time step is set to $\Delta t = 0.01$ s. The elliptic relaxation constant a_w is set to $a_w = 10^{-4}$. Primarily the test case is used to test the boundary conditions given in Sec. 5.2.2 for the neo-Hookean material. The factor F_{wall} is set to 10^3 for the boundary conditions in the momentum equations, and displacement as well as artificial solid velocity are set to zero at the walls.

In Fig. 5.16 (a), a good agreement can be observed for the present FV, VoF model results at $t = 100$ s with the literature values. In the published results by Richter et al. [104], the cavity has a length and height of $L = 1.0$ m and the elastic bottom has a height of 0.25 m. The lid speed is defined by $v_2 = 0$ m/s, $v_1 = 4x_1(1 - x_1)$ m/s. The present FV, VoF model results are obtained with a regular mesh with $\Delta x_1 = \Delta x_2 = L/64$ and $\Delta t = 5 \cdot 10^{-3}$ s. The elliptic relaxation constant is set to $a_w = 10^{-3}$, and the same boundary conditions (except the lid speed) are applied as for the last test case. Results of an elastic material with Lamé constant $\eta_S = 0.05$ N/m^2, a fluid viscosity set to $\mu^A = 0.01$ Pa s, and material densities $\rho^S = \rho^A = 1.0$ kg/m^3 are compared against Richter et al. [104] in Fig. 5.16 (b). As for the former test case, a good agreement can be found between present model results at $t = 10$ s and literature values, where the displacement of the present model is slightly higher than the reference.

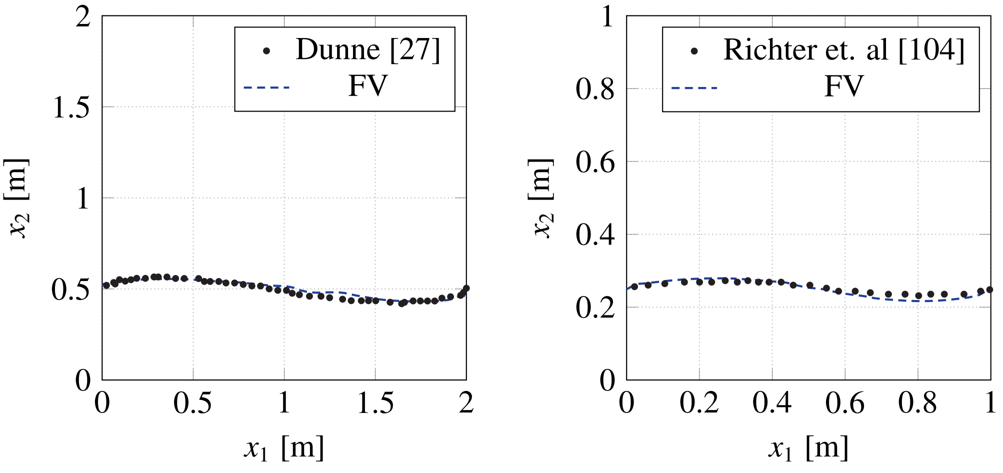

(a) Dunne [27]

(b) Richter et al. [104]

Figure 5.16: Comparison of present (FV) and literature reported bottom boundary shapes predicted for two different 2D lid-driven cavity cases using a neo-Hookean bottom material.

Overall, a good performance for the implemented present method can be observed for a neo-Hookean material in cavities. Nevertheless, the used neo-Hookean materials in all test cases are softer than the intended real-world applications.

Chapter 6

Application Studies

In this chapter, case studies are performed based on previously introduced models to show the applicability of the models for real-world granular cargo transport. As a starting point for the investigations, the incident conditions of the loss of the vessel ”Jian Fu Star” [85] will be described and cargo properties of iron ore fines and nickel ore are assembled from the literature. Then, results of 2D cargo hold simulations which are externally forced by various rolling motions are presented and finally a proof of concept of an entire 3D vessel in waves with granular cargo is carried out.

6.1 ”Jian Fu Star” Incident Conditions

One of the incidents of which the accident’s sequence of events is known is the sinking of the bulk carrier ”Jian Fu Star” on 27th October 2010. This is due to detailed reports given by the surviving seamen, which are included in the investigation of the ”Panama Maritime Authority” [85].

The incident occurred on 27th October after 21 hours of high Northerly winds between 5 and 8 Beaufort while sailing from Indonesia to South China. The vessel was pitching heavily, and water came on the forward deck. Due to the prevention of surcharge of the engines, the vessel speed was reduced to 4.5 kn. The rolling motion of the vessel was moderate [85]. The bulk carrier ”Jian Fu Star” had a length over all of 189.8 m, a width of 31.2 m, a summer draught of 11.43 m, and transported Indonesian nickel ore in five cargo holds. These are typical dimensions for a vessel experiencing a liquefaction/cargo shift incident (cf. Tab. 1.1). At the cargo loading before the incident, no immediate *MC* tests were carried out, and the cargo was distributed as given in Tab. 6.1 among the five holds depicted in Fig. 6.1.

The moisture content *MC* of the cargo on board ”Jian Fu Star” was certified to be 34.45%, and

Table 6.1: Stowage Plan of "Jian Fu Star" at time of the incident as given in the investigation of the "Panama Maritime Authority" [85]

Hold 1	6100 t	2542 m^3
Hold 2	9300 t	3875 m^3
Hold 3	9500 t	3958 m^3
Hold 4	9500 t	3958 m^3
Hold 5	9400 t	3917 m^3

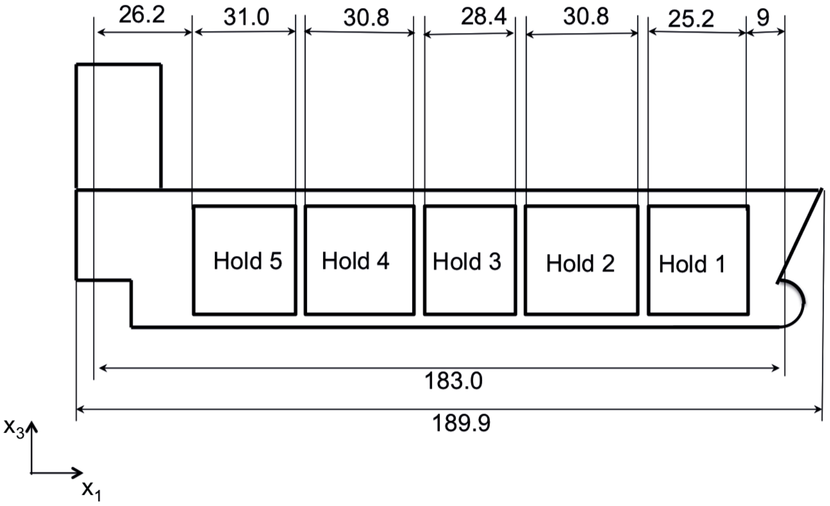

Figure 6.1: Arrangement of holds in bulk carrier "Jian Fu Star". Dimensions are given in meters.

the measured particle size did not exceed 200 mm. A can test was not repeated before leaving the port, and only a visual check of the cargo, which was reported to look "dry", was carried out. The incident report [85] concludes that a higher MC during carriage cannot be excluded and is the possible reason for cargo failure.

A first sudden list of 5° to port occurred at 7 AM on 27th October 2010, and ballast water pumping as counteraction was started. However, these measures did not have the desired effect, and the vessel further listed to 10°. The vessel then rolled around this list angle, taking on high seas on board, and sank 20 minutes after the first list had occurred. Twelve seamen were rescued, and thirteen seamen were lost.

6.2 Cargo Material Properties

Vessels lost due to cargo liquefaction/ cargo shift are listed in Tab. 1.1 in Sec. 1, and it can be seen that mostly iron ore fines and nickel ores are responsible for the deadly incidents. Therefore, in this chapter, a collection of cargo properties from the literature is presented and used for the setup of further studies.

Some terminology used in the next sections is defined first. The dry density ρ_d is defined as the grain mass divided by the total cargo volume and, therefore,

$$\rho_d = (1 - n)\rho^S + n\rho^A \ . \tag{6.1}$$

The last term can be neglected to simplify calculations due to the high-density ratio between air and soil grains. The wet density ρ_{wet} is the overall cargo density (total mass by total volume) and, therefore

$$\rho_{wet} = (1 + w_c)\rho_d \tag{6.2}$$

with w_c being the water content m^W/m^d (water mass divided by dry soil mass). In this relation, the air mass is neglected. Another related measure is the moisture content MC which is defined by the IMO to be the water mass inside the cargo divided by the total cargo mass (also called wet mass) $MC = m^W/m^{total}$. The moisture content MC relates to the water content w_c via

$$MC = w_c \frac{\rho_d}{\rho_{wet}} \ . \tag{6.3}$$

Finally, the degree of saturation s^W is given by V^W/V^F (water volume divided by void volume), and the void ratio e associates with the porosity n via

$$n = \frac{e}{1 + e} \ . \tag{6.4}$$

6.2.1 Nickel Ore Properties

Mechanical properties of eight nickel ore samples from two different locations are given in the "Guidelines for safe carriage of nickel ores" by ClassNK [12] and are reported in the appendix in Tab. C.1. The angle of repose ϕ together with the given cohesion C defines the material's yield stress in the above perfectly-plastic granular model. Both properties were obtained by tri-axial testing. Also, results of DEM simulations are reported in the ClassNK guidelines [12], and the properties chosen for these simulations are given in the appendix in Tab. C.2, where the given density is the wet density ρ_{wet}. Simulation condition one represents the Indonesian sample at a MC of 29 %, and the second simulation condition "expresses a typical behavior of nickel cargo" [12].

As a second source for nickel ore properties, results from the French Institute of Science and Technology for Transport, Development and Networks (IFSTTAR) presented at a project meeting in Hamburg [115] are used in this study. The examined nickel ore sample has a natural water content w_c of 49%, a mean particle diameter of $D_{50} = 10^{-4}$ m, and a grain density of $\rho^S = 3.66$ g/cm^3. Dry density ρ_d is measured at set water contents, and four of these values are reported in Tab. C.3. The wet density ρ_{wet} is determined from the dry density and water content by Eqn. (6.2) and the porosity from Eqn. (6.1).

From the wet density given in the appendix in Tab. C.3, it can be concluded that the second simulation condition in the appendix in Tab. C.2 has a MC below 23 %. Derived from the presented information, the nickel ore properties applied for the simulations are a grain density of 3660 kg/m^3, a porosity of $n \approx 0.62$, a cargo density (wet density) between 1700 kg/m^3 and 2000 kg/m^3 and a dry density between 1300 kg/m^3 and 1450 kg/m^3. Therefore, the constitutive properties for drier soil can be taken as simulation condition one or two in the appendix in Tab. C.2 and for wetter soil (also exceeding moisture limit) as e.g., $\phi = 0°$ and $C = 2700$ Pa.

6.2.2 Iron Ore Fines Properties

The material properties of iron ore fines are collected from four different sources. First, the IFSTTAR sample test results [115] present an iron ore grain density $\rho^S = 4.89$ g/cm^3 and mean grain diameter of $D_{50} = 2 \cdot 10^{-4}$ m. For water contents w_c between 4% and 11%, the iron ore dry density is around $\rho_d = 3.0$ g/cm^3. Therefore the wet density follows to be between $\rho_{wet} = 3.12$ g/cm^3 and $\rho_{wet} = 3.33$ g/cm^3 and the porosity n is 0.39.

Corresponding values are given by Wang et al. [129] for two samples of iron ore fines. The mean grain diameter D_{50} in one sample equals 10^{-3} m; in the other, it is $2 \cdot 10^{-3}$ m. The grain densities are 4.44 g/cm^3 and 4.84 g/cm^3, respectively, and the iron ore dry density is found to be 2.79 g/cm^3 for a water content w_c of 12%. Therefore the wet density ρ_{wet} of iron ore fines gets 3.13 g/cm^3.

A higher number of samples of one heap of iron ore fine was studied by Munro et al. [90]. The grain density was found to be $\rho^S = 4.15$ g/cm^3, which is slightly smaller than in the two studies presented before, and the mean grain diameter coincides with the second sample of Wang et al. [129] ($D_{50} = 2 \cdot 10^{-3}$ m). The different samples' other material properties, including the needed constitutive properties, are given in Tab. C.4 in the appendix.

For the coupled model, the porous cargo's resistance force must be calculated. In Marinho et. al [86] the saturated iron ore permeability k is found to be smaller than $8.9 \cdot 10^{-4}$ m/s.

Deriving specific material properties from the given information for simulations leads to a grain density of $\rho^S \approx 4500 \text{kg/m}^3$, a mean grain diameter of 10^{-3} m, a dry density of around 2700 kg/m^3 and a wet density of 3100 kg/m^3. The porosity is around $n = 0.4$, the angle of repose $\phi \approx 44°$, and the cohesion $C \approx 2.0 \cdot 10^4$ Pa.

6.3 Modeling of Granular Cargo in 2D Holds

This section introduces a two-dimensional model of an externally accelerated hold. Results for rigid-perfectly plastic cargo, cf. Chapt. 3, and unsaturated granular cargo (coupled approach), cf. Chap. 4, are presented in this section. The Drucker-Prager yield criterion is applied in both models. Since the cargo shape can be arbitrary, different loaded cargo scenarios, material properties, and several rolling motions are simulated. The coupled approach simulates both the ”wet base” scenario and the ”dynamic separation” scenario, and the rigid-perfectly plastic models simulates ”cargo shifting”.

The first-oder implicit Eulerian time discretization is applied for all cases in this section. The QUICK scheme is used to discretize the convective flux in the momentum equations, and the HRIC scheme is applied for convective flux in the mixture equations.

One hold of the generic ”Oldendorff” bulk carrier is chosen for the two-dimensional tank studies since the generic bulk carriers’ dimensions are similar to the dimensions of the ”Jian Fu Star”. The hold geometry depicted in Fig. 6.2 is taken from a construction plan from the generic ”Oldendorff” bulk carrier provided by ”Oldendorff Carriers” [21] and serves as the computational domain with a length of $L = 32.26$ m. An unstructured mesh is used for the

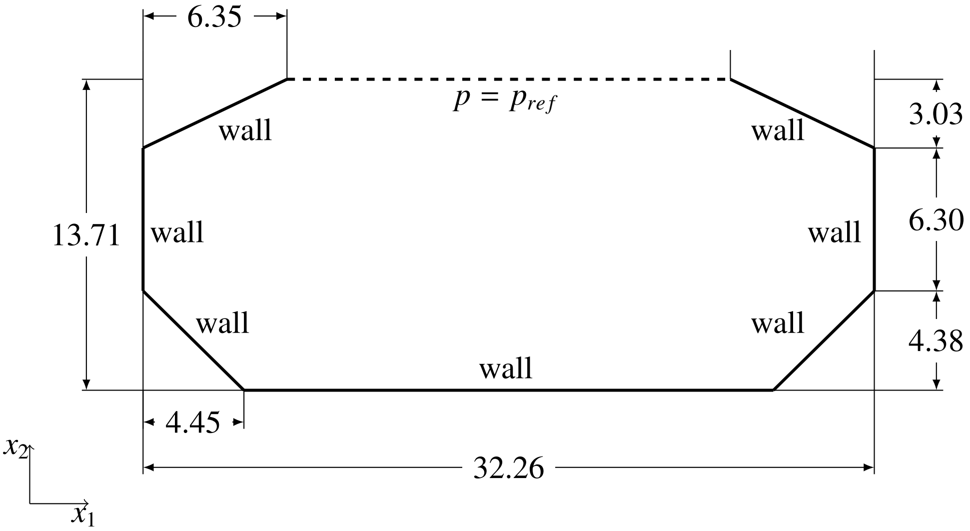

Figure 6.2: 2D vessel hold: Geometry of the hold of a generic ”Oldendorff” bulk carrier, all measurements given in meters.

simulations in this section which consists of 194252 predominantly quadratic cells with a size of $\Delta x_1 = \Delta x_2 = L/1075$ where the cargo is initialized and coarsening of the cells towards the top of the domain. In the vicinity of the domain boundaries, the cells are not rectangular. A time step of $\Delta t = 5 \cdot 10^{-4}$ s is applied for all simulations in this section. The gravitational load inside the cargo is initialized by applying a hydrostatic pressure inside the granular material. All other variables are initially at rest. The computational domain is bounded by all walls of the hold, applying wall boundary conditions, and the dashed line at the top of the domain, at which the pressure is set as Dirichlet boundary condition to the reference pressure of zero Pascal.
Furthermore, the factor m_c (which determines the maximum viscosity in Eqn. (3.22)) is set to be 10^3 and the factor N for the nonlinear treatment of soil properties at the interface (cf. Sec. 3.52) is 5 with M being zero.

6.3.1 External Acceleration Defining the Rolling Motion of the Vessel

The rolling motion of the hull is simulated by using a static mesh, and the rotation of the gravity vector around the x_3-axis by defining a body force vector b_i. The body force vector b_i replaces the gravity vector g_i in the momentum equations. The general external body force vector due to translational and rotational motions in the moving coordinate system (coordinate system moving with the hold) b_i^l is given by

$$b_i^l = g_i - a_i - \epsilon_{ijk}\frac{d\omega_j}{dt} r_{P,k} - 2\epsilon_{ijk}\omega_j\frac{dr_{P,k}}{dt} - \epsilon_{ijk}\omega_j\epsilon_{kmn}\omega_m r_{P,n} \tag{6.5}$$

as stated e.g. in Arai et al. [2] and Zou et al. [141]. Here g_i denotes the gravitational acceleration, and a_i is the acceleration due to translational motions. The third term represents the acceleration due to angular forces where ω_i is the angular velocity vector and $r_{P,i}$ denotes the vector between the center of gravity of the rigid moving hold and a certain point P in the hold. The fourth term accounts for the acceleration due to the Coriolis force, and the fifth term represents centrifugal forces. Since the vector b_i^l is now given in the moving coordinate system, a transformation has to be carried out before it can be applied to the present fixed computational domain.
Since only rotational rolling motion around the x_3-axis will be applied in the following cases ($\omega_1 = \omega_2 = 0$, $a_1 = a_2 = a_3 = 0$) and gravity is acting in the x_2-direction, Eqn. (6.5) can be expressed as

$$b_i^l = \begin{bmatrix} 0 \\ -g \end{bmatrix} - \begin{bmatrix} -\frac{d\omega_3}{dt} r_{P2} \\ \frac{d\omega_3}{dt} r_{P1} \end{bmatrix} - 2\begin{bmatrix} \omega_3 \frac{dr_{P2}}{dt} \\ \omega_3 \frac{dr_{P1}}{dt} \end{bmatrix} - \begin{bmatrix} -\omega_3^2 r_{P1} \\ -\omega_3^2 r_{P2} \end{bmatrix} . \tag{6.6}$$

To further simplify, the distances between the points in the hold and the center of gravity do not change over time, and therefore the rate $dr_{P,i}/dt$ is equal to zero, and the external acceleration vector in moving coordinates gets

$$b_i^l = \begin{bmatrix} \frac{d\omega_3}{dt} r_{P2} + \omega_3^2 r_{P1} \\ -g - \frac{d\omega_3}{dt} r_{P1} + \omega_3^2 r_{P2} \end{bmatrix} . \tag{6.7}$$

The forced rolling motion of the hull is described via the time-dependent roll angle α_R

$$\alpha_R = A_R \sin\left(\frac{2\pi}{T_R} t\right) \tag{6.8}$$

where A_R is the maximum amplitude and T_R is the period of the rolling motion. Therefore the angular velocity around x_3 gets

$$\omega_3 = \frac{2\pi}{T_R} A_R \cos\left(\frac{2\pi}{T_R} t\right) \tag{6.9}$$

and the angular acceleration is

$$\frac{d\omega_3}{dt} = -\left(\frac{2\pi}{T_R}\right)^2 A_R \sin\left(\frac{2\pi}{T_R} t\right) . \tag{6.10}$$

To transform the vector b_i^l to the fixed reference system, the transformation matrix of a 2D rotation around the x_3-axis with angle α_R is multiplied with b_i^l to obtain

$$\begin{aligned} b_i &= \begin{pmatrix} \cos\alpha_R & -\sin\alpha_R \\ \sin\alpha_R & \cos\alpha_R \end{pmatrix} \cdot \begin{pmatrix} \frac{d\omega_3}{dt} r_{P2} + \omega_3^2 r_{P1} \\ -g - \frac{d\omega_3}{dt} r_{P1} + \omega_3^2 r_{P2} \end{pmatrix} \\ &= \begin{pmatrix} \cos\alpha_R \left(\frac{d\omega_3}{dt} r_{P2} + \omega_3^2 r_{P1}\right) + \sin\alpha_R \left(g + \frac{d\omega_3}{dt} r_{P1} - \omega_3^2 r_{P2}\right) \\ \sin\alpha_R \left(\frac{d\omega_3}{dt} r_{P2} + \omega_3^2 r_{P1}\right) + \cos\alpha_R \left(-g - \frac{d\omega_3}{dt} r_{P1} + \omega_3^2 r_{P2}\right) \end{pmatrix} . \end{aligned} \tag{6.11}$$

6.3.2 2D Holds with Rigid Perfectly-Plastic Granular Cargo

The granular model described and validated in chapter 3 is used to study different cargo scenarios in a two-dimensional hold accelerated by the external forcing given in Sec. 6.3.1. Three different initial cargo shapes with varying steepness are studied. Also, cargo behavior with two different sets of material properties is compared, and two different rolling angles are simulated. In all simulations, the vessel's center of gravity (*CoG*) is set to be in the middle of the hold in the x_1-direction ($CoG_{x_1} = 16.13$ m) and at 7.6 m in the x_2-direction. Since the rigid perfectly-plastic granular model describes the properties of the whole soil, including the water, the wet density ρ_{wet} is used.

Variation of Initial Cargo Shapes

The first study includes three differently initialized cargo shapes. As material properties, an Indonesian nickel ore with *MC* around 26% is selected from Tab. C.1 in the appendix providing

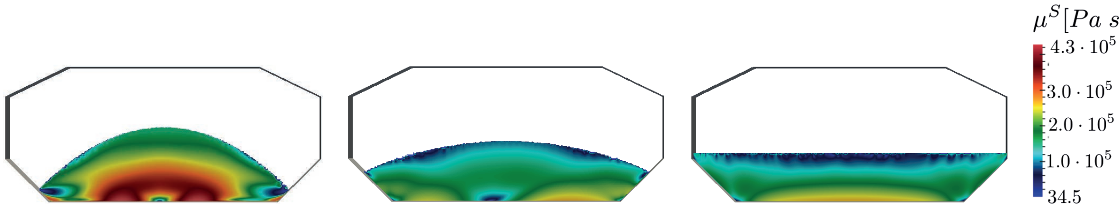

(a) $h_{max} = 7.750$ m; $s = 0.040$ (b) $h_{max} = 6.200$ m; $s = 0.015$ (c) $h_{max} = 4.977$ m; $s = 0.000$

Figure 6.3: 2D vessel hold: Static pressure induced viscosity field values inside the cargo heap for rigid-perfectly plastic cargo with properties $\phi = 7.4°$, $C = 7.9$ kPa and $\rho_{wet} = 1.7 \cdot 10^3$ kg/m^3 at time $t = 1.0$ s for varied loading scenarios.

the material properties as $\phi = 7.4°$, $C = 7.9$ kPa and $\rho_{wet} = 1.7 \cdot 10^3$ kg/m^3. The shape of the initial cargo heap is defined by the quadratic function

$$h_{cargo}(x_1) = h_{max} - s\,(x_1 - 16.13)^2 \tag{6.12}$$

where h_{cargo} is the pile height over the x_1-axis, h_{max} is the maximum pile height and s determines the steepness of the pile. The mass of cargo is kept constant in this study. The steepest cargo heap initialization uses a maximum pile height of $h_{max} = 7.75$ m and steepness of $s = 0.04$, the flatter heap of cargo is initialized with a maximum pile height of $h_{max} = 6.2$ m and steepness of $s = 0.015$ and the completely flat loaded cargo with a maximum pile height of $h_{max} = 4.977$ m. As an external forcing, a pure rolling motion of the cargo hold with a roll angle of 5° and a rolling period of 10 s is applied.

In Fig. 6.3, the viscosity of the granular cargo is plotted at time $t = 1.0$ s for the three different loading scenarios, and the influence of the pile height respectively the soil pressure on the viscosity can be observed at an early time step where the static soil pressure plays a dominant role. Higher viscosities follow from large static soil pressure induced by higher cargo piles.

Considering the norm of the Euler-Almansi strain $||e_{ij}||$, cf. (3.35), displayed for the different loading scenarios at time steps $t = 1.0$ s, $t = 20.0$ s, $t = 40.0$ s and $t = 60.0$ s in Fig. 6.4, the settling of the cargo heaps can be observed. Due to the angle of repose being only $\phi = 7.4°$, the initial heap geometries of the steeper cargo heaps cannot be preserved. When the cargo is loaded flat, the likelihood of cargo shift is greatly reduced. Interestingly, a lump in the middle of the cargo hold growing with time can be observed for all initial loading conditions, being most pronounced for the steepest initial heap. Cargo sliding occurs for the steepest heap and therefore, the viscosity from the Bingham rigid-plastic approach is smaller at later time steps than for the other heap configurations, leading to more dynamic behavior when externally accelerated. The circular nature of the external forcing triggers the lump close to the center of gravity in the hold.

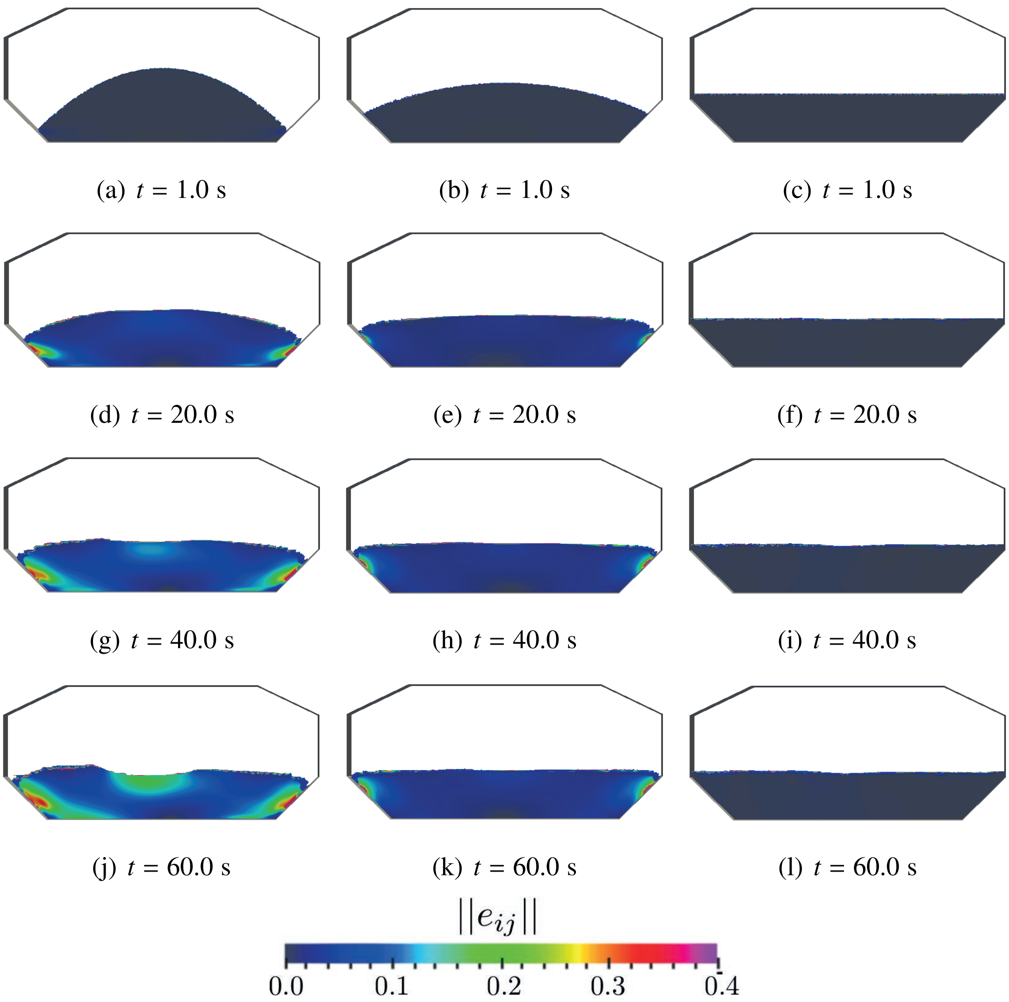

(a) $t = 1.0$ s (b) $t = 1.0$ s (c) $t = 1.0$ s

(d) $t = 20.0$ s (e) $t = 20.0$ s (f) $t = 20.0$ s

(g) $t = 40.0$ s (h) $t = 40.0$ s (i) $t = 40.0$ s

(j) $t = 60.0$ s (k) $t = 60.0$ s (l) $t = 60.0$ s

Figure 6.4: 2D vessel hold: Deviatoric Euler-Almansi strain norm field values inside cargo heap for rigid-perfectly plastic cargo with properties $\phi = 7.4°$, $C = 7.9$ kPa and $\rho_{wet} = 1.7 \cdot 10^3$ kg/m^3 at four different time steps for varied loading conditions. Left: $h_{max} = 7.750$ m; $s = 0.040$, Middle: $h_{max} = 6.200$ m; $s = 0.015$, Right: $h_{max} = 4.977$ m; $s = 0.000$.

Variation of Cargo Material Properties

The second comparison of cargo behavior is carried out between simulations with two different materials: Indonesian nickel ore with MC around 26% ($\phi = 7.4°$, $C = 7.9$ kPa, $\rho_{wet} = 1.7 \cdot 10^3$ kg/m^3, cf. Tab. C.1) and nickel ore from the Philippines with a MC of 45% ($\phi = 0°$, $C = 2.7$ kPa, $\rho_{wet} = 2.05 \cdot 10^3$ kg/m^3, cf. Tab. C.1). Both simulations are initialized with a flat cargo pile, and the external rolling is applied with a period of $T = 10$ s and amplitude of $A_R = 5°$. The factor m_c in Eqn. (3.22) is $5 \cdot 10^2$ for both cases.

The resulting norm of the Euler-Almansi strain $||e_{ij}||$ for both materials is compared in Fig. 6.5 for different time steps. Again, the influence of the high gradients in the resulting Eulerian displacement due to the definition of the soil velocity (explained in chapter 3) can be seen in the high strains at the soil/air boundary. Both materials exhibit small displacements for the rolling amplitude of 5° at all time steps, and therefore the shape of the cargo boundary only visibly differs at time $t = 50$ s. Looking at the norm of the Euler-Almansi strain, it can be seen that for the defined wet nickel ore, the strain is around double the strain of the drier nickel ore for all time steps. The normal integrated pressure and viscous forces over the bottom right diagonal

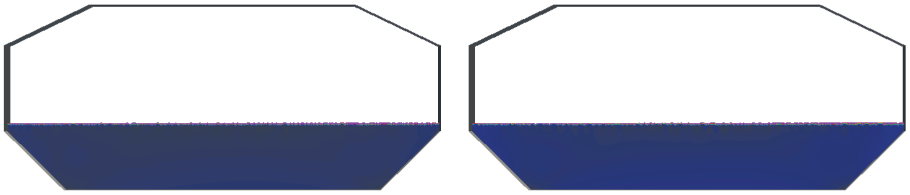

(a) $t = 1.0$ s (b) $t = 1.0$ s

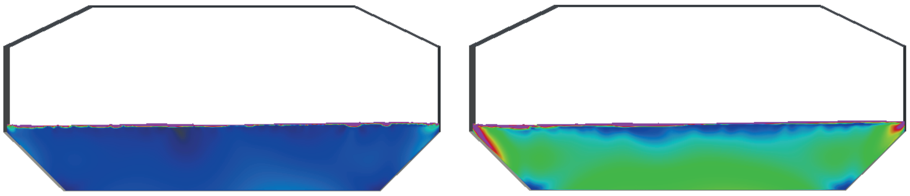

(c) $t = 15.0$ s (d) $t = 15.0$ s

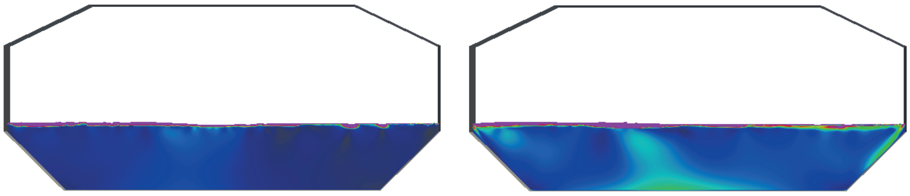

(e) $t = 30.0$ s (f) $t = 30.0$ s

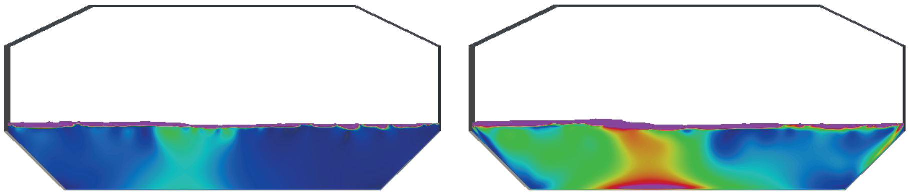

(g) $t = 50.0$ s (h) $t = 50.0$ s

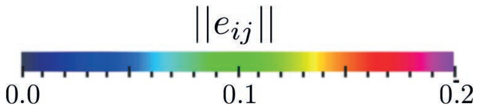

Figure 6.5: 2D vessel hold: Deviatoric Euler-Almansi strain norm field values inside flat loaded cargo heap at four different time steps for different rigid-perfectly plastic cargo material properties. Left: Indonesian nickel ore with *MC* around 26% ($\phi = 7.4°$, $C = 7.9$ kPa, $\rho_{wet} = 1.7 \cdot 10^3$ kg/m^3); Right: nickel ore from the Philippines with a *MC* of 45% ($\phi = 0°$, $C = 2.7$ kPa, $\rho_{wet} = 2.05 \cdot 10^3$ kg/m^3).

wall of the hold are plotted over time in Fig. 6.6. Two observations can be made: the mean over time of the total forces of the wet material is higher than for the dry material. This results

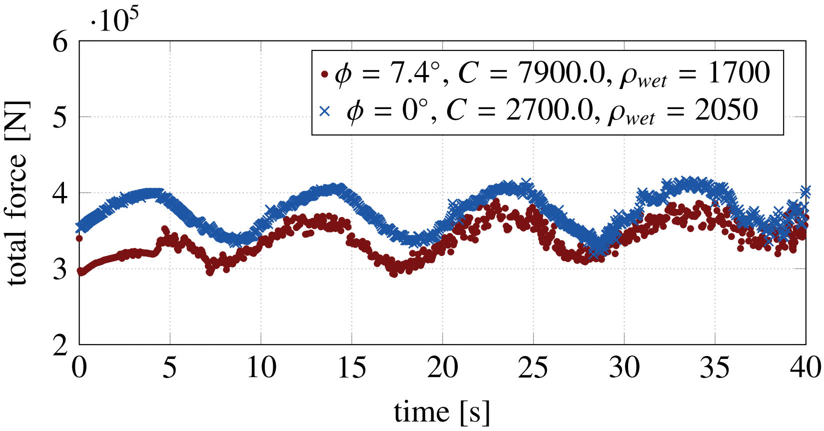

Figure 6.6: 2D vessel hold: Total normal force (pressure and viscous forces) acting on the right diagonal bottom wall for varying cargo properties of a flat loaded rigid-perfectly plastic cargo.

from the higher wet density of the wet material. Secondly, the total normal force of the wetter material has a smoother trend than that of the drier material, which can be explained by the higher maximum viscosity μ_{max} obtained by the increased cohesion and angle of repose. Due to small changes in the velocity gradient, greater changes in the viscous forces are obtained. Overall the rigid-perfectly plastic approach leads to oscillating forces at the walls, which could be improved by an elasto-plastic approach.

Variation of Rolling Motion

Another exemplary study with the rigid-perfectly plastic granular model in a two-dimensional hold is the behavior of the cargo due to a variation of the rolling motion defined by Eqn. (6.11). Again the cargo is initialized as a plane with the maximum height h_{max} of the cargo being 4.977 m. To study what possibly happens in a cargo vessel experiencing a cargo shifting incident, the relatively wet nickel ore (MC of 45%) with properties $\phi = 0°$, $C = 2.7$ kPa and $\rho_{wet} = 2.05 \cdot 10^3$ kg/m^3 is loaded into the 2D hold and exposed to three different rolling motions. Two of the rolling motions (amplitude A_R being 5° and 2°) are defined with a period of $T = 10$ s, and the third movement has a period of $T = 15$ s with an amplitude of $A_R = 10°$.

As in the last sections, a comparison of the accumulated strain for the different rolling motions is displayed in Fig. 6.7. For the rolling motions with lower amplitudes 2° and 5° the flat loaded cargo does not experience cargo shift. The small displacements lead to small strain values wherever a rolling motion with a 10° amplitude leads to cargo shifting for the given material properties. For the rolling motion with amplitude 10°, the slip plane can be observed clearly in Fig. 6.7 at $t = 15$ s and $t = 45$ s.

In Fig. 6.7 (f), a time step shortly after the maximum amplitude of the rolling motion has

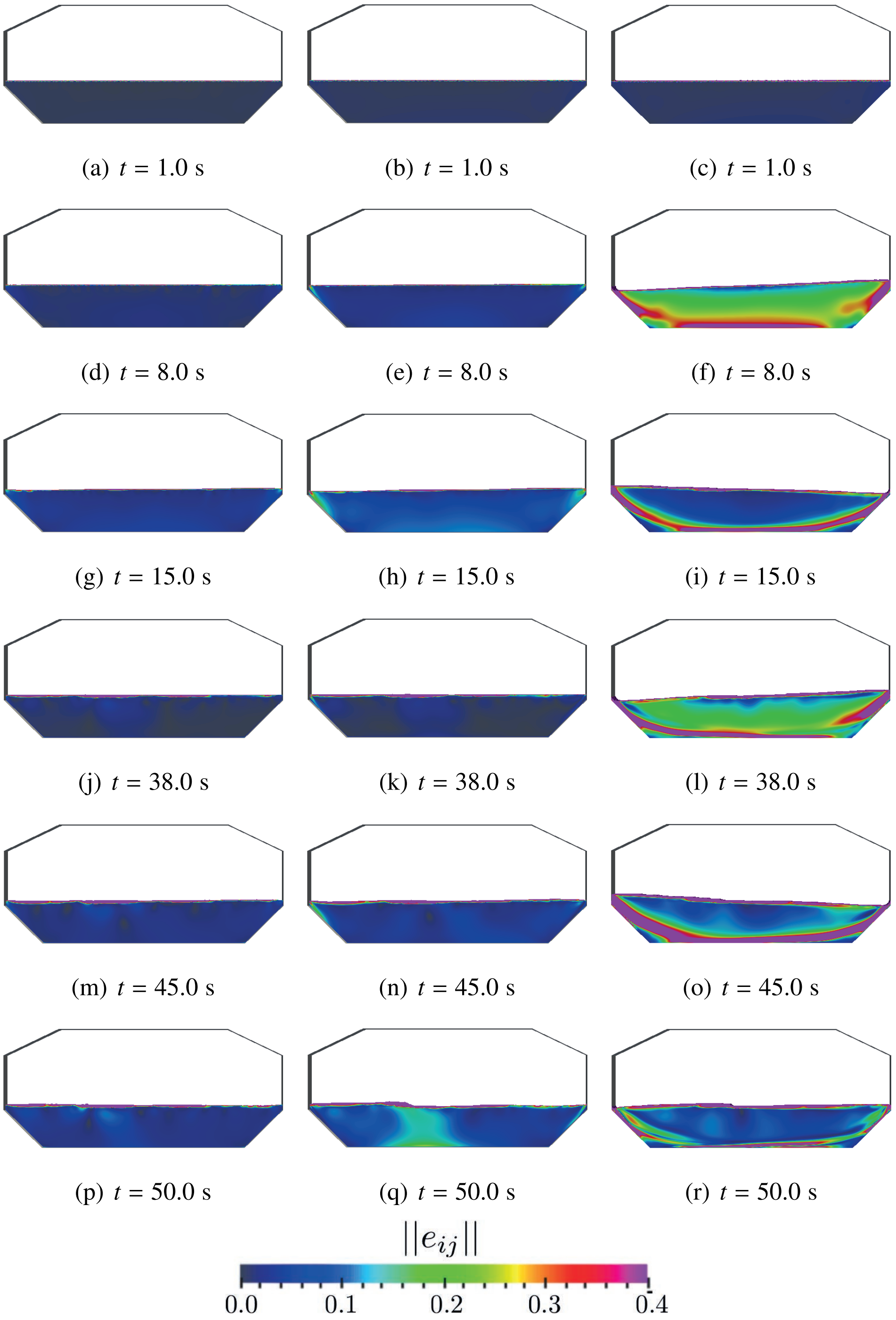

Figure 6.7: 2D vessel hold: Deviatoric Euler-Almansi strain norm field values inside flat loaded cargo heap at six different time steps for rigid-perfectly plastic cargo (properties $\phi = 0°$, $C = 2.7$ kPa and $\rho_{wet} = 2.05 \cdot 10^3$ kg/m^3) and varied rolling motions. Left: amplitude $A_R = 2°$, period $T = 10$ s; Middle: amplitude $A_R = 5°$, period $T = 10$ s; Right: amplitude $A_R = 10°$, period $T = 15$ s .

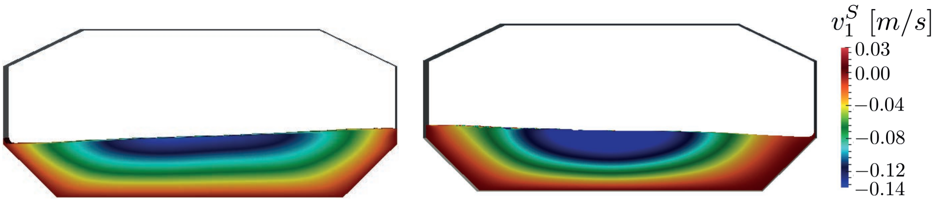

(a) t = 8.0 s (b) t = 15.0 s

Figure 6.8: 2D vessel hold: Field value of the solid velocity in x_1 -direction in the flat loaded rigid-perfectly plastic (properties $\phi = 0°$, $C = 2.7$ kPa and $\rho_{wet} = 2.05 \cdot 10^3$ kg/m^3) cargo heap at two time steps which differ in the Euler-Almansi strain norm patterns.

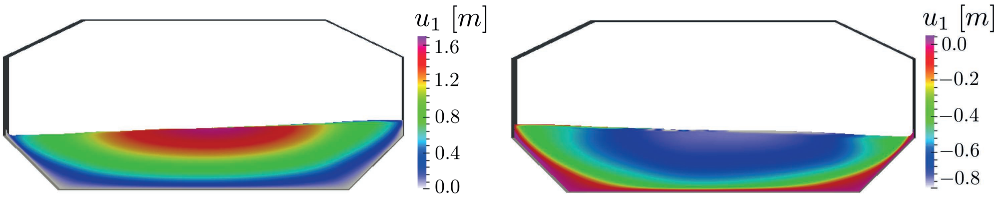

(a) t = 8.0 s (b) t = 15.0 s

Figure 6.9: 2D vessel hold: Field value of the displacement in x_1 -direction in the flat loaded rigid-perfectly plastic (properties $\phi = 0°$, $C = 2.7$ kPa and $\rho_{wet} = 2.05 \cdot 10^3$ kg/m^3) cargo heap at two time steps which differ in the Euler-Almansi strain norm patterns.

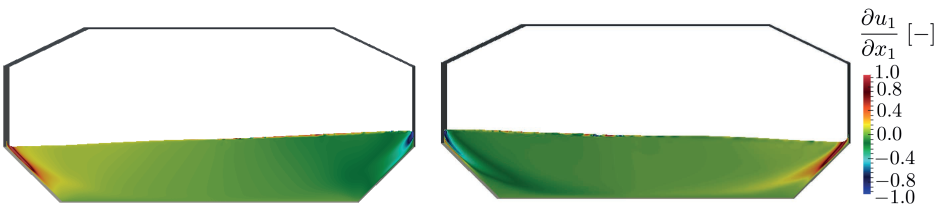

(a) t = 8.0 s (b) t = 15.0 s

Figure 6.10: 2D vessel hold: Field value of first component of the displacement gradient in the flat loaded rigid-perfectly plastic (properties $\phi = 0°$, $C = 2.7$ kPa and $\rho_{wet} = 2.05 \cdot 10^3$ kg/m^3) cargo heap at two time steps which differ in the Euler-Almansi strain norm patterns.

occurred is displayed. It is interesting to note that at this time step and in Fig. 6.7 (l) and 6.7 (r), the slip plane is discontinuous. To display the underlying mechanism, the cargo velocity, displacement, and gradient of the displacement in the x_1-direction are shown at $t = 8.0$ s and $t = 15.0$ s in Figs. 6.8, 6.9 and 6.10. The granular cargo is moving with a slight positive velocity in the x_1-direction close to the wall of the cargo hold. In the middle top of the cargo pile, the cargo moves in the negative x_1-direction with a higher speed at both time steps. It has to be noted that the cargo or solid velocity in the x_1-direction is obtained from Eqn. (3.34) and is displayed in Fig. 6.8 inside the cargo volume. Resulting from the integration of the cargo velocity, the displacement in the x_1-direction is shown in Fig. 6.9 where a change in sign can be observed at $t = 15$ s. It can also be noted that due to the integration of Eqn. (3.34), the displacement at the upper boundary of the cargo is artificially low since the velocity is multiplied by the phase values in Eqn. (3.34). This leads to high displacement gradients (cf. Fig. 6.10) at the top of the cargo pile and, therefore, to the observed high values of the deviatoric Euler-Almansi strain norm at the interface between air and granular materials in all previous and following results. The reason for the difference in slip plane appearance between time $t = 8$ s and $t = 15$ s results from the difference in displacement gradient. When the displacement is entirely positive or negative as at $t = 8$ s, the slip plane is discontinuous in the lower corners of the hold due to a smaller displacement gradient than when a sign change of displacement induces large displacement gradients, cf. $t = 15.0$ s in Fig. 6.10. The values for the x_2-direction are not displayed here but lead to the same conclusion.

The total integrated normal force consisting of pressure and viscous forces on the bottom right diagonal wall of the cargo hold is displayed in Fig. 6.11 for the three different rolling motions. The motion periods directly translate into the periods of the forces. Interestingly the shape of the total force over time for the 10° rolling motion is not sinusoidal but resembles an inertia triggered zig-zag function induced by the abrupt slipping of the cargo.

6.3.3 2D Holds with Granular Cargo Including a Water Phase

This section applies the coupled model of a free surface flowing through a dry granular material described in chapter 4 to the cargo inside the two-dimensional cargo hold. Different initializations of the water content inside the cargo are simulated. Furthermore, the coupled model is used to study both a material with a saturation-dependent cohesion and one with a cohesion independent of the saturation. It is focused on three scenarios due to the immiscible formulation of the present water-air free surface formulation: a cargo heap with a wet base layer, a cargo heap with a wet top layer, and a cargo heap with a pure water layer on top. The last two

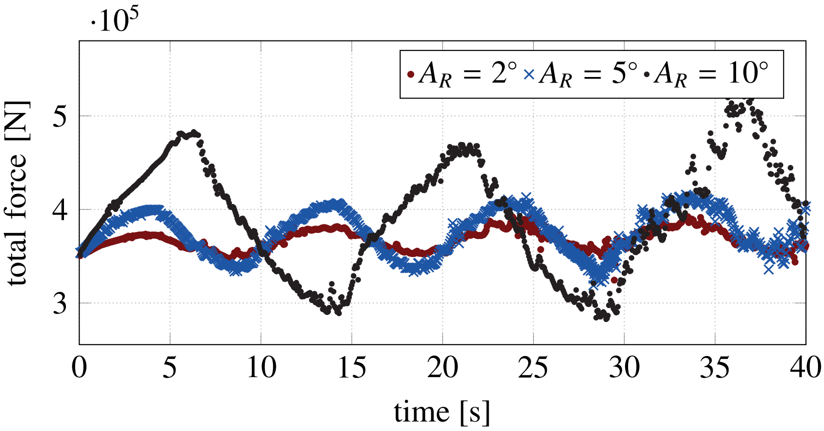

Figure 6.11: 2D vessel hold: Total normal force (pressure and viscous forces) acting on the right diagonal bottom wall for varying external rolling motion of a flat loaded rigid-perfectly plastic cargo.

scenarios study the cargo behavior after ”dynamic saturation” has occurred.

The same mesh as in the previous Sec. 6.3.2 is used for the simulations, as well as the same time step and identical settings for the discrete equations. Also the Drucker-Prager yield criterion is applied as the granular skeletons’ constitutive equation.

Since in the coupled approach, the granular phase consists of the soil skeleton with the grain density ρ^S, the overall density follows from the water and air densities (ρ^W, ρ^A) as well as the porosity n and phase concentrations (c_S, c_A)

$$\rho_{wet} = c_S \left((1-n)\rho^S + n\left(c_A \rho^A + (1-c_A)\rho^W \right) \right) . \tag{6.13}$$

If not mentioned otherwise in the following sections, the material properties for the general cargo are chosen to resemble the property condition one of the DEM studies by ClassNK given in the appendix in Tab. C.2 and therefore, the wet density ρ_{wet} is equal to $1.75 \cdot 10^3$ kg/m^3, the angle of repose $\phi = 4°$ and cohesion 7.8 kPa. From a porosity of $n = 0.62$, which follows from the nickel ore properties given by IFSTTAR (cf. Tab. C.3), together with the water density ρ^W set to $1.025 \cdot 10^3$ kg/m^3 and the air density ρ^A set to 1.2 kg/m^3, a grain density ρ^S of $3.66 \cdot 10^3$ kg/m^3 is calculated. The grain diameter is taken from the IFSTTAR results to be $D_{50} = 10^{-4}$ m, and since the small diameter leads to low permeability, the Darcy resistance law is adopted. The factor $\tilde{A}$ is calculated by Ergun’s porous resistance force model (cf. Tab. 2.1) with a factor α equal to 10^2.

Studies of Unsaturated Cargo with Fully Saturated Bottom Layer and Saturation-Based Cohesion - Wet Base

A possible cargo failure mechanism already mentioned in the report of the ”Technical Working Group” [56] is the ”wet base” theory. This theory assumes that the water inside the unsaturated cargo settles down over time, leading to a fully saturated bottom layer of the cargo and drier cargo at the top of the cargo pile. A second way a ”wet base” is formed could be by intentionally loading the wet cargo underneath dry cargo according to [109].

Figure 6.12 displays the initialization of the phases for the simulations studying the ”wet base” failure mechanism. The water surface is initialized as a plane. Therefore, depending on the water level height, the so-called expressed water is present at the beginning of the simulations. The term ”expressed water” is used for water pressed out of the wet cargo during the vessel’s voyage by compression of the soil skeleton. It has to be noted that the real domain geometry is still the hold geometry displayed in Fig. 6.2 for all simulated cases. The soil skeleton’s cohesion depends linearly on the saturation level as in Eqn. (4.59) and therefore is set to a smaller value for the wet base layer than for the drier cargo. Here, the cohesion of the unsaturated cargo is 7.8 kPa (where c_A is equal to one), and the cohesion of the fully saturated cargo (wet base layer) is 1.0 kPa.

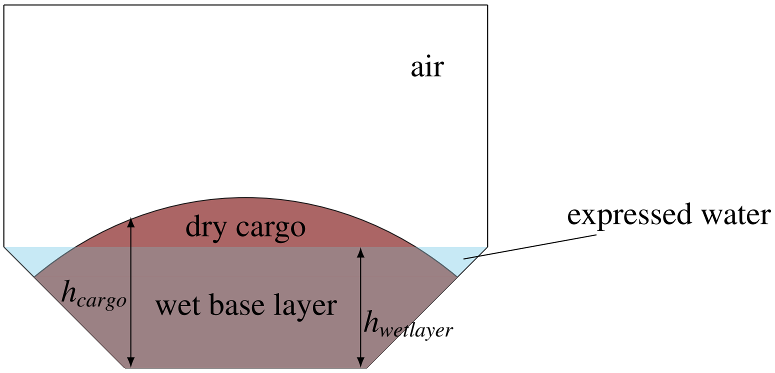

Figure 6.12: 2D wet base cargo in hold: Sketch of a cargo hold initialization for the ”wet base” scenario where h_{cargo} represents the surface of the porous rigid-perfectly plastic granular material and $h_{wetlayer}$ is the height of the initialized water-air free surface.

In Fig. 6.13, the viscosities for a wet base initialization and the viscosity of a constant cohesion also in the wet layer are displayed. The difference beween the viscosities in the wet layer in Fig. 6.13 (a) and Fig. 6.13 (b) already predicts larger cargo movements for the saturation-based variable cohesion.

The comparison of the behavior of the wet base material with constant (Fig. 6.14, right) and non-constant cohesion (Fig. 6.14, left) is shown for a rolling motion with amplitude 20° and

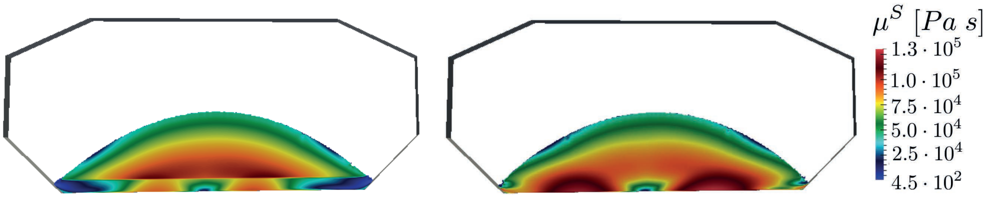

(a) (b)

Figure 6.13: 2D wet base cargo in hold: Static pressure induced viscosity field values in a cargo heap with a wet base layer with height $h_{wetlayer} = 1.0$ m at time $t = 1.0$ s for two different materials. Left: $\phi = 12°$, $C_{max} = 7.8$ kPa ,$C_{sat} = 1.0$ kPa; Right: $\phi = 12°$, $C_{max} = 7.8$ kPa ,$C_{sat} = 7.8$ kPa.

period of 18.0 s in Fig. 6.14. The free surface of the air/water interface is displayed as a black line. The wet base layer with non-constant cohesion in Fig. 6.14 (d) significantly sloshes higher on the right hold wall than the wet layer with constant cohesion in Fig. 6.14 (f). The cargo movement above the wet layer from a heap to a plane also advances faster for the cargo heap with a wet layer with saturation-dependent cohesion.

In the middle column of Fig. 6.14, the behavior of a cargo pile with a wet base layer with saturation-dependent cohesion for a larger rolling angle is studied. Large cargo shifts due to the wet material at the bottom of the pile can be observed. In all cases, the wet base layer flows along the hold walls, where the forming of two humps of the air/water-free surface in the corners of the hold can be noted for the larger rolling amplitude.

To study an extreme case, a cargo material that is assumed to have zero cohesion when fully saturated and a maximum cohesion of $C_{max} = 7.8$ kPa is suspected of having a rolling motion of $A_R = 5°$ and $T_R = 10.0$ s. The wet base height is determined by the MC, which was set to 20% and therefore resembles a value of dry nickel ore during cargo transport. In Fig. 6.15, the results for this extreme case are presented where the fluid behavior of the wet base is apparent, and the body of the cohesive material can still be distinguished at $t = 100.0$ s. At $t = 1.0$ s, a high displacement gradient is present at the air/water interface, translating into a high norm of the Euler-Almansi strain at the top boundary of the wet base layer. It has to be noted that the assumption of zero cohesion is not thought to be valid for realistic cases.

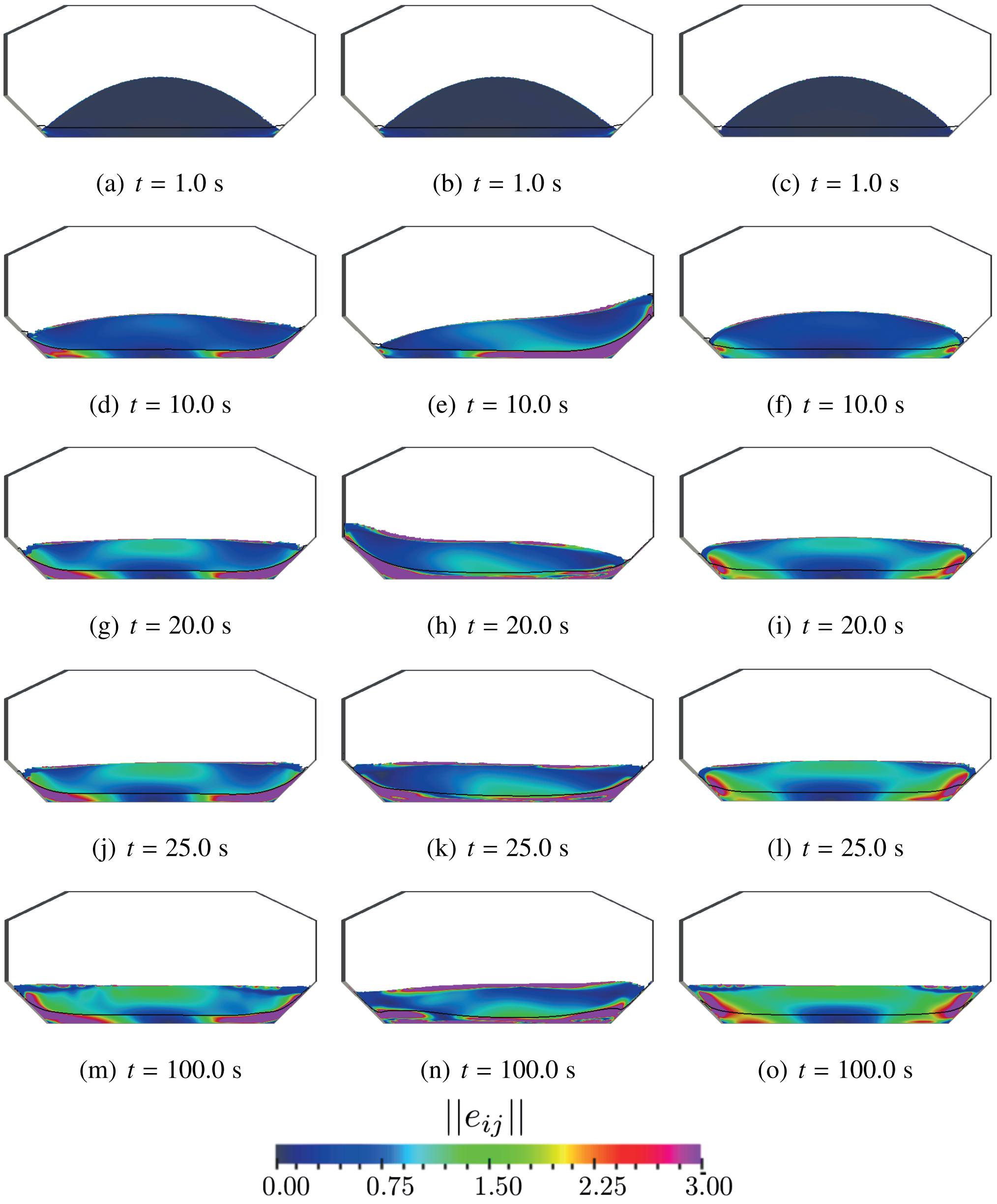

(a) t = 1.0 s (b) t = 1.0 s (c) t = 1.0 s

(d) t = 10.0 s (e) t = 10.0 s (f) t = 10.0 s

(g) t = 20.0 s (h) t = 20.0 s (i) t = 20.0 s

(j) t = 25.0 s (k) t = 25.0 s (l) t = 25.0 s

(m) t = 100.0 s (n) t = 100.0 s (o) t = 100.0 s

Figure 6.14: 2D wet base cargo in hold: Field values of the deviatoric Euler-Almansi strain norm in a cargo heap (quadratic function h_{max} = 7.750 m) and a wet base ($h_{wetlayer}$ = 1.0 m) at five different time steps for varied rolling motions and wet phase cohesions and properties angle of repose $\phi = 12°$ and maximum cohesion C_{max} = 7.8 kPa. Left: amplitude $A_R = 5°$, period T = 10.0 s, cohesion C_{sat} = 1.0 kPa in (4.59); Middle: amplitude $A_R = 20°$, period T = 18.0 s, cohesion C_{sat} = 1.0 kPa in (4.59); Right: amplitude $A_R = 5°$, period T = 10.0 s, constant cohesion C_{sat} = 7.8 kPa.

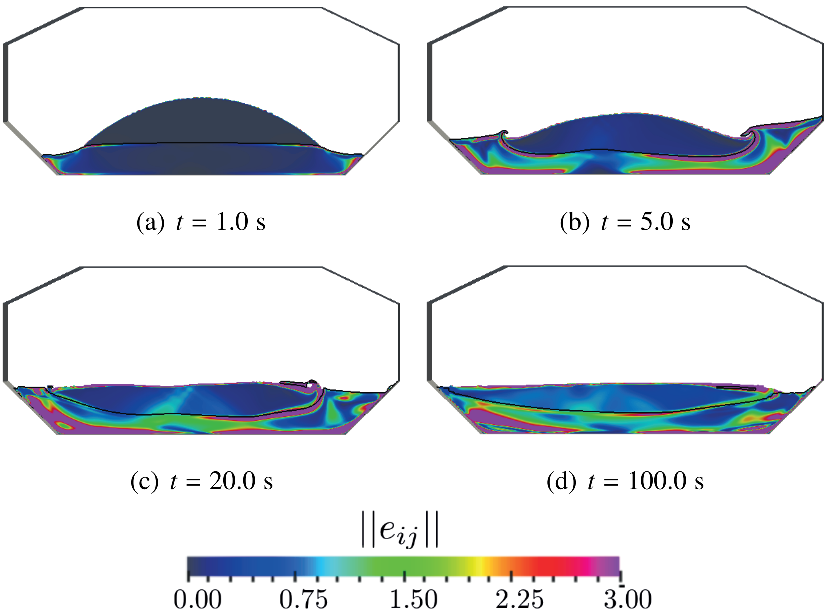
(a) t = 1.0 s (b) t = 5.0 s

(c) t = 20.0 s (d) t = 100.0 s

Figure 6.15: 2D wet base cargo in hold: Field values of the deviatoric Euler-Almansi strain norm in a cargo heap (initialized with quadratic function h_{max} = 7.750 m) for a wet base scenario with MC 20%, angle of repose ϕ = 4°, maximum cohesion C_{max} = 7.8 kPa, C_{sat} = 0.0 kPa and a rolling motion of amplitude A_R = 5°, period T_R = 10.0 s.

Studies of Unsaturated Cargo with Fully Saturated Top Layer - Dynamic Separation

The same method as in the last section is applied to a different assumption of water movement inside the cargo hold during the voyage. Here a compaction of the cargo heap is thought to lead to an upward flow of the water inside the cargo material. The process was introduced as "dynamic separation" in [41]. A wet top layer is initialized to model the cargo behavior after "dynamic separation" as displayed in Fig. 6.16. The top layer is thought to exhibit a smaller cohesion (C_{sat} = 1.0 kPa) than the bottom part of the cargo. Two different external rolling

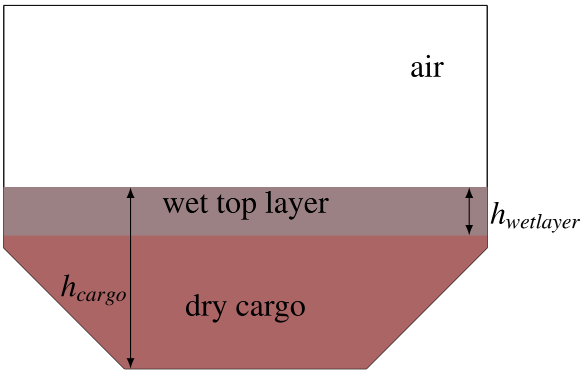

Figure 6.16: 2D cargo in hold, wet top layer: Sketch of a cargo hold initialization for the scenario of cargo with a fully saturated top cargo layer.

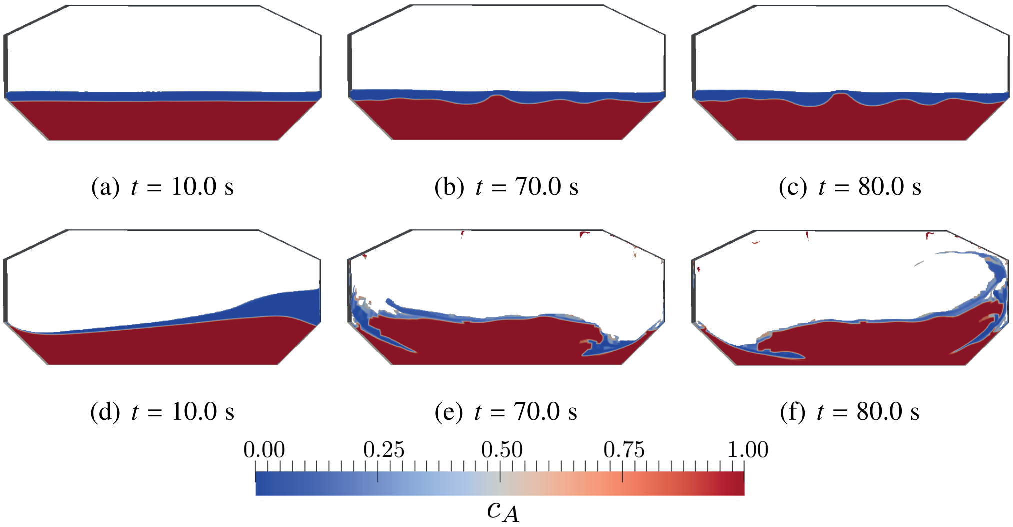

Figure 6.17: 2D cargo in hold, wet top layer: Snap shots of air volume fraction c_A in flatly initialized cargo heap (h_{cargo} = 5.0 m) with wet top layer ($h_{wetlayer}$ = 1.0 m) at three different time steps for two different rolling motions. The field value of the air volume fraction is cut at c_S = 0.5. Top: amplitude A_R = 5°, period T_R = 10.0 s ; Bottom: amplitude A_R = 20°, period T_R = 18.0 s.

motions are applied to a cargo with a plane initialization of the cargo heap and a wet top layer of 1.0 m (h_{cargo} = 5.0 m, $h_{wetlayer}$ = 1.0 m). The angle of repose is set to 4° for this scenario.

In Fig. 6.17, the development of the air and water phases inside the cargo are displayed for a rolling motion with A_R = 5° and period T_R = 10.0 s and a rolling motion with higher amplitude of A_R = 20° and also higher period of T_R = 18.0 s. For the rolling amplitude, which is close to the angle of repose of the cargo material, the internal interface between the fully saturated top layer and fully unsaturated cargo exhibits a wave pattern that amplifies over time. The cargo interface is only subject to small displacements, as shown in Fig. 6.18. Larger strains can be observed in the fully saturated cargo layer.

Subjecting the same cargo material to a larger rolling amplitude of 20.0°, cargo failure is induced, which would lead to catastrophic consequences when occurring on a vessel during a voyage as can be seen in Figs. 6.17 and 6.19. Due to the different cohesion strength of the saturated and unsaturated cargo, high sloshing of the saturated cargo occurs, as well as sliding of the unsaturated cargo on a slip plane (cf. Fig. 6.19). At later time steps, the saturated cargo has crept into the slip plane as can be seen in Fig. 6.17, forming a moist layer around a drier cargo lump on which the unsaturated cargo is sliding higher with each rolling motion of the vessel (cf. Fig. 6.19).

Comparing the scenarios with high rolling motions for the saturated top cargo layer and saturated bottom cargo layer, it is apparent that a cargo layer with high MC on top of an unsaturated

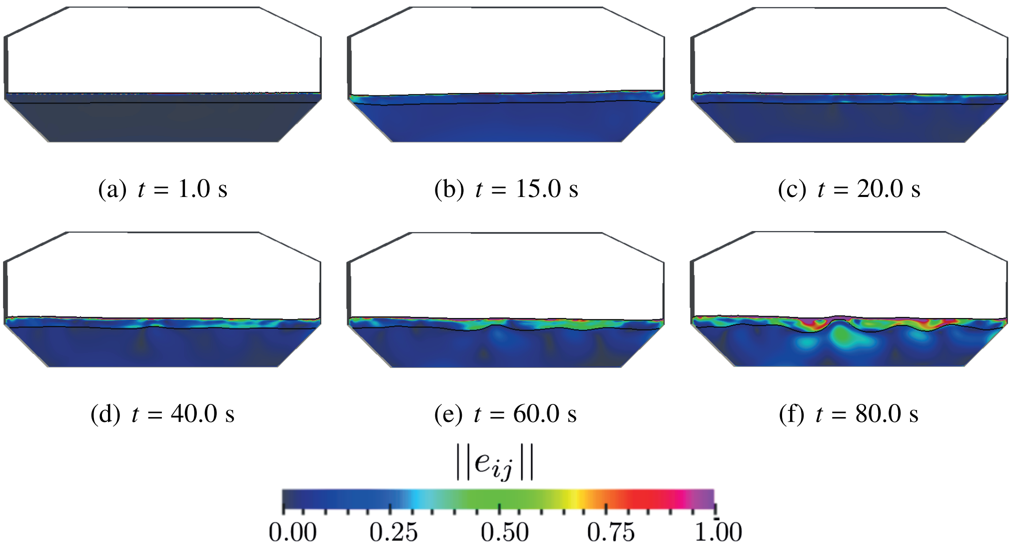
(a) t = 1.0 s (b) t = 15.0 s (c) t = 20.0 s (d) t = 40.0 s (e) t = 60.0 s (f) t = 80.0 s

Figure 6.18: 2D cargo in hold, wet top layer: Field values of deviatoric Euler-Almansi strain norm inside the cargo and internal air/water free surface (black line) at six different time steps for a rolling motion with amplitude A_R = 5.0° and rolling period T_R = 10.0 s. The cargo is initialized with a flat fully saturated cargo layer on top of a flat fully unsaturated cargo where the cohesion of the cargo depends on the saturation level (h_{cargo} = 5.0 m, $h_{wetlayer}$ = 1.0 m).

cargo leads to a higher potential for a capsize of a bulk carrier than a cargo with a fully saturated bottom layer. Note that in the case of catastrophic cargo movement, the VoF approach for both the granular/air phase concentration and the water/ air phase concentration has the advantage that arbitrarily large movements can be depicted.

Planar Expressed Water on Top of Granular Cargo - Dynamic Separation

Two more scenarios are simulated to examine cargo behavior with expressed water on top of the cargo pile (plane initialization with cargo heap height of 5.0 m). In the first of these scenarios, a pure water phase is initialized on top of the cargo pile, which can mix with the unsaturated cargo due to the porosity of the cargo. A second case where the water is initialized on top and inside the cargo phase is simulated under the same rolling motion conditions (amplitude A_R = 5°, rolling period T_R = 10.0 s). Here the same material conditions as in the last two sections are applied for the cargo material (ϕ = 4°, C_{max} = 7.8 kPa and C_{sat} = 1.0 kPa) with the assumption of saturation dependent cohesion.

Both initializations and snapshots at different time steps are displayed in Fig. 6.20 and a zoom into the right upper corner of the hold for both cases is displayed in Fig. 6.21. For the case where 0.5 m of water is initialized on top of the granular cargo, it can be observed that the water flows into the granular cargo over time (cargo porosity n = 0.62). As shown in Figs. 6.20 and

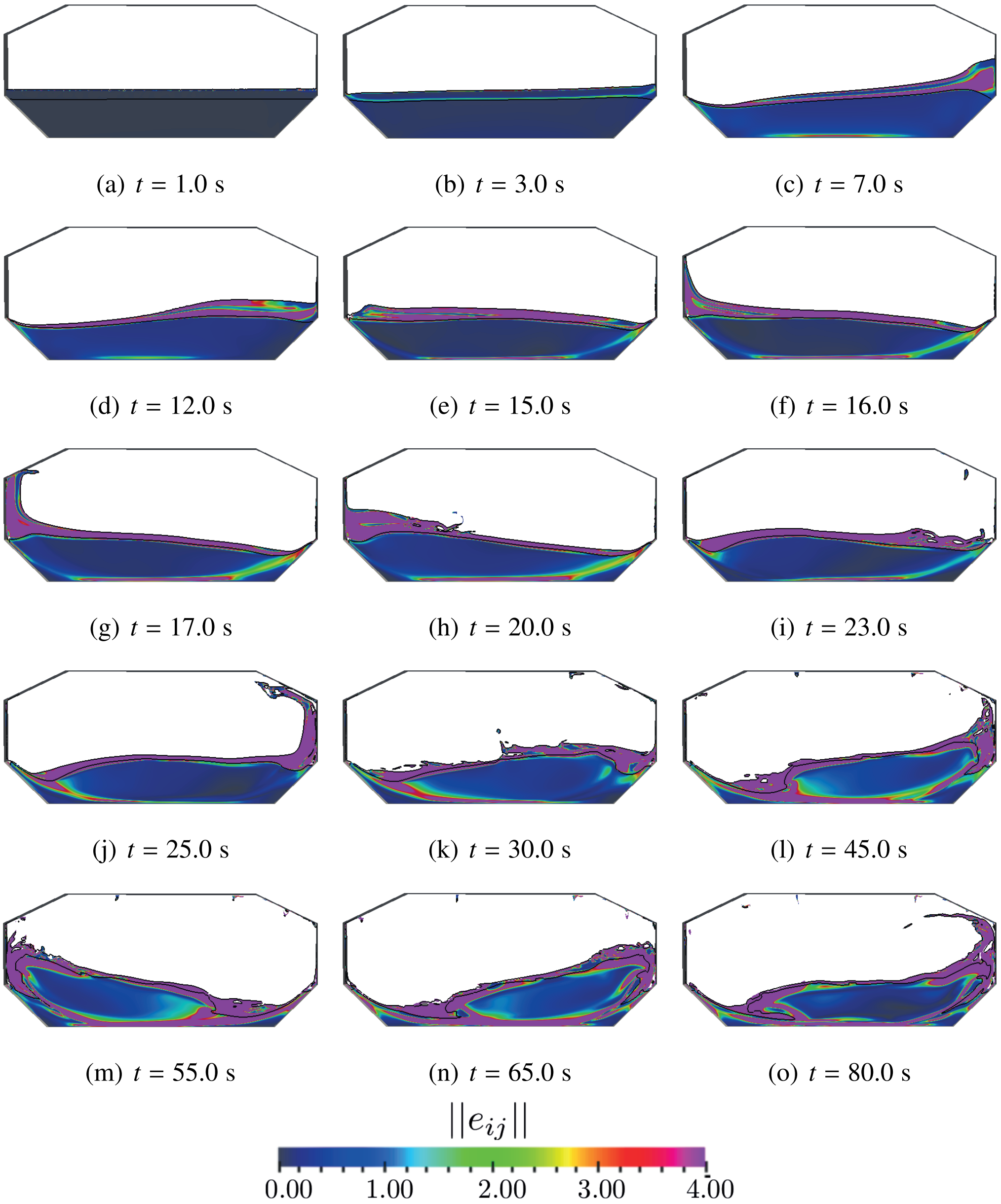

(a) t = 1.0 s
(b) t = 3.0 s
(c) t = 7.0 s
(d) t = 12.0 s
(e) t = 15.0 s
(f) t = 16.0 s
(g) t = 17.0 s
(h) t = 20.0 s
(i) t = 23.0 s
(j) t = 25.0 s
(k) t = 30.0 s
(l) t = 45.0 s
(m) t = 55.0 s
(n) t = 65.0 s
(o) t = 80.0 s

Figure 6.19: 2D cargo in hold, wet top layer: Field values of deviatoric Euler-Almansi strain norm inside the cargo and internal air/water free surface (black line) at fifteen different time steps for a rolling motion with amplitude A_R = 20.0° and period T_R = 18.0 s. The cargo is initialized with a flat fully saturated cargo layer on top of a flat fully unsaturated cargo where the cohesion of the cargo depends on the saturation level (h_{cargo} = 5.0 m, $h_{wetlayer}$ = 1.0 m).

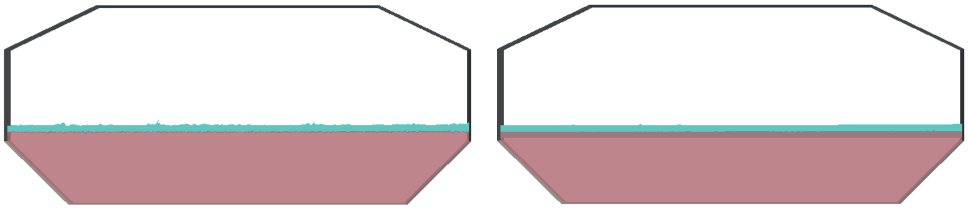

(a) t = 1.0 s (b) t = 1.0 s

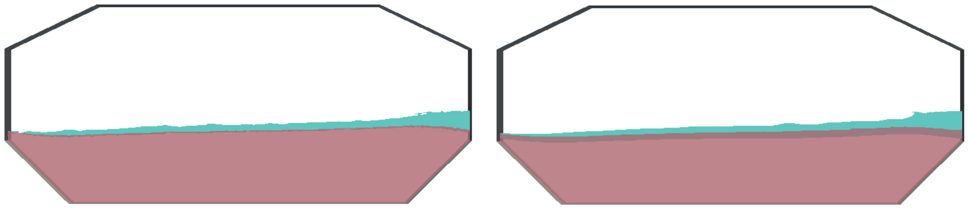

(c) t = 5.0 s (d) t = 5.0 s

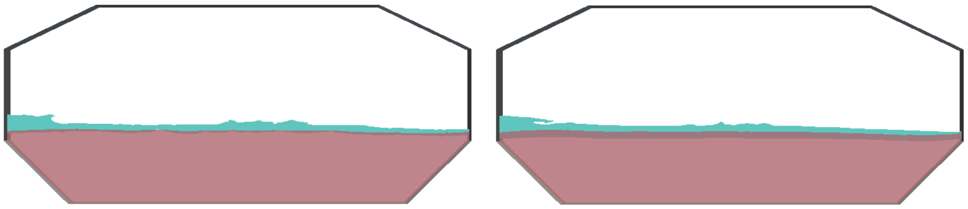

(e) t = 20.0 s (f) t = 20.0 s

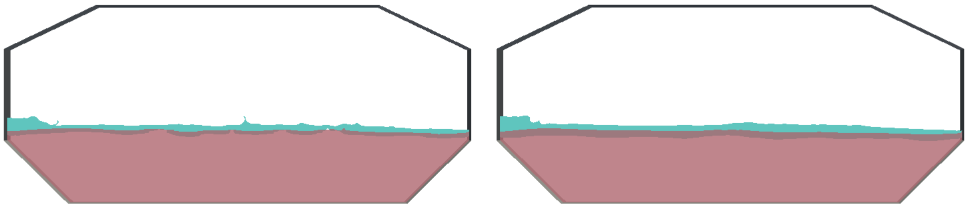

(g) t = 50.0 s (h) t = 50.0 s

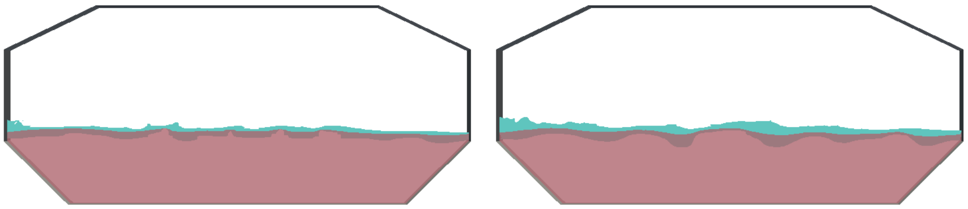

(i) t = 100.0 s (j) t = 100.0 s

Figure 6.20: 2D cargo in hold, expressed water: Snap shots of intersecting water phase (turquois) and unsaturated granular cargo phase (light red) as well as fully saturated cargo (light brown) for two initialization conditions at five different time steps. Left: initialization of 0.5 m water on top. Right: initialization of 0.5 m water on top + top 0.5 m fully saturated cargo.

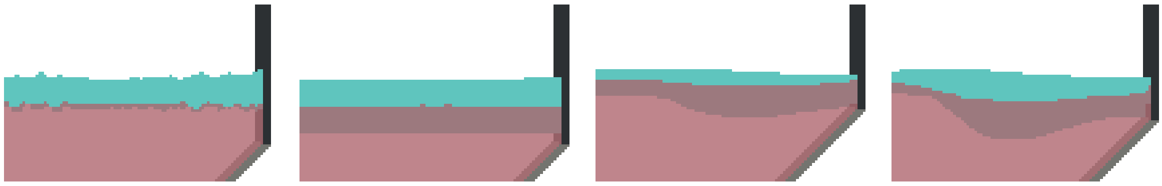

(a) t = 1.0 s (b) t = 1.0 s (c) t = 100.0 s (d) t = 100.0 s

Figure 6.21: 2D cargo in hold, expressed water: Snap shots of intersecting water phase (turquois) and unsaturated granular cargo phase (light red) as well as fully saturated cargo (light brown) for two initialization conditions (a)/(c) 0.5 m water on top, and (b)/(d) 0.5 m water on top + 0.5 m saturated cargo.

Fig. 6.21, the resulting fully saturated cargo layer after 100.0 s has nearly the same thickness as in the second case where half of the water is initialized inside the cargo. It is also interesting to note the shape of the cargo/ air interface at t = 100.0 s for the simulation with 0.5 m on top of the cargo and 0.5 m fully saturated cargo below this layer. The circular motion of the cargo hold leads to a wave-shaped interface similar to a seabed under waves.

To further illustrate the wave-shaped interface of unsaturated and fully saturated cargo interface after 100.0 s for both cases, the deviatoric Euler-Almansi strain norm is displayed in Fig. 6.22 inside the cargo volume. The present results suggest that a scenario with expressed water shall be avoided for the safety of bulk carriers and crew.

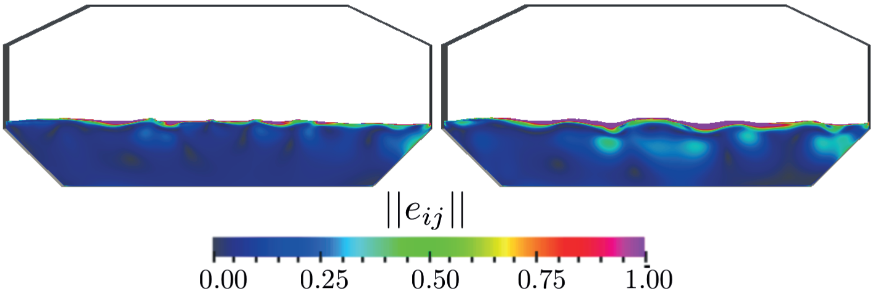

Figure 6.22: 2D cargo in hold, expressed water: Field value of the norm of the deviatoric Euler-Almansi strain at t = 100 s inside the cargo phase. Left: initialization of 0.5 m water on top. Right: initialization of 0.5 m water on top + top 0.5 m fully saturated cargo.

Variation of Moisture Content of Cargo with a Saturation Independent Cohesion

Since water-dependent cohesion was assumed in the past sections, a study of the influence of the coupled model without the dependency is conducted. Here differing moisture contents of the cargo are exhibited for saturation-independent cohesion. The pure water content will lead to different cargo behavior due to the formulation of direct coupling in chapter 4.

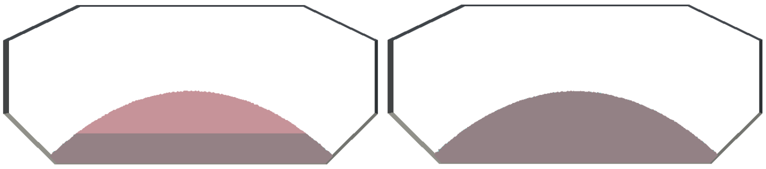

Figure 6.23: 2D cargo in hold, saturation-independent cohesion: Initialization of cargo saturation levels for MC equal to 20% (left) and 36% (right) for a cargo heap with height h_{max} = 7.75 m and steepness s = 0.04. Light red represents the fully unsaturated cargo, and dark red represents the fully saturated cargo.

Three simulations with a saturation-independent cohesion are compared for different MCs 20%, 36%, and 43.5%. The MC is discretely calculated by summation of the densities over all cells

$$MC = \frac{m^W}{m^{total}} = \frac{\rho^W V^W}{\rho_{wet} V} = \frac{\rho^W \sum_{CV} c_S (1 - c_A) n}{\rho_{wet} \sum_{CV} c_S} \tag{6.14}$$

where the phase definitions c_S and c_A are initialised in an iterative process. The cargo heap is initialized with a maximum pile height h_{max} = 6.5 m and steepness s = 0.04. The top boundary of the initial water phase is a plane, and the side boundaries coincide with the boundaries of the cargo heap as is displayed in Fig. 6.23. For a porosity of $n = 0.62$, a MC of 36% results if the complete cargo heap with given properties is fully saturated. To study a material with higher MC, the porosity is set to $n = 0.75$ to obtain a MC of 43.5%. The cargo hold is forced by a 10° rolling motion with a 10 s period in all three simulations.

In Fig. 6.24, the higher displacements of the cargo when initialized with a higher MC of 36% instead of 20% can be observed. Therefore the present method can depict the cargo behavior difference for changing MC without saturation-dependent cohesion in the yield criterion. To compare results for MCs 36% and 43.5%, a cutout of the cargo hold is displayed in Fig. 6.25. Both cargo heaps do behave similarly for all time steps. However, the dissolution of the water phase from the cargo occurs faster for the granular material with higher porosity and MC. The water phase slowly disseparates from the cargo in the left and right top corners.

Remark

It is important to remark that the cargo properties assumed above are based on the information gathered in Sec. 6.2. Since the sources for material property data of nickel and iron ore cargoes are scarce, especially for the properties obtained from tri-axial stress tests, more precise data on the material properties are needed to make scientifically relevant statements. The aforementioned studies have to be viewed as methodological proof of cargo modeling. They can visualize which scenarios can lead to the loss of a bulk carrier.

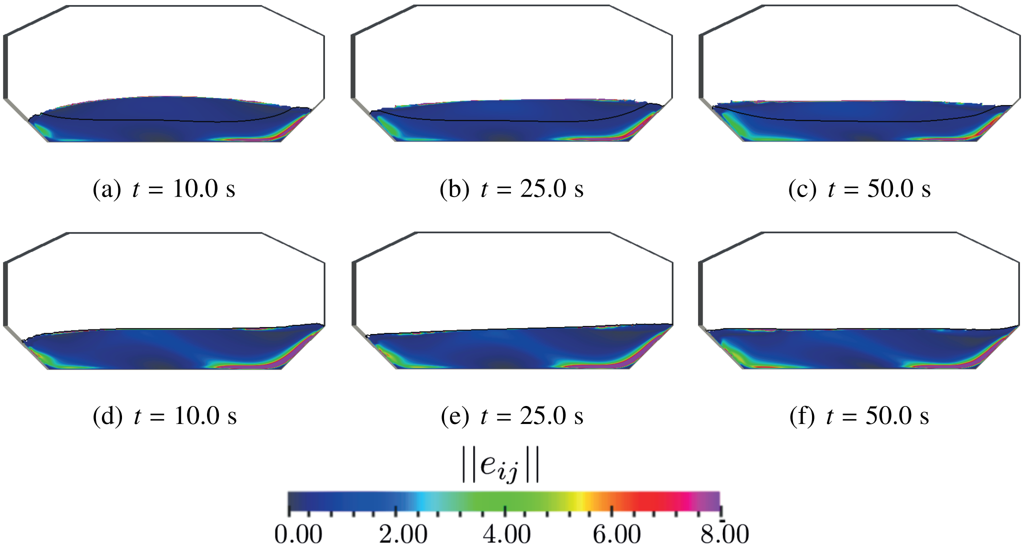

(a) t = 10.0 s (b) t = 25.0 s (c) t = 50.0 s

(d) t = 10.0 s (e) t = 25.0 s (f) t = 50.0 s

Figure 6.24: 2D cargo in hold, saturation-independent cohesion: Field values of the norm of the deviatoric Euler-Almansi strain in the granular cargo phase and water-free surface (black line) for different cargo saturation levels with constant cohesion excited by a 10° rolling motion with a period of 10 s at three different time steps. Top: MC = 20%; Bottom: MC = 36%.

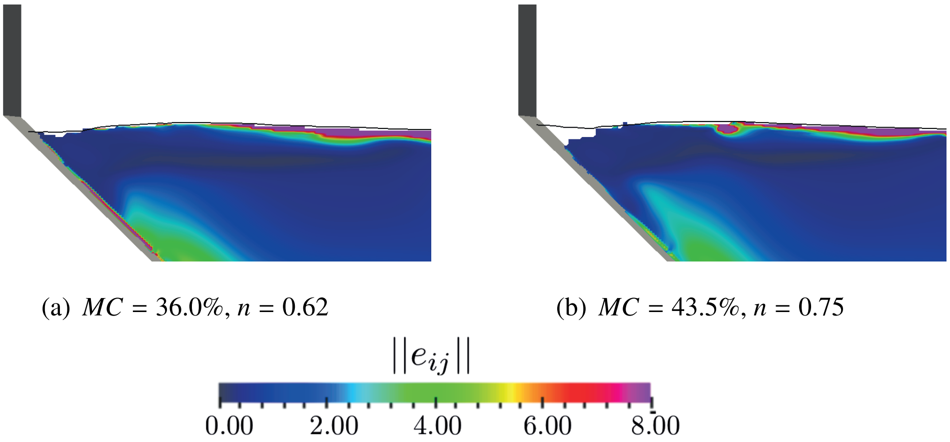

(a) MC = 36.0%, n = 0.62 (b) MC = 43.5%, n = 0.75

Figure 6.25: 2D cargo in hold, saturation-independent cohesion: Enlargement of the left side of the cargo hold with the black line being the water-free surface and the norm of the Euler-Almansi strain displayed inside the granular cargo phase at t = 100 s for two different MC and porosity values.

6.4 Proof of Concept: 3D Loaded Bulk Carrier in Waves

This section presents a proof of concept of a three-dimensional simulation of a vessel in waves with loaded cargo. Initial and boundary conditions are derived from the incident report of the sinking of the ”JianFuStar” [85], and vessel properties are obtained from generic formulas. Therefore the presented results cannot be viewed as an exact depiction of the actual course of the accident but rather as proof that the monolithic approach to simulate granular cargo on vessels is feasible.

The vessel’s cargo is modeled using the rigid-perfectly-plastic material model described in chapter 3. Additional model components for the fully coupled problem of bulk carrier in waves are applied in this chapter and briefly explained below.

6.4.1 Additional Model Components

Three model components are required in addition to the previously described models to simulate the movement of an entire bulk carrier in 3D with cargo. The ship hull is considered a rigid body and its movements are excited by the forces resulting from the cargo, air, and water phases. To save computational time, a three-phase model is used instead of the coupled porous media model in the 3D application case. The boundary conditions forcing the sea state to enter the VoF surface between air and water are also briefly described in this chapter.

Immiscible Incompressible Three-phase Flow

An extension of the two-phase VoF approach to three-phase flows is implemented in the current method in order to be able to represent granular cargo in a vessel in waves without the porous media coupling described in chapter 4.

Applying a three-phase flow where the granular cargo is seen as an immiscible continuum with water and air surrounding the cargo leads to a more efficient scheme for realistic 3D cases. The higher efficiency follows from using only one velocity and pressure field and therefore the momentum and continuity equations are only needed to be solved once, including the velocities and pressures of all three phases. The work in this chapter is based on results presented in Völkner [124] and Völkner et al. [126]. Nevertheless, some effects presented in the last sections, e.g., water seepage flow inside the cargo cannot be solved with this approach.

To represent three immiscible phases with volumes V^A, V^G and V^W in the volume V, two mixture fractions $c_A = V^A/V$ and $c_S = V^G/V$ are introduced leading to the third phase fraction being defined by

$$\frac{V^W}{V} = 1 - c_A - c_S \ . \tag{6.15}$$

Therefore a second mixture equation is introduced in the standard FV, VoF pressure correction algorithm presented in Yakubov et al. [136] and Völkner et al. [125]. In this work, the three-phase flow approach represents granular materials as an extension of the model described in chapter 3. Therefore the second mixture fraction will be called soil mixture fraction hereafter. It shall be remarked that the second mixture equation can be used for arbitrary materials.

Assuming the three phases are incompressible and immiscible, the condition $Dc_S/Dt = 0$ has to be fulfilled, leading to the soil mixture fraction equation over the complete volume V

$$\int_V \left(\frac{\partial c_S}{\partial t} + \frac{\partial (c_S v_i)}{\partial x_i} \right) dV = 0 \ . \tag{6.16}$$

Here v_i is the velocity field, including the velocities of all three immiscible phases. Accordingly, the air mixture fraction equation gets

$$\int_V \left(\frac{\partial c_A}{\partial t} + \frac{\partial (c_A v_i)}{\partial x_i} \right) dV = 0 \tag{6.17}$$

due to the immiscible condition $Dc_A/Dt = 0$. Substituting v_i for v_i^F, p for p^F, and V for V^F in Eqns. (2.5) and (2.12) yields the continuity and momentum equations for the incompressible immiscible three-phase flow.

The material properties, as well as the field variables, can now be assigned to the three phases via the mixture fractions by

$$\Theta = c_A \Theta^A + c_S \Theta^S + (1 - c_A - c_S)\Theta^F \tag{6.18}$$

where Θ can be substituted by all the mentioned properties and components of field variables above. The results of a verification case for the three-phase flow are briefly described in Appendix D.

Wave Generating Boundary Conditions

To generate waves in the water/air-free surface, the approach introduced by Wöckner et al. [132] and Wöckner-Kluwe [133] is applied. An inviscid far-field boundary condition is imposed on the solution of the viscous Navier-Stokes equations within a defined zone. The far-field solution can be defined from different wave theories, and the linear Airy theory is used in this section. Within the impingement zone, the system of equations of the momentum equations and the air mixture fraction equation is manipulated to a solution in between the linear wave theory and the viscous solution by

$$\left[1 + \beta_w\ \alpha_w(x_w)\ \right] A_P^\Theta\ \Theta_P + \sum_{NB} A_{NB}^\Theta\ \Theta_{NB} = S_P^\Theta + \left[A_P^\Theta\ \beta_w\ \alpha_w(x_w)\ \Theta_P^{Airy}\right] \tag{6.19}$$

where Θ represents either a velocity component or the air mixture fraction. The factor β_w can be chosen for optimal results depending on the application and is set to $2 \cdot 10^{-3}$ in this study. To prevent reflections from the sponge layer, a smooth function $\alpha_w(x_w)$ of the order three is used, which exhibits values of one at the domain boundary and zero at the defined inner edge of the sponge layer.

A combination of the Higdon boundary condition introduced by Higdon [45] with the boundary condition presented here was investigated and documented in Voß [128] and found that no improvement could be obtained for a vessel in waves. Therefore, the numerically more efficient boundary conditions described in this section are used.

Rigid Body Motion

The applied rigid body motion solver is based on work by Koliha [62] and Manzke [83] and is only briefly explained here. For more in-depth information, the reader is referred to Luo et al. [80], Luo-Theilen et al. [81], Theilen [114] and Wöckner-Kluwe [133]. To avoid strong cell deformation during expected large ship motions while applying a re-meshing technique, the whole computational domain is moved with the accelerations and velocities of the vessel. Thus, the conservation equations must consider the mesh velocity $v_{m,i}$. This is achieved by using the relative velocity $(v_i - v_{m,i})$ in all transport terms of the conservation equations. For example, the discrete mass flux at each face $\dot{m} = (\rho v_i A_i)_f$ gets $\dot{m} = (\rho(v_i - v_{m,i})A_i))_f$ in this formulation.

The implemented 6DoF solver is based on quaternions to avoid Gimbal lock singularities that can occur in formulating the motion solver in Eulerian angles. Hereafter the equations of motion are formulated in Eulerian coordinates for illustration purposes. The equations for translational motions follow from Newton's second law

$$F_i = ma_i \tag{6.20}$$

where m is the mass of the rigid body, F_i are the forces acting on the body, and a_i is the acceleration of the body. In coupling the rigid body motion with the incompressible viscous flow equations, the forces are obtained from integrating the pressure and viscous shear stresses over the rigid body's boundary. The angular momentum equation in a body-fixed system of coordinates is given by

$$M_j = I_{ij}\dot{\omega}_i + \epsilon_{jki}\omega_k \left(I_{ij}\omega_j\right) \tag{6.21}$$

Table 6.2: Main vessel data of ”Jian Fu Star” at incident

LoA (length overall)	189.9 m
Lpp (length between perpendiculars)	183.0 m
B (width)	31.2 m
D (draft)	11.8 m
F (freeboard)	6.7 m
GM (metacentric height)	5.0 m

where M_j are the moments acting from the fluid on the rigid body, I_{ij} is the inertia tensor, and ω_i is the local angular velocity.

A second-order implicit trapezoidal time integration scheme is applied to solve the rigid body motion. The rigid body motion equations are solved in each outer iteration and under-relaxation is applied.

6.4.2 Case Description

The starting point of the simulation is given by the description of the accident event (cf. Sec. 6.1), and simulation conditions are chosen accordingly. Properties of the cargo are selected to match Indonesian nickel ore with a MC of 29%, and therefore the angle of repose ϕ gets 4.0°, the cohesion C is equal to 7.9 kPa and the cargo density is set to the wet density of $1.7 \cdot 10^3$ kg/m^3. The Drucker-Prager yield condition is applied for the rigid-perfectly plastic approach.

Vessel dimensions length overall LoA, width B, metacentric height GM at departure, and departure draft D are given in the incident report [85] and are presented in Tab. 6.2. To fill in the missing dimensions, these are taken from generic bulk carrier plans provided by ”Oldendorff Carriers” and the HSVA, and therefore the freeboard F and length between perpendiculars L_{PP} are obtained as given in Tab. 6.2.

A generic bulk carrier hull geometry provided by the HSVA with the same main proportions as presented in Tab. 6.2 is adapted to a bulk carrier with cargo holds. However, unlike in reality, the cargo holds are not closed with lids but are connected to the air, creating a contiguous domain for solving the conservation equations. The dimensions of these holds were taken from a general plan provided by ”Oldendorff carriers” [21] and are shown in Figs. E.1, E.2 and E.3 in Appendix E.1. The arrangement of the cargo compartments corresponds to Fig. 6.1, and the final ship geometry is shown in Fig. 6.26. In the same figure, the dimensions of

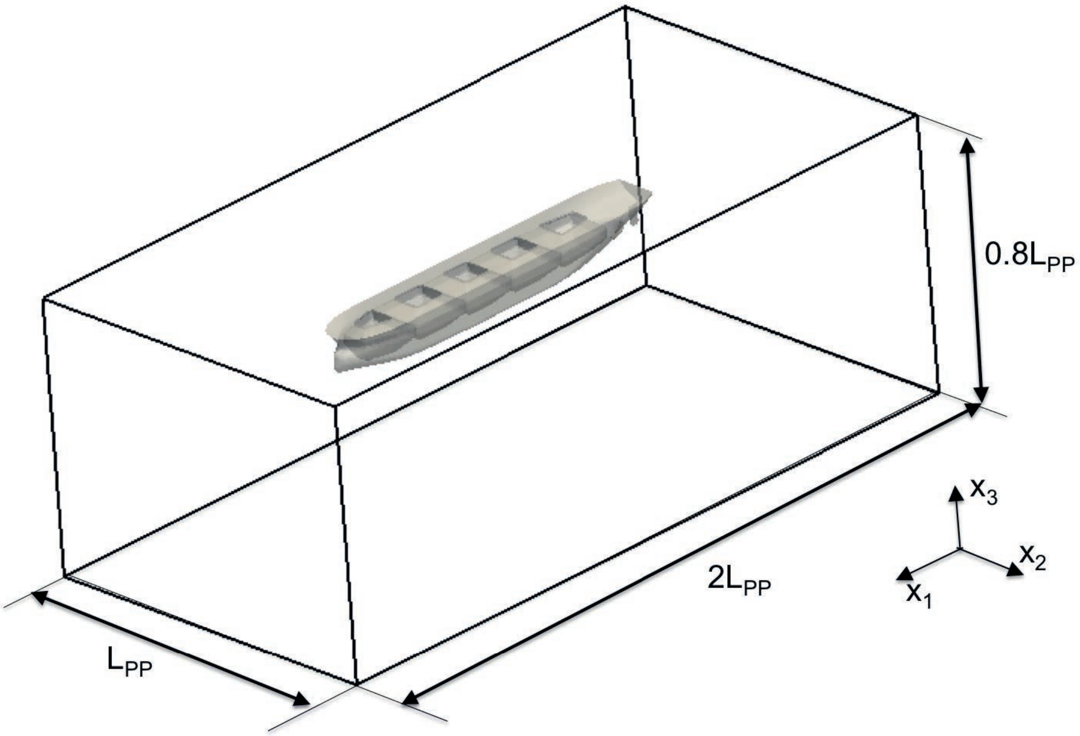

Figure 6.26: 3D cargo vessel in waves: Domain dimensions and bulk carrier geometry.

the computational domain in relation to the length between perpendiculars are displayed. Since large rotations are expected for the rigid body motion of the vessel, and the entire mesh is moved due to rigid body motions, an evenly distributed discretization is chosen for the unstructured mesh. For efficiency reasons, a mesh with 9.07 Mio cells translating into a mean cell size of $\Delta x_1 \approx 2L_{PP}/368$ is used for this proof of concept study. The time step is 10^{-4} s, and the applied time discretization method is an implicit Crank-Nicholson method for all equations. Due to the coarse mesh resolution, the arctangent interpolation method is applied with factor N being 5 for the soil-air interface and M being zero.

High-Reynolds wall boundary conditions are applied at the vessel hull and all other domain boundaries except the top boundary. The negative vessel velocity is set as Dirichlet boundary conditions for the velocity vector. A vessel speed of 4.5 kn is assumed following the incident report leading to a Froude number $Fn = 0.055$, a Reynolds number $Re = 3.8 \cdot 10^8$ and a Courant number of $Co = 2.3 \cdot 10^{-4}$. At the top of the domain, the pressure is set to 0 Pa as a reference pressure.

The position of the center of gravity, the mass, and the moments of inertia of the bulk carrier are required to calculate the rigid body motion. First, the fully loaded vessel data are derived from hydrostatic formulas and the dimensions given in Tab. 6.2, and the calculation path is outlined in Appendix E.2. In this case, the simulated vessel refers to an empty hull, and the cargo is realized

Table 6.3: Data of empty bulk carrier "JianFu Star" at incident

m_{empty}	13634.643 t
CoG_{empty}	(92.875 | 0.0 | 8.497) m
$I_{11,empty}$	$3.3548749750 \cdot 10^9$ kg m^2
$I_{22,empty}$	$4.0278141357 \cdot 10^{10}$ kg m^2
$I_{33,empty}$	$4.5380647175 \cdot 10^{10}$ kg m^2
$I_{23,empty} = I_{32,empty}$	$-4.3608019573 \cdot 10^7$ kg m^2

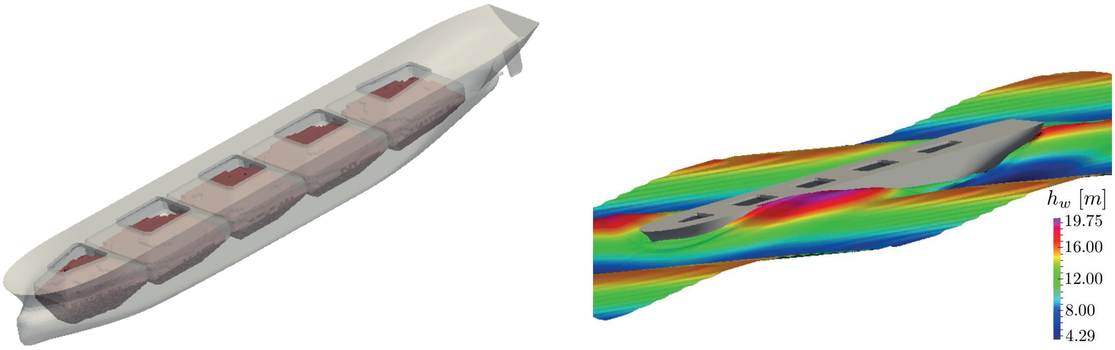

(a) Bulk carrier geometry with initialized cargo

(b) Free surface height h_w

Figure 6.27: 3D cargo vessel in waves: Loaded bulk carrier geometry and wave conditions at an early time step. The free surface height h_w of the water phase refers to the origin of the coordinate system which is positioned at the bottom of the vessel hull.

by a continuum whose mass acts on the ship as a pressure force in hydrostatic conditions. Therefore, the data of an empty bulk carrier is derived in Appendix E.2 by subtracting the loaded cargo from the fully loaded bulk carrier's properties. Loading conditions do coincide with Tab. 6.1 and are given in detail for the initialized cargo in Appendix E.3 Tab. E.2. The resulting rigid body properties of the simulated empty bulk carrier are presented in Tab. 6.3. Following the departure draft D, the mean level of the free surface between air and water is initialized at the height of 11.8 m. Applying Airy's potential wave theory, a wave with a height of 8 m and length 0.57 L_{PP} is initialized and taken as a far-field solution Θ^{Air} in the efficient wave generation approach. The waves hit the bulk carrier diagonally from the front with an angle of 48° towards the vessel's longitudinal axis. In Fig. 6.27, the vessel in waves is depicted for an early time step.

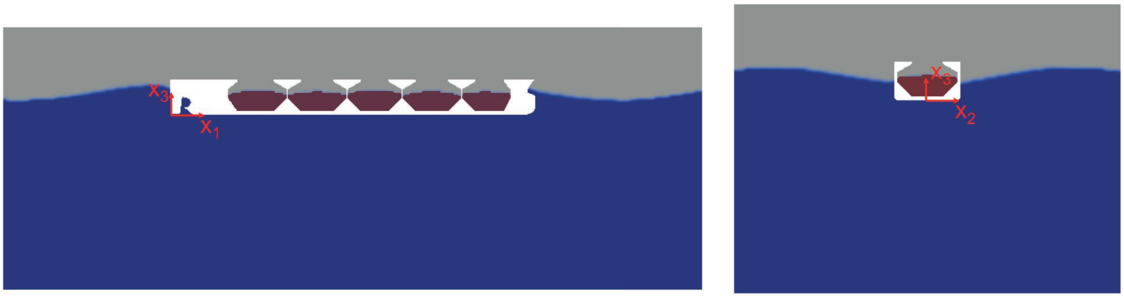

(a) Longitudinal section through bulk carrier (b) Cross-section through bulk carrier

Figure 6.28: 3D cargo vessel in waves: Initialization of granular cargo (red), water (blue), and air phases (light grey) is displayed in two different sections through the computational domain.

As can be seen on the left in Fig. 6.27, all five holds are filled with cargo following Tab. 6.1 by setting the soil mixture fraction to one to define the loading conditions. A more detailed look at the initial conditions of the three phases, air, water, and granular material, is presented in Fig. 6.28. The density of air and sea water are set to 1.185 kg/m^3 and $1.025 \cdot 10^3$ kg/m^3 and the viscosities to $1.831 \cdot 10^{-5}$ Pa s and $1.132 \cdot 10^{-3}$ Pa s. A three degrees of freedom (3DoF) approach is applied for this feasibility study, with heave, pitch, and roll being the degrees of freedom. A high under-relaxation of the rigid body motion by a factor of 0.025 is needed due to the pressure and viscous forces from the rigid part of the plastic material approach on the holds. Without the elastic formulation, the high viscosities needed to obtain rigid behavior (m_c is set to 10^2) lead to rapidly changing viscous forces at the wall boundaries.

6.4.3 Results of 3D Proof of Concept

The cargo vessels' movement in waves is simulated for 30.0 s on a HPC. For these 30.0 s seconds, $13 \cdot 10^4$ Central Processing Unit (CPU) hours were needed. In Fig. 6.29 the viscosity of the cargo μ^S calculated by the Drucker-Prager yield criterion (3.13) is displayed where the soil mixture fraction is smaller than 0.5. At the early time $t = 1.0$ s, the cargo loading shape leads to circular smaller viscosities due to the tendency of the cargo to flatten out over time. In the next figure at $t = 15.5$ s, the flattening already happened, and the vessel's pitch motion leads to high accelerations in the front hold. Therefore the viscosity is smallest in this hold and becomes gradually larger towards the back holds. The same general tendency can also be observed at later displayed times, where the effect is less prominent for lower pitch angles.

The 3DoF motions of the vessel during the simulation are given in Fig. 6.30, and the snapshots in 6.29 are chosen at times of minimum and maximum pitch angle. The successive rolling of the vessel leads to the supposition that the vessel experienced cargo shift and will capsize. Looking

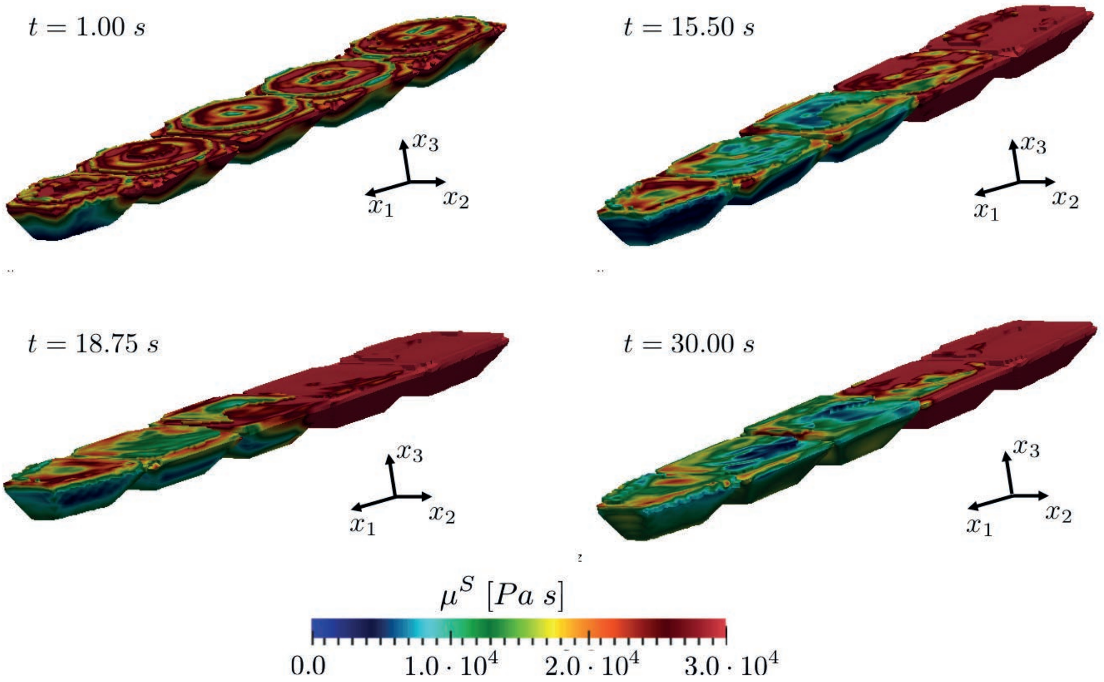

Figure 6.29: 3D cargo vessel in waves: Viscosity of the rigid perfectly-plastic cargo at four times during voyage in waves.

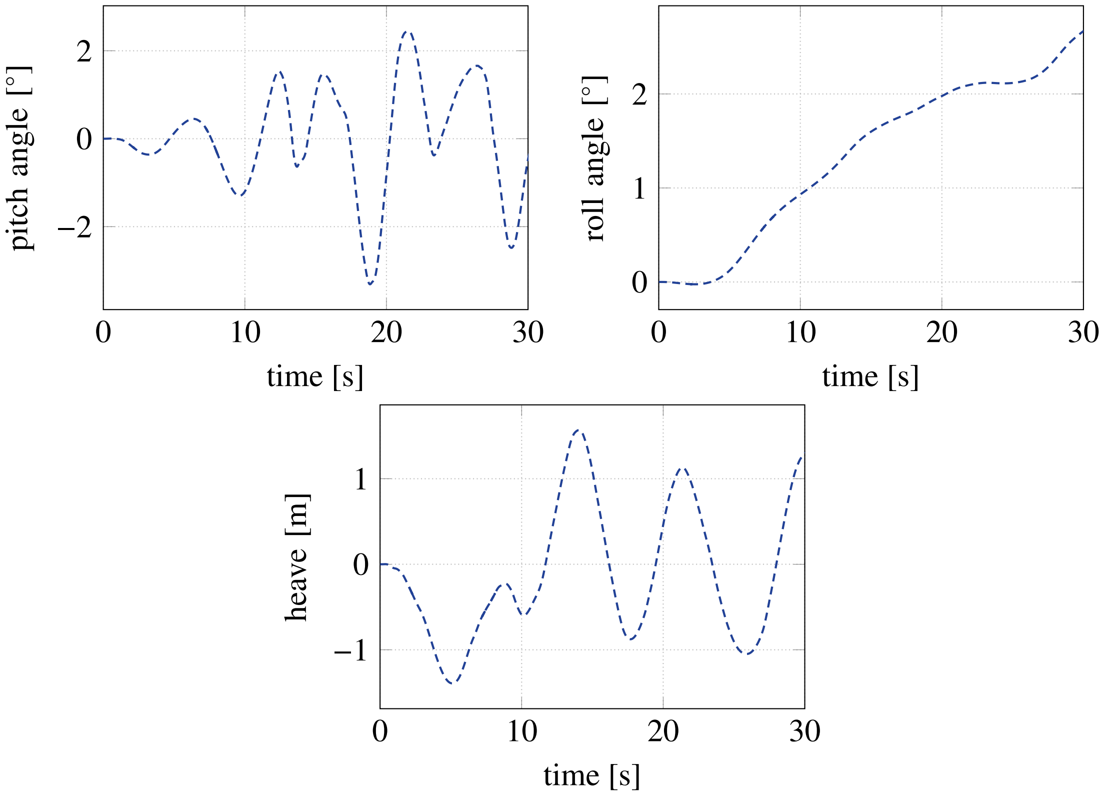

Figure 6.30: 3D cargo vessel in waves: Motions of feasibility study of 3DoF vessel in waves with rigid perfectly-plastic cargo and high under-relaxation of motion over time.

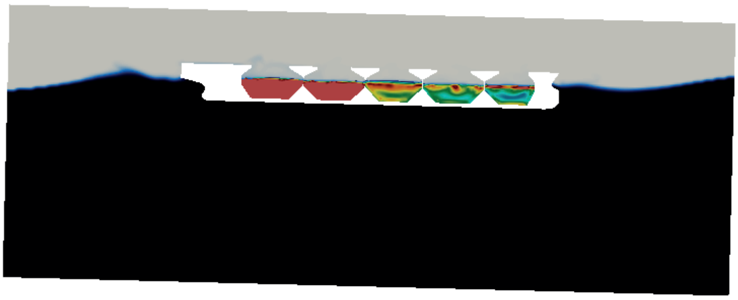

(a) 15.50 s

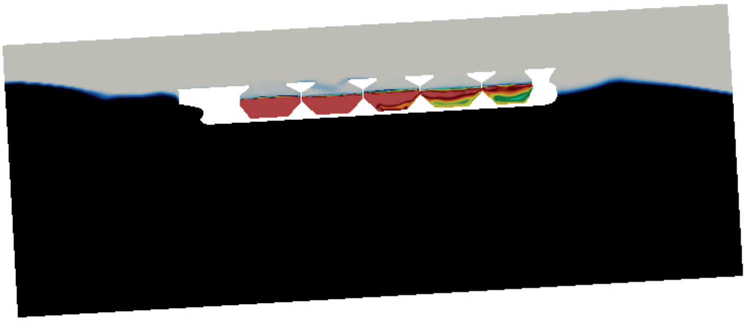

(b) 18.75 s

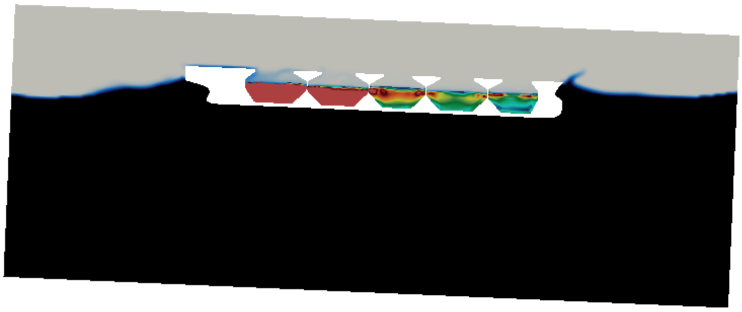

(c) 21.50 s

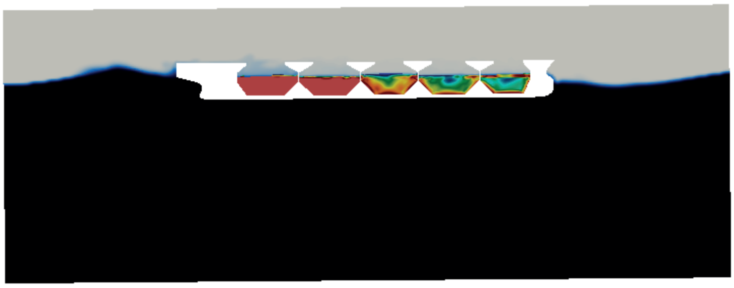

(d) 30.00 s

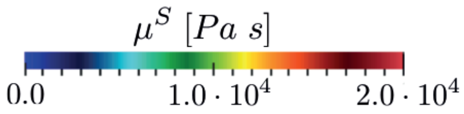

Figure 6.31: 3D cargo vessel in waves: Field values of the cargo viscosity in the x_1-x_3-plane at $x_2 = 0$ m at four different time steps where black represents the water, and grey the air phase outside the vessel. The computational domain is rotating according to the rigid body motions of the vessel.

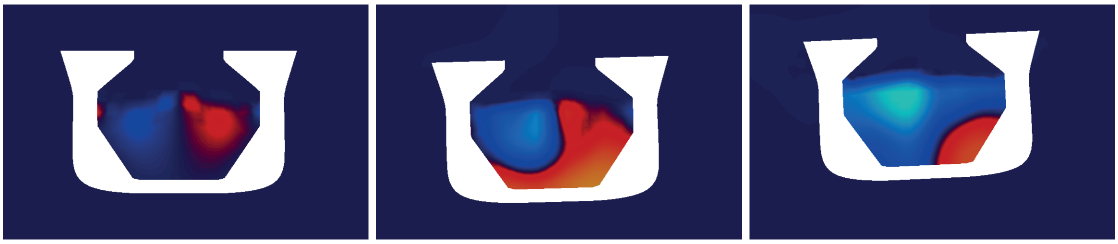

(a) Hold 1 ($x_1 = 162$ m)

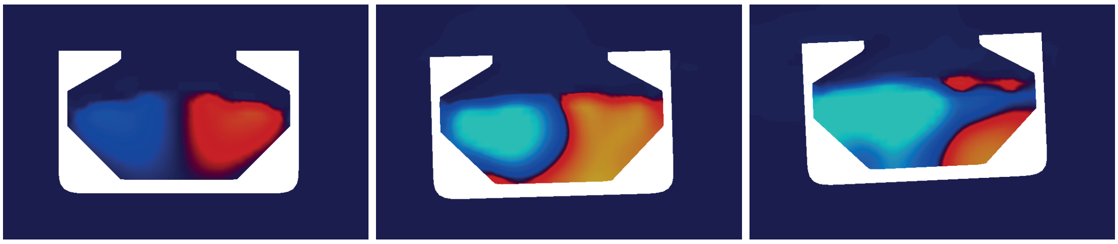

(b) Hold 2 ($x_1 = 134$ m)

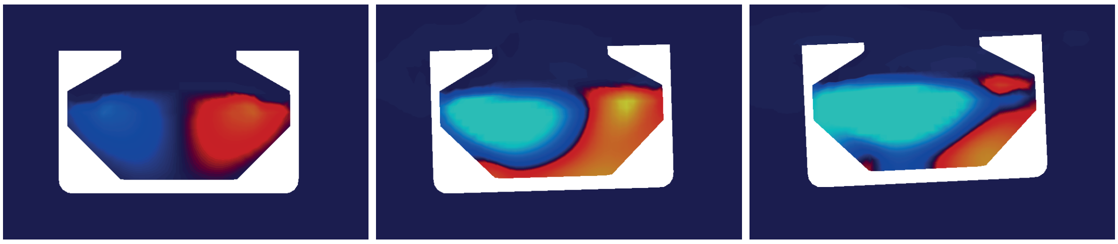

(c) Hold 3 ($x_1 = 104$ m)

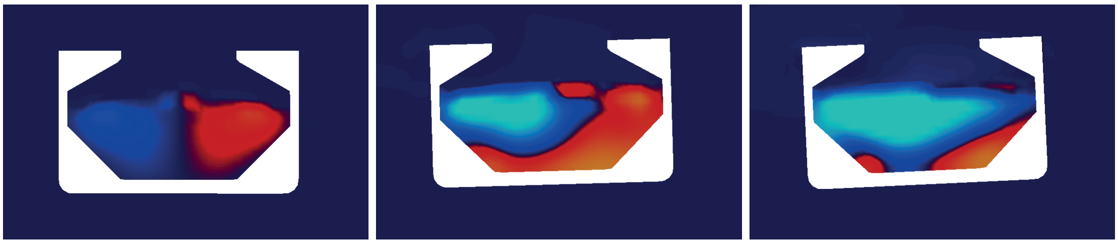

(d) Hold 4 ($x_1 = 74$ m)

(e) Hold 5 ($x_1 = 40$ m)

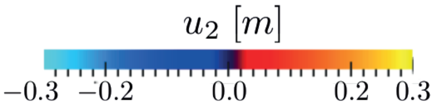

Figure 6.32: 3D cargo vessel in waves: Cargo displacement in the x_2-direction at times $t = 1.0$ s (left), $t = 15.5$ s (middle) and $t = 30.0$ s (right) displayed on x_2-x_3-planes through all five holds.

closely at the top cells in Fig. 6.29, a slight shift of cargo towards starboard can be noticed from 15.5 s onwards.

The viscosity in the holds, as well as the water and air phase, are displayed at a slice through the computational domain at $x_2 = 0$ m in Fig. 6.31 to visualize the vessel's position in waves. Here, black to blue represents the water phase, and it can be seen at $t = 18.75$ s, $t = 21.5$ s, and $t = 30.0$ s that the vessel is taking water on board. Due to the immiscible formulation of the cargo model, this does not affect the cargo properties except in the phase boundaries. Furthermore, the taking of water on board is in line with the incident report of the "Jian Fu Star," but in reality, the water is prevented from sloshing into the cargo holds by lids. Again in Fig. 6.31, it can be seen that the cargo is behaving softer in the holds to the front. Especially if the vessel is pitching downward (e.g., pitch angle maxima at $t = 21.5$ s), the viscosity is smallest at the bottom of the front hold.

In Lee [73], the consistency of the cargo after the vessel "Alam Manis" sailed through a typhoon is given in detail for each cargo hold. In line with the presented feasibility study, the highest accelerations acted on the cargo in the front holds, and the largest cargo shifts did occur in the front hold. The cargo shift angle given by Lee [73] gradually decreases in each hold going from front to aft. Also, in the report of the IMO "Technical Working Group" [56], the highest acting accelerations were found in the front hold during bulk carrier voyages which fit with the presented results.

To visualize the influence on the cargo of the successive rolling of the vessel, cf. Fig. 6.30, the second component of the Eulerian cargo displacement u_2 is displayed at three times in Fig. 6.32. The displacement is displayed at planes through each hold of the vessel going from top (front hold) to bottom (aft hold). A shift to starboard (negative displacement) can be observed at times $t = 15.5$ s (middle) and $t = 30.0$ s. The line of zero displacements continues to move further to the port side (right side in the figures) of the vessel over time. Interestingly, the largest displacement is observed in the middle of the cargo holds two and three. The narrower hold geometry in the front hold (hold one) restricts the displacement, and the viscosity is smallest in the middle of the holds, as seen in Figs. 6.29 and 6.31.

Overall the feasibility study proves that a monolithic coupled 3D case can reproduce observed cargo behavior for a rigid perfectly-plastic material approach. However, a solid amount of computational power is needed resulting from the direct monolithic coupling approach of the multi-physics problem of cargo behavior on a vessel in waves, including physical processes with different time scales. Applying the coupled approach in a 3D case of a bulk carrier in waves to account for the "wet base" or "dynamic separation" scenarios would lead to even higher computational costs, due to the solution of double the amount of governing equations.

Chapter 7

Conclusion and Outlook

Modeling the granular cargo of bulk carrier vessels is a complex coupled problem, which requires a multi-physics approach. To numerically model possible cargo failure mechanisms, monolithic VoF-based FV approaches are presented in this thesis, which can capture ”cargo sliding”, ”wet base scenarios” and ”dynamic separation” scenarios.

The sliding cargo model grounds on implementing and validating a rigid perfectly-plastic material model. To study the influence of saturation-dependent material behavior and the failure mechanisms ”wet base” and ”dynamic separation,” the rigid perfectly-plastic material is coupled to a two-phase flow through porous media. A thorough validation of the two-phase flow through a rigid porous medium and the rigid perfectly-plastic model is performed as a foundation for the coupled model. Furthermore, a monolithic incompressible neo-Hookean material model is implemented into the VoF-based FV approach and validated for generic materials. Implemented models are not only applicable to cargo behavior studies but can also be used for more general coastal, geotechnical, and ocean engineering applications. Examples of engineering interest might include landslides, scouring, and deformable seabeds under waves.

In this work, the introduced computational models are applied to the problem of cargo transport on vessels. Studies for a two-dimensional cargo hold under the influence of prescribed motion render the cargo behavior for different properties, loading conditions, and roll motions. As a clear result of these studies, it is found that the cargo shall always be loaded as flat as possible to prevent cargo motion. Sliding can be observed for rolling amplitudes larger than 10°, and wet cargo on top of dry cargo resulting from ”dynamic separation” is demonstrated to initiate catastrophic cargo sloshing. Though coupled studies of a cargo loaded vessel in seaways are possible, the use of guided motion on cargo holds is an appropriate way to obtain insight into cargo behavior and can be extended to three-dimensional cargo holds.

Another possible but unlikely cargo failure mechanism refers to geotechnical liquefaction. Studies in this regard require a compressible elasto-plastic model, including kinematic hardening effects. A mathematical formulation of a compressible neo-Hookean material is derived in Appendix F.1 using the compressibility approach for the pressure correction scheme. At several points in the thesis, it becomes clear that an elasto-plastic material model is needed to adequately address the material behavior and avoid numerical issues along walls. Therefore an elasto-plastic approach for the current FV method based on the general finite strain theory, cf., Neto et al. [92] and Simo et al. [108], is proposed in the Appendix F.2.

Monolithic coupled studies of cargo behavior for vessels in waves include physical processes with different time scales and therefore results in substantial computational efforts. Nevertheless, a 3D feasibility study of the fully coupled problem is conducted and displays promising results that match the reported cargo behavior. Higher accelerations in the front holds of the vessel lead to more significant cargo shifts in these holds when the vessel experiences extreme wave conditions.

Bibliography

[1] A. J. Abbo and S. W. Sloan. A smooth hyperbolic approximation to the Mohr-Coulomb yield criterion. *Computers and Structures*, 54:427–441, 1993.

[2] M. Airai, L. Cheng, and Y. Inoue. 3D Numerical Simulation of Impact Load due to Liquid Cargo Sloshing. *J. of the Society of Naval Architecture of Japan*, 171:177 –184, 1994.

[3] D. W. Airey and J. Ghorbani. Analysis of unsaturated soil columns with application to bulk cargo liquefaction in ships. *Computers and Geotechnics*, 140:104402, 2021.

[4] D. Anderson, G. McFadden, and A. Wheeler. Diffuse-interface methods in fluid mechanics. *Annu. Rev. Fluid Mech.*, 30:139 –165, 1998.

[5] J. P. Bardet. Bounding Surface Plasticity Model for Sands. *Journal of Engineering Mechanics*, 112(11):1198–1217, 1986.

[6] J. Bear. *Dynamics of Fluids in Porous Media.* American Elsevier, New York, 1972.

[7] H. Bian and I. Shahrour. Numerical model for unsaturated sandy soils under cyclic loading: Application to liquefaction. *Soil Dynamics and Earthquake Engineering*, 29:237–244, 2009.

[8] R. I. Borja. On the mechanical energy and effective stress in saturated and unsaturated porous continua. *International Journal of Solids and Structures*, 43:1764–1786, 2006.

[9] H. Bui, R.Fukagawa, K. Sako, and S. Ohne. Lagrangian meshfree particles method (SPH) for large deformation and failure flows of geomaterial using elastic-plastic soil constitutive model. *International Journal for Numerical and Analytical Methods in Geomechanics*, 32:1537–1570, 2008.

[10] H. H. Bui and G. D. Nguyen. A coupled fluid-solid SPH approach to modelling flow through deformable porous media. *International Journal of Solids and Structures*, 125:244–264, 2017.

[11] L. Caretto, A. Gosman, S. Patankar, and D. Spalding. Two Calculation Procedures for Steady Three-Dimensional Flows with Recirculation. *Proceedings of 3rd International Conf. on Numerical Methods in Fluid Mechanics. Univ. Paris*, II, 1972.

[12] ClassNK. Guidelines for the Safe Carriage of Nickel Ore. Guidelines, Nippon Kaiji Kyokai, February 2012.

[13] G. F. Correia. *Bauxite mining and shipping: transportable moisture limit (TML) tests and further cargo assessments for safe shipping*. PhD thesis, Escola Politécnica da Universidade de São Paulo, 2020.

[14] G. H. Cottet, E. Maitre, and T. Milcent. Eulerian formulation and level set models for incompressible fluid-structure interaction. *Mathematical Modelling and Numerical Analysis*, 42:471–492, 2008.

[15] C. A. Coulomb. Essai sur une application des règles de maximis et minimis à quelques problèmes de statique, relatifs à l'architecture. *Mem. Acad. Roy. Div. Sav.*, 7:343–387, 1776.

[16] L. Davidson. Lecture Notes - Numerical Methods for Turbulent Flow. *Chalmers University of Technology*, 2005.

[17] R. de Boer and W. Ehlers. The development of the concept of effective stresses. *Acta Mechanica*, 83:77–92, 1990.

[18] M. J. S. de Lemos. *Turbulence in Porous Media.* Elsevier Science Ltd., 2006.

[19] M. J. S. de Lemos and M. H. J. Pedras. Recent Mathematical Models for Turbulent Flow in Saturated Rigid Porous Media. *Journal of Fluids Engineering*, 123(4):935 – 940, 2001.

[20] M. del Jesus, J. Lara, and I. Losada. Three-dimensional interaction of waves and porous coastal structures. part I: Numerical model formulation. *Coastal Engineering*, 64:57 – 72, 2012.

[21] DELTAMARIN. 38330 DWT GENERAL CARGO CARRIER Jinling Shipyard Oldendorff - Light Weight Calculations. Technical report, DELTAMARIN, 2013.

[22] Y. Di and T. Sato. Computational Modeling of Large Deformation of Saturated Soils Using An ALE Finite Element Method. *Annuals of Disas. Prev. Res. Ins*, 47(C):171–182, 2004.

[23] Y. Di and T. Sato. A practical numerical method for large strain liquefaction analysis of saturated soils. *Soil Dynamics and Earthquake Engineering*, 24:251–260, 2004.

[24] DNV GL. BULK CARGO LIQUEFACTION - Guideline for design and operation of vessels with bulk cargo that may liquefy. Technical report, DNV GL, October 2015.

[25] D. C. Drucker and W. Prager. Soil mechanics and plastic analysis or limit design. *Quarterly of Applied Mathematics*, 10:157–165, 1952.

[26] T. Dunne. An Eulerian approach to fluid-structure interaction and goal-oriented mesh adaptation. *International Journal for Numerical Methods in Fluids*, 51(9-10):1017–1039, 2006.

[27] T. Dunne, R. Rannacher, and T. Richter. Numerical Simulation of Fluid-Structure Interaction Based on Monolithic Variational Formulations. *Institute of Applied Mathematics, University of Heidelberg*, 2009.

[28] W. Düsterhöft-Wriggers, A. Larese, E. Oñate, and T. Rung. Assessment of simplified momentum equations for free surface flows through rigid porous media. *Experimental and Computational Multiphase Flow*, 5:159–177, 2022.

[29] W. Düsterhöft-Wriggers, S. Schubert, and T. Rung. A two-phase Volume of Fluid approach to model rigid-perfectly plastic granular materials. *International Journal for Numerical Methods in Fluids*, in press.

[30] W. Ehlers. Effective Stresses in Multiphasic Porous Media: A thermodynamic investigation of a fully non-linear model with compressible and incompressible constituents. *Geomechanics for Energy and the Environment*, 15:35–46, 2018.

[31] A. Elgamal, Z. Yang, and E. Parra. Computational modeling of cyclic mobility and post-liquefaction site response. *Soil Dynamics and Earthquake Engineering*, 22:259–271, 2002.

[32] F. Engelund. *On the laminar and turbulent flows of ground water through homogeneous sand.* Danish Academy of Technical Sciences / Transactions. Akademiet for de tekniske videnskaber, 1953.

[33] S. Ergun. Fluid Flow through Packed Columns. *Chemical Engineering Progress*, 48:89–94, 1952.

[34] S. E. Feghali. *Novel monolithic stabilized finite element method for Fluid-Structure Interaction*. PhD thesis, Paris Institute of Technology, 2012.

[35] J. H. Ferziger and M. Perić. *Numerische Strömungsmechanik*. Springer, 2002.

[36] J. H. Ferziger and M. Perić. *Numerische Strömungsmechanik*. Springer Verlag, 2008.

[37] P. Forchheimer. Wasserbewegung durch Boden. *Z. Ver. Deutsch. Ing.*, 45:1782–1788, 1901.

[38] M. V. Gent. Formulae to describe porous flow. *Communications on hydraulic and geotechnical engineering, No. 1992-02, Delft University of Technology*, 1992.

[39] M. V. Gent. *Wave Interaction with Permeable Coastal Structures*. PhD thesis, Faculty of Civil Engineering, Delft University of Technology, 1995.

[40] U. Ghia, K. N. Ghia, and C. T. Shin. High-Re Solutions for Incompressible Flow Using the Navier- Stokes Equations and a Multigrid Method. *Journal of Computational Physics*, 48:387–411, 1982.

[41] Global Bauxite Working Group. Report on Research into the Behaviour of Bauxite during Shipping. Technical report, IMO, May 2017.

[42] R. Grin and S. Ruano. On the Prediction of Radii of Inertia and their Effect on Seakeeping. *12th International Marine Design Conference*, Proceedings Volume 3:189 –203, 2015.

[43] Z. Gu and H. Wang. Gravity waves over porous bottoms. *Coastal Engineering*, 15:497–524, 1991.

[44] P. He and R. Qiao. A full-Eulerian solid level set method for simulation of fluid-structure interactions. *Microfluid Nanofluid*, 11:557–567, 2011.

[45] R. Higdon. Absorbing Boundary Conditions for Difference Approximations to the Multi-Dimensional Wave Equation. *Mathematics of Computation*, 47(176):437–459, 1986.

[46] P. Higuera. *Application of computational fluid dynamics to wave action on structures*. PhD thesis, Univ. de Cantabria, Santander, Spain, 2015.

[47] P. Higuera, J. L. Lara, and I. J. Losada. Three-dimensional interaction of waves and porous coastal structures using OpenFOAM. Part I: Formulation and validation. *Coastal Engineering*, 83:243 – 258, 2014.

[48] C. Hirt and B. Nicholls. Volume of Fluid (VOF) Method for the Dynamics of Free Boundaries. *J. Comput. Phys.*, 39:201 – 221, 1981.

[49] P. A. A. V. Hoogstraten, P. M. A. Slaats, and F. P. T. Baaijens. A Eulerian approach to the finite element modelling of neo-Hookean rubber material. *Applied Scientific Research*, 48:193–210, 1991.

[50] T.-J. Hsu, T. Sakakiyama, and P. L.-F. Liu. A numerical model for wave motions and turbulence flows in front of a composite breakwater. *Coastal Engineering*, 46:25 – 50, 2002.

[51] S. Ii, X. Gong, K. Sugiyama, J. Wu, H. Huang, and S. Takagi. A Full Eulerian Fluid-Membrane Coupling Method with a Smoothed Volume-of-Fluid Approach. *Commun. Comput. Phys.*, 12:544–576, 2012.

[52] IMO. AMENDMENTS TO THE INTERNATIONAL MARITIME SOLID BULK CARGOES (IMSBC) CODE, RESOLUTION MSC. 500(105). Technical report, International Maritime Organization, April 2022. Accessed: 2023-05-24.

[53] IMO. AMENDMENTS TO THE INTERNATIONAL MARITIME SOLID BULK CARGOES (IMSBC) CODE, RESOLUTION MSC. 462(101). Technical report, International Maritime Organization, June 2019. Accessed: 2023-05-24.

[54] INTERCARGO. Bulk Carrier Casualty Report - Years 2009 to 2018 and trends. Technical report, International Association of Dry Cargo Shipowners, 2019.

[55] INTERCARGO. Bulk Carrier Casualty Report - Years 2012 to 2021 and trends. Technical report, International Association of Dry Cargo Shipowners, 2021.

[56] Iron Ore Technical Working Group. Development of Amendments to the IMSBC code and suppplements, including evaluation of properties of solid bulk cargoes. The Technical Working Group (TWG) Report #4 ”Reference Tests”. DSC 18/INF.13, International Maritime Organization (IMO), May 2013.

[57] I. Jánosi, D. Jan, K. Szabó, and T. Tél. Turbulent drag reduction in dam-break flows. *Experiments in Fluids*, 37(2):219–229, 2004.

[58] B. Jensen, N. G. Jacobsen, and E. D. Christensen. Investigations on the porous media equations and resistance coefficients for coastal structures. *Coastal Engineering*, 84:56 – 72, 2014.

[59] L. Ju, D. Vassalos, Q. Wang, and Y. Liu. Solid bulk cargo instability during marine transport. *Ocean Engineering*, 186:106089, 2019.

[60] L. Ju, D. Vassalos, Q. Wang, Y. Wang, and Y. Liu. Numerical investigation of solid bulk cargo liquefaction. *Ocean Engineering*, 159:333–347, 2018.

[61] P. Kelly. Mechanics Lecture Notes: An introduction to Solid Mechanics. Part IV. https://pkel015.connect.amazon.auckland.ac.nz/SolidMechanicsBooks/Part_IV/Chapter_1_Hyperelasticity/PDF/Elasticity_04_Isotropic_Hyperelasticity.pdf, 2013. Accessed: 2023-06-05.

[62] N. Koliha. Entwicklung eines 6DOF-Moduls auf der Basis von Quaternionen zur Simulation freier Bewegungen schwimmender Körper. Bachelor thesis, Technische Universität Hamburg, Insitute for Fluid Dynamics and Ship Theory, 2011.

[63] J. Kozeny. Über kapillare Leitung des Wassers im Boden. *Sitzungberg. Akad. Wiss. Wien*, 136:271–306, 1927.

[64] N. Kühl. *Adjoint-Based Shape Optimization Constraint by Turbulent Two-Phase Navier-Stokes Systems.* PhD thesis, Hamburg University of Technology, 2021.

[65] N. Kühl, M. Hinze, and T. Rung. Cahn-Hilliard Navier-Stokes Simulations for Marine Free-Surface Flows. *Experimental and Computational Multiphase Flow*, 4 (3):274–290, 2021.

[66] N. Kühl, J. Kröger, M. Siebenborn, M. Hinze, and T. Rung. Adjoint complement to the volume-of-fluid method for immiscible flows. *Journal of Computational Physics*, 440:110411, 2021.

[67] N. Kühl and T. Rung. Discrete Adjoint Momentum-Weighted Interpolation Strategies. *J. Comput. Phys.*, 467:111474, 2022.

[68] A. Laadhari, R. R. Baier, and A. Quarteroni. Fully Eulerian finite element approximation of a fluid-structure interaction problem in cardiac cells. *Int. J. Numer. Meth. Engng*, 96:712–738, 2013.

[69] A. Larese. *A Coupled Eulerian-PFEM Model for the Simulation of overtopping in Rockfill Dams.* PhD thesis, International Center for Numerical Methods in Engineering, 2012.

[70] A. Larese, R. Rossi, and E. Oñate. Finite Element Modeling of Free Surface Flow in Variable Porosity Media. *Arch. Computat. Methods. Eng.*, 22 (4):637–653, 2015.

[71] A. Larese, R. Rossi, and E. Oñate. Theme B: simulation of the behavior of prototypes of rockfill dams during overtopping scenarios: seepage evolution and beginning of failure. *Proceeding of the XI ICOLD Benchmark Workshop on Numerical Analysis of Dams*, ISBN: 978-84-695-1816-8, 2011.

[72] A. Larese, R. Rossi, and E. Oñate. Simulation of the beginning of failure in rockfill dams caused by overtopping. A: "Dam protections against overtopping and accidental leakage". *CRC Press Taylor & Francis Group*, pages 111–117, 2015.

[73] H. L. Lee. Nickel ore bulk liquefaction a handymax incident and response. *Ocean Engineering*, 139:65–73, 2017.

[74] B. P. Leonard. A stable and accurate convective modelling procedure based on quadratic upstream interpolation. *Computer Methods in Applied Mechanics and Engineering*, 19 (1):59–98, 1979.

[75] C. Leppert. *Mehrphasenmodell fur granulare Medien zur numerischen Untersuchung des Phasenübergangs bei der Entleerung von Silos.* PhD thesis, Technische Universität Carolo-Wilhelmina zu Braunschweig., 2007.

[76] P. Lin. *Numerical modeling of breaking waves.* PhD thesis, Cornell University, 1998.

[77] C. Liu and N. J. Walkington. An Eulerian Description of Fluids Containing Visco-Elastic Particles. *Arch. Rational Mech. Anal.*, 159:229–252, 2001.

[78] P. L.-F. Liu, P. Lin, and T. Sakakiyama. Numerical Modeling of Wave Interaction with Porous Structures. *Journal of Waterway Port Coastal and Ocean Engineering*, 125(6):322 – 330, 1999.

[79] I. J. Losada, J. L. Lara, and M. del Jesus. Modeling the Interaction of Water Waves with Porous Coastal Structures. *Journal of Waterway Port Coastal and Ocean Engineering*, 142(6):03116003, 2016.

[80] X. Luo, J. Brunswig, M. Manzke, N. Koliha, F. Matin, C. Janßen, and T. Rung. Analyses of Coupled Floating Bodies in Seaway. In *2nd International Conference on Violent Flows*, pages 25–27, Nantes, 2012. Editions Publibook.

[81] X. Luo-Theilen and T. Rung. Numerical analysis of the installation procedures of offshore structures. *Ocean Engineering*, 179:116–127, 2019.

[82] R. Manceau, J. R. Carlson, and T. B. Gatski. A rescaled elliptic relaxation approach: Neutralizing the effect on the log layer. *Physics of Fluids*, 14(11):3868–3879, 2002.

[83] M. Manzke. Numerical Simulation of Unsteady Body Motion in Turbulent Flow. Diplom thesis, Technische Universität Hamburg, Insitute for Fluid Dynamics and Ship Theory, 2008.

[84] M. Manzke. *Development of a Scalable Method for the Efficient Simulation of Flows using Dynamic Goal-Oriented Local Grid-Adaptation.* PhD thesis, Hamburg University of Technology, 2019.

[85] Marine Accident Investigation Department. REPORT: M/V ”JIAN FU STAR” R-011-11-DIAM. Investigation Report, Panama Maritime Authority, February 2011.

[86] F. Marinho and C. Pinto. Investigating the water retention in iron ore. In *Unsaturated Soils*, volume 3. 3rd International Conference on Unsaturated Soils, UNSAT 2002, Brazil, CRC Press, 2004.

[87] S. Mirjalili, S. Jain, and M. Dodd. Interface-capturing methods for two-phase flows: An overview and recent developments. *Annual Research Briefs, Center for Turbulence Research, Stanford University*, pages 117–135, 2017.

[88] Z. Mrŏz, V. A. Norris, and O. C. Zienkiewicz. An anisotropic hardening model for soils and its application to cyclic loading. *International Journal for Numerical and Analytical Methods in Geomechancis*, 2:203–221, 1978.

[89] M. C. Munro and A. Mohajerani. Liquefaction Incidents of Mineral Cargoes on Board Bulk Carriers. *Advances in Materials Science and Engineering*, 2016(1):5219474, 2016.

[90] M. C. Munro and A. Mohajerani. Slope stability evaluation of iron ore fines during marine transportation in bulk carriers. *Canadian Geotechnical Journal*, 55(2):258–278, 2018.

[91] S. Muzaferija, M. Peric, P. Sames, and T. Schelin. A two-fluid Navier-Stokes solver to simulate water entry. In *Proc. Twenty-Second Symposium on Naval Hydrodynamics*, pages 638–651. National Academy Press, 1999.

[92] E. Neto, D. Perić, and D. Owens. *Computational Methods for Plasticity - Theory and Applications*. John Wiley & Sons Ltd, 2008.

[93] OEC. New Multidimensional Economic Complexity Rankings, Nickel ore in China. https://oec.world/en/profile/bilateral-product/nickel-ore/reporter/chn?yearExportSelector=exportYear9. Accessed: 2023-05-23.

[94] S. Okazawa, K. Kashiyama, and Y. Kaneko. Eulerian formulation using stabilized finite element method for large deformation solid dynamics. *Int. J. Numer. Meth. Engng*, 72:1544–1559, 2007.

[95] E. Oñate, S. Idelsohn, F. D. Pin, and R. Aubry. The particle finite element method. an overview. *International Journal of Computational Methods*, 1 (2):267–307, 2004.

[96] T. C. Papanastasiou. Flows of Materials with Yield. *Journal of Rheology*, 31(5):385–404, 1987.

[97] S. Patankar and D. Spalding. A calculation procedure for heat, mass and momentum transfer in three-dimensional parabolic flows. *International Journal of Heat and Mass Transfer*, 15(10):1787–1806, 1972.

[98] P. Polubarinova-Kochina and J. M. Roger De Wiest. Theory of Groundwater Movement. *Princeton University Press*, 1962.

[99] J. Poulsen. The deadliest cargo. In Seaways, the Nautical Institute. https://www.nautinst.org/static/uploaded/873739ba-5f22-4835-a40a43fdaf6f9313.pdf, December 2013. Accessed: 2024-07-20.

[100] W. Rankine. On the Stability of Loose Earth. *Philosophical Transactions of the Royal Society of London*, 147:9–27, 1857.

[101] C. M. Rhie and W. L. Chow. Numerical Study of the Turbulent Flow Past an Airfoil with Trailing Edge Separation. *AIAA*, 21(11):1525–1532, 1983.

[102] T. Richter. A Fully Eulerian Formulation for Fluid-Structure- Interaction Problems. *Institute of Applied Mathematics, University of Heidelberg*, 2012.

[103] T. Richter. A Fully Eulerian formulation for Fluid-Structure Interaction Problems. *Journal of Computational Physics*, 233:227–240, 2013.

[104] T. Richter and T. Wick. Finite elements for fluid-structure interaction in ALE and fully Eulerian coordinates. *Comput. Methods Appl. Mech. Engrg.*, 199:2633–2642, 2010.

[105] A. Robinson-Mosher, C. Schroeder, and R. Fedkiw. A symmetric positive definite formulation for monolithic fluid structure interaction. *Journal of Computational Physics*, 230(4):1547–1566, 2011.

[106] G. S. Schajer. Mohr-Coulomb Failure Criterion Expressed in Terms of Stress Invariants. *Journal of Applied Mechanics*, 65:1066–1068, 1998.

[107] M. Schuler. Liquefaction continues to be the deadliest risk for bulk ships. https://gcaptain.com/cargo-liquefaction-continues-to-pose-deadly-risk-to-bulk-carrier-seafarers-intercargo-says/, 2022. Accessed: 2023-05-24.

[108] J. C. Simo and T. J. R. Hughes. *Computational Inelasticity*. Springer, 1998.

[109] SKULD. Nickel ore - a liquefaction risk. https://www.skuld.com/topics/cargo/solid-bulk/cargo-liquefaction/nickel-ore---a-liquefaction-risk/, 2018. Accessed: 2023-05-23.

[110] K. Sugiyama, S. I. S. Takeuchi, S. Takagi, and Y. Matsumoto. A full Eulerian finite difference approach for solving fluid-structure coupling problems. *Journal of Computational Physics*, 230:596–627, 2011.

[111] W. Sumelka. A note on non-associated Drucker-Prager plastic flow in terms of fractional calculus. *Journal of Theoretical and Applied Mechanics*, 52:571–574, 2014.

[112] M. Sussmann. *A Level Set Approach for Computing Solutions to Incompressible Two-Phase Flow*. PhD thesis, University of California, Los Angeles, 1998.

[113] K. Terzaghi. *Erdbaumechanik auf bodenphysikalischer Grundlage*. Wien: F. Deuticke, 1925.

[114] E. Theilen. *Numerical modelling of multi-body hydrodynamics in multi-phase simulations*. PhD thesis, Hamburg University of Technology, 2020.

[115] L. Thorel. LiquefAction: Experiments at Ifsttar. Institut français des sciences et technologies des transports, de láménagement et des réseaux, Presentation, Hamburg, September 2015.

[116] H. Tresca. Mémoire sur l'écoulement des corps solides soumis à de fortes pressions. *C. R. Acad. Sci. Paris*, 59:754–758, 1864.

[117] G. Tryggvason, R. Scardovelli, and S. Zaleski. *Direct Numerical Simulations of Gas-Liquid Multiphase Flows.* Cambridge University Press, 2011.

[118] O. Ubbink. *Numerical Prediction of Two Fluid Systems with Sharp Interfaces*. PhD thesis, Imperial College of Science, Technology & Medicine, 1997.

[119] O. Ubbink and R. Issa. A Method for Capturing Sharp Fluid Interfaces on Arbitrary Meshes. *Journal of Computational Physics*, 153:26–50, 1999.

[120] C. Ulrich. *Smoothed-Particle-Hydrodynamics Simulation of Port Hydrodynamic Problems*. PhD thesis, Technical University Hamburg-Harburg, 2013.

[121] C. Ulrich, M. Leonardi, and T. Rung. Multi-physics SPH simulation of complex marine-engineering hydrodynamic problems. *Ocean Engineering*, 64:109–121, 2013.

[122] T. Unno, M. Kazama, R. Uzuoka, and N. Sento. Liquefaction of Unsaturated Sand Considering the Pore Air Pressure and Volume Compressibility of the Soil Particle Skeleton. *Soils and Foundations*, 48:87–99, 2008.

[123] R. Uzuoka and R. I. Borja. Dynamics of unsaturated poroelastic solids at finite strain. *International Journal for Numerical and Analytical Methods in Geomechanics*, 36:1535 – 1573, 2012.

[124] S. Völkner. Modellierung granularer Bodenphasen in maritimen Mehrphasensimulationen. Master thesis, Technische Universität Hamburg, Insitut für Fluiddynamik und Schiffstheorie, 2013.

[125] S. Völkner, J. Brunswig, and T. Rung. Analysis of non-conservative interpolation techniques in overset grid finite-volume methods. *Computers & Fluids*, 148:39–55, 2017.

[126] S. Völkner, W. R. Wriggers, X. Luo-Theilen, and T. Rung. An Overset-Grid Three-Phase Flow Model for Offshore Operations. *In VI International Conference on Computational Methods in Marine Engineering*, 2015.

[127] R. von Mises. Mechanik der festen Körper im plastisch-deformablen Zustand. *Nachrichten von der Gesellschaft der Wissenschaften zu Göttingen. Mathematisch-Physikalische Klasse.*, 1:582–592, 1913.

[128] J. P. Voß. Entwicklung effizienter Fernfeldrandbedingungen zur simulation des Seegangsverhaltens schwimmender Körper. Diplom thesis, Technische Universität Hamburg, Insitut für Fluiddynamik und Schiffstheorie, 2013.

[129] H. Wang and T. Nishimura. Water retention characteristics of iron ore fines. *Canadian Geotechnical Journal*, 57:1427–1437, 2020.

[130] Z. Wang, J. Zhang, and H. Zhou. Numerical Study on the Influence of Angles of Repose on the Stability of Cargo in a Cargo Hold. *Journal of Physics: Conference Series*, 2195:012001, 2022.

[131] L. Willing. Monolitische Fluid-Struktur Interaktion innerhalb eines Eulerschen Finite-Volumen Verfahrens. Master thesis, Technische Universität Hamburg, Institut für Fluiddynamik und Schiffstheorie, 2015.

[132] K. Wöckner, W. Drazyk, and T. Rung. An efficient VOF-Based RANS Method to Capture Complex Sea States. In *ASME 29th International Conference on Ocean, Offshore and Arctic Engineering (OMAE2010), Shanghai, China*, 2010.

[133] K. Wöckner-Kluwe. *Evaluation of the Unsteady Propeller Performance behind Ships in Waves.* PhD thesis, Hamburg University of Technology, 2013.

[134] W. R. Wriggers and T. Rung. Numerical Modelling of Granular Cargo on Bulk Carriers in Seaway. *In VI International Conference on Computational Methods in Marine Engineering*, 2015.

[135] W. Wu, Y. Li, Z. Zhao, Q. Zheng, C. Zhang, H. Ji, X. Yu, and S. Yu. Quantitative analysis of liquefaction risk of liquefiable solid bulk cargoes during sea transport. *Ocean Engineering*, 258:111751, 2022.

[136] S. Yakubov, T. Maquil, and T. Rung. Experience using pressure-based CFD methods for Euler-Euler simulations of cavitating flows. *Computers & Fluids*, 111:91–104, 2015.

[137] Z. Yang, A. Elgamal, and E. Parra. Computational Model for Cyclic Mobility and Associated Shear Deformation. *Journal of Geotechnical and Geoenvironmental Engineering*, 129:1119–1127, 2003.

[138] H.-S. Yu. *Plasticity and Geotechnics*. Springer, 2006.

[139] J. Zhang, W. Wu, Z. Zhao, and Y. Chen. Numerical study on coupled effect of a vessel loaded with liquefied nickel ore. *Journal of Marine Science and Technology*, 25:520–535, 2019.

[140] H. Zhao, J. B. Freund, and R. D. Moser. A fixed-mesh method for incompressible flow-structure systems with finite solid deformations. *Journal of Computational Physics*, 227:3114–3140, 2008.

[141] Y. Zou, C. Shen, and X. Xi. Numerical Simulations on the Capsizing of Bulk Carriers with Nickel Ores. *The Journal of Navigation*, 66:919–930, 2013.

Appendix A

Finite Volume Method

Details of the applied FVM in the in-house solver FreSCo$^+$, which are not given in the main part of the document, are provided here.

A.1 Interpolation of Face Values

Different approaches can be applied to obtain the value of a variable at a face from the cell centers of the known left and right neighbor cells. Here, the Upwind Differencing Scheme (UDS), Central Differencing Scheme (CDS), flux-blending scheme, and non-orthogonality correction for unstructured meshes are given.

First-Order Upwind Convection Discretization

First-order UDS is given by the definition of the generic variable at the face Θ_f

$$\Theta_f^{UDS} = \begin{cases} \Theta_L, & \dot{m} \geq 0 \\ \Theta_R, & \dot{m} < 0 \end{cases} \tag{A.1}$$

where the mass flux $\dot{m}$ is defined to be positive for flow from the left cell (denoted L) to the right cell (denoted R).

Second-Order Central Differencing Scheme

Linear interpolation of the generic variable in the left cell L and the right cell R to the face by

$$\Theta_f^{CDS} = (1 - \lambda_{CDS})\,\Theta_L + \lambda_{CDS}\,\Theta_R \tag{A.2}$$

gives the CDS. Here λ_{CDS} is determined by the distance of the face to the center of the control volume to the right of the face and $\lambda_{CDS} = 0.5$ for uniform grids.

Flux-Blending Schemes

The flux-blending scheme follows from a linear combination of UDS and CDS by a factor θ

$$\Theta_f = \Theta_f^{UDS} + \theta\left(\Theta_f^{CDS} - \Theta_f^{UDS}\right) . \tag{A.3}$$

Here θ can be chosen by the user to obtain good convergence in specific simulation cases.

Higher-Order Approximations for Convection

For higher-order approximations of the convection term, the face value is reconstructed at three points: downstream D, upstream U, and further upstream UU. Here the further upstream UU point has to be reconstructed for unstructured meshes. A unified formulation for unbounded higher-order face interpolation is given by

$$\Theta_f \approx \Theta_U + \frac{1}{4}\Big[(1+\kappa)(\Theta_D - \Theta_U) + (1-\kappa)(\Theta_U - \Theta_{UU})\Big] \tag{A.4}$$

where κ is the coefficient that determines the convection scheme. For the QUICK scheme by Leonard [74], the coefficient κ is 0.5. The higher-order terms are implemented as deferred corrections in the solution algorithm.

A.2 Non-Orthogonality Correction

Here the non-orthogonality corrections for different terms in the governing equations are presented.

Non-orthogonality Correction for Convection

Applying CDS on an unstructured mesh, the point at which Θ_f is obtained is denoted f' and is not guaranteed to be the real face center. The interpolated value Θ_f is corrected by the multiplication of the derivative of the general variable at point f' with the distance between the positions of f' and f

$$\Theta_f = (1-\lambda_{CDS})\,\Theta_L + \lambda_{CDS}\,\Theta_R + \left(x_i(f) - x_i(f')\right)\left(\frac{\partial\Theta}{\partial x_i}\right)_{f'} . \tag{A.5}$$

The gradient at f' is obtained by linear combinations of the gradients in the left and right neighbor cells, and the gradient approximation given in A.4 is applied.

Non-Orthogonality Correction for Diffusion

To obtain the diffusive flux 2.26 on a non-orthogonal grid, the face area normal A_i is split into an orthogonal part $A_i^{orthog.}$ and a non-orthogonal part $A_i^{non-orthog.}$

$$\left(\frac{\partial\Theta}{\partial x_i}\right)_f A_i = A_i^{orthog.}\left(\frac{\partial\Theta}{\partial x_i}\right)_f + A_i^{non-orthog.}\left(\frac{\partial\Theta}{\partial x_i}\right)_f . \tag{A.6}$$

Decompositions of A_i are chosen according to the stability of the equation system. Three decompositions called minimal correction approach, orthogonal correction approach, and over-relaxed correction are summarized in the unified formulation

$$\left(\frac{\partial\Theta}{\partial x_i}\right)_f A_i = \frac{A}{d}\left[\frac{1}{(\frac{d_m}{d}\frac{A_m}{A})^{\gamma_c}}(\Theta_R - \Theta_L) + \left(\frac{\partial\Theta}{\partial x_i}\right)_f \left(A_i\frac{d}{A} - \frac{d_i}{(\frac{d_m}{d}\frac{A_m}{A})^{\gamma_c}}\right)\right] \tag{A.7}$$

where $\gamma_c = -1$ gives the minimal correction, $\gamma_c = 0$ the orthogonal correction and $\gamma_c = 1$ the over-relaxed correction. The orthogonal part is treated implicitly, whereas the non-orthogonal part is treated as a deferred correction in the solution algorithm.

A.3 Rhie and Chow Interpolation

Using a collocated grid approach with a pressure correction scheme and a CDS interpolation of the face values leads to oscillating pressure and velocity values due to the independence of the pressure gradient on the value at the control volume center P. Therefore Rhie and Chow introduced an interpolation procedure for face values of corrected velocities in [101].

Following a derivation by Davidson [16], a Rhie-Chow velocity in which the pressure gradient is excluded (by addition) is used to interpolate the Rhie-Chow velocity at the faces linearly. To obtain the velocity values at faces from the Rhie-Chow velocity at the faces, the pressure gradient term is subtracted from the Rhie-Chow velocity, and the pressure derivative is evaluated at that face. Therefore the corrected velocity flux becomes

$$\dot{v}^* = \sum_{f(\Delta V_P)} v_{f,i}^* A_{f,i} + \sum_{f(\Delta V_P)} -\left(\frac{A_i d_i}{A_P^{v_i}}\frac{A}{d}\right)_f \left(p_{NB} - p_P - \left(\left(\alpha_{int}\frac{\partial p_P}{\partial x_i} + (1-\alpha_{int})\frac{\partial p_{NB}}{\partial x_i}\right) d_{f,i}\right)\right) \tag{A.8}$$

where the gradient of the pressure in cell centers NB and P is discretized as stated in Eqn. A.9 in appendix A.4 and α_{int} is a constant weighting factor for the Rhie-Chow interpolation.

A.4 Gradient Approximation

Throughout this work, the second-order accurate least square method is applied for approximating gradients at control volume centers. Assembling a regularised equation system over all neighboring cell centers denoted P_j with d_j being the distance from P_j to P gives

$$\operatorname{grad}\Theta_P = \left(d_j^T d_j\right)^{-1} d_j^T \left(\Theta_{P_j} - \Theta_P\right) . \tag{A.9}$$

Solving the equation system gives the least square approximation for the gradient at control volume P.

A.5 Wall Boundary Condition

In the present FV method, the wall boundary condition for the momentum equations is implemented as described in Ferziger and Peric [35]. A non-permeable wall where no slip occurs has to fulfill the condition that the fluid velocity at the wall equals the wall velocity. In the momentum equations, viscous shear forces are used to substitute diffusive fluxes at the wall. Integrating the shear stresses τ_{P_B} at the wall along the wall boundary faces f_b with area A_f in tangential unity direction t_i, the shear force acting on the fluid $f_{i,expl}$ can be obtained from

$$f_{i,expl} \approx t_i \tau_{P_B} A_f \tag{A.10}$$

where the tangential unity vector along the wall t_i can be found by

$$t_i = \frac{(v_{i,P} - v_{i,P_B}) - \left((v_{i,P} - v_{i,P_B}) \cdot A_{i,f}\right) A_{i,f}}{||(v_{i,P} - v_{i,P_B}) - \left((v_{i,P} - v_{i,P_B}) \cdot A_{i,f}\right) A_{i,f}||} . \tag{A.11}$$

The velocity difference between the first cell in the fluid domain P and boundary cell P_B multiplied with the normal vector with the size of the face area $A_{i,f}$ gives the component of the velocity difference along the wall-normal and the subtraction then the tangential component. The shear stress in the boundary cell τ_{P_B} can be expressed by

$$\tau_{P_B} = \mu_{P_B} \left(\frac{(v_{i,P} - v_{i,P_B}) \cdot t_i}{d_{i,f} \cdot A_{i,f}} \right) \tag{A.12}$$

where μ_{P_B} is the viscosity in the boundary cell, and $d_{i,f}$ is the distance vector between the boundary cell and the first inner cell. If $f_{i,expl}$ is applied to the momentum equations explicitly, convergence can be worsened (Ferziger and Peric [35]). Therefore a mixed implicit/explicit formulation with implicit force $f_{i,impl}$

$$f_{i,impl} = \left(\frac{\mu A}{d_i \cdot A_i} \right)_f (v_{i,P} - v_{i,P_B}) \tag{A.13}$$

is used in the coefficient matrix of the momentum equations in the boundary cell

$$A^{v_i}_{i,P_B} -> A^{v_i}_{i,P_B} + f_{i,impl} \tag{A.14}$$

and added on the right hand side of the momentum equations

$$RHS_{i,P_B} -> RHS_{i,P_B} + f_{i,impl} - f_{i,expl} . \tag{A.15}$$

Appendix B

Tables and Conversion Methods

The tables on which the results of the error study for the simplified momentum equations for the free surface flow through rigid porous media are based are presented in this Appendix as well as the methods of the error conversion and derivation of the empiric formulas. In Tab. B.1, the material properties used to create the simulation matrix for the error deviation study are presented. The obtained deviation errors for the simulation matrix are given in Tab. B.2.

B.1 Conversion of Error

The initial geometry ($l_0 = 0.28\text{m}$, $h_0 = 0.14\text{m}$) in Fig. 2.25 of the water column is varied by a specified length increment Δl to a length l and height h. The length l and the height h of the water column are changed such that the area of the column A_{col} ($h \cdot l$) stays constant. A change in the geometry of the remaining water is not carried out. The deviation error E_{c_A} between the air concentration fields of the stated geometries (cf. Tab. B.3) and the initial geometry is calculated according to Eqn. (2.61). Then the deviation error E_{c_A} (given in Tab. B.3) is related to the error measurement in percent, which stems from the division of the length increment Δl by the initial length l_0 of the water column.

Furthermore, to be able to convert all absolute deviation errors E_{c_A} to relative companions, all rows of Tab. B.3 are normalized to an error of 10^{-4} (cf. Tab. B.4). The maximum value of the normalized error in percent is hereafter used to convert the values of the errors of the simulations in percent. This gives conservative results for the estimation of the errors later on.

Table B.1: Properties of porous dam break and corresponding resistance force factor $\tilde{A}$ and $\tilde{B}$ (Engelund) as used in simulations.

D_{50} n	10^{-3} [m]	10^{-2} [m]	10^{-1} [m]	1 [m]
0.1	$\tilde{A} = 7.29 \cdot 10^{3}$ $\tilde{B} = 9.00 \cdot 10^{4}$	$\tilde{A} = 7.29 \cdot 10^{1}$ $\tilde{B} = 9.00 \cdot 10^{3}$	$\tilde{A} = 7.29 \cdot 10^{-1}$ $\tilde{B} = 9.00 \cdot 10^{2}$	$\tilde{A} = 7.29 \cdot 10^{-3}$ $\tilde{B} = 9.00 \cdot 10^{1}$
0.2	$\tilde{A} = 2.56 \cdot 10^{3}$ $\tilde{B} = 2.00 \cdot 10^{4}$	$\tilde{A} = 2.56 \cdot 10^{1}$ $\tilde{B} = 2.00 \cdot 10^{3}$	$\tilde{A} = 2.56 \cdot 10^{-1}$ $\tilde{B} = 2.00 \cdot 10^{2}$	$\tilde{A} = 2.56 \cdot 10^{-3}$ $\tilde{B} = 2.00 \cdot 10^{1}$
0.3	$\tilde{A} = 1.14 \cdot 10^{3}$ $\tilde{B} = 7.77 \cdot 10^{3}$	$\tilde{A} = 1.14 \cdot 10^{1}$ $\tilde{B} = 7.77 \cdot 10^{2}$	$\tilde{A} = 1.14 \cdot 10^{-1}$ $\tilde{B} = 7.77 \cdot 10^{1}$	$\tilde{A} = 1.14 \cdot 10^{-3}$ $\tilde{B} = 7.77 \cdot 10^{0}$
0.4	$\tilde{A} = 5.40 \cdot 10^{2}$ $\tilde{B} = 3.75 \cdot 10^{3}$	$\tilde{A} = 5.40 \cdot 10^{0}$ $\tilde{B} = 3.75 \cdot 10^{2}$	$\tilde{A} = 5.40 \cdot 10^{-2}$ $\tilde{B} = 3.75 \cdot 10^{1}$	$\tilde{A} = 5.40 \cdot 10^{-4}$ $\tilde{B} = 3.75 \cdot 10^{0}$
0.5	$\tilde{A} = 2.50 \cdot 10^{2}$ $\tilde{B} = 2.00 \cdot 10^{3}$	$\tilde{A} = 2.50 \cdot 10^{0}$ $\tilde{B} = 2.00 \cdot 10^{2}$	$\tilde{A} = 2.50 \cdot 10^{-2}$ $\tilde{B} = 2.00 \cdot 10^{1}$	$\tilde{A} = 2.50 \cdot 10^{-4}$ $\tilde{B} = 2.00 \cdot 10^{0}$
0.6	$\tilde{A} = 1.07 \cdot 10^{2}$ $\tilde{B} = 1.11 \cdot 10^{3}$	$\tilde{A} = 1.07 \cdot 10^{0}$ $\tilde{B} = 1.11 \cdot 10^{2}$	$\tilde{A} = 1.07 \cdot 10^{-2}$ $\tilde{B} = 1.11 \cdot 10^{1}$	$\tilde{A} = 1.07 \cdot 10^{-4}$ $\tilde{B} = 1.11 \cdot 10^{0}$
0.7	$\tilde{A} = 3.86 \cdot 10^{1}$ $\tilde{B} = 6.13 \cdot 10^{2}$	$\tilde{A} = 3.86 \cdot 10^{-1}$ $\tilde{B} = 6.13 \cdot 10^{1}$	$\tilde{A} = 3.86 \cdot 10^{-3}$ $\tilde{B} = 6.13 \cdot 10^{0}$	$\tilde{A} = 3.86 \cdot 10^{-5}$ $\tilde{B} = 6.13 \cdot 10^{-1}$
0.8	$\tilde{A} = 1.00 \cdot 10^{1}$ $\tilde{B} = 3.12 \cdot 10^{2}$	$\tilde{A} = 1.00 \cdot 10^{-1}$ $\tilde{B} = 3.12 \cdot 10^{1}$	$\tilde{A} = 1.00 \cdot 10^{-3}$ $\tilde{B} = 3.12 \cdot 10^{0}$	$\tilde{A} = 1.00 \cdot 10^{-5}$ $\tilde{B} = 3.12 \cdot 10^{-1}$
0.9	$\tilde{A} = 1.11 \cdot 10^{0}$ $\tilde{B} = 1.23 \cdot 10^{2}$	$\tilde{A} = 1.11 \cdot 10^{-2}$ $\tilde{B} = 1.23 \cdot 10^{1}$	$\tilde{A} = 1.11 \cdot 10^{-4}$ $\tilde{B} = 1.23 \cdot 10^{0}$	$\tilde{A} = 1.1 \cdot 10^{-6}$ $\tilde{B} = 1.23 \cdot 10^{-1}$

Table B.2: Maximum deviation errors E_{c_A} for all simulated material properties.

D_{50} n	10^{-3} [m]	10^{-2} [m]	10^{-1} [m]	1 [m]
0.1	$E_{c_A} = 3.726 \cdot 10^{-4}$	$E_{c_A} = 1.141 \cdot 10^{-3}$	$E_{c_A} = 2.976 \cdot 10^{-3}$	$E_{c_A} = 2.184 \cdot 10^{-2}$
0.2	$E_{c_A} = 3.149 \cdot 10^{-4}$	$E_{c_A} = 9.382 \cdot 10^{-4}$	$E_{c_A} = 3.736 \cdot 10^{-3}$	$E_{c_A} = 3.287 \cdot 10^{-2}$
0.3	$E_{c_A} = 4.690 \cdot 10^{-4}$	$E_{c_A} = 6.393 \cdot 10^{-4}$	$E_{c_A} = 6.264 \cdot 10^{-3}$	$E_{c_A} = 2.565 \cdot 10^{-2}$
0.4	$E_{c_A} = 5.286 \cdot 10^{-4}$	$E_{c_A} = 2.555 \cdot 10^{-3}$	$E_{c_A} = 8.325 \cdot 10^{-3}$	$E_{c_A} = 2.416 \cdot 10^{-2}$
0.5	$E_{c_A} = 4.420 \cdot 10^{-4}$	$E_{c_A} = 9.498 \cdot 10^{-4}$	$E_{c_A} = 7.780 \cdot 10^{-3}$	$E_{c_A} = 2.316 \cdot 10^{-2}$
0.6	$E_{c_A} = 3.737 \cdot 10^{-4}$	$E_{c_A} = 1.059 \cdot 10^{-3}$	$E_{c_A} = 8.600 \cdot 10^{-3}$	$E_{c_A} = 3.007 \cdot 10^{-2}$
0.7	$E_{c_A} = 3.933 \cdot 10^{-4}$	$E_{c_A} = 1.635 \cdot 10^{-3}$	$E_{c_A} = 9.421 \cdot 10^{-3}$	$E_{c_A} = 2.773 \cdot 10^{-2}$
0.8	$E_{c_A} = 3.021 \cdot 10^{-4}$	$E_{c_A} = 2.275 \cdot 10^{-3}$	$E_{c_A} = 1.086 \cdot 10^{-2}$	$E_{c_A} = 2.256 \cdot 10^{-2}$
0.9	$E_{c_A} = 2.341 \cdot 10^{-4}$	$E_{c_A} = 2.785 \cdot 10^{-3}$	$E_{c_A} = 1.253 \cdot 10^{-2}$	$E_{c_A} = 1.929 \cdot 10^{-2}$

Table B.3: Conversion of error E_{c_A} in percentage

Δl[m]	l[m]	$h = A_{col}/l$[m]	E_{c_A}	$\Delta l/l_0$[%]
$5 \cdot 10^{-4}$	0.2805	0.13975	$2.3576 \cdot 10^{-4}$	0.2
$1 \cdot 10^{-3}$	0.2810	0.13950	$4.7568 \cdot 10^{-4}$	0.3
$5 \cdot 10^{-3}$	0.2850	0.13754	$2.3199 \cdot 10^{-3}$	1.8
$1 \cdot 10^{-2}$	0.2900	0.13517	$4.5427 \cdot 10^{-3}$	3.6
$5 \cdot 10^{-2}$	0.3300	0.11879	$1.9697 \cdot 10^{-2}$	17.9
$1 \cdot 10^{-1}$	0.3800	0.10316	$3.3595 \cdot 10^{-2}$	35.7

Table B.4: Normalised values of Δl and $\Delta l/l_0$ for an error of 10^{-4}.

Δl^*[m]	$E^*_{c_A}$	$\Delta l^*/l_0$[%]
$0.21208 \cdot 10^{-3}$	10^{-4}	0.08
$0.21202 \cdot 10^{-3}$	10^{-4}	0.08
$0.21553 \cdot 10^{-3}$	10^{-4}	0.08
$0.22013 \cdot 10^{-3}$	10^{-4}	0.08
$0.25384 \cdot 10^{-3}$	10^{-4}	0.09
$0.29766 \cdot 10^{-3}$	10^{-4}	0.10

B.2 Derivation of Error Estimation Formula

First, a fit of the data generated in the error study was made using the formula

$$E^{est.}_{c_A} = a_{fit} \left(\frac{D_{50}}{n^{b_{fit}}} \right)^{c_{fit}} \quad . \tag{B.1}$$

The fitting was done for each porosity n individually, applying the NLLS Marquardt-Levenberg algorithm. This led to the constants a_{fit}, b_{fit}, and c_{fit} for each porosity value n. A dependency of a, b and c on the porosity value was observed, and therefore the formula to estimate the error $E^{est.}_{c_A}$ yields

$$E^{est.}_{c_A} = 9.50n \left(\frac{D_{50}}{n^{9.46n}} \right)^{\left(1-n^{1.63}\right)} \quad . \tag{B.2}$$

Appendix C

Nickel and Iron Ore Properties

Material property tables of nickel ore and iron ore cargoes C.1, C.2, C.3 and C.4 are assembled from the literature and given here for completeness.

Table C.1: Properties of nickel ore taken from [12]

Sample origin	Moisture content MC [%]	Angle of repose ϕ [°]	Cohesion C [Pa]
Indonesia	24	7.4	300.0
Indonesia	29	4.0	7900
Indonesia	34	0.0	5200
Phillipines	33	1.1	1800
Phillipines	36	0.0	10700
Phillipines	39	0.0	8300
Phillipines	42	0.0	4500
Phillipines	45	0.0	2700

Table C.2: Properties used for DEM simulations in [12]

Condition	Wet density [kg/m^3]	Angle of repose ϕ [°]	Cohesion C [Pa]
1	1745	4.0	7800
2	1500	11.0	5000

Table C.3: Nickel ore properties from IFSTTAR [115]

Water content w_c [%]	Dry density ρ_d [kg/m^3]	Wet density ρ_{wet} [kg/m^3]	Porosity n	MC [%]
30	1300	1690	0.65	23
34	1360	1820	0.63	25
40	1470	2060	0.60	29
43	1430	2040	0.61	30

Table C.4: Properties of iron ore fines as reported in Munro et al. [90]

Sample Nr.	1	2	3	4	5	6	7	8	9
Initial wet density ρ_{wet} [kg/m^3]	2550	2900	2930	2950	2740	2600	2500	2790	2710
Initial dry density ρ_d [kg/m^3]	2320	2570	2580	2620	2490	2410	2270	2490	2430
Initial void ratio e	0.79	0.62	0.61	0.59	0.67	0.72	0.83	0.67	0.71
Initial porosity n	0.44	0.38	0.38	0.37	0.40	0.42	0.45	0.40	0.42
Initial moisture content MC [%]	9.11	11.53	11.97	11.45	9.17	7.23	9.23	10.72	10.51
Initial degree of saturation s^W [%]	52	88	92	91	63	45	51	75	69
Internal friction angle ϕ [°]	43	49	46	44	43	42	39	48	44
Cohesion C [kPa]	18	6	17	20	28	21	17	18	21

Appendix D

Verification of Immiscible Three-Phase Flow

As not to repeat the already detailed description of the FVM in the last chapters, especially Sec. 2.2, here only the governing equation system will be presented for the incompressible immiscible three-phase flow, including the Eulerian displacement equation to determine strains in the granular material

$$\oint_A v_i \, dA_i = 0 \tag{D.1}$$

$$\int_V \frac{\partial}{\partial t} (\rho v_i) \, dV + \oint_A \left(\rho v_i v_j \right) dA_j = - \oint_A p dA_i + \int_V \rho g_i dV + \oint_A \mu \left(\frac{\partial v_i}{\partial x_j} + \frac{\partial v_j}{\partial x_i} \right) dA_j \tag{D.2}$$

$$\int_V \frac{\partial c_A}{\partial t} dV + \oint_A c_A v_i \, dA_i = 0 \tag{D.3}$$

$$\int_V \frac{\partial c_S}{\partial t} dV + \oint_A c_S v_i \, dA_i = 0 \tag{D.4}$$

$$\int_V \frac{\partial u_i}{\partial t} dV + \oint_A c_S v_j u_i \, dA_j = c_S v_i \, . \tag{D.5}$$

The equations are discretized accordingly to the discrete equations given in the main document, where the fluxes in the momentum and pressure equation are discretized by a blended upwind-central differencing scheme, and the QUICK scheme is applied for both mixture equations. Algorithmically the equations are solved as in the coupled model displayed in Fig. 4.3 without the second loop over the momentum and pressure equation.

After the solution of the second mixture fraction, the soil mixture fraction clipping occurs when the sum of the air and soil mixture fractions are greater than one with $c_S = 1 - c_A$. This also determines the handling at the bifurcation point. It is important to note that with the current formulation (6.15), the water mixture fractions could theoretically occur at the air/soil interface when different discretization methods are applied for the two mixture fraction equations.

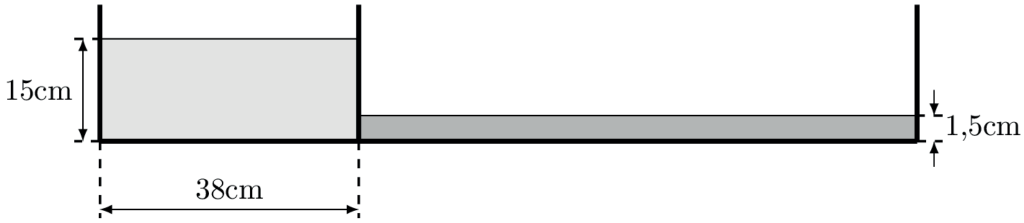

Figure D.1: Initial geometry of three-phase dam break experiments by Jánosi et al. [57]

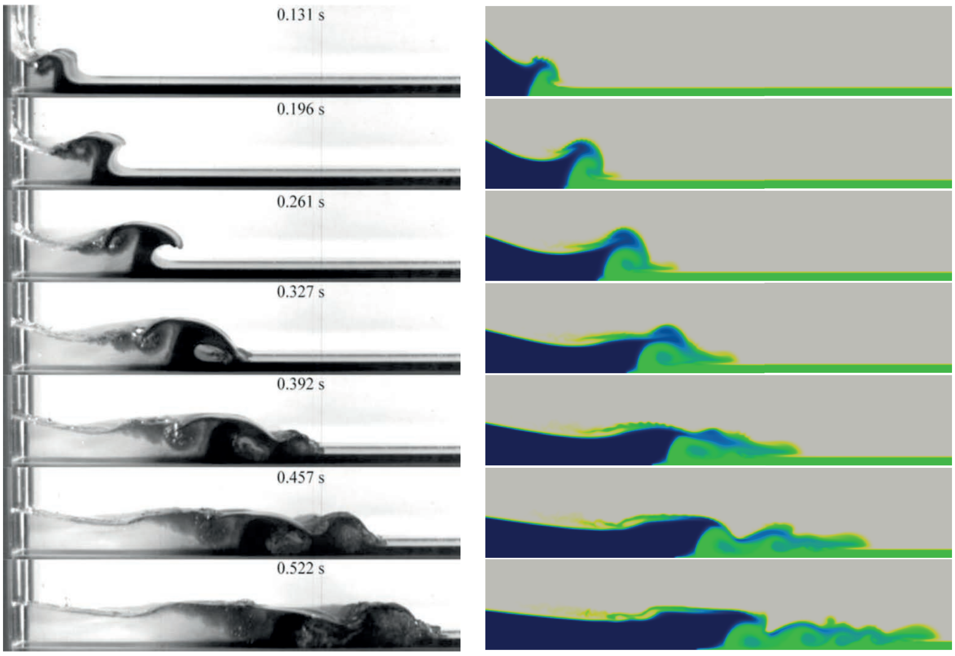

(a) Experiment Jánosi et. al [57]

(b) Numerical results present method

Figure D.2: Snap shots of experimental results from Jánosi et al. [57] and numerical results from the present three-phase VoF, FV method.

To verify the current three-phase approach, a dam break experiment by Jánosi et al. [57] was simulated in Völkner [124] and the results are briefly presented here. Jánosi et al. [57] carried out a series of dam break experiments where a higher column of clear water breaks into a layer of colored water. In the present method, the air phase is considered; therefore, the three phases air, clear water, and colored water are simulated. Figure D.1 displays the dimensions of the experiment's initial state. The clear water is initially separated from the colored water by a floodgate pulled up at the beginning of the experiment. A computational domain with height $h = 0.2$ m and width $L = 1.2$ m is discretized by a rectangular grid with cell sizes $\Delta x_1 = \Delta x_2 = h/100$ and a time step of 10^{-3} s is used. A visual comparison of results from the present method with the experimental data is displayed in Fig. D.2 where grey represents air, green is the colored water, and blue is the clear water.

The front of the numerical results coincides well with the experiments for all time steps. A different breaking behavior at $t = 0.131$ s results from the floodgate opening in the experiments, which is not mimicked in the simulations. The velocity profile in the dam differs when the floodgate is opened, or the dam is left free to break with a higher velocity to the right at the top of the dam in the numerical results than in the experiments. Therefore a higher proportion of clear water at the top of the dam in the numerical results can be observed, and this effect remains present for all subsequent time steps. Interestingly, the shape of the breaking water-free surface at $t = 0.196$ s and $t = 0.261$ s of the three-phase VoF method exhibit a less strong representation than the experimental results. Looking at the two-phase VoF results in Sec. 2.3.5, Fig. 2.23, the same breaking shape outside the porous material exists in the numerical results of both VoF approaches (present method and Del Jesus et al. [20]). In contrast, the level-set approach of Larese et al. [70] gives a sharper representation of the breaking-free surface.

Appendix E

Proof of Concept: ”Jian Fu Star” in Waves

In this appendix, the cargo hold dimensions, as well as the derivation of the vessel properties, are presented.

E.1 Cargo Hold Dimensions

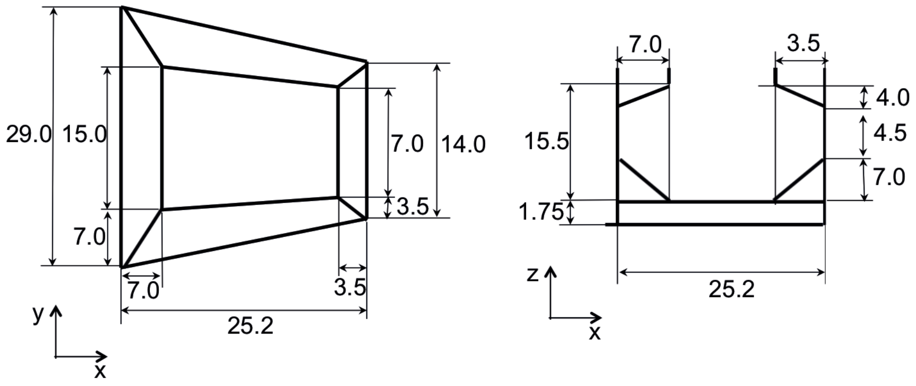

Figure E.1: Geometry of hold one with dimensions given in metres.

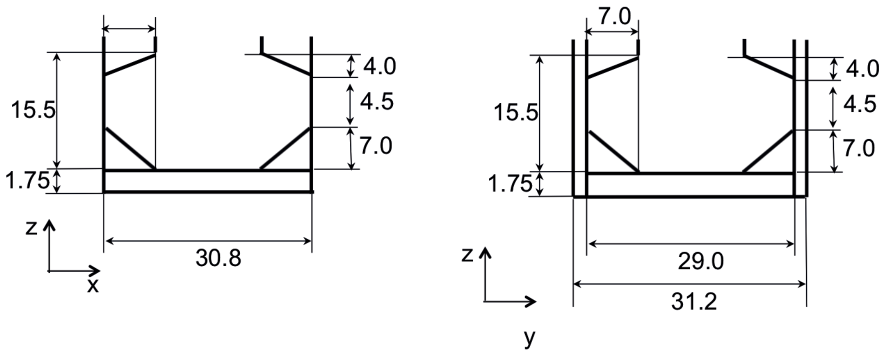

Figure E.2: Geometry of hold two, hold three and hold four with dimensions given in metres.

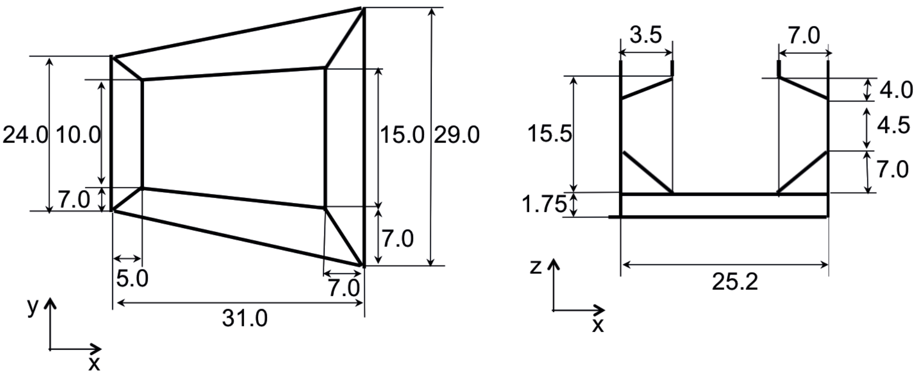

Figure E.3: Geometry of hold five with dimensions given in metres.

E.2 Vessel Data at Incident

The displacement, the center of buoyancy, and the transverse moment of inertia of the water plane area are obtained from hydrostatic calculations of the simulated bulker geometry where the free surface plane is initialised at a draft of 11.8 m. A total mass of the vessel $m_s = 5.7474825 \cdot 10^7$ kg follows from the displacement of $V_w = 5.6073 \cdot 10^4$ m^3 with the density of seawater taken as $\rho^W = 1.025 \cdot 10^3 \frac{kg}{m^3}$. The distance from the keel to the center of buoyancy KB (in the x_3-direction) is 5.859 m.

The Metacentric Radius BM is the distance between the center of buoyancy and the metacentric centrum GM in the x_3-direction. It is calculated by $BM = I_{wl}/V_w$ where I_{wl} is the transverse moment of inertia of the water plane area ($I_{wl} = 2\int_0^L 1/3y^3dx$) of the vessel, and V_w is the volume which is displaced by the vessel. The transverse moment of inertia of the water plane of the vessel I_{wl} follows from the hydrostatic calculations to be $3.809039 \cdot 10^5$ m^4 and therefore BM is equal to 6.793 m. Using formula

$$GM = KB + BM - KG \tag{E.1}$$

to obtain the distance between the keel and the center of gravity KG, KG is found to be 7.652 m. The x_1-coordinate of the center of gravity is the same as the x_1-coordinate of the center of buoyancy and was found to be at $x_1 = 96.660$ m by the hydrostatic calculations. Due to symmetry, the x_2-coordinate of the center of gravity lies midships.

The moments of inertia I_{11}, I_{22} and I_{33} are calculated via the standard assumption that the radii of gyration divided by the width/length of the vessel have a certain ratio. The moments of inertia and the radii of gyration k_{11}, k_{22} and k_{33} are related by

$$I_{11} = k_{11}^2 m_s \tag{E.2}$$

$$I_{22} = k_{22}^2 m_s \tag{E.3}$$

$$I_{33} = k_{33}^2 m_s \ . \tag{E.4}$$

Moreover, in Grin et al. [42], the ratios for a fully loaded bulk carrier are obtained from a detailed weight distribution calculation to be $k_{11} = 0.317\,B$, $k_{22} = 0.244\,Lpp$ and $k_{33} = 0.247\,Lpp$. The final data of the fully loaded vessel is depicted in Tab. E.1.

Table E.1: Derived vessel data for the fully loaded ”Jian Fu Star” at the incident.

V_w (Displacement)	$5.6073 \cdot 10^4\ m^3$
m_s (Weight of ship)	$5.7474825 \cdot 10^4\ t$
KG	$7.652\ m$
x_1-coord. center of gravity	$96.660\ m$
I_{11}	$5.622188080 \cdot 10^9\ kg\ m^2$
I_{22}	$1.14593369537 \cdot 10^{11}\ kg\ m^2$
I_{33}	$1.17428562250 \cdot 10^{11}\ kg\ m^2$

E.3 Empty Hull Properties

Using the information about the data at the incident from Sec. 6.1 and E.2, the cargo in the bulk carrier is initialized via the phase c_S as given in Tab. E.2 using Eqn. (6.12) and integrating the phase c_S over the cells in each hold CV_{hold}

$$m_{ch} = \sum_{CV_{hold}} c_{S,P}\,\rho_P \Delta V_P \tag{E.5}$$

with a cargo density of $\rho_{wet} = 1.7 \cdot 10^3$ kg/m^3 in order to represent the stowage values presented in Tab. 6.1. Therefore the complete cargo mass m_{cargo} results to be 43840.182 t. The complete mass is subtracted from the fully loaded vessel mass m_s to obtain the empty bulk carrier mass m_{emtpy}

$$m_{empty} = m_s - m_{cargo} = 13634.643\ t\ . \tag{E.6}$$

The center of gravity of the empty bulk carrier CoG_{empty} is derived from the center of gravity of the fully loaded vessel CoG_s (96.660 | 0.0 | 7.652) m and the cargos center of gravity CoG_{cargo} by

$$CoG_{i,empty} = \frac{\left(CoG_{i,s}\ m_s - CoG_{i,cargo}\ m_{cargo}\right)}{m_{empty}} \tag{E.7}$$

Table E.2: Cargo initialisiation

	$h_{max} in [m]$	s	cargo mass m_{ch}
Hold 1	12.00	0.008	6140.474 t
Hold 2	12.18	0.010	9329.364 t
Hold 3	12.60	0.009	9468.291 t
Hold 4	12.00	0.008	9483.754 t
Hold 5	12.60	0.010	9418.299 t

to be (92.875 | 0.0 | 8.497) m. The cargo center of gravity is determined by integrating over all cells in the domain

$$CoG_{i,cargo} = \sum_{CV} c_{S,P} \rho_P \Delta V_P x_{i,P} \ , \tag{E.8}$$

where x_i is the position vector of each cell.

The moments of inertia of the cargo around the center of gravity of the fully loaded carrier $CoG_{i,s}$ are obtained by

$$I_{11,cargo} = \sum_{CV} c_{S,P} \rho_P \Delta V_P ((CoG_{2,s} - x_{2,P})^2 + (CoG_{3,s} - x_{3,P})^2) \tag{E.9}$$

$$I_{22,cargo} = \sum_{CV} c_{S,P} \rho_P \Delta V_P ((CoG_{1,s} - x_{1,P})^2 + (CoG_{3,s} - x_{3,P})^2) \tag{E.10}$$

$$I_{33,cargo} = \sum_{CV} c_{S,P} \rho_P \Delta V_P ((CoG_{1,s} - x_{1,P})^2 + (CoG_{2,s} - x_{2,P})^2) \tag{E.11}$$

where $I_{11,cargo}$, $I_{22,cargo}$ and $I_{33,cargo}$ are equal to $2.257577629 \cdot 10^9$ kg m^2, $7.4110159741 \cdot 10^{10}$ kg m^2 and $7.1852582112 \cdot 10^{10}$ kg m^2 respectively. These are subtracted from the moments of inertia of the fully loaded carrier to obtain the moments of inertia of the empty vessel around $CoG_{i,s}$. The moments of inertia tensor $I_{ij,empty}$ around the center of gravity of the empty bulk carrier $CoG_{i,empty}$ are calculated by Steiner's theorem

$$\begin{aligned} I_{ij,empty} &= (I_{ij,s} - I_{ij,cargo}) - \\ m_{empty} &\left(\sum_k \left(CoG_{k,s} - CoG_{k,empty} \right)^2 \delta_{ij} - \left(CoG_{i,s} - CoG_{i,empty} \right) \left(CoG_{j,s} - CoG_{j,empty} \right) \right) . \end{aligned} \tag{E.12}$$

These calculations are done in a user coding environment of the FV framework FreSCo$^+$.

Appendix F

Outlook

The mathematical derivations of a compressible monolithic approach and an elasto-plastic material model approach for FV, VoF are given in this appendix.

F.1 Monolithic Compressible Elastic Model

A different constitutive equation is needed to extend the incompressible elastic material model described in chapter 5 to a compressible model. For further derivation, a compressible neo-Hookean constitutive from Kelly [61]

$$\sigma_{ij} = J^{-1}\left(\lambda ln(J)\delta_{ij} + \eta_S(B_{ij} - \delta_{ij})\right) \tag{F.1}$$

could be used, but the approach could also be extended to other constitutive equations. The volumetric part of the constitutive equation is set to be the pressure

$$p = \frac{\lambda ln(J)}{J} \tag{F.2}$$

which follows from the constitutive equation (F.1). Knowing that J is equal to the determinant of the Lagrangian deformation tensor, the inverse of the determinant of the Eulerian deformation tensor is equal to J

$$J^{-1} = det(F_{ij})\ . \tag{F.3}$$

Also, J is equal to the relationship of the initial and current densities

$$J = \frac{\rho_0}{\rho} \tag{F.4}$$

and therefore, the pressure can be expressed as

$$p = \lambda ln\left(\frac{\rho_0}{\rho}\right) det(F_{ij}) \tag{F.5}$$

or

$$p = \frac{\rho \lambda ln\left(\frac{1}{det(F_{ij})}\right)}{\rho_0} \, . \tag{F.6}$$

If Eqn. (F.6) is reorganised to

$$\rho = \frac{p\rho_0}{\lambda ln\left(\frac{1}{det(F_{ij})}\right)} \, , \tag{F.7}$$

the current density ρ can be calculated from the pressure, the Eulerian deformation tensor, the initial density, and the material constant λ. The derivative of the density in regards to the pressure follows from Eqn. (F.7) to be

$$\frac{\partial \rho}{\partial p} = \frac{\rho_0}{\lambda ln\left(\frac{1}{det(F_{ij})}\right)} \, . \tag{F.8}$$

The derivative $\partial\rho/\partial p$ is used for the extension of the pressure equation (3.2) to compressible materials as described in Yakubov et al. [136] and is furthermore used to link the density correction to the pressure correction. The relationship derived here can replace the equation of state otherwise used to obtain a compressible elastic material.

F.2 Approach for a Monolithic Eulerian Elasto-Plastic Model

In order to obtain an elasto-plastic behavior of the granular material, the incompressible Neo-Hookean elastic model can be extended to an elasto-plastic model. The elasto-plastic model should be formulated in the finite strain space as is already done for the elastic model in chapter 5 since large deformations of the cargo are possible. The presented approach is only valid for perfectly plastic materials and is a combination of the presented elastic model in chapter 5 and the perfectly-plastic model given in chapter 3.

The basic assumption for this approach is that the plastic deformation tensor does not change during the elastic behavior (which complies with the normal elasto-plastic theory) and the elastic deformation tensor does not change during plastic behavior (this does not comply with the standard elasto-plastic theory).

The presented algorithm is a simplification of an elastic predictor/corrector algorithm to obtain the Cauchy stress outlined in Neto et al. [92]

1) Calculate new deformation gradient tensor (Eulerian) from displacement:

$$F_{ij}^{n+1} \tag{F.9}$$

2) Calculate elastic trial state:

$$F_{ij}^{P,n+1,0} = F_{ij}^{P,n} \tag{F.10}$$

$$F_{ij}^{e,n+1,0} = \left(F_{ij}^{P,n}\right)^{-1} F_{ij}^{n+1} \tag{F.11}$$

$$\tau_{ij}^{n+1,0} = -p\delta_{ij} + \eta_S \left(\left(F_{ij}^{e,n+1,0}\right)^{-1} \left(F_{ij}^{e,n+1,0}\right)^{-T} - \delta_{ij}\right) \tag{F.12}$$

2) Check for yielding:

$$\Phi^{n+1,0} = \Phi(\tau_{ij}^{n+1,0}) \tag{F.13}$$

$$If \quad \Phi^{n+1,0} \leq 0 \;\; then: \;\; F_{ij}^{P,n+1} = F_{ij}^{P,n+1,0},\; F_{ij}^{e,n+1} = F_{ij}^{e,n+1,0},\; \tau_{ij}^{n+1} = \tau_{ij}^{n+1,0} \tag{F.14}$$

Exit and use stress in momentum equation

$$\begin{aligned} If \quad \Phi^{n+1,0} > 0 \;\; then: \;\; F_{ij}^{e,n+1} = F_{ij}^{e,n},\; F_{ij}^{p,n+1} &= F_{ij}^{n+1} \left(F_{ij}^{e,n}\right)^{-1}, \\ \mu^{S,n+1} &= \frac{3\alpha_\phi p + k_c}{\sqrt{2\dot{\epsilon}_{ij}\dot{\epsilon}_{ij}}} \end{aligned} \tag{F.15}$$

Exit and use viscous term in momentum equation to add stress

The significant advantage of this method is that time is saved by not having to solve an additional equation system for each outer iteration. A mask differentiates between control volumes in the elastic and plastic regimes. A challenge lies in the approach leading to a disconnected elastic/plastic mask.